SYNTHESIS AND REACTIVITY OF ACETYL COENZYME A SYNTHASE ACTIVE SITE ANALOGUES

by

Megan P. Shalaida

A dissertation submitted to the Faculty of the University of Delaware in partial fulfillment of the requirements for the degree of Doctor of Philosophy in Chemistry and Biochemistry

Fall 2014

ProQuest LLC.
789 East Eisenhower Parkway
P.O. Box 1346
Ann Arbor, MI 48106 - 1346

SYNTHESIS AND REACTIVITY OF ACETYL COENZYME A SYNTHASE ACTIVE SITE ANALOGUES

by

Megan P. Shalaida

Approved: _____
Murray V. Johnston, Ph.D.
Chair of the Department of Chemistry and Biochemistry

Approved: _____
George H. Watson, Ph.D.
Dean of the College of Arts and Sciences

Approved: _____
James G. Richards, Ph.D.
Vice Provost for Graduate and Professional Education

I certify that I have read this dissertation and that in my opinion it meets the academic and professional standard required by the University as a dissertation for the degree of Doctor of Philosophy.

Signed: _____

Charles G. Riordan, Ph.D.
Professor in charge of dissertation

I certify that I have read this dissertation and that in my opinion it meets the academic and professional standard required by the University as a dissertation for the degree of Doctor of Philosophy.

Signed: _____

Joseph M. Fox, Ph.D.
Member of dissertation committee

I certify that I have read this dissertation and that in my opinion it meets the academic and professional standard required by the University as a dissertation for the degree of Doctor of Philosophy.

Signed: _____

John L. Burmeister, Ph.D.
Member of dissertation committee

I certify that I have read this dissertation and that in my opinion it meets the academic and professional standard required by the University as a dissertation for the degree of Doctor of Philosophy.

Signed: _____

George W. Luther III, Ph.D.
Member of dissertation committee

ACKNOWLEDGMENTS

As a little girl, I was taught about faith with regard to religion and Santa Claus or the Easter Bunny. As an adult, while I still believe in the teachings of my early childhood, my understanding of faith has expanded. Faith is not only believing in religious dogma and in a person that you can not see; it is also about believing and having confidence in people. No one has had more faith in me and in my ability to complete the research presented in this dissertation than my teachers, friends and family. I owe my deepest gratitude to the following people for helping me finish this academic journey. I would like to thank my advisor, Dr. Charles G. Riordan, for his continued patience, guidance, support, encouragement and mentorship throughout this entire process. I am also very appreciative of my dissertation committee members, Prof. George Luther, John Burmeister, and Joseph Fox, for taking time out of their schedule to serve on my doctoral committee. I would like to thank Steve Tereniak for his initial studies on the synthesis of the $(S^{iPr}PS^{iPr})Ni(PPh_3)_2$ model system. A special thanks to Glenn Yap (X-ray crystallography), Steve Bai (NMR Spectroscopy), John Dykins (Mass Spectroscopy), Jim Draper and John Famiglietti (instrument shop) and Doug Nixon (glass shop) for all of their friendly conversations, laboratory trainings and assistance. It has been a privilege to work and become friends with the past and present members of Team Riordan. I am grateful for the numerous insightful conversations and fun times we have had and feel lucky to have had a chance to work and learn from all of you. A special thanks to my lab-mates: Tina Maynes, Molly O'Hagan, Piyal Ariyananda, and Jessica Wallick for always being around to chat and

lend a helping hand. I am particularly grateful for the support and encouragement of my friends and family. I would like to thank Erin Heckler, Matthew Kieber-Emmons, Fernando Jove, Kaitlin Schwenk, and Kelly Welsh for their invaluable support and friendship. I am indebted to Matt and Erin for being the best proofreaders anyone could have and the best family away from home. Most of all I would like to thank my family, Mommy, Daddy, John and Peter, for all of your love and for being my biggest supporters during this journey; none of this would have been possible without all of you. And although they are no longer here, I would like to thank Mary and Hugh Marren, John and Helen Shalaida, Joseph E. Boland, and Father William P. Gardner for always watching over me from heaven. Without the faith, confidence and support of those listed above and many others not mentioned this dissertation would not have been completed. So, to everyone who has believed in me, from the bottom of my heart, thank you.

TABLE OF CONTENTS

LIST OF TABLES

LIST OF FIGURES

LIST OF ABBREVIATIONS

ACDS	acetyl-coenzyme A decarbonylase/synthase
acetyl-CoA	acetyl coenzyme A
ACS	acetyl coenzyme A synthase
APT	Attached Proton Test
arom-PS	$Ph_2P(o\text{-}C_6H_4)S$
arom-PSMe	*o*-(diphenylphosphino)thioanisole, $Ph_2P(o\text{-}C_6H_4)SMe$
ATP	adenosine triphosphate
but	1,4-diaminobutane
CH_3-CoFeSP	methylated corrinoid iron-sulfur protein
CH_3-H_4folate	methyl tetrahydrofolate
CoA	coenzyme A
cod	1,5-cyclooctadiene
COdH	carbon monoxide dehydrogenase
CoFeSP, CFeSP	corrinoid iron-sulfur protein
Cys	cysteine
Cys-Gly-Cys	acetyl-CysGlyCys-$C(O)NH_2$
$dadt^{Et}$	*N*,*N'*-diethyl-3,3-diazanonane-1,9-dithiolate
depe	1,2-bis(diethylphosphino)ethane
dimph	4,5-dimethyl-1,2-phenylenediamine
$dmgBF_2$	(difluoroboryl)dimethylglyoximato
Dmp	2,6-dimesitylphenyl
dppe	1,2-bis(diphenylphosphino)ethane
en	1,2-diaminoethane
EPR	Electron Paramagnetic Resonance
equiv.	equivalents
ESI	Electrospray Ionization
Et	ethyl, CH_2CH_3
Fc	Ferrocene
Fc^+	Ferrocinium
Gly	glycine
H_4folate	tetrahydrofolate
His	histidine
HMQC	Heteronuclear Multiple Quantum Correlation
^{i}Pr	isopropyl, $CH(CH_3)_2$
LIFDI	Liquid Injection Field Desorption Ionization
LMCT	ligand-to-metal charge transfer
MAD	multiwavelength anomalous dispersion

Me	methyl, CH_3
MLCT	metal-to-ligand charge transfer
NHE	Normal Hydrogen Electrode
Ni(3-MOC-tsalR)	*N,N'*-bis(3-methoxycarbonylthiosalicylidene)-R-diaminonickel(II)
Ni(tsalR)	*N,N'*-bis(*o*-thiobenzylidene)-diamino nickel(II)
NMR	Nuclear Magnetic Resonance
OTf	triflate, trifluoromethanesulfonate
P^nS	(3-diphenylphosphanyl)-2-thionaphtholato
P-SEt	1-(thioethyl)-2-(diphenylphosphino)ethane
PCy_3	tricyclohexylphosphine
phen	1,2-phenylenediamine
phma	N,N'-1,2-phenylenebis(2-mercaptoacetamide)
PhPepS	N,N'-phenylenebis(o-mercaptobenzamide)
PMe_3	trimethylphosphine
PPh_3	triphenylphosphine
pr	1,3-diaminopropane
PS	$Ph_2PCH_2CH_2S$
PSSP	$Ph_2P(CH_2)_2S(CH_2)_3S(CH_2)_2PPh_2$
py	pyridine
salen	*N,N'*-ethylenebis(salicylideneiminate)
salphen	*N,N'*-1,2-phenylenebis(salicylideneiminato)
salpr	*N,N'*-1,3-propylenebis(salicylideneiminate)
$S^{Et}PS^{Et}$	bis[2-(ethylthio)ethyl]phenylphosphine
$S^{i\text{Pr}}PS^{i\text{Pr}}$	bis[2-(isopropylthio)ethyl]phenylphosphine, $PhP(CH_2CH_2SPr^i)_2$
TEMPO	2,2,6,6-tetramethylpiperidinyloxy
TEMPO-Me	2,2,6,6-tetramethyl-1-piperidinylmethoxide
THF	tetrahydrofuran
tmc	1,4,8,11-tetramethyl-1,4,8,11-tetraazacyclotetradecane
triphos	bis(2-diphenylphosphinoethyl)phenylphosphine

ABSTRACT

Acetyl coenzyme A synthase (ACS) produces acetyl coenzyme A (acetyl-CoA) by combining CH_3 from a methylated corrinoid iron-sulfur protein (CH_3-CoFeSP), CO from carbon monoxide dehydrogenase (COdH) and coenzyme A (CoA). The metalloenzyme facilitates autotrophic growth of anaerobic organisms such as acetogenic, methanogenic, and sulfate-reducing archaea and bacteria. Located in the α-subunit of a 310 kDa $\alpha_2\beta_2$ heterodimer, the active site (A-cluster) contains a Fe_4S_4 cubane bridged by a Cysteine (Cys) residue to a nickel atom (Ni_p, proximal to the Fe_4S_4 cubane) which in turn is bridged through two Cys residues to another nickel atom (Ni_d, distal to the Fe_4S_4 cubane) coordinated by the backbone nitrogen atoms of Glycine (Gly) and Cys residues. Biologically unprecedented nickel-methyl, nickel-carbonyl, and acetyl-nickel intermediates are proposed to occur during catalysis. Notwithstanding extensive experimental and spectroscopic studies, the mechanism of acetyl-CoA synthesis via ACS remains unresolved. The synthesis and reactivity of Ni complexes designed to model the active site of ACS are reported.

To probe the feasibility of Ni(II)Ni(I) or Ni(II)Ni(0) intermediates during catalysis, the synthesis of a dinucleating thiol macrocycle with asymmetric coordination sites was targeted. En route to this ligand, a series of mononuclear nickel thiol-based Schiff base complexes, *N*,*N*'-bis(3-methoxycarbonylthiosalicylidene)-R-diaminonickel(II) (Ni(3-MOC-tsalR)) where R = 1,2-diaminoethane (en), 1,3-diaminopropane (pr), 1,4-diaminobutane (but), 1,2-phenylenediamine (phen), and 4,5-dimethyl-1,2-phenylenediamine (dimph), were synthesized by the reaction of *S*-

(methyl-3-formylsalicylate) dimethylthiocarbamate with the appropriate diamine. The resultant air stable, square-planar complexes were characterized spectroscopically and crystallographically. Structural and electronic effects of altering the diamine backbone from a polymethylene (en, pr, but) to a phenylenediamine (phen, dimph) bridge were observed in the X-ray crystal structures and infrared and NMR spectral properties of the complexes. Cyclic voltammetry studies of Ni(3-MOC-tsalR) (R = en, pr, but, phen, dimph) reveal contrasting results for the different diamine backbones. The cyclic voltammograms for Ni(3-MOC-tsalR) (R = en, pr, but) showed one reversible cathodic wave, assigned as the Ni(II)/Ni(I) reduction. Ni(3-MOC-tsalR) (R = phen, dimph) exhibited an irreversible cathodic peak assigned as a ligand reduction. Attempts to synthesize the asymmetric dinucleating thiol macrocycle using various starting diamines and starting materials at different temperatures and reaction times all failed to produce the desired product. A combination of the poor solubility of Ni(3-MOC-tsalR) (R = en, pr, but, phen, dimph) and the mediocre reactivity of a methyl ester toward amide formation are the main reasons cited for the inability to yield the desired macrocycles.

The tridentate ligand bis[2-(isopropylthio)ethyl]phenylphosphine ($S^{iPr}PS^{iPr}$, ($PhP(CH_2CH_2SPr^i)_2$)) with two thioether donors to mimic the cysteine coordination found in the active site of ACS has been used to investigate the mechanism of methyl transfer. Reaction of $S^{iPr}PS^{iPr}$ with $Ni(cod)_2$ (cod = 1,5-cyclooctadiene) and two equivalents of triphenylphosphine (PPh_3) generated (κ^2- $S^{iPr}PS^{iPr}$)$Ni(PPh_3)_2$. The resultant air and moisture sensitive, tetrahedral complex was characterized spectroscopically and crystallographically. (κ^2- $S^{iPr}PS^{iPr}$)$Ni(PPh_3)_2$ was found to decompose over time in solution to (κ^2-$S^{iPr}PS)_2Ni$. The alkyl transfer reactivity of (κ^2-

$S^{iPr}PS^{iPr})Ni(PPh_3)_2$ was assayed through reactions with alkylcobaloximes, i.e., methyl, methyl-d_3, ethyl, isopropyl and neopentyl. The reaction of methyl and methyl-d_3 derivatives of $RCo(dmgBF_2)_2py$ ($dmgBF_2$ = (difluoroboryl)dimethylglyoximato, py = pyridine) with (κ^2- $S^{iPr}PS^{iPr}$)$Ni(PPh_3)_2$ proceeded in quantitative spectroscopic yields forming the respective alkyl species, [(κ^2-$S^{iPr}PS^{iPr}$)$Ni(PPh_3)R]^+$ (R = CH_3 or CD_3) and $[Co(dmgBF_2)_2PPh_3]^-$. Reactions of (κ^2- $S^{iPr}PS^{iPr}$)$Ni(PPh_3)_2$ with $RCo(dmgBF_2)_2py$, where R = CH_3CH_2 or $CH(CH_3)_2$, yielded ethylene and propylene, respectively, rather than the corresponding Ni-alkyl complex, implicating successful alkyl transfer followed by facile β-hydrogen elimination for these nickel complexes. Kinetics data obtained for the transfer of alkyls (CH_3, CH_3CH_2) to (κ^2- $S^{iPr}PS^{iPr}$)$Ni(PPh_3)_2$ support an S_N2 mechanism similar to that found in the enzyme. This model system suggests that the S_N2 methyl-transfer in ACS can proceed through a Ni(0) intermediate.

Chapter 1

INTRODUCTION

1.1 Nickel

In 1751 at the age of 28, Swedish chemist and metallurgist Alex Frederick Cronstedt isolated a white metal from ore originating in the Los Cu-Co mines in Sweden, and called it nickel.[1] Unaware of its importance, Cronstedt, whose main ambition was to introduce a system for the classification of minerals, found the discovery incidental.[2] Furthermore, well-known chemists of the time were skeptical of Cronstedt's finding. They believed that the substance was an impure regulus of cobalt, comprised of arsenic, copper, and iron. Twenty-four years after its initial characterization, Swedish chemist, Torbern Bergman disproved this theory and confirmed Cronstedt's nickel as a new element. Bergman prepared a large range of alloys and compounds from arsenic, copper and iron to demonstrate that no combination of these elements could duplicate the properties of nickel as described by Cronstedt. While he did concede that Cronstedt's nickel may have been contaminated with some arsenic and cobalt, he believed the bulk material consisted of a new element.[2,3] Despite these results, without the isolation of nickel in a pure form and a practical use, many chemists were still reserved about accepting it as an element.[3] Richter prepared the first pure sample of nickel approximately twenty-five years later and provided a surprisingly accurate description of its properties. Soon after, an alloy, known as German Silver, consisting of copper, nickel, and zinc in varying proportions was found to be a popular substitute for silver in the manufacturing of cutlery, coins

and a variety of other things.[3,4] The popularity of this alloy increased as the development of electroplating allowed silver plating on a German Silver base.[4] The ease of casting and fabrication, the relative resistance to tarnish, and its reasonable cost led to a gradual but steady recognition of nickel as an element by chemists.[3] In 1890 the chemistry of nickel blossomed with Ludwig Mond's observation of nickel tetracarbonyl, the first metal carbonyl.[5] Shortly afterward, the foundations of modern coordination chemistry were laid out by Alfred Werner[6] and research pertaining to nickel began to flourish.

In recent years, chemists were surprised to uncover a positive and significant biological role for nickel in Nature. Until the landmark observation by Bartha and Ordal in 1965, most noteworthy discourses on the topic pertained to its toxicity in plants and organisms.[7] While characterizing two strains of *Alcaligenes* (formerly *Hydrogenomonas*), they noticed that chemolithotrophic growth is dependent on the presence of nickel in the medium.[7,8] The subsequent identification of growth stimulation in plants (*Chlorella vulgaris*)[9a,b] and evidence of its beneficial role in chickens[10a,b] was motivation for numerous studies concerning nickel in biology. In 1975, Dixon, *et al.* reported the seminal finding that jack bean urease possesses tightly associated nickel that is required for activity.[11] As the first description of a nickel-containing enzyme, this find is a milestone in the study of transition metals in Nature. Efforts to shed light on other enzymatic systems that require nickel for catalysis has yielded nine nickel-dependent enzymes: urease, NiFe hydrogenase, carbon monoxide dehydrogenase, acetyl CoA synthase, methyl-coenzyme M reductase, glyoxalase I, acireductone dioxygenase, lactase racemase, and superoxide dismutase.[12] Extensive studies have revealed varying sites, from mononuclear to complex metal clusters, and

a diverse array of chemical transformations for each enzyme. Progress in understanding the structures and mechanisms of these enzymes has been augmented by the design of nickel complexes that mimic their active sites.

Although the initial discovery of nickel was undervalued, over time chemists have developed an appreciation for its significance in industry and remarkable impact in Nature. From its use in the manufacturing of coins, jewelry and automobiles or as a catalyst for numerous industrial and research applications[1], this transition element is nonexclusive. Nickel metalloenzymes play important roles in the global carbon, nitrogen and oxygen cycles and have been implicated in the beginning of life. The coordination chemistry of this ubiquitous metal encompasses a variety of geometries and oxidation states. In this dissertation, the relevance and promiscuity of nickel is discussed through a study of coordination complexes employed as biomimetic models of the metalloenzyme, acetyl coenzyme A synthase (ACS).

1.2 Acetyl Coenzyme A Synthase/Carbon Monoxide Dehydrogenase

Acetyl coenzyme A synthase/carbon monoxide dehydrogenase (ACS/COdH) is a Ni-Fe-S bifunctional metalloenzyme that catalyzes the following important biological reactions, equations 1 and 2:

$$CO_2 + 2H^+ + 2e^- \rightleftharpoons CO + H_2O \quad (1)$$

$$CH_3\text{-}Co(III)FeSP + CO + CoA\text{-}SH \rightleftharpoons CoA\text{-}S(CO)CH_3 + Co(I)FeSP + H^+ \quad (2)$$

COdH is responsible for the reversible two-electron reduction of atmospheric CO_2 into CO, eq. 1. ACS combines CH_3 from a methylated corrinoid iron-sulfur protein (CH_3-CoFeSP), CO from COdH and coenzyme A (CoA) to synthesize acetyl coenzyme A (acetyl-CoA), eq. 2. Once formed, acetyl-CoA is converted into cellular carbon or

respired as acetate depending on the metabolic needs of the cell.[1] Microorganisms containing the ACS/COdH enzyme are found in a diverse range of anaerobic environments from bogs to cow rumen to the human intestines to extreme environments such as volcanic and hydrothermal vents.[13,14] More specifically, this enzyme is present in acetogenic, methanogenic, and sulfate-reducing archaea and bacteria that utilize the Wood-Ljungdahl pathway for autotrophic carbon fixation.[15,16] ACS/COdH catalyzes the final steps of this organometallic pathway involving biologically unprecedented methyl-nickel, nickel-carbonyl and acetyl-nickel intermediates.[17,18] Collectively, these organisms play a significant role in the global carbon cycle through the introduction and removal of greenhouse gases from the environment.[19] The ability of these primitive microbes to use CO and CO_2 as a source of energy has implicated them in the chemoautotrophic origin of life.[20] The presence of this enzyme at the beginning of life, its position in the global carbon cycle and the biological organometallic intermediates that are formed in its catalytic cycle has generated motivation and interest for the study of nickel in biochemistry. Understanding the mechanism of this enzyme will provide insight into the geometries, coordination numbers and oxidation states of nickel in biological systems.

1.2.1 Chemoautotrophic Origin of Life

It is hypothesized that life began approximately four billion years ago within a 0.5 billion-year period, between when Earth is thought to have cooled enough to allow life and when photosynthetic organisms appeared.[21] The materials presumed to be present during this time period define the theories outlining life-promoting events. Chemoautotrophic models assume a primordial environment consisting of simple inorganic molecules.[21] H_2, CO_2, CO, N_2, NH_3, sulfides, phosphates and trace amounts

of several transition metals including iron, nickel, manganese, cobalt and zinc are suggested to have been present at volcanic and hydrothermal vents, where the first set of autocatalytic reactions may have occurred.[1,20,22] Independent, but complimentary ideas concerning their reactions suggest Ni-Fe-S minerals similar to greigite, (SNiS)(Fe_4S_4)(SFeS), as Nature's first catalyst.[20,23] Wächtershäuser and coworkers demonstrated that an aqueous slurry of coprecipitated nickel and iron sulfides converted CO and CH_3SH into the activated thioester CH_3-CO-SCH_3, which hydrolyzed to acetic acid. In the absence of nickel no reaction was observed, indicating that iron alone does not afford carbon fixation under these conditions.[20] The thioester intermediate in this reaction is akin to the formation of acetyl-CoA in equation 2 above. Analogous to the nickel and iron sulfides, the Ni-Fe-S ACS enzyme condenses CO, a methyl group donated by CH_3-CoFeSP and CoA. Likewise, just as acetyl-CoA is a universal source of carbon and energy to the modern cell of acetogenic, methanogenic, and sulfate-reducing archaea and bacteria, the thioester produced here is an energy-rich and highly reactive compound utilized as fuel for primordial organisms.[23] The reactivity and elemental parallels between the Ni-Fe-S minerals and ACS/COdH suggests the Wood-Ljungdahl pathway of carbon fixation, of which ACS/COdH is an integral piece, as the first biochemical pathway. This finding insinuates that ACS/COdH is an ancient enzyme responsible for the existence of early organisms in CO_2-rich atmospheres at the origin of life.[16,20,23]

1.2.2 ACS/COdH as part of the Global Carbon Cycle

ACS/COdH is a key player in the biological process of microbial fixation, linking it to the global carbon cycle.[24] This biogeochemical cycle exchanges carbon between four major reservoirs: atmosphere, land, ocean and sediments. Movement of

carbon within the biosphere is the result of various chemical, physical, geological and biological processes.[19,25] The global carbon cycle encompasses the fundamental idea that one organism's waste products are another organism's fuel. Specifically the reduction of CO_2 to organic carbon, followed by the oxidation of carbon molecules to CO_2 provides the biomass and energy required for life, respectively. The cycling of atmospheric gases such as CO_2, CO, and CH_4, usually thought of as harmful pollutants and by-products, are essential to anaerobic metabolism.[19] Figure 1.1 shows ACS/COdH as well as acetyl-CoA decarbonylase/synthase (ACDS) and their contributions to CO_2, CO and CH_4 production and consumption on earth.[24]

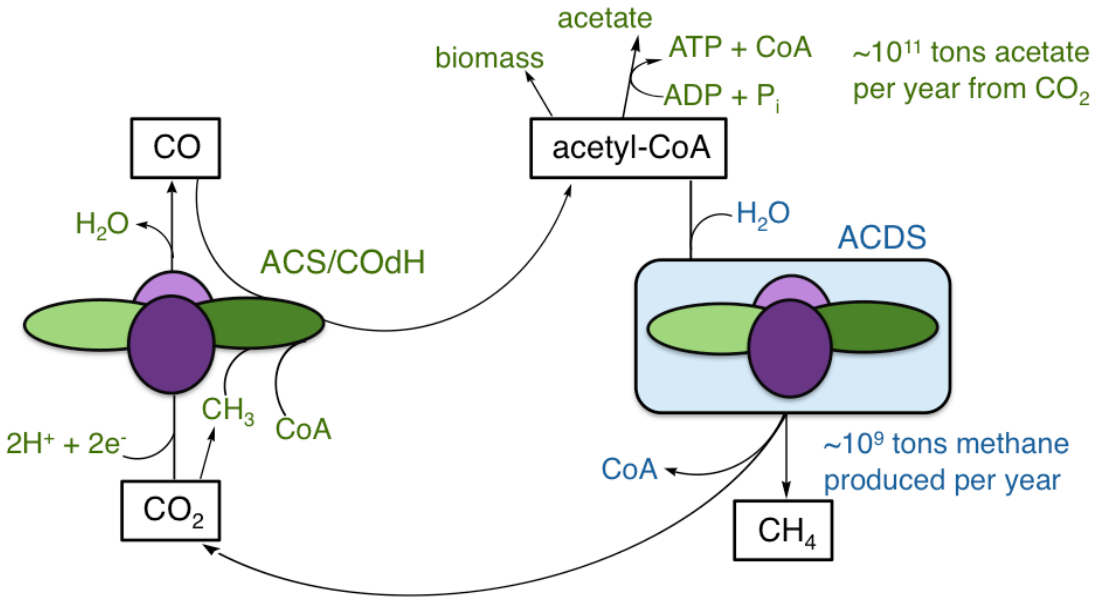

Figure 1.1. The production and consumption of CO_2, CO and CH_4 by ACS/COdH and ACDS in the microbial carbon cycle. Reprinted with permission.[24]

Widely spread in Nature, ACS/COdH by way of the Wood-Ljungdahl pathway serves multiple functions for a variety of anaerobic organisms. Acetogenic bacteria produce approximately 10^{11} tons of acetate from CO_2 annually by autotrophic growth in a variety of places: surface soils, deep subsurface sediments, the gastrointestinal tracts of animals and the digestive system of humans. These organisms use ACS/COdH to convert CO_2 into acetyl-CoA as a means to biomass or acetate.[24,26,27] Methanogenic archaea generate an estimated 10^9 tons of methane per year via ACDS, a multimeric complex variant of ACS/COdH. In these organisms the Wood-Ljungdahl pathway functions in reverse, decomposing acetyl-CoA into methane and CO_2.[24,28] Sulfate-reducing bacteria also operate ACS/COdH in reverse, generating metabolic energy by coupling the oxidation of acetate to H_2 and CO_2 with the reduction of sulfate to sulfide.[26,29] To complete the microbial carbon cycle, the excess acetate and methane formed is oxidatively recycled back to CO_2 by additional organisms and enzymes.[19] Collectively, microbes make a living on the cycling of oxidized and reduced carbon.

The global carbon cycle circulates carbon among atmosphere, land and ocean reservoirs on timescales from days to many millennia while geologic reservoirs exhibit even longer timescales. Increased anthropogenic emissions upset the balance of CO_2 in the atmosphere; the oxidation of carbon molecules to CO_2 surpasses the reduction of CO_2 to organic carbon.[30] The atmospheric CO_2 levels measured 400 ppm at Mauna Loa Observatory in May 2013, the highest level recorded since the inception of continuous CO_2 monitoring in the 1950's. Amidst the trend of an approximately 2 ppm per year level increase, the long-term evolution of this balance will determine the extent of human induced climate change and the necessary requirements for stabilizing

atmospheric CO_2 concentrations at any given level.[30] Through the formation and removal of greenhouse gases, it is evident that ACS/COdH via the Wood-Ljungdahl pathway is an essential part of life and the global carbon cycle. Understanding the catalytic mechanisms that encompass this pathway is key in the development of new catalysts to lower greenhouse gas levels, restoring the balance of CO_2 in the atmosphere.

1.2.3 The Wood-Ljungdahl Pathway of Carbon Fixation

Although previously described as the first biochemical avenue of life the Wood-Ljungdahl pathway of carbon fixation remained unacknowledged until 1936. The discovery of the first acetogenic bacterium, *Clostridium Aceticum*, which synthesizes acetate from CO_2 and H_2, sparked interest in the mechanism of autotrophic CO_2 fixation.[31] An early experiment by Barker and Kamen showed that $^{14}CO_2$ was converted to both the methyl and carboxyl groups of acetate.[32] Several reviews highlight the historical developments that led to the resolution of the Wood-Ljungdahl pathway, shown in Figure 1.2.[14,16,26]

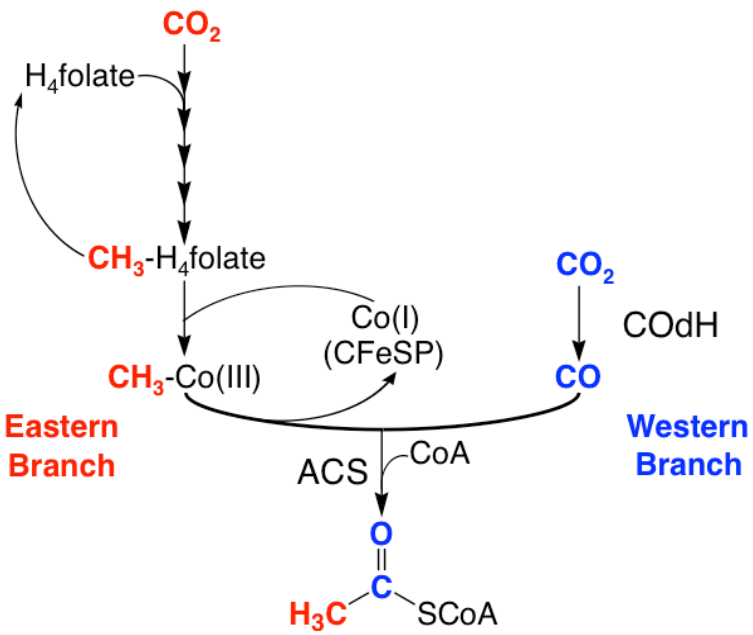

Figure 1.2. Wood-Ljungdahl pathway of autotrophic carbon fixation.[26,33] Reprinted with permission from Hegg, E.L. *Acc. Chem. Res.* **2004**, *37*, 775-783. Copyright 2004 American Chemical Society.[33]

Overall, two molecules of CO_2 are converted to the methyl and carbonyl groups of acetyl-CoA via the formation and cleavage of a series of organometallic bonds. There are two entrances for CO_2 into the pathway, the eastern and western branches. The eastern branch requires six electrons and six enzymes for the synthesis and transfer of a methyl group from CO_2 to a corrinoid iron-sulfur protein (CoFeSP).[26] Formate dehydrogenase converts CO_2 to formate then formyl-H_4folate synthetase catalyzes its conversion to 10-formyl-H_4folate. Next, a cyclohydrolase converts 10-

formyl-H_4folate to 5,10-methenyl-H_4folate. Subsequently, 5,10-methenyl-H_4folate is reduced by dehydrogenase to 5,10-methylene-H_4folate, which is further reduced by reductase to methyl tetrahydrofolate (CH_3-H_4folate). Lastly, methyltransferase catalyzes the methyl group shift from CH_3-H_4folate to CH_3-CoFeSP initiating the western branch of the pathway.[13]

The western branch of the Wood-Ljungdahl pathway is deceptively simple. Despite consisting of only one bifunctional enzyme, ACS/COdH, this branch is the central component of the entire pathway. The second molecule of CO_2 is reduced to CO and then combined with a methyl group from CH_3-CoFeSP and CoA to synthesize acetyl-CoA according to equations 1 and 2 above. As discussed already, acetyl-CoA is then used in cellular biosynthesis or respired as acetate in the generation of ATP.[13] The discovery of ACS/COdH activity was a fundamental breakthrough in the research of this pathway.[34] Consequently, studies of the pathway have focused on characterizing the active site and mechanism of ACS/COdH.

1.3 ACS/COdH Crystal Structure

Several crystal structures of the bifunctional enzyme, ACS/COdH have been reported.[35,36,37] The 310 kDa $\alpha_2\beta_2$ heterodimer is comprised of a variety of metalloclusters in different subunits. As shown in Figure 1.3A, the β subunits located in the middle of the protein are made up of two C- and B-clusters bridged by one D-cluster; while the α subunits found at the terminal ends of the protein each contain one A-cluster. The catalytic functions of the enzyme are fairly independent, with β subunits responsible for COdH activity and α subunits responsible for ACS activity, equations 1 and 2, respectively.

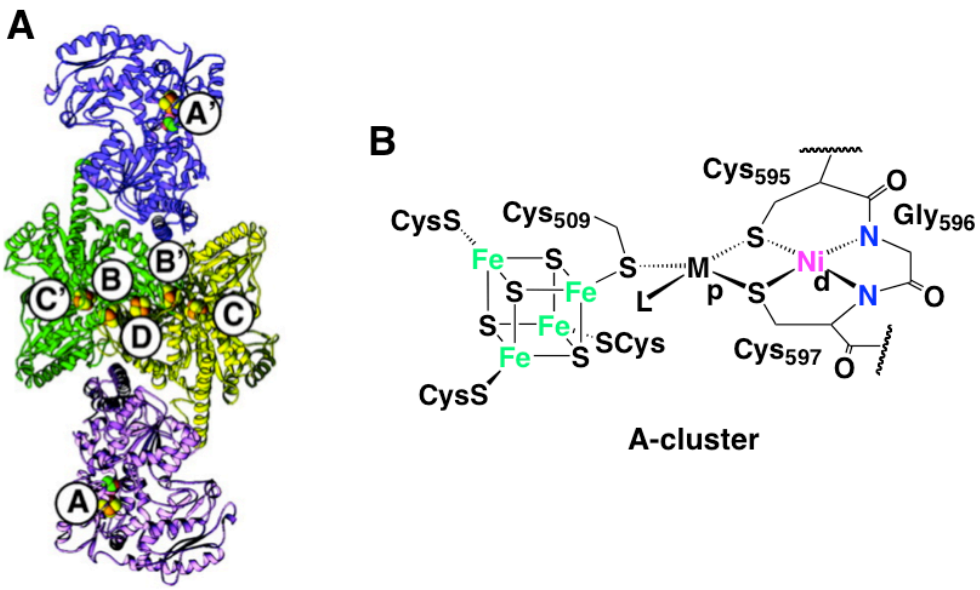

Figure 1.3. (**A**) X-ray crystal structure of ACS/COdH from *M. thermoacetica* with metallocluster locations identified. From Doukov, T.I., Iverson, T.M., Seravalli, J., Ragsdale, S. W., Drennan, C.L. *Science* **2002**, *298*, 567-572. Reprinted with permission from AAAS.[35] (**B**) Structure of the A-cluster.[35, 36, 37]

Crystal structures of the A-cluster, Figure 1.3B, reveal a unique assembly of metals. The active site contains a Fe_4S_4 cubane bridged by a Cysteine (Cys) residue to a metal site (M_p, proximal to the Fe_4S_4). M_p is then bridged through two Cys side chain residues to a square planar nickel (Ni_d, distal to the Fe_4S_4) coordinated by the backbone nitrogen atoms of Glycine (Gly) and Cys residues. Additionally a fourth, still unidentified, non-protein ligand is bound to M_p, completing its coordination sphere.[35,36,37] Using multiwavelength anomalous dispersion (MAD) X-ray experiments

the composition of M_p has been shown to be variable with either Ni, Zn, or Cu occupying the site.[35,36,37] Despite its promiscuous nature, research has shown that Ni occupies the M_p site in the catalytically active enzyme.[38,39,40,41] Overall, these results indicate that the M_p site can have different geometries and oxidation states, whereas the Ni_d site always corresponds to a square-planar nickel suggesting that the M_p site is involved in catalysis.

X-ray analysis of the β subunits unveil the B- and D-clusters as $[Fe_4S_4]^{2+}$ cubanes that provide an electron transfer pathway between external redox agents and the C-cluster.[36,42] The structure of cluster C, responsible for COdH activity, has been uncovered in several different proteins. Collectively, all of the structures revealed an unprecedented metallocluster described as a distorted [Ni-Fe_3-S_4] cubane coordinated to a unique Fe site, Figure 1.4.[36,35,42,43] The Fe_3S_4 subsite is coordinated by three Cys residues and has two bridging sulfides to Ni and one bridging sulfide to the unique Fe site, which is also bound to Cys and Histidine (His) residues. Discrepancies between the reported structures arise in the coordination sphere of Ni; the structures possess a bridging cysteine thiolate[42], a sulfide bridge[43,44], or no bridge[36,35] between the Ni and unique Fe site. Ligands ranging from Cys residues[43,35], to possibly CO[36], to unidentifiable[42] are also reported to be attached to Ni. Attempts to resolve these inconsistencies and identify the catalytic active site involve crystallizing the C-cluster with bound substrate.[45,46,47,48,49] Collectively, these structural studies do not support a catalytic role for a bridging sulfide in the enzyme mechanism.

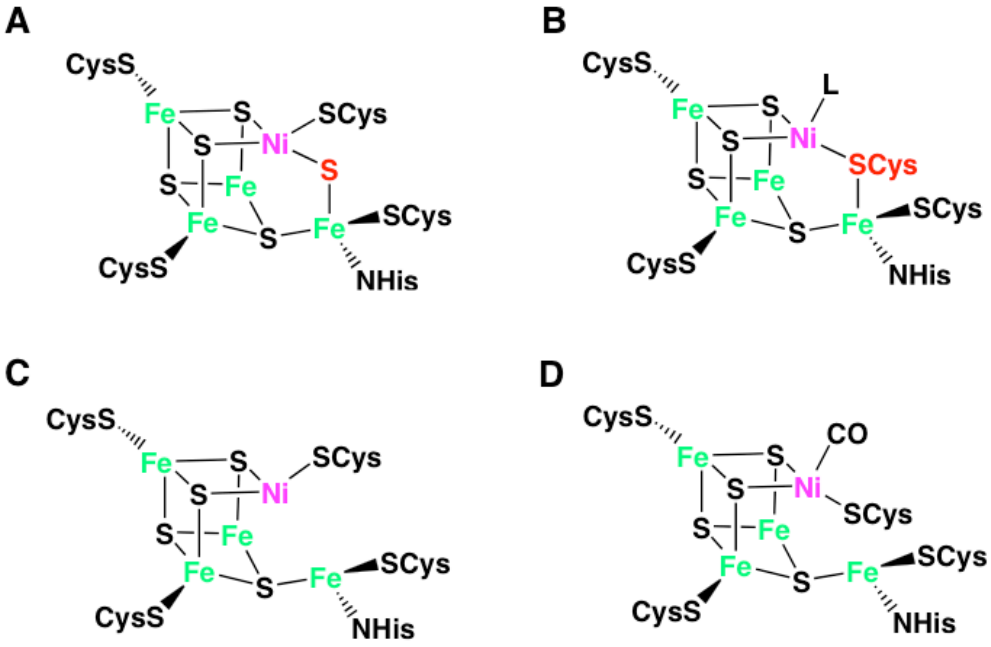

Figure 1.4. (**A**) Structure of the C-cluster from *C. hydrogenoformans*.[43] (**B**) Structure of the C-cluster from *R. rubrum*.[42] (**C**) Structure of the C-cluster from *M. thermoacetica.*[35] (**D**) Structure of the C-cluster from *M. thermoacetica* with CO modeled in the apical coordination site at the Ni ion.[36]

The catalytic activities of ACS and COdH are linked together by the production and use of CO. CO_2 reduced to CO at the C-cluster migrates through a hydrophobic tunnel to the A-cluster to participate in the synthesis of acetyl-CoA.[35,36,50,51,52] The long, narrow, interior channel spans ~138 Å from A-cluster to A-cluster with branches to each C-cluster, Figure 1.5. The most direct route for the shuttling of CO is the ~67 Å stretch of tunnel between A' and C' or A and C.[35]

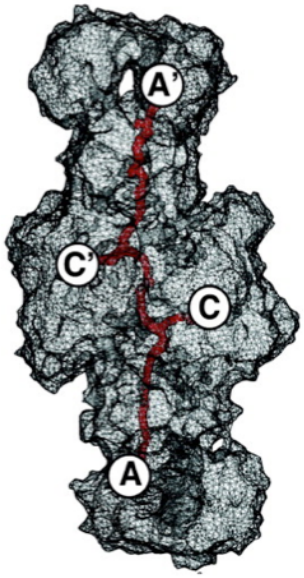

Figure 1.5. X-ray crystal structure of ACS/COdH from *M. thermoacetica* with the ~138 Å hydrophobic tunnel outlined in red. From Doukov, T.I., Iverson, T.M., Seravalli, J., Ragsdale, S. W., Drennan, C.L. *Science* **2002**, *298*, 567-572. Reprinted with permission from AAAS.[35]

In addition to binding CO, ACS interactions with CH_3-CoFeSP and CoA are essential to catalytic progression. Therefore it is not surprising that crystallographic studies have captured two conformations of the α subunit with regard to the CO tunnel: open and closed.[36] In the closed conformation the A-cluster is buried within the protein with limited solvent access and is connected to the C-cluster via the CO-tunnel. Conversely, in the open conformation the entrance to the CO tunnel is blocked, exposing the A-cluster to the protein surface providing greater solvent/substrate accessibility.[36] These structurally characterized conformations are proposed to serve a

mechanistic role in ACS catalysis. The observed structural changes may control the sequence of events in the catalytic cycle by choreographing the binding and dissociation of the substrates and products required for catalysis. The flexible architecture of the α subunit also accounts for the diverse catalytic intermediates involved in the mechanism.

Although ACS and COdH catalysis are coupled together via the CO-tunnel, the two reactions catalyzed are distinct from one another. They occur in different subunits of the protein and at disparate active sites. To characterize the reaction intermediates and elucidate the catalytic mechanisms of ACS and COdH it is easier to regard them as separate entities. Despite the thought provoking controversies and fascinating chemistry surrounding COdH catalysis, this dissertation will focus on the equally intriguing debates and lingering questions concerning the mechanism of ACS catalysis. Detailed reviews highlighting the important facets of COdH chemistry are available elsewhere.[30,53,24]

1.4 Characterized States of the A-cluster

Two forms of the A-cluster have been spectroscopically characterized, an oxidized state (A_{ox}) and a one electron reduced CO-adduct (A_{red}-CO). In the absence of exogenous reductants or CO, the A-cluster exists in its most oxidized form, A_{ox}. The electronic configuration of A_{ox} is described as diamagnetic (S = 0) with an $[Fe_4S_4]^{2+}$ cluster and two Ni^{2+} centers occupying the proximal and distal metal sites.[54] The absence of an EPR signal and Mössbauer parameters diagnostic of an $[Fe_4S_4]^{2+}$ cluster are positive evidence for this assignment.[55,56] The paramagnetic (S = ½) A_{red}-CO state is produced by the reduction of A_{ox} under an atmosphere of CO.[57] The A_{red}-CO state exhibits a characteristic rhombic EPR signal, g = 2.08, 2.07 and 2.03, often

referred to as the NiFeC signal. The label is derived from the observed hyperfine broadening of the EPR spectrum upon isotopic perturbation with either ^{61}Ni or ^{57}Fe or when reduced under ^{13}CO.[58] This isotope sensitivity of the NiFeC signal implies spin coupling among the three nuclei in the A_{red}-CO state. This state is also characterized by a strong carbonyl stretching band (ν_{CO}) in the infrared spectrum of the protein at 1996 cm^{-1}, consistent with a terminally bound CO molecule.[59,60] Based on the observed ^{13}CO hyperfine splitting in the EPR spectrum, CO is expected to bind to a reduced Ni site. Additionally, Mössbauer experiments in conjunction with the UV-visible spectrum of the A_{red}-CO state indicate that the [Fe_4S_4] cluster remains oxidized, [Fe_4S_4]$^{2+}$.[56] Collectively, the spectroscopically observed data described the electronic configuration of the A_{red}-CO state as [Fe_4S_4]$^{2+}$-Ni_p^{1+}(CO)-Ni_d^{2+}.[54]

1.5 Proposed Mechanisms of ACS Catalysis

The key to ACS catalysis is nickel's ability to form bonds with carbon. Amidst the possibility of multiple oxidation states and geometries for nickel and the different conformations of the ACS/COdH protein structure, it is not surprising that a variety of mechanisms are proposed and debated in the literature.[18,13,17,36,35] Collectively, they can be placed into one of two distinct categories based on the electronic structure of the intermediates formed during catalysis: paramagnetic or diamagnetic. Introduced by Ragsdale and coworkers, the paramagnetic mechanism assumes a one-electron reduction of the A_{ox} state, to a Ni(I) species followed by methylation or carbonylation.[61,18] Alternatively, Lindahl and coworkers suggest a two electron reduction of the A_{ox} state to a Ni(0) species followed by methylation in the diamagnetic mechanism.[62,63,17] In conjunction with the contrasting oxidation states of the A-cluster during catalysis a key distinction between these mechanisms relates to

whether or not the paramagnetic A_{red}-CO state is a catalytically relevant intermediate in acetyl-CoA synthesis. The paramagnetic mechanism insists that it is, while the diamagnetic mechanism maintains the opposite viewpoint.[64,63] Regardless of the differences, both mechanisms propose substrate binding exclusively at the Ni_p site as shown below in Figures 1.6 and 1.7.

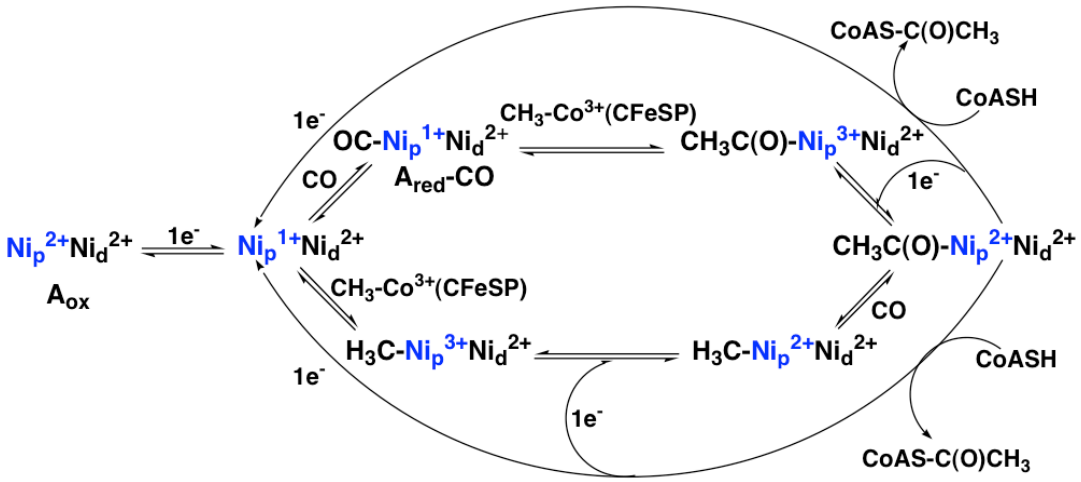

Figure 1.6. Proposed paramagnetic mechanism of ACS catalysis.[18]

1.5.1 Paramagnetic Mechanism

Initiation of the paramagnetic catalytic cycle, Figure 1.6, involves the reductive activation of the inactive A_{ox} state to a $Ni_p^{1+}Ni_d^{2+}$ species followed by carbonylation or methylation.[18] Pulse-chase studies demonstrate that the methyl and carbonyl groups bind to ACS in a random manner.[61] In the "carbonylation-first" branch of the

mechanisms, the $Ni_p^{1+}Ni_d^{2+}$ species bind CO to form the A_{red}-CO intermediate. Next the addition of a methyl group produces an acetyl-$Ni_p^{3+}Ni_d^{2+}$ intermediate, which is quickly reduced to form an acetyl-$Ni_p^{2+}Ni_d^{2+}$ species by a one-electron shuttle. In the "methylation-first" branch of the mechanism, the $Ni_p^{1+}Ni_d^{2+}$ species binds a methyl group producing a methyl-$Ni_p^{3+}Ni_d^{2+}$ intermediate, which is rapidly reduced through a one-electron shuttle to bring about a methyl-$Ni_p^{2+}Ni_d^{2+}$ species. Carbonylation of the methyl-$Ni_p^{2+}Ni_d^{2+}$ intermediate then occurs, resulting in the same acetyl-$Ni_p^{2+}Ni_d^{2+}$ species formed above. The nucleophilic attack of CoA on the acetyl-$Ni_p^{2+}Ni_d^{2+}$ intermediate completes the catalytic cycle by releasing two electrons and the product acetyl-CoA. One electron is transferred to the A-cluster regenerating the active $Ni_p^{1+}Ni_d^{2+}$ state, and the other is dispatched to the internal electron shuttle for reduction of the Ni_p^{3+} intermediates formed during the next cycle of catalysis.[18]

The identity of the electron shuttle in the catalytic cycle is unknown. Nevertheless, ferredoxin and the $[Fe_4S_4]$ cube of the A-cluster have been suggested as possible external and internal electron transfer agents, respectively.[18,13] The $[Fe_4S_4]$ cube of the A-cluster is an unlikely candidate however, since its rate of reduction is approximately 200 times slower than the methyl transfer, which is quickly reduced by an internal electron shuttle in the paramagnetic mechanism.[65] Studies have shown that ferredoxin can stimulate the CO/[1-^{14}C]-acetyl-CoA exchange reaction and it forms an electrostatically stabilized complex with ACS/COdH.[34,66] Recently, researchers have demonstrated that ferredoxin can also act as an electron donor for the reductive activation of the A_{ox} state, as well as play a role in an internal electron transfer that occurs during the reaction of CoA with acetyl-$Ni_p^{2+}Ni_d^{2+}$ in the final step of the catalytic cycle.[18] In spite of the positive evidence for ferredoxin as the electron shuttle,

experiments have revealed that it is not required in the final reaction of the catalytic cycle, indicating that another shuttle for electron transfer must exist, working separately or in concert with ferrodoxin.[18]

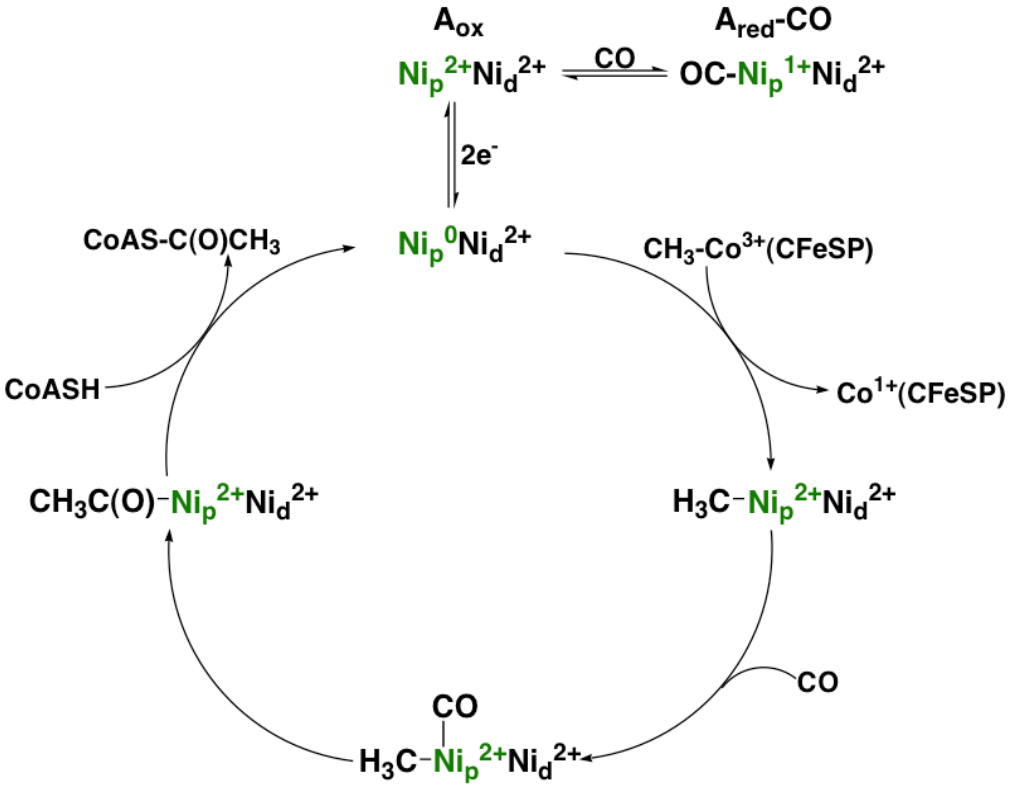

Figure 1.7. Proposed diamagnetic mechanism of ACS catalysis.[63]

1.5.2 Diamagnetic Mechanism

An alternate mechanism, Figure 1.7, proposed by Lindahl and coworkers avoids the requirement of an one-electron shuttle to stabilize Ni_p^{3+} species, by

consisting solely of diamagnetic intermediates.[62,67] A two-electron reduction of A_{ox} to $Ni_p^0Ni_d^{2+}$ begins the catalytic cycle. Although zero valent nickel is biologically unprecedented, it has been suggested that the $[Fe_4S_4]^{2+}$ cluster, as well as Ni_d modify the properties of the thiolate ligands of Ni_p producing a stabilizing effect. The reductively activated state, $Ni_p^0Ni_d^{2+}$, then accepts a methyl group from CH_3-Co^{3+}FeSP generating a CH_3-$Ni_p^{2+}Ni_d^{2+}$ intermediate via oxidative addition. Next, CO originating from the C-cluster binds and inserts into the nickel-methyl bond affording the acetyl intermediate, $CH_3C(O)$-$Ni_p^{2+}Ni_d^{2+}$. To complete catalysis, nucleophilic attack of CoA liberates the product acetyl-CoA and regenerates the active $Ni_p^0Ni_d^{2+}$ state.[17,62,63] This mechanistic proposal does not assign a catalytic role to the A_{red}-CO species, instead it considers the A_{red}-CO to be an inhibitory state. Researchers have shown that high CO concentrations suppress acetyl-CoA synthesis, as a result they suggest the A_{red}-CO state is a reversible, non-productive off-pathway species.[68,69]

1.6 Outstanding Issues in ACS Catalysis

Besides the on-going debate concerning the position of the A_{red}-CO state within the catalytic cycle, there are also a number of additional controversies pertaining to the mechanism. Advocates of the diamagnetic mechanism cite the lack of observable EPR signals for the acetyl-$Ni_p^{3+}Ni_d^{2+}$ and methyl-$Ni_p^{3+}Ni_d^{2+}$ intermediates as major flaws in the paramagnetic cycle. Supporters of the paramagnetic mechanism note that the occurrence of a $Ni_p^0Ni_d^{2+}$ state in the active site of the enzyme, as proposed by the diamagnetic cycle, would be unprecedented in biology. Critics of both mechanisms point out that only one possible catalytic intermediate, A_{red}-CO, out of the many suggested has been spectroscopically characterized. Regardless of the detailed

mechanism, more research is needed to understand the synthesis of acetyl-CoA and to elucidate the mechanism of catalysis by the enzyme and by synthetic complexes.

Some of the key issues that need to be addressed include but are not limited to the following: the order and location of substrate binding, the source and number of electrons required for reductive activation of the A-cluster, and structural and conformational changes of the A-cluster and the protein during catalysis, respectively. Another unsettled issue is the oxidation state of the nickel-methyl intermediate and the mechanism of methyl transfer from CoFeSP to nickel. Further studies are also required to establish the role of A_{red}-CO as an inhibited state or catalytic intermediate. The preparation of ACS model systems for structural and spectroscopic comparison with the enzymatic intermediates is an appealing idea. It is conceivable that organometallic nickel complexes can embody similar properties of the A-cluster if designed appropriately. The concerns above combined with the potential knowledge to be gained from biomimetic complexes of ACS prompted an investigation of A-cluster analogues.

The research results presented in this dissertation focus on the design, synthesis and reactivity of synthetic analogues of the A-cluster. In Chapter 2, binuclear mixed valent, Ni(II)Ni(I) or Ni(II)Ni(0), complexes were pursued to gain insight into the electronic structures of the catalytic intermediates present during ACS catalysis. Amid this investigation, a series of mononuclear nickel Schiff base complexes, *N,N'*-bis(3-methoxycarbonylthiosalicylidene)-R-diaminonickel(II) (Ni(3-MOC-tsalR)) where R = 1,2-diaminoethane (en), 1,3-diaminopropane (pr), 1,4-diaminobutane (but), 1,2-phenylenediamine (phen), and 1,2-dimethyl-4,5-phenylenediamine (dimph), were synthesized and spectroscopically characterized. In

Chapter 3, a new ligand, bis[2-(isopropylthio)ethyl]phenylphosphine ($S^{iPr}PS^{iPr}$, ($PhP(CH_2CH_2SPr^i)_2$), and its metal complex, (κ^2- $S^{iPr}PS^{iPr}$)$Ni(PPh_3)_2$ (PPh_3 = triphenylphosphine), were synthesized to address the lingering questions surrounding the oxidation state of the nickel-methyl intermediate and the mechanism of methyl transfer from CoFeSP to nickel. To test the viability of a zero valent nickel intermediate, the reaction of (κ^2- $S^{iPr}PS^{iPr}$)$Ni(PPh_3)_2$ with $MeCo(dmgBF_2)_2py$ (Me = methyl, $dmgBF_2$ = (difluoroboryl)dimethylglyoximato, py = pyridine) was monitored by ^1H, ^{31}P, ^2H NMR, electronic absorption and mass spectroscopies. Furthermore, the mechanism of alkyl transfer was characterized through kinetic studies and comparison to other alkyl substrates. The preparation and study of these active site model systems provides a platform to understand mechanistic aspects of ACS catalysis and more broadly the structure-function relationship of nickel in this fascinating metalloenzyme.

Chapter 2

SYNTHESIS AND STRUCTURE OF BIOMIMETIC MODELS OF THE A-CLUSTER IN ACETYL COENYZME A SYNTHASE

2.1 Introduction

During the catalytic synthesis of acetyl coenzyme A (acetyl-CoA), acetyl coenzyme A synthase (ACS) combines methyl (CH_3) from a methylated corrinoid iron-sulfur protein (CH_3-CoFeSP), carbon monoxide (CO) from carbon monoxide dehydrogenase (COdH) and coenzyme A (CoA). Biologically unprecedented nickel-methyl, nickel-carbonyl and acetyl-nickel intermediates are proposed to form during catalysis. In spite of widespread spectroscopic and biochemical studies, the mechanism by which acetyl-CoA is synthesized remains elusive. Unraveling this mystery will provide insight into the chemistry of nickel in biological systems. This chapter focuses on synthesizing biomimetic models of the enzyme active site.

2.1.1 Questions surrounding the mechanism of acetyl-coenzyme A synthase

The catalytic synthesis of acetyl-CoA occurs at the A-cluster of acetyl-coenzyme A synthase (Figure 1.3b). The molecular structure of the active-site cluster for ACS catalysis contains an Fe_4S_4 cubane bridged by a cysteine (Cys) residue to a nickel atom (Ni_p, proximal to the Fe_4S_4 cubane). Ni_p is then bridged through two Cys side chain residues to a square planar nickel (Ni_d, distal to the Fe_4S_4 cubane) coordinated by the backbone nitrogen atoms of glycine (Gly) and Cys residues. Additionally a fourth, still unidentified, non-protein ligand is bound to Ni_p, completing

its coordination sphere.[35,36,37] The catalytic assembly of CH_3, CO, and CoA to yield acetyl-CoA is proposed to occur at a single metal center, Ni_p, however the metal oxidation states for each step are unknown. The oxidized form of the A-cluster (A_{ox}) which has been formulated as $\{[Fe_4S_4]^{2+}\text{-}Ni_p^{2+}\text{-}Ni_d^{2+}\}$, cannot accept CH_3 from a CoFeSP[65,62] or bind CO[64]; therefore, before substrate binding can occur, a reductive activation is required. Two competing mechanisms have been proposed, paramagnetic and diamagnetic. These differ in the assignment of the Ni_p oxidation state, and highlight lingering questions concerning the mechanism. The paramagnetic mechanism proposes a one-electron reduction of the A_{ox} state to a $Ni_p^{1+}Ni_d^{2+}$ species, and random binding of the methyl and carbon monoxide substrates followed by ordered binding of coenzyme A.[61,18] The diamagnetic mechanism proposes a two-electron reduction of the A_{ox} state to a $Ni_p^{0}Ni_d^{2+}$ species, and an ordered binding of all of the substrates, methyl followed by carbon monoxide and then coenzyme A.[17,62,63] Additionally, a key distinction between these mechanisms relates to whether or not the paramagnetic A_{red}-CO state, produced by the reduction of A_{ox} under an atmosphere of CO, is a catalytically relevant intermediate in acetyl-CoA synthesis. The paramagnetic mechanism suggests that the A_{red}-CO state is on the catalytic pathway[61,18], while the diamagnetic mechanism ascribes the A_{red}-CO species to a CO-inhibited form of the enzyme.[68,69] An integral part of the proposed reaction mechanisms for catalysis at the A-cluster, is the flexibility of the Ni_p site, which accommodates a variety of oxidation state and coordination geometries. X-ray crystallography has found the geometry of Ni_p in the oxidized form of the A-cluster to be square planar.[35,36,37] Upon activation to the low valent Ni(I) or Ni(0) state, this geometry is proposed to change to tetrahedral.[36] The desire to understand the unique chemistry that occurs at the A-

cluster of ACS has prompted the preparation of model systems for structural and spectroscopic comparison.

2.1.2 Synthetic Model Studies

Reviews provide a succinct survey of model compounds that have been synthesized and analyzed.[33,70,71] Numerous structural analogues, ignoring the Fe_4S_4 cubane unit, have been prepared and studied in attempts to resolve the uncertainties surrounding the reaction mechanism of ACS. One approach focuses on the synthesis of binuclear models; specifically, the generation of reduced Ni_p sites and their reactivity with CO. Typical models of the active site include N_2S_2 coordinating ligands mimicking the Ni_d site, which sulfur bridge to a Ni_p model site coordinated by chelating diphosphine ligands (Figure 2.1-2.3). Phosphine ligands are able to stabilize low oxidation states; hence, they provide a useful environment for studying the various oxidation states proposed for Ni_p. Mascharak and coworkers reported the synthesis of a binuclear model with a dicarboxamide-dithiolate ligated Ni(II) atom sulfur-bridged to a Ni(II) center chelated by 1,2-bis(diphenylphosphino)ethane (dppe), [Ni^{II}(dppe)Ni^{II}(PhPepS)] (PhPepS = N,N'-phenylenebis(o-mercaptobenzamide) (Figure 2.1)[72,73] [Ni^{II}(dppe)Ni^{II}(PhPepS)] was easily reduced with sodium dithionite or sodium borohydride forming a one-electron reduced Ni(I)Ni(II) species, based on its EPR spectrum. Passage of CO through a dimethylformamide solution of the reduced species generated the CO-adduct, [Ni^{I}(CO)(dppe)Ni^{II}(PhPepS)]$^{-}$, which displayed a strong ν(C=O) band at 1997 cm^{-1}, as well as an EPR signal consistent with a five-coordinate, distorted square-pyramidal P_2S_2N ligation to a Ni(I) center, $g_1 = 2.20$, $g_2 = 2.12$, $g_3 = 2.05$.[72,73] This model exhibited chemical properties similar to those

proposed for the binuclear active site of ACS; however, no X-ray structural characterization of the reduced Ni(I) species or the CO-adduct was reported.

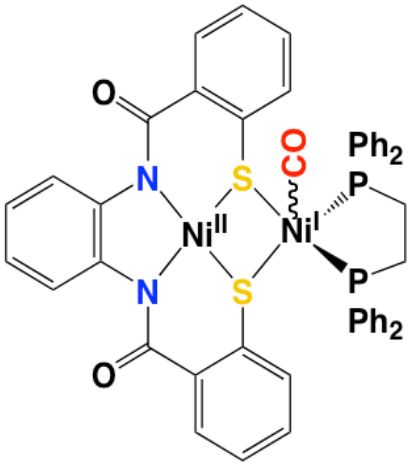

Figure 2.1. $[Ni^{I}(CO)(dppe)Ni^{II}(PhPepS)]^{-}$ model complex synthesized by Mascharak and coworkers.[72]

Krishnan et al. utilized a Cys-Gly-Cys peptide to generate a square planar Ni(II) complex, and a binuclear derivative of this complex, Ni(CysGlyCys)Ni(depe) (depe = 1,2- bis(diethylphosphino)ethane (Figure 2.2a).[74] Cyclic voltammograms of Ni(CysGlyCys)Ni(depe) displayed two one-electron reduction processes, a reversible reduction at -828 mV and a quasi-reversible event at -1641 mV (vs. NHE in acetonitrile). These consecutive reductions were assigned to the mixed valent species, Ni(II)Ni(I) and Ni(II)Ni(0), in which the diphosphine coordinated Ni is reduced. Although the Ni(II)Ni(II) state of this complex does not react with CO, cyclic voltammetry experiments performed under CO (1 atm) showed that the reduced form

binds CO. Krishnan et al. proposed that CO binding occurred in a three-step process involving reduction of the Ni(II)Ni(II) state to a Ni(II)Ni(I) state followed by the binding of CO to the one-electron reduced metal and further reduction to a Ni(II)Ni(0)-CO state (Figure 2.2b).[74] These results are consistent with the proposal that the Ni_p site is suitable for reduction and is a possible binding site for CO in the ACS mechanism; however, neither the reduced or CO-bound Ni(CysGlyCys)Ni(depe) species have been characterized by spectroscopic or structural studies.

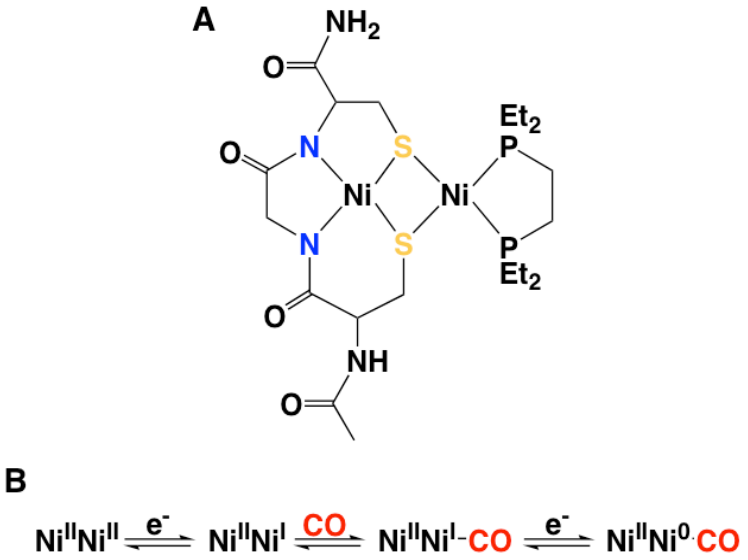

Figure 2.2. (**A**) Ni(CysGlyCys)Ni(depe) model complex synthesized by Krishnan et al.[74] (**B**) Proposed electrochemical process for the reaction of Ni(CysGlyCys)Ni(depe) with CO.[74]

A similar complex, Ni(phma)Ni(depe) (phma = N,N'-1,2-phenylenebis(2-mercaptoacetamide), was synthesized by Dougherty (Figure 2.3).[75] Electrochemical

experiments revealed that the binuclear complex exhibited behavior similar to that previously observed for the reaction of Ni(CysGlyCys)Ni(depe) with CO. According to cyclic voltammetry, Dougherty proposed that the Ni(II)Ni(II) state was reduced to a Ni(II)Ni(I) state followed by binding of CO to the one-electron reduced metal and then reduction to a Ni(II)Ni(0)-CO species. In an effort to spectroscopically and structurally characterize these complexes, Ni(phma)Ni(depe) was reduced chemically using sodium/mercury amalgam or decamethylcobaltocene, producing a mixed-valent Ni(II)Ni(I) binuclear complex in solution as evidenced by EPR spectroscopy. Solutions of the reduced species in dimethylformamide react rapidly with CO; however, the apparent instability of the reduced species ultimately formed trinuclear $[Ni_3(phma)_2]^{2-}$ and $Ni(depe)(CO)_2$ (Figure 2.3).[75] All of these models exhibit chemical properties akin to those proposed for the binuclear active site of ACS; however, further studies are necessary to synthesize an isolable reduced or CO-bound binuclear species.

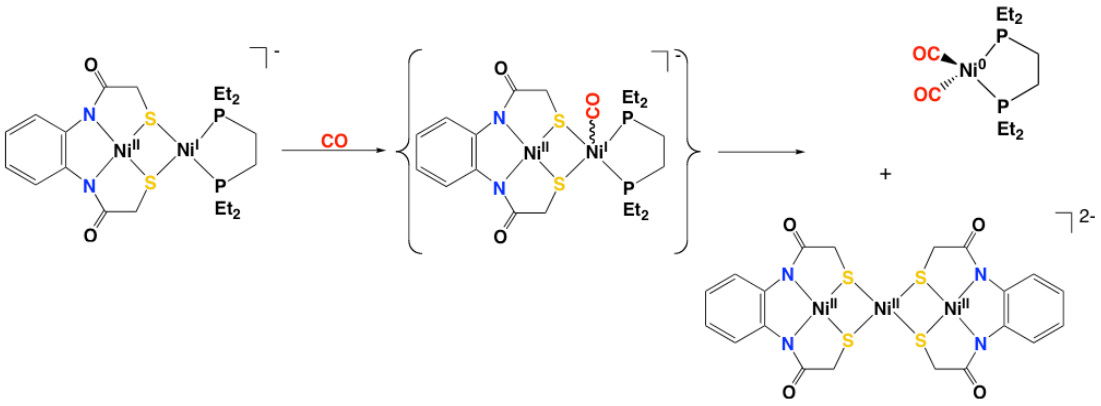

Figure 2.3. Reactivity of the model complex Ni(phma)Ni(depe) with CO.[75]

To evaluate the possibility of isolating mixed valent, Ni(II)Ni(I) or Ni(II)Ni(0), binuclear models, as are proposed in the reaction mechanism of ACS, the synthesis of a dinucleating macrocycle was undertaken. Tanaka et al. previously synthesized a dinucleating macrocycle, H_4L^2, with asymmetric coordination sites, imine and amide sites.[76] (Figure 2.4)

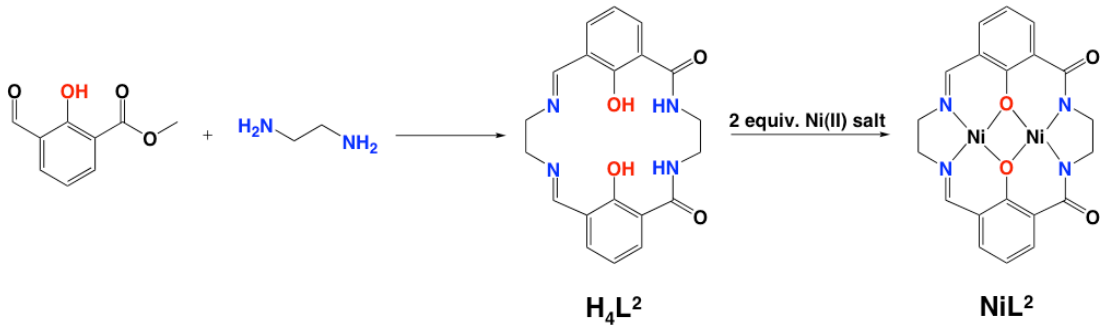

Figure 2.4. Synthesis of dinucleating macrocycle, H_4L^2, and its nickel complex by Tanaka et al.[76]

The dissimilar coordinate sites provide an attractive way to distinguish between two coordinated metals, while the macrocyclic cavity should aid in stabilizing various oxidation states of the metals. The constrained geometry at both metal sites should assist in the isolation and structural characterization of mixed valent species. This chapter focuses on the development of a route to a complimentary macrocycle, H_4L^1 (Figure 2.5), where the phenol "head unit" is substituted with a thiol "head unit".

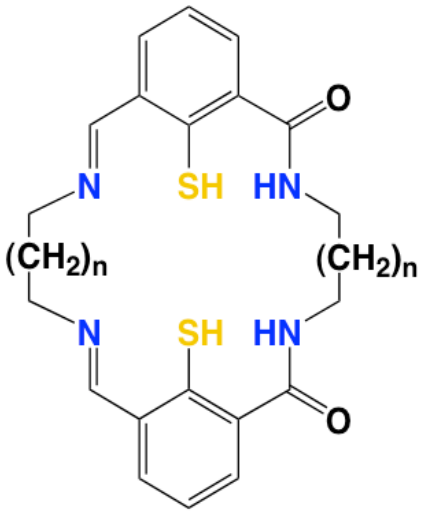

Figure 2.5. Proposed model for the study of mixed valent reaction intermediates formed during acetyl-coenzyme A synthesis.

In an attempt to mirror the direct synthesis proposed by Tanaka et al.[76] the synthesis of methyl 3-formylthiosalicylate from methyl-3-formylsalicylate[77] was pursued. During this endeavor, a family of nickel Schiff-base complexes, *N,N'*-bis(3-methoxycarbonylthiosalicylidene)-R-diaminonickel(II) (Ni(3-MOC-tsalR)) where R = 1,2-diaminoethane (en), 1,3-diaminopropane (pr), 1,4-diaminobutane (but), 1,2-phenylenediamine (phen), and 4,5-dimethyl-1,2-phenylenediamine (dimph), were also isolated. The precursor complexes *O*-(methyl-3-formylsalicylate) dimethylthiocarbamate and *S*-(methyl-3-formylsalicylate) dimethylthiocarbamate were synthesized as well. This chapter contains the synthesis, structural characterization and

spectroscopic properties of these complexes. In addition, the electrochemical properties of Ni(3-MOC-tsalR) (R = en, pr, but, phen, dimph) have been studied.

2.2 Experimental

2.2.1 General Procedures

Air and moisture sensitive reactions were carried out in a nitrogen or argon-filled Vacuum Atmosphere glovebox or on a manifold using standard Schlenk techniques.[78] All glassware was dried at 140 °C for at least 4 hours.

2.2.2 Physical Methods

NMR spectra were recorded using Bruker AV 400 MHz or DRX 400 MHz spectrometers equipped with 5 mm AMT BBI and 5 mm QNP probes respectively. Data processing was performed using Bruker Topspin software. Chemical shifts are denoted as δ (ppm) with coupling constants reported in Hz. NMR abbreviations are as follows: s, singlet; d, doublet; t, triplet; m, multiplet; br, broad. Proton and carbon chemical shifts were referenced to residual solvent signals. Electronic absorption data were collected using a Hewlett-Packard 8453 diode array spectrometer at room temperature. Infrared spectra were recorded on a Mattson Genesis Series FTIR spectrometer under N_2 purge at ambient temperature. Solid-state FT-IR samples were prepared as KBr pellets. Low resolution mass spectrometry was conducted on a ThermoFinnigan LCQ Advantage ESI mass spectrometer. High resolution mass spectrometry was performed with the assistance of Mr. John Dykins, University of Delaware, using a 7-T Fourier transform ion cyclotron resonance (FT-ICR) mass spectrometer. Cyclic voltammetry experiments were performed on a BAS 50W electrochemical analyzer. All experiments were conducted in an Ar-filled glovebox in

a cell containing a glassy carbon working electrode, an Ag^+/Ag reference electrode and a Pt wire as the counter electrode with 0.1M nBu$_4$NPF$_6$ as a supporting electrode. The analyte solution concentrations ranged from 1-5 mM and scan rates of 100 mV/s were employed. All potentials were referenced internally to Fc^+/Fc and reported vs. NHE.

Crystallographic data were collected and reduced by Dr. Glenn P. A. Yap, Mr. William Dougherty or Ms. Tina Tao, University of Delaware. Samples were mounted onto a glass fiber using Paratone oil and cooled to the data collection temperature. Data were collected on a Bruker-AXS APEX CCD diffractometer with 0.7101 Å Mo-Kα radiation employing SMART software. The data sets were treated with SADABS absorption corrections based on redundant multi-scan data (Sheldrick, G., Bruker-AXS, 2001) and solved in the appropriate space group derived from systematic absences with SHELXTL 6.12. Crystal data collection and refinement parameters are given in Table 2.1-2.4. Elemental analyses were performed by Columbia Analytical Laboratories, Inc., Tucson, AZ.

2.2.3 Materials

With the exception of acetone and methanol, solvents were dried by passage through activated alumina columns[79] and oxygen was removed by sparging with nitrogen. Under an atmosphere of nitrogen, acetone was distilled from calcium sulfate. Methanol was distilled from magnesium metal/calcium hydride prior to use. Dimethylformamide (99.8%, extra dry) was purchased from Acros Organics and used as received. Deuterated solvents were purchased from Cambridge Isotope Laboratories and dried over molecular sieves. Sodium hydride (Acros Organics), dimethylthiocarbamoyl chloride (Sigma Aldrich), nickel(II) nitrate hexahydrate

($Ni(NO_3)_2 \cdot 6H_2O$) (Acros Organics), 1,2-diaminoethane (Acros Organics), 1,3-diaminopropane (Sigma Aldrich), 1,4-diaminobutane (Sigma Aldrich), 1,2-diaminobenzene (Acros Organics) and 4,5-dimethylbenzene-1,2-diamine (Sigma Aldrich) were obtained from the indicated suppliers and used without further purification. All other reagents were purchased from commercial sources and used as received, unless described otherwise. Methyl-3-methylsalicylate[80], methyl-3-methylacetylsalicylate[80], and methyl-3-formylsalicylate[77] were prepared according to previously published procedures. Methyl-3-bromomethylacetylsalicylate was synthesized with a slight modification of the procedure previously reported for methyl-3-(1,1-dibromo)methylacetylsalicylate.[77] A lamp equipped with an incandescent light bulb (120 W) was used to irradiate the reaction mixture for ~20 hours in lieu of irradiating the reaction mixture with a UV lamp (500 W) for approximately 30 minutes. Methyl-3-(1,1-dibromo)methylacetylsalicylate was synthesized in a similar manner.[77] The preparative method of brominating the methyl group in two separate reactions instead of one to obtain the desired product produced higher yields and a purer product than the previously reported route.

2.2.4 Chemical Synthesis

2.2.4.1 Synthesis of Precursor Complexes

O-(methyl-3-formylsalicylate) dimethylthiocarbamate (**1**)

A schlenk flask was charged with methyl-3-formylsalicylate (5.00 g, 27.8 mmol) dissolved in ~40 mL of dimethylformamide. To this stirring solution, sodium hydride (1.00 g, 41.6 mmol) was added in small portions generating a yellow colored solution. Once the evolution of gas (H_2) subsided, dimethylthiocarbamoyl chloride

(4.46 g, 36.1 mmol) was added to the mixture in ~10 mL of dimethylformamide. The solution was then heated to 80 °C for ~1 hour under nitrogen, during which time the color turned orange. The solution was subsequently cooled and placed in a separatory funnel containing water (300 mL). The organic layer was extracted with 4:1 benzene/petroleum ether (3 x 100 mL). The combined organic extracts were washed with water (3 x 100 mL), a 5% aqueous potassium hydroxide solution (3 x 100 mL) and a saturated aqueous solution of sodium chloride (2 x 100 mL). The resulting solution was filtered through anhydrous magnesium sulfate and the solvent was removed in vacuo producing an off-white/yellow solid. This solid was re-dissolved in a concentrated 1:1 chloroform/diethyl ether solution and cooled down to yield crystals of *O*-(methyl-3-formylsalicylate) dimethylthiocarbamate. Yield: 2.60 g, 35%. ^{1}H NMR ($CDCl_3$): δ 3.48 (s, 3H, N(CH_3)$_2$), 3.50 (s, 3H, N(CH_3)$_2$), 3.88 (s, 3H, OCH_3), 7.45 (t, 1H, *p*-C$_6H_3$), 8.13 (d, 1H, *m*-C$_6H_3$), 8.24 (d, 1H, *m*-C$_6H_3$), 10.16 (s, 1H, C*H*O).

S-(methyl-3-formylsalicylate) dimethylthiocarbamate (**2**)

A 100-mL round bottom flask was charged with *O*-(methyl-3-formylsalicylate) dimethylthiocarbamate (1.00 g, 3.74 mmol) and attached to a reflux condenser. While stirring, the dry compound was heated for 2-3 hours to ~120 °C using a heating mantel. The solid melted and its color turned dark red. To determine when the reaction was complete, samples were periodically abstracted from the flask and analyzed by ^{1}H NMR spectroscopy. The final product was used without any further purification. Yield 0.95 g, 95%. ^{1}H NMR ($CDCl_3$): δ 2.91 (s, 3H, N(CH_3)$_2$), 3.08 (s, 3H, N(CH_3)$_2$), 3.83 (s, 3H, OCH_3), 7.50 (t, 1H, *p*-C$_6H_3$), 7.87 (d, 1H, *m*-C$_6H_3$), 8.03 (d, 1H, *m*-C$_6H_3$), 10.29 (s, 1H, C*H*O).

2.2.4.2 Synthesis of *N,N'*-bis(3-methoxycarbonylthiosalicylidene)-R-diaminonickel(II), Ni(3-MOC-tsalR)

N,N'-bis(3-methoxycarbonylthiosalicylidene)ethylenediaminonickel; Ni(3-MOC-tsalen) (**3**)

A multi-neck 500-mL round bottom flask equipped with a reflux condenser was charged with *S*-(methyl-3-formylsalicylate) dimethylthiocarbamate (1.07 g, 4.00 mmol) dissolved in ~200 mL of isopropyl alcohol and brought to reflux. Ground sodium hydroxide (0.16 g, 4.00 mmol) was added to the yellow/orange solution causing an instantaneous change from clear to cloudy. After the reaction mixture was refluxed for 5 hr, a solution of $Ni(NO_3)_2 \cdot 6H_2O$ (0.58 g, 2.00 mmol) in ~20 mL of isopropyl alcohol was added, immediately followed by the addition of 1,2-diaminoethane (0.13 mL, 2.00 mmol). The solution color changed swiftly from yellow/orange to red. The reaction was heated at refluxing temperature overnight and then filtered while hot. The resulting precipitate was washed with water (3 x 100 mL) and acetone (3 x 100 mL) and dried under vacuum. Yield 0.57 g, 60%. ^{1}H NMR ($(CD_3)_2SO$): δ 3.76 (s, 4H, NCH_2CH_2N), 3.82 (s, 6H, OCH_3), 7.11 (t, 2H, C$_6H_3$, $^3J_{H\text{-}H}$ = 7.41), 7.49 (d, 2H, C$_6H_3$, $^3J_{H\text{-}H}$ = 7.41), 7.66 (d, 2H, C$_6H_3$, $^3J_{H\text{-}H}$ = 7.41), 8.66 (s, 2H, NC*H*). ^{13}C{^{1}H} NMR ($(CD_3)_2SO$): δ 52.52 (s, 2C, O*C*H$_3$), 61.79 (s, 2C, *C*H$_2$), 121.58 (s, 2C, *C*$_6$H$_3$), 131.52 (s, 2C, *C*$_6$H$_3$), 131.83 (s, 2C, *C*$_6$H$_3$), 133.75 (s, 2C, *C*$_6$H$_3$), 137.92 (s, 2C, *C*$_6$H$_3$), 143.57 (s, 2C, *C*$_6$H$_3$), 164.75 (s, 2C, *C*H), 168.78 (s, 2C, *C*O). UV-vis ($(CH_3)_2SO$), λ_{max} (ε, M^{-1} cm^{-1}): 271 (76900), 299 (25700), 387 (11600), 447 (3240), 590 (161). IR (KBr): $\nu_{C=O}$ = 1722 cm^{-1}, $\nu_{C=N}$ = 1615 cm^{-1}. ESI MS: $C_{20}H_{18}N_2NiO_4S_2$ calculated *m/z*$^+$: 472.0 [M$^+$], found *m/z*$^+$: 472.1 [M$^+$]. Elemental Analysis: Anal. Calcd. for $C_{20}H_{18}N_2NiO_4S_2$: %C, 50.76; %H, 3.83; %N, 5.92. Found: %C, 50.40; %H, 4.09, %N, 5.94.

N,N'-bis(3-methoxycarbonylthiosalicylidene)propylenediaminonickel; Ni(3-MOC-tsalpr) (**4**)

S-(methyl-3-formylsalicylate) dimethylthiocarbamate (1.00 g, 3.74 mmol) was dissolved in ~200 mL of isopropyl alcohol and brought to refluxing temperature in a multi-neck 500-mL round bottom flask equipped with a reflux condenser. Ground sodium hydroxide (0.15 g, 3.74 mmol) was added to the yellow/orange solution causing an instantaneous change from clear to cloudy. After the reaction mixture was refluxed for 5 hr, a solution of $Ni(NO_3)_2 \cdot 6H_2O$ (0.54 g, 1.87 mmol) in ~20 mL of isopropyl alcohol was added, immediately followed by the addition of 1,3-diaminopropane (0.16 mL, 1.87 mmol). The solution color changed swiftly from yellow/orange to red. The reaction was heated at refluxing temperature overnight and then filtered while hot. The resulting precipitate was washed with water (3 x 100 mL) and acetone (3 x 100 mL) and dried under vacuum. Yield 0.47 g, 52%. ^{1}H NMR ($(CD_3)_2SO$): δ 2.02 (m, 2H, $NCH_2CH_2CH_2N$), 3.81 (s, 6H, OCH_3), 3.90 (m, 4H, $NCH_2CH_2CH_2N$), 7.12 (t, 2H, C_6H_3, $^3J_{H\text{-}H} = 7.41$), 7.44 (d, 2H, C_6H_3, $^3J_{H\text{-}H} = 7.39$), 7.57 (d, 2H, C_6H_3, $^3J_{H\text{-}H} = 7.39$), 8.25 (s, 2H, CH). $^{13}C\{^1H\}$ NMR ($(CD_3)_2SO$): δ 26.41 (s, 1C, $NCH_2CH_2CH_2N$), 52.64 (s, 2C, OCH_3), 55.65 (s, 2C, $NCH_2CH_2CH_2N$), 121.67 (s, 2C, C_6H_3), 131.39 (s, 2C, C_6H_3), 133.04 (s, 2C, C_6H_3), 133.74 (s, 2C, C_6H_3), 136.52 (s, 2C, C_6H_3), 143.06 (s, 2C, C_6H_3), 166.47 (s, 2C, CH), 168.78 (s, 2C, CO). UV-vis ($(CH_3)_2SO$), λ_{max} (ε, M^{-1} cm^{-1}): 270 (37400), 310 (15100), 387 (5920), 447sh (1840), 600 (110). IR (KBr): $\nu_{C=O}$ = 1725 cm^{-1}, $\nu_{C=N}$ = 1616 cm^{-1}. ESI MS: $C_{21}H_{20}N_2NiO_4S_2$ calculated m/z^+: 486.0 [M^+], found m/z^+: 486.9 [M^+]. Elemental Analysis: Anal. Calcd. for $C_{21}H_{20}N_2NiO_4S_2$: %C, 51.77; %H, 4.14; %N, 5.75. Found: %C, 51.66; %H, 4.10; %N, 5.55.

N,N'-bis(3-methoxycarbonylthiosalicylidene)tetramethylenediaminonickel; Ni(3-MOC-tsalbut) (**5**)

A multi-neck 500-mL round bottom flask equipped with a reflux condenser was charged with *S*-(methyl-3-formylsalicylate) dimethylthiocarbamate (1.14 g, 4.26 mmol) dissolved in ~200 mL of isopropyl alcohol and brought to a reflux. Ground sodium hydroxide (0.17 g, 4.26 mmol) was added to the yellow/orange solution causing an instantaneous change from clear to cloudy. After the reaction mixture was refluxed for 5 hr, a solution of $Ni(NO_3)_2 \cdot 6H_2O$ (0.62 g, 2.13 mmol) in ~20 mL of isopropyl alcohol was added, immediately followed by the addition of 1,4-diaminobutane (0.21 mL, 2.13 mmol). The solution color changed swiftly from yellow/orange to red. The reaction was heated at refluxing temperature overnight and then filtered while hot. The resulting precipitate was washed with water (3 x 100 mL) and acetone (3 x 100 mL) and dried under vacuum. Yield 0.77 g, 73%. ^{1}H NMR ($(CD_3)_2SO$): δ 1.89 (br, 4H, $NCH_2C\mathit{H}_2C\mathit{H}_2CH_2N$), 3.80 (br, 10H, $NC\mathit{H}_2CH_2CH_2C\mathit{H}_2N$, $OC\mathit{H}_3$), 7.12 (t, 2H, $C_6\mathit{H}_3$, $^3J_{H\text{-}H}$ = 7.64), 7.45 (d, 2H, $C_6\mathit{H}_3$, $^3J_{H\text{-}H}$ = 7.64), 7.61 (d, 2H, $C_6\mathit{H}_3$, $^3J_{H\text{-}H}$ = 7.64), 8.25 (s, 2H, C*H*). $^{13}C\{^1H\}$ NMR ($(CD_3)_2SO$): δ 31.34 (s, 2C, $NCH_2\mathit{C}H_2\mathit{C}H_2CH_2N$), 52.78 (s, 2C, OCH_3), 62.06 (s, 2C, $NCH_2CH_2CH_2CH_2N$), 121.73 (s, 2C, C_6H_3), 131.44 (s, 2C, C_6H_3), 133.79 (s, 2C, C_6H_3), 134.69 (s, 2C, C_6H_3), 135.99 (s, 2C, C_6H_3), 143.18 (s, 2C, C_6H_3), 167.86 (s, 2C, *C*H), 168.81 (s, 2C, *C*O). UV-vis ($(CH_3)_2SO$), λ_{max} (ε, M^{-1} cm^{-1}): 271 (51300), 309 (24400), 394 (4810), 430(sh) (3400), 580 (234). IR (KBr): $\nu_{C=O}$ = 1726 cm^{-1}, $\nu_{C=N}$ = 1618 cm^{-1}. HR ESI MS: $C_{22}H_{22}N_2NiO_4S_2$ calculated m/z^+: 501.0453 [MH^{1+}], found m/z^+: 501.0449 [MH^+]. Elemental Analysis: Anal. Calcd. for $C_{22}H_{22}N_2NiO_4S_2$: %C, 52.72; %H, 4.42; %N, 5.59. Found %C, 51.36; %H, 4.62; %N, 5.96.

N,N'-bis(3-methoxycarbonylthiosalicylidene)-*o*-phenylenediaminonickel; Ni(3-MOC-tsalphen) (**6**)

S-(methyl-3-formylsalicylate) dimethylthiocarbamate (1.17 g, 4.38 mmol) was dissolved in ~200 mL of isopropyl alcohol and brought to refluxing temperature in a multi-neck 500-mL round bottom flask equipped with a reflux condenser. Ground sodium hydroxide (0.17 g, 4.38 mmol) was added to the yellow/orange solution causing an instantaneous change from clear to cloudy. After the reaction mixture was refluxed for 5 hr, a solution of $Ni(NO_3)_2 \cdot 6H_2O$ (0.64 g, 2.19 mmol) in ~20 mL of isopropyl alcohol was added, immediately followed by the addition of 1,2-diaminobenzene (0.24 g, 2.19 mmol) in ~10 mL of isopropyl alcohol. The solution color changed swiftly from yellow/orange to red. The reaction was heated at refluxing temperature overnight and then filtered while hot. The resulting precipitate was washed with water (3 x 100 mL) and acetone (3 x 100 mL) and dried under vacuum. Yield 0.87 g, 76%. ^{1}H NMR ($(CD_3)_2SO$): δ 3.87 (s, 6H, OCH_3), 7.24 (t, 2H, C_6H_3, $^3J_{H-H}$ = 7.42), 7.56 (br, 2H, C_6H_4), 7.65 (d, 2H, C_6H_3, $^3J_{H-H}$ = 7.15), 8.14 (d, 2H, C_6H_3, $^3J_{H-H}$ = 7.55), 8.33 (br, 2H, C_6H_4), 9.50 (s, 2H, C*H*). $^{13}C\{^1H\}$ NMR ($(CD_3)_2SO$): δ 52.74 (s, 2C, O*C*H$_3$), 118.35 (s, 2C, *C*$_6$H$_4$), 121.67 (s, 2C, *C*$_6$H$_3$), 129.72 (s, 2C, *C*$_6$H$_4$), 132.88 (s, 2C, *C*$_6$H$_3$), 140.72 (s, 2C, *C*$_6$H$_3$), 160.61 (s, 2C, *C*H), 168.47 (s, 2C, *C*O), 131.71, 133.18, 144.61, 145.25 (s, 8C, *C*$_6$H$_3$, *C*$_6$H$_4$). UV-vis ($(CH_3)_2SO$), λ_{max} (ε, M^{-1} cm^{-1}): 292 (53100), 395 (13700), 552 (1880), 631 (1220). IR (KBr): $\nu_{C=O}$ = 1718 cm^{-1}, $\nu_{C=O}$ = 1707 cm^{-1}, $\nu_{C=N}$ = 1532 cm^{-1}. ESI MS: $C_{24}H_{18}N_2NiO_4S_2$ calculated *m/z*$^+$: 520.0 [M^+], found *m/z*$^+$: 520.2 [M^+]. Elemental Analysis: Anal. Calcd. for $C_{24}H_{18}N_2NiO_4S_2$: %C, 55.30; %H, 3.48; %N, 5.37. Found: %C, 55.13; %H, 3.77; %N, 5.56.

N,N'-bis(3-methoxycarbonylthiosalicylidene)dimethyl-*o*-phenylenediaminonickel; Ni(3-MOC-tsaldimph) (**7**)

A multi-neck 500-mL round bottom flask equipped with a reflux condenser was charged with *S*-(methyl-3-formylsalicylate) dimethylthiocarbamate (1.11 g, 4.15 mmol) dissolved in ~200 mL of isopropyl alcohol and brought to a reflux. Ground sodium hydroxide (0.17 g, 4.15 mmol) was added to the yellow/orange solution causing an instantaneous change from clear to cloudy. After the reaction mixture was refluxed for 5 hr, a solution of $Ni(NO_3)_2 \cdot 6H_2O$ (0.60 g, 2.08 mmol) in ~20 mL of isopropyl alcohol was added, immediately followed by the addition of 4,5-dimethylbenzene-1,2-diamine (0.28 g, 2.08 mmol) in ~10 mL of isopropyl alcohol. The solution color changed swiftly from yellow/orange to red. The reaction was heated at refluxing temperature overnight and then filtered while hot. The resulting precipitate was washed with water (3 x 100 mL) and acetone (3 x 100 mL) and dried under vacuum. Yield: 0.81 g, 72%. ^{1}H NMR ($(CD_3)_2SO$): δ 2.33 (s, 6H, CH_3), 3.86 (s, 6H, OCH_3), 7.21 (t, 2H, C_6H_3, $^3J_{H\text{-}H}$ = 7.35), 7.61 (d, 2H, C_6H_3, $^3J_{H\text{-}H}$ = 7.35), 8.06 (m, 2H, C_6H_3), 8.09 (m, 2H C_6H_2), 9.39 (s, 2H, C*H*). ^{13}C{^{1}H} NMR ($(CD_3)_2SO$): δ 20.12 (s, 2C, *C*H_3), 52.72 (s, 2C, O*C*H_3), 118.39 (s, 2C, *C*$_6H_2$), 121.57 (s, 2C, *C*$_6H_3$), 132.60 (s, 2C, *C*$_6H_3$), 140.35 (s, 2C, *C*$_6H_3$), 159.38 (s, 2C, *C*H), 168.52 (s, 2C, *C*O), 131.70, 133.12, 138.87, 142.50, 144.79 (s, 10C, *C*$_6H_3$, *C*$_6H_2$). UV-vis ($(CH_3)_2SO$), λ_{max} (ε, M^{-1} cm^{-1}): 294 (38400), 310sh (33600), 391 (17500), 548 (1730), 620 (1130). IR (KBr): $\nu_{C=O}$ = 1711 cm^{-1}, $\nu_{C=O}$ = 1677 cm^{-1}, $\nu_{C=N}$ = 1528 cm^{-1}. HR ESI MS: $C_{26}H_{22}N_2NiO_4S_2$ calculated *m/z*$^+$: 549.0453 [MH^+], found *m/z*$^+$: 549.0449 [MH^+].

2.2.5 X-ray Crystallography

2.2.5.1 *O*-(methyl-3-formylsalicylate) dimethylthiocarbamate

Crystal data collection and refinement parameters are given in Table 2.1. A single crystal was harvested and mounted using Paratone oil on a MiTeGen MicroMount. Data were collected at 120(2) K. Yellow crystals of protected complex were grown by slow evaporation of chloroform. The assigned space group was P2(1)/n.

2.2.5.2 *N,N'*-bis(3-methoxycarbonylthiosalicylidene)ethylenediaminonickel

Crystal data collection and refinement parameters are given in Table 2.1. A single crystal was harvested and mounted using Paratone oil on a MiTeGen MicroMount. Data were collected at 120(2) K. Orange blocks of Ni(3-MOC-tsalen) were grown by slow evaporation of a concentrated dimethyl sulfoxide solution. The assigned space group was P2(1)/n.

2.2.5.3 *N,N'*-bis(3-methoxycarbonylthiosalicylidene)propylenediaminonickel

Crystal data collection and refinement parameters are given in Table 2.2. A single crystal was harvested and mounted using Paratone oil on a MiTeGen MicroMount. Crystallographic data were collected on two separate occasions for this molecule. Red needles of Ni(3-MOC-tsalpr) were grown by slow evaporation of a concentrated dimethyl sulfoxide solution. The assigned space group was P2(1)/c. Alternatively, orange plates of Ni(3-MOC-tsalpr) were grown by slow evaporation of a concentrated dimethyl sulfoxide solution. The assigned space group was C2/c. Data were collected at 170(2) and 120(2) K, respectively.

2.2.5.4 *N,N'*-bis(3-methoxycarbonylthiosalicylidene)-tetramethylenediaminonickel

Crystal data collection and refinement parameters are given in Table 2.3. A single crystal was harvested and mounted using Paratone oil on a MiTeGen MicroMount. Data were collected at 120(2) K. Orange plates of Ni(3-MOC-tsalbut) were grown by slow evaporation of a concentrated dimethyl sulfoxide solution. The asymmetric unit contained two crystallographically independent molecules and three molecules of acetone. The assigned space group was P-1.

2.2.5.5 *N,N'*-bis(3-methoxycarbonylthiosalicylidene)-*o*-phenylenediaminonickel

Crystal data collection and refinement parameters are given in Table 2.3. A single crystal was harvested and mounted using Paratone oil on a MiTeGen MicroMount. Data were collected at 120(2) K. Red blocks of Ni(3-MOC-tsalphen) were grown by slow evaporation of a concentrated dimethyl sulfoxide solution. The assigned space group was P-1.

2.2.5.6 *N,N'*-bis(3-methoxycarbonylthiosalicylidene)dimethyl-*o*-phenylenediaminonickel

Crystal data collection and refinement parameters are given in Table 2.4. A single crystal was harvested and mounted using Paratone oil on a MiTeGen MicroMount. Data were collected at 200(2) K. Red needles of Ni(3-MOC-tsaldimph) were grown by slow evaporation of a concentrated dimethyl sulfoxide solution. The assigned space group was P2(1)/c.

Table 2.1: Crystallographic data for *O*-(methyl-3-formylsalicylate) dimethylthiocarbamate and Ni(3-MOC-tsalen).

Compound	*O*-(methyl-3-formylsalicylate) dimethylthiocarbamate	Ni(3-MOC-tsalen)
Identification Code	Char148	Char171
Empirical Formula	$C_{12}H_{13}NO_4S$	$C_{20}H_{18}N_2NiO_4S_2$
Formula Weight	267.29	473.19
Color, Habit	Colorless, plates	Orange, block
Crystal System	Monoclinic	Monoclinic
Space Group	P2(1)/n	P2(1)/n
a, Å	12.079(3)	13.017(4)
b, Å	7.1355(16)	12.429(3)
c, Å	14.497(3)	13.222(4)
α, deg	90	90
β, deg	98.779(3)	112.545(4)
γ, deg	90	90
V (Å^3)	1234.8(5)	1975.7(9)
Z	4	4
Temperature (K)	120(2)	120(2)
Density$_{calc}$, (g/cm^3)	1.438	1.591
2θ range, deg	2.05-28.21	1.87-28.23
GOF (F^2)	1.035	1.072
μ(Mo, Kα), mm^{-1}	0.268	1.224
$R(F)/R_w(F)$	0.0386/0.1029	0.0327/0.0836

Quantity minimized = $R(wF^2) = \Sigma[w(F_0^2-F_c^2)^2]/\Sigma[(wF_0^2)^2]^{0.5}$; $R = \Sigma\Delta/\Sigma(F_0)$, $\Delta = |(F_0-F_c)|$, $w = 1/[\sigma^2(F_0^2) + (aP)^2 + bP]$, $P = [2F_c^2 + \text{Max}(F_0, 0)]/3$

Table 2.2: Crystallographic data for Ni(3-MOC-tsalpr), two crystalline phases, α and β.

Compound	Ni(3-MOC-tsalpr)-α	Ni(3-MOC-tsalpr)-β
Identification Code	Char208a	Char215a
Empirical Formula	$C_{21}H_{20}N_2NiO_4S_2$	$C_{21}H_{20}N_2NiO_4S_2$
Formula Weight	487.22	487.22
Color, Habit	Orange, Plate	Red, Needle
Crystal System	Monoclinic	Monoclinic
Space Group	C2/c	P2(1)/c
a, Å	23.195(4)	14.866(3)
b, Å	8.4050(11)	11.221(2)
c, Å	11.3494(15)	13.502(3)
α, deg	90	90
β, deg	110.946(3)	106.600(4)
γ, deg	90	90
V (Å^3)	2066.4(5)	2158.3(7)
Z	4	4
Temperature (K)	120(2)	170(2)
$Density_{calc}$, (g/cm^3)	1.566	1.499
2θ range, deg	1.88-28.32	2.31-28.29
GOF (F^2)	1.026	1.039
μ(Mo, Kα), mm^{-1}	1.173	1.123
R(F)/R_w(F)	0.0352/0.0969	0.0469/0.0938

Quantity minimized = $R(wF^2) = \Sigma[w(F_0^2-F_c^2)^2]/\Sigma[(wF_0^2)^2]^{0.5}$; $R = \Sigma\Delta/\Sigma(F_0)$, $\Delta = |(F_0-F_c)|$, $w = 1/[\sigma^2(F_0^2) + (aP)^2 + bP]$, $P = [2F_c^2 + Max(F_0, 0)]/3$

Table 2.3: Crystallographic data for Ni(3-MOC-tsalbut) and Ni(3-MOC-tsalphen).

Compound	Ni(3-MOC-tsalbut)	Ni(3-MOC-tsalphen)
Identification Code	Char221	Char179
Empirical Formula	$C_{26.50}H_{31}N_2O_{5.50}S_2$	$C_{24}H_{18}N_2NiO_4S_2$
Formula Weight	588.36	521.23
Color, Habit	Orange, Plate	Red, Block
Crystal System	Triclinic	Triclinic
Space Group	P-1	P-1
a, Å	11.312(3)	8.2883(13)
b, Å	13.983(3)	11.6618(18)
c, Å	18.281(4)	12.5263(19)
α, deg	101.223(4)	62.672(2)
β, deg	96.231(4)	79.706(2)
γ, deg	91.975(4)	88.896(2)
V (Å^3)	2814.9(11)	1055.6(3)
Z	4	2
Temperature (K)	120(2)	120(2)
$Density_{calc}$, (g/cm^3)	1.388	1.640
2θ range, deg	1.49-28.34	1.86-28.23
GOF (F^2)	1.055	1.042
μ(Mo, Kα), mm^{-1}	0.878	1.154
$R(F)/R_w(F)$	0.0600/0.1313	0.0317/0.0746

Quantity minimized = $R(wF^2) = \Sigma[w(F_0^2-F_c^2)^2]/\Sigma[(wF_0^2)^2]^{0.5}$; $R = \Sigma\Delta/\Sigma(F_0)$, $\Delta = |(F_0-F_c)|$, $w = 1/[\sigma^2(F_0^2) + (aP)^2 + bP]$, $P = [2F_c^2 + \text{Max}(F_0, 0)]/3$

Table 2.4: Crystallographic data for Ni(3-MOC-tsaldimph).

Compound	Ni(3-MOC-tsaldimph)
Identification Code	Char266a
Empirical Formula	$C_{26}H_{22}N_2NiO_4S_2$
Formula Weight	549.28
Color, Habit	Red, Needle
Crystal System	Monoclinic
Space Group	P2(1)/c
a, Å	13.157(3)
b, Å	25.248(7)
c, Å	6.897(7)
α, deg	90
β, deg	94.437(19)
γ, deg	90
V (Å^3)	2284(2)
Z	4
Temperature (K)	200(2)
$Density_{calc}$, (g/cm^3)	1.597
2θ range, deg	1.749-24.999
GOF (F^2)	1.016
μ(Mo, Kα), mm^{-1}	1.071
$R(F)/R_w(F)$	0.0794/0.1484

Quantity minimized = $R(wF^2) = \Sigma[w(F_0^2-F_c^2)^2]/\Sigma[(wF_0^2)^2]^{0.5}$; $R = \Sigma\Delta/\Sigma(F_0)$, $\Delta = |(F_0-F_c)|$, $w = 1/[\sigma^2(F_0^2) + (aP)^2 + bP]$, $P = [2F_c^2 + Max(F_0, 0)]/3$

2.3 Results and Discussion

The synthesis of an asymmetric dinucleating macrocycle, H_4L^1, was initiated to evaluate the likelihood of isolating mixed valent, Ni(II)Ni(I) or Ni(II)Ni(0), binuclear complexes as are proposed to form in the ACS reaction mechanism. Tanaka et al.[76] previously established the direct synthesis of a dinucleating phenolate-bridged macrocycle with dissimilar coordination sites (imine and amide sites) by the reaction of methyl-3-formylsalicylate with 1,2-diaminoethane (Figure 2.4). The proposed

synthetic route to an analogous dinucleating thiophenolate-bridged macrocycle, H_4L^1 (Figure 2.5), emulated the preceding reaction by beginning with the formation of methyl 3-formylsalicylate followed by its conversion from a phenol to a thiophenol via a Newman-Kwart rearrangement (Figure 2.6).

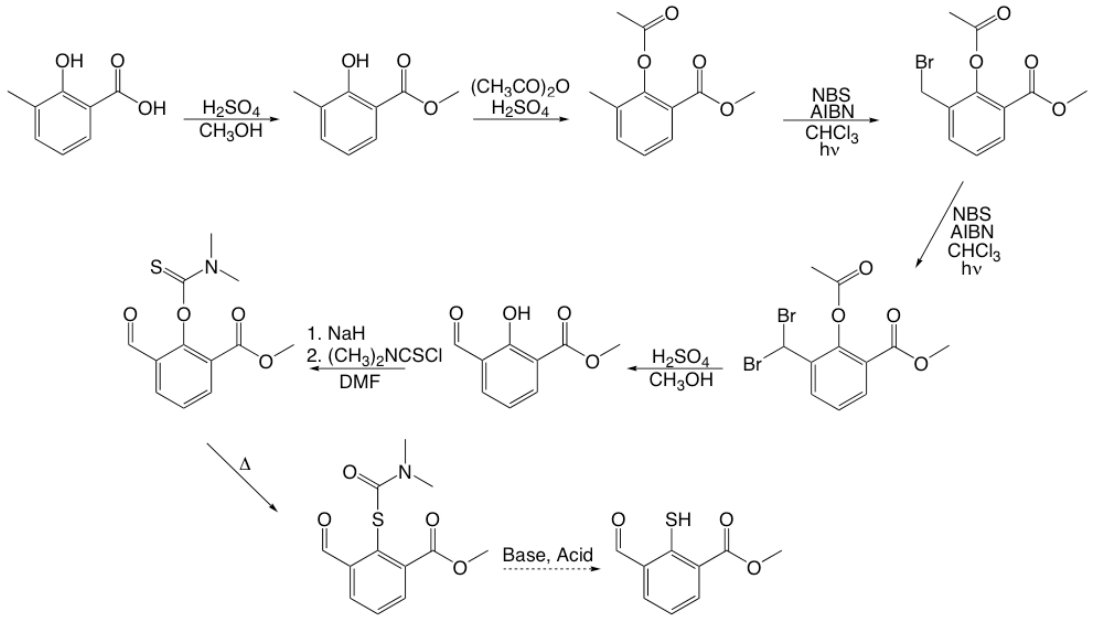

Figure 2.6. Synthetic route to methyl 3-formysalicylate followed by its conversion from a phenol to a thiophenol via a Newman-Kwart rearrangement.

The reaction scheme began with the conversion of 3-methylsalicyclic acid to its methyl ester followed by protection of the phenolic OH group with acetate. The methyl group of methyl-3-methylacetylsalicylate was then brominated with *N*-bromosuccinimide twice to form methyl-3-(1,1-dibromo)methylacetylsalicylate.

Subsequent reaction with sulfuric acid and methanol produced methyl-3-formylsalicylate. Literature methods were utilized for the preparation of the precursor complexes, methyl-3-methylsalicylate[80], methyl-3-methylacetylsalicylate[80], methyl-3-bromomethylacetylsalicylate[77], methyl-3-(1,1-dibromo)methylacetylsalicylate[77] and methyl-3-formylsalicylate[77] and therefore will not be discussed here. Replacement of the phenol substituent of methyl-3-formylsalicylate with a thiol substituent required the synthesis of *O*-(methyl-3-formylsalicylate) dimethylthiocarbamate (**1**) followed by its thermolysis yielding *S*-(methyl-3-formylsalicylate) dimethylthiocarbamate (**2**) and base hydrolysis. The synthesis and characterization of both *O*- and *S*-arylthiocarbamates are discussed below. However, the conversion of *S*-(methyl-3-formylsalicylate) dimethylthiocarbamate to the thiol, methyl 3-formylthiosalicylate, was unsuccessful. All efforts at isolating the compound failed to produce a characterizable product. Despite this, *S*-(methyl-3-formylsalicylate) dimethylthiocarbamate was used as a starting material in the pursuit of an asymmetric thiophenolate-bridged macrocycle, H_4L^1. Although all attempts to generate a macrocycle also failed, a family of Schiff-base complexes, Ni(3-MOC-tsalR) (R = en, pr, but, phen, dimph) was obtained. The synthesis, structural characterization, spectroscopic and electrochemical properties of these complexes are reported in this chapter, alongside a discussion concerning the failure to synthesize an asymmetric dinucleating thiophenolate-bridged macrocycle.

2.3.1 Synthesis of ligand precursors *O*- and *S*-(methyl-3-formylsalicylate) dimethylthiocarbamate

O-(methyl-3-formylsalicylate) dimethylthiocarbamate was prepared according to a general procedure for the conversion of phenols to thiophenols reported by

Newman and Karnes.[81] The phenolic OH group of methyl-3-formylsalicyclate was deprotonated with sodium hydride and reacted with dimethylthiocarbamoyl chloride to form **1** in a 35% overall crystalline yield. The complex was stable in air and soluble in most organic solvents, including chloroform, ether, and isopropyl alcohol. The identity and purity of *O*-(methyl-3-formylsalicylate) dimethylthiocarbamate was established by ^{1}H NMR spectroscopy and X-ray crystallography.

X-ray quality crystals were grown by slow evaporation of a concentrated chloroform solution. A thermal ellipsoid plot of the molecular structure of *O*-(methyl-3-formylsalicylate) dimethylthiocarbamate is shown in Figure 2.7. Table 2.5 contains selected metric parameters. The X-ray structure revealed a planar thiocarbamoyl moiety directed away from the aldehyde and methyl ester ortho substituents, such that the aromatic and thiocarbamoyl fragments were not coplanar. This resulted in a short distance between S and C1 (3.036 Å), a requirement for the subsequent exchange of the oxygen and sulfur atom in the molecule. The observed bond lengths and angles are comparable to those found for other *O*-arylthiocarbamate complexes, e.g., 2,4-dimethylphenyl-*N,N*-dimethyl-*O*-thiocarbamate.[82]

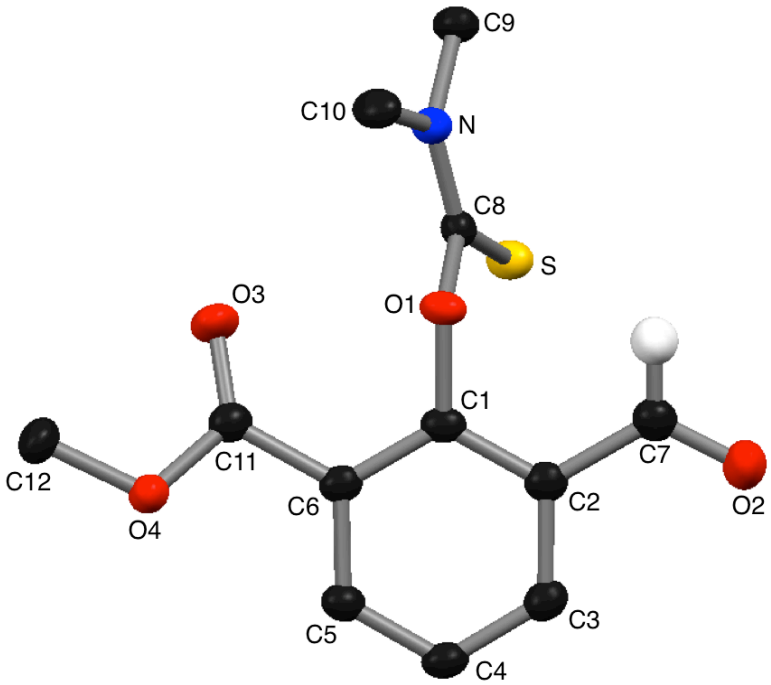

Figure 2.7. Molecular structure of *O*-(methyl-3-formylsalicylate) dimethylthiocarbamate. Hydrogen atoms have been omitted for clarity.

Table 2.5: Selected bond lengths (Å) and bond angles (°) for *O*-(methyl-3-formylsalicylate) dimethylthiocarbamate.

	Length (Å)		**Angle (°)**
S-C8	1.6699(2)	C8-O1-C1	120.79(1)
O1-C8	1.3711(2)	N-C8-O1	110.15(1)
O1-C1	1.3936(2)	N-C8-S	126.18(1)
N-C8	1.3184(2)	O1-C8-S	123.62(1)

Figure 2.8 displays the ^{1}H NMR spectrum of *O*-(methyl-3-formyl)salicylate dimethylthiocarbamate in $CDCl_3$. It exhibits multiple resonances with the correct integration ratio, in the aromatic and aliphatic regions. Two overlapping resonances for the -$N(CH_3)_2$ moiety were observed at δ 3.48 and 3.50, while a singlet at δ 3.88 was assigned to the -$COOCH_3$ group. The phenyl protons were found in the aromatic region at δ 7.45, 8.13 and 8.24. The resonance for the aldehyde proton was detected downfield at δ 10.16. Similar chemical shifts and non-equivalency of the nitrogen bound methyl groups has been previously reported for related compounds.[82,83]

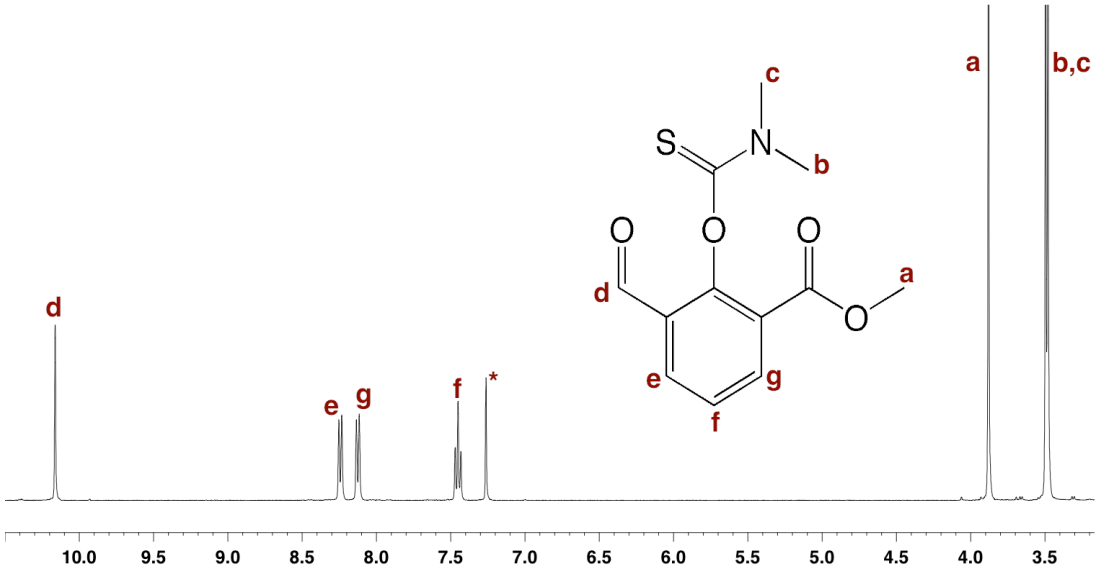

Figure 2.8. ^{1}H NMR spectrum of *O*-(methyl-3-formyl)salicylate dimethylthiocarbamate in $CDCl_3$. * denotes a solvent signal.

Thermolysis of *O*-(methyl-3-formylsalicylate) dimethylthiocarbamate led to the formation of *S*-(methyl-3-formylsalicylate) dimethylthiocarbamate. Crystals of **1** were heated for 2-3 hours at ~120 °C, producing **2** as a dark red solid in a 95% overall yield. Rearrangement proceeded through a four-membered cyclic transition state with nucleophilic attack by the sulfur atom on the ipso carbon atom of the benzene ring.[81] The temperature and time span of the reaction were critical to the success of this step; heating at very high temperatures or for too long resulted in total destruction of the compound. The progress of the reaction was monitored by the chemical shift change of the signals ascribed to the N-methyl groups of the thiocarbamoyl moiety in the ^{1}H NMR spectrum. Figure 2.9 displays the ^{1}H NMR spectrum of *S*-(methyl-3-formylsalicylate) dimethylthiocarbamate. It exhibits multiple resonances with the correct integration ratio, in the aromatic and aliphatic regions. The two overlapping resonances assigned to -N(CH_3)$_2$, δ 3.48 and 3.50, in **1** are separated and shifted upfield to δ 2.91 and 3.08 in **2**. A singlet located at δ 3.83 is ascribed to the methyl protons of the -COOCH_3 substituent and the phenyl protons were found in the aromatic region at δ 7.50, 7.87, and 8.03. The resonance for the aldehyde proton was detected downfield at δ 10.29. Analogous spectral features have been previously observed for related *S*-arylthiocarbamate compounds.[82,83] All attempts to grow X-ray quality crystals of *S*-(methyl-3-formylsalicylate) dimethylthiocarbamate were unsuccessful; however, the ^{1}H NMR spectrum is consistent with its formation.

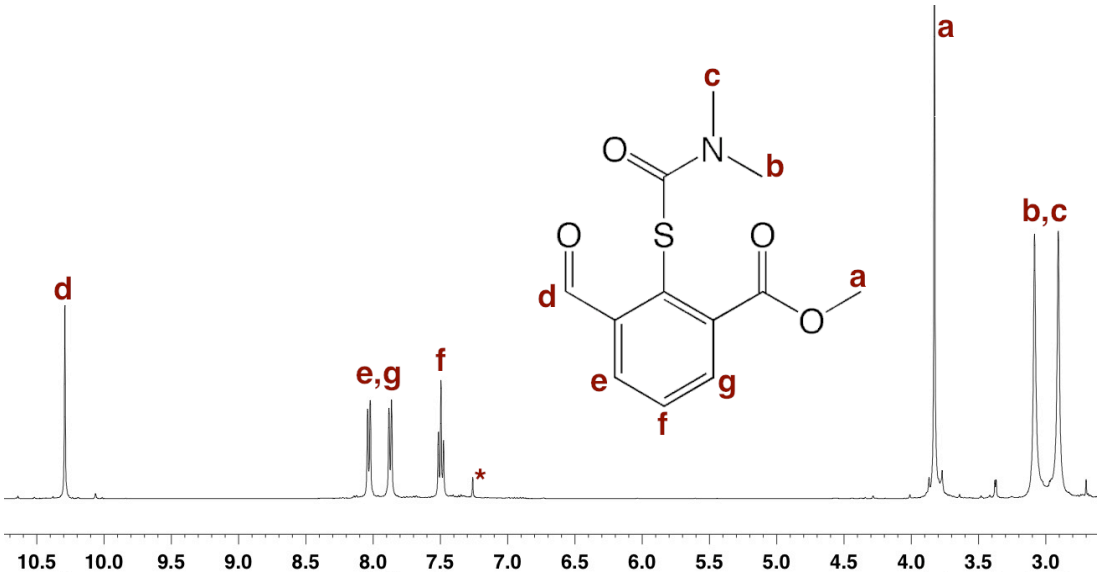

Figure 2.9. ^{1}H NMR spectrum of *S*-(methyl-3-formylsalicylate) dimethylthiocarbamate in $CDCl_3$. * denotes a solvent signal.

2.3.2 Nickel Complexes Ni(3-MOC-tsalR), R = en, pr, but, phen, dimph

2.3.2.1 Synthesis and Properties of Ni(3-MOC-tsalR) complexes

A series of *N,N*'-bis(3-methoxycarbonylthiosalicylidene)-R-diaminonickel(II) complexes (Ni(3-MeOC-tsalR)) (R = en, pr, but, phen, dimph) were synthesized according to the general procedure presented in Figure 2.10.

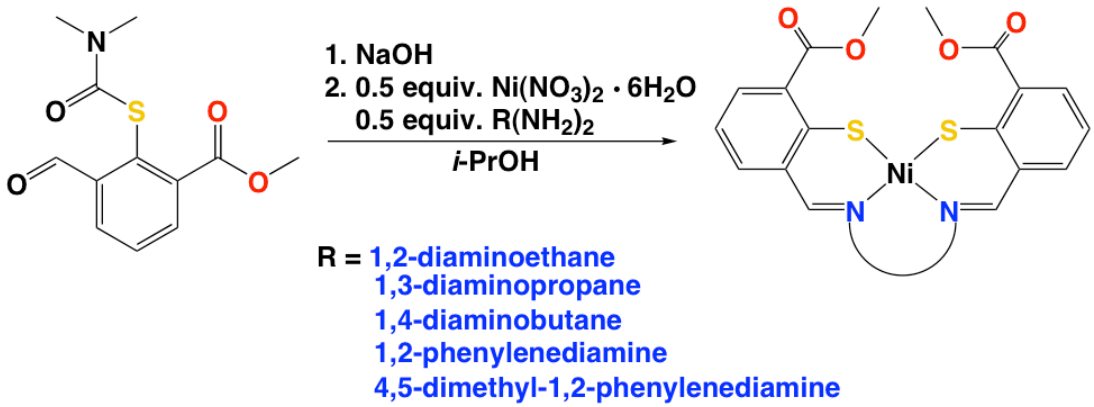

Figure 2.10. General Procedure for the synthesis of a series of *N,N'*-bis(3-methoxycarbonylthiosalicylidene)-R-diaminonickel(II) complexes, (Ni(3-MOC-tsalR)).

Sodium hydroxide was added to a refluxing isopropyl alcohol solution of *S*-(methyl-3-formylsalicylate) dimethylthiocarbamate, producing a change in the appearance of the yellow/orange solution from clear to cloudy. After the solution was refluxed for approximately five hours, an isopropyl alcohol solution of nickel(II) nitrate hexahydrate and the appropriate diamine were added consecutively to the refluxing solution, resulting in a rapid color change from yellow/orange to red. The reaction was filtered while hot and the resulting precipitate was washed with water and acetone and dried under vacuum, affording the nickel complexes in good yields (52-76%). This series of Ni(II) complexes is air and moisture stable. They are soluble in dimethyl sulfoxide, dimethylformamide, and slightly soluble in methylene chloride. Crystals

appropriate for X-ray crystallographic analysis were grown by slow evaporation of concentrated dimethyl sulfoxide solutions.

2.3.2.2 Molecular Structures of Ni(3-MOC-tsalR) (R = en, pr, but, phen, dimph) complexes

Thermal ellipsoid plots of Ni(3-MOC-tsalen) (**3**), Ni(3-MOC-tsalpr) (**4**), and Ni(3-MOC-tsalbut) (**5**) are shown in Figure 2.11. The unit cell of Ni(3-MOC-tsalbut) contained two crystallographically independent, but metrically similar molecules. The average bond lengths and angles for both complexes are discussed below. Table 2.6 contains selected metric parameters for each molecule. Thermal ellipsoid plots of Ni(3-MOC-tsalphen) (**6**) and Ni(3-MOC-tsaldimph) (**7**) are shown in Figure 2.12. Table 2.7 contains selected metric parameters for each molecule. The X-ray structures revealed that all of these complexes possess a square-planar Ni atom, coordinated by two imino nitrogen atoms and two thiolate sulfur atoms. The *trans* N-Ni-S angles (Table 2.6 and Table 2.7) support this geometrical assignment; however they also indicate a small tetrahedral distortion. This deviation from planarity was further observed in the dihedral angle between the N(1)NiS(1) and N(2)NiS(2) planes of 0.35°, 9.79°, 10.73° and 15.86° for Ni(3-MOC-tsalen), Ni(3-MOC-tsalpr), Ni(3-MOC-tsalbut)(1) and Ni(3-MOC-tsalbut)(2), respectively. Furthermore, while the S(1)-Ni-N(1) and S(2)-Ni-N(2) angles are similar, the S(1)-Ni-S(2) angles are smaller than the N(1)-Ni-N(2) angles for these complexes.(Table 2.6) For example, the S(1)-Ni-N(1) and S(2)-Ni-N(2) angles of Ni(3-MOC-tsalpr) are 93.59(8)° and 94.15(8)°, compared to the S(1)-Ni-S(2) and N(1)-Ni-N(2) angles of 81.44(3)° and 91.71(11)°. As the number of methylene units in the diamine chain was increased, the polymethylene bridges became more flexible augmenting the N(1)-Ni-N(2) angles and the tetrahedral

distortion. The dihedral angles between the planes defined by N(1)NiS(1) and N(2)NiS(2) for Ni(3-MOC-tsaldimph) and Ni(3-MOC-tsalphen) were, 9.50° and 12.35°, respectively. Compared to Ni(3-MOC-tsalen) (0.35°), these complexes exhibit a significant distortion from planarity, despite having the same number of methylene units in their respective diamine bridges. The ethylenediamine bridge in Ni(3-MOC-tsalen) is *not* forced to be planar since there is no conjugation of electron density as there is in Ni(3-MOC-tsaldimph) and Ni(3-MOC-tsalphen). This allows the bridge in Ni(3-MOC-tsalen) to be more flexible and result in a more planar structure. Previous studies on *N,N'*-bis(*o*-thiobenzylidene)-diamine nickel(II) complexes (Ni(tsalR)), where R = en[84], pr[85], but[86], phen[87], and dimph[88] have demonstrated similar effects. The average Ni-S and Ni-N bond distances are consistent with those observed previously for NiN_2S_2 complexes. Table 2.8 lists average Ni-N and Ni-S bond distances for the complexes discussed here and the related Ni(tsalR) complexes, where R = en, pr, but, phen, and dimph.

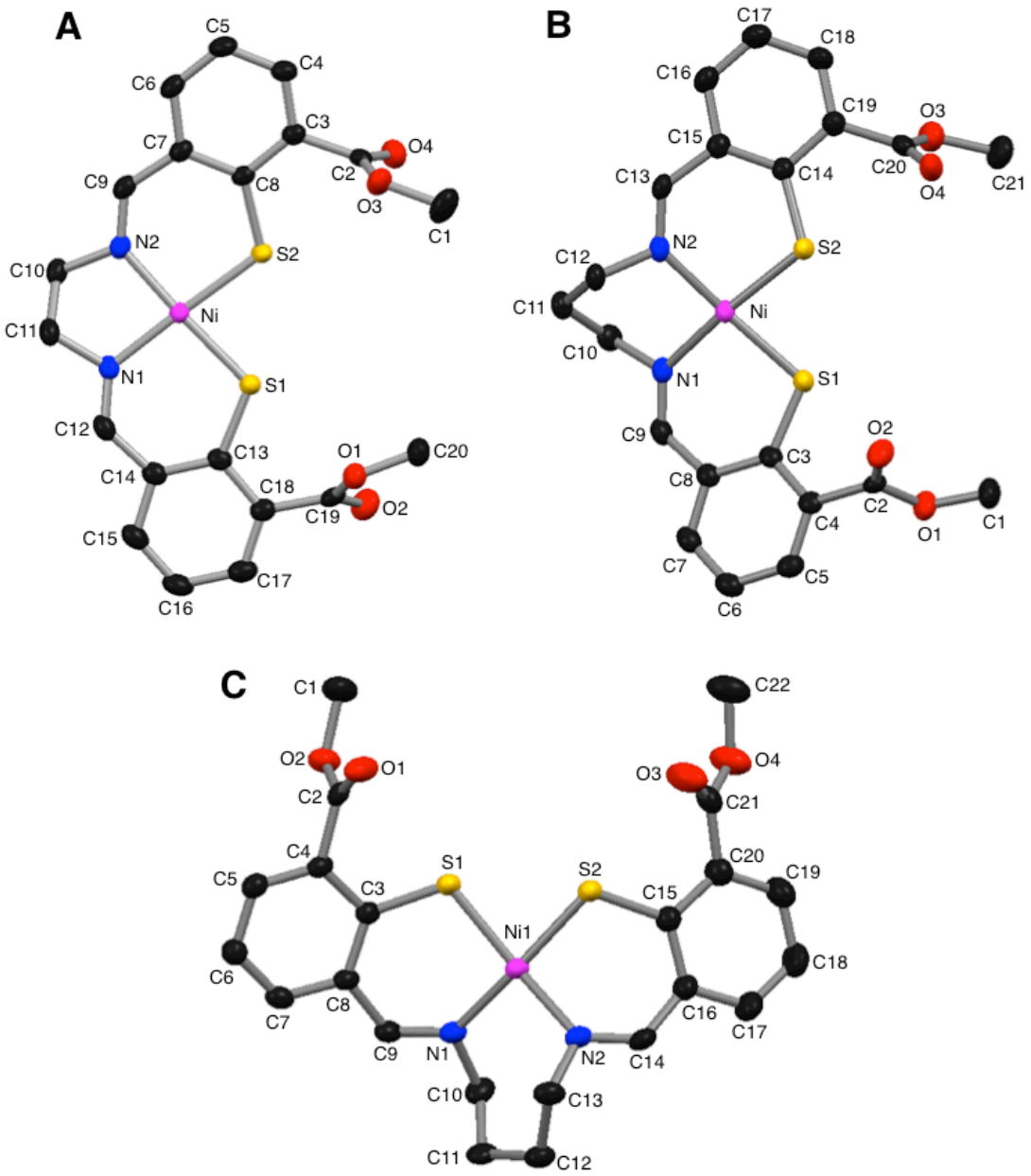

Figure 2.11. Molecular Structure of (**A**) Ni(3-MOC-tsalen), (**B**) Ni(3-MOC-tsalpr), and (**C**) Ni(3-MOC-tsalbut). Hydrogen atoms have been omitted for clarity.

Table 2.6: Selected bond lengths (Å) and bond angles (°) for Ni(3-MOC-tsalen), Ni(3-MOC-tsalpr), and each crystallographically independent molecule of Ni(3-MOC-tsalbut).

Compound		Length (Å)		Angle (°)
Ni(3-MOC-tsalen)	Ni-N1	1.8967(10)	N2-Ni-N1	86.98(7)
	Ni-N2	1.8910(15)	N2-Ni-S1	177.23(5)
	Ni-S1	2.1490(6)	N2-Ni-S2	94.98(5)
	Ni-S2	2.1628(7)	N1-Ni-S1	95.77(5)
			N1-Ni-S2	178.04(5)
			S1-Ni-S2	82.27(3)
Ni(3-MOC-tsalpr)	Ni-N1	1.919(2)	N2-Ni-N1	91.71(11)
	Ni-N2	1.902(3)	N2-Ni-S1	171.01(8)
	Ni-S1	2.1670(9)	N2-Ni-S2	94.15(8)
	Ni-S2	2.1515(9)	N1-Ni-S1	93.59(8)
			N1-Ni-S2	171.35(8)
			S1-Ni-S2	81.44(3)
Ni(3-MOC-tsalbut) (1)	Ni1-N1	1.914(3)	N2-Ni1-N1	91.58(12)
	Ni1-N2	1.901(3)	N2-Ni1-S1	170.02(10)
	Ni1-S1	2.1715(10)	N2-Ni1-S2	92.29(9)
	Ni1-S2	2.1587(10)	N1-Ni1-S1	93.96(9)
			N1-Ni1-S2	172.35(9)
			S1-Ni1-S2	83.20(4)
Ni(3-MOC-tsalbut) (2)	Ni2-N4	1.914(3)	N3-Ni2-N4	91.99(12)
	Ni2-N3	1.898(3)	N3-Ni2-S4	166.20(9)
	Ni2-S4	2.1545(10)	N3-Ni2-S3	91.95(9)
	Ni2-S3	2.1713(10)	N4-Ni2-S4	95.32(9)
			N4-Ni2-S3	168.93(10)
			S4-Ni2-S3	83.04(4)

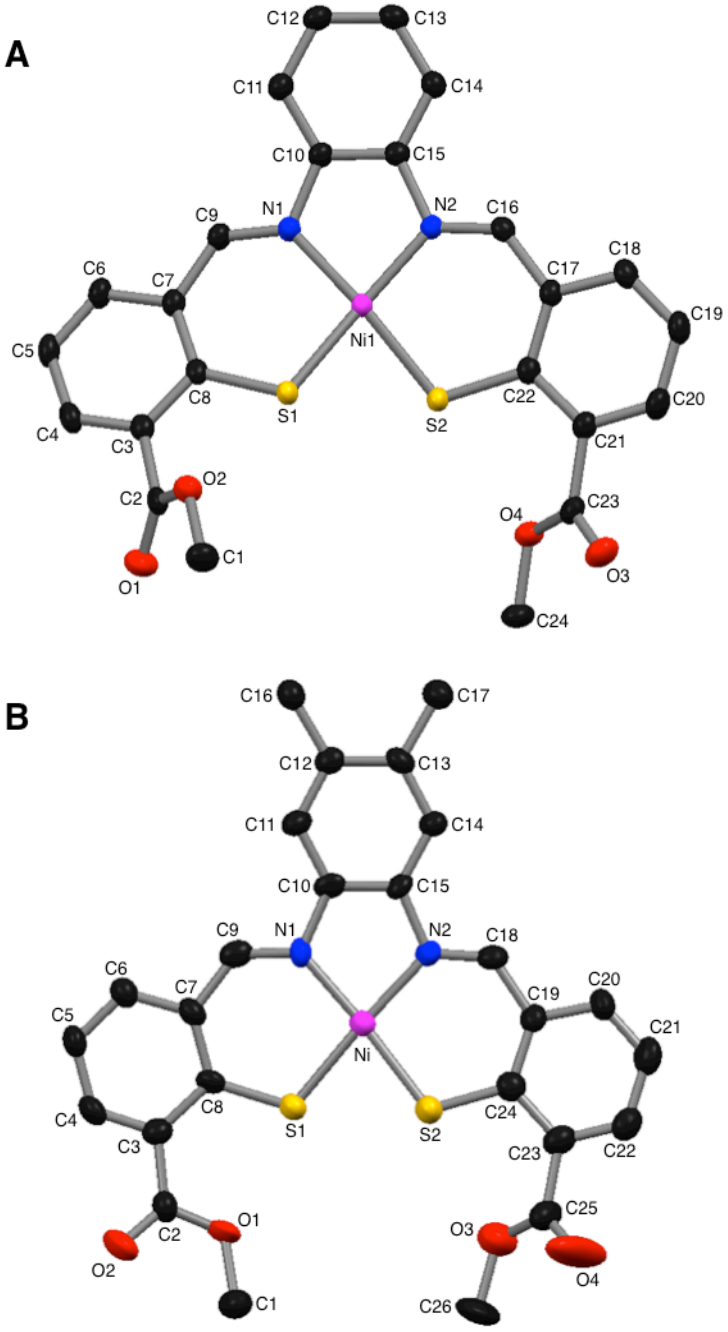

Figure 2.12. Molecular Structure of (**A**) Ni(3-MOC-tsalphen) and (**B**) Ni(3-MOC-tsaldimph). Hydrogen atoms have been omitted for clarity.

Table 2.7: Selected bond lengths (Å) and bond angles (°) for Ni(3-MOC-tsalphen) and Ni(3-MOC-tsaldimph).

Compound		Length (Å)		Angle (°)
Ni(3-MOC-tsalphen)	Ni-N1	1.8930(16)	N2-Ni-N1	86.32(7)
	Ni-N2	1.8922(16)	N2-Ni-S1	171.06(5)
	Ni-S1	2.1591(6)	N2-Ni-S2	97.04(5)
	Ni-S2	2.1534(6)	N1-Ni-S1	96.05(5)
			N1-Ni-S2	170.04(5)
			S1-Ni-S2	82.08(2)
Ni(3-MOC-tsaldimph)	Ni-N1	1.853(6)	N2-Ni-N1	86.3(3)
	Ni-N2	1.895(7)	N2-Ni-S1	172.3(2)
	Ni-S1	2.166(2)	N2-Ni-S2	97.2(2)
	Ni-S2	2.150(3)	N1-Ni-S1	96.9(2)
			N1-Ni-S2	172.5(2)
			S1-Ni-S2	80.48(9)

Table 2.8: Comparison of average Ni-N and Ni-S bond lengths (Å) in Ni(3-MOC-tsalR) (R = en, pr, but, phen, dimph) and Ni(tsalR) (R = en, pr, but, phen, dimph).

Compound	Ni-N (Å)	Ni-S (Å)
Ni(3-MOC-tsalen)	1.894(2)	2.156(7)
Ni(tsalen)[84]	1.884(5)	2.151(2)
Ni(3-MOC-tsalpr)	1.911(3)	2.159(9)
Ni(tsalpr)[85]	1.913(2)	2.159(9)
Ni(3-MOC-tsalbut)	1.907(3)	2.164(1)
Ni(tsalbut)[86]	1.915(4)	2.165(1)
Ni(3-MOC-tsalphen)	1.893(2)	2.156(6)
Ni(tsalphen)[87]	1.900(2)	2.155(6)
Ni(3-MOC-tsaldimph)	1.874(7)	2.158(3)
Ni(tsaldimph)[88]	1.920(3)	2.174(1)

2.3.2.3 Proton and Carbon NMR Spectral Characterization of Ni(3-MOC-tsalR) (R = en, pr, but, phen, dimph)

Ni(3-MOC-tsalR) (R = en, pr, but, phen, dimph) compounds were characterized by ^{1}H and ^{13}C NMR spectroscopies. The proton NMR spectrum of Ni(3-MOC-tsalen) is representative of the entire series, Figure 2.13. The proton and carbon NMR spectra of Ni(3-MOC-tsalpr), Ni(3-MOC-tsalbut), Ni(3-MOC-tsalphen), and Ni(3-MOC-tsaldimph) are similar in appearance (Appendix A) and their NMR spectral data can be found in Section 2.2.4.2. Proton NMR assignments were determined by chemical shift, signal integration and multiplicity of the resonances. The ^{1}H spectral feature at δ 3.76 was attributed to the methylene protons of the ethylenediamine bridge. A singlet, located at δ 3.82, was assigned to the two equivalent methoxycarbonyl groups. The protons of the phenyl ring were observed in the aromatic region of the spectrum at δ 7.11, 7.49 and 7.66. The imine proton for Ni(3-MOC-tsalen) was observed at δ 8.66. For this series of complexes the imine proton chemical shift ranged from δ 8.25 for both Ni(3-MOC-tsalpr) and Ni(3-MOC-tsalbut) to δ 9.39 and 9.50 for Ni(3-MOC-tsaldimph) and Ni(3-MOC-tsalphen). The downfield shift observed for Ni(3-MOC-tsaldimph) and Ni(3-MOC-tsalphen) is consistent with decreased electron density around the imine proton due to the presence of the electron-withdrawing phenylenediamine bridges. A similar downfield shift in the imine proton resonance was observed upon comparing Ni(3-MOC-tsalR) and the corresponding Ni(tsalR) complexes; the electron-withdrawing methoxycarbonyl substituent in Ni(3-MOC-tsalR) decreases the electron density of the complex. A comparison of the imine proton chemical shift resonances of Ni(3-MOC-tsalR) (R = en, pr, but, phen, dimph) and Ni(tsalR) (R = en, pr, but, phen, and dimph) are contained in Table 2.9.

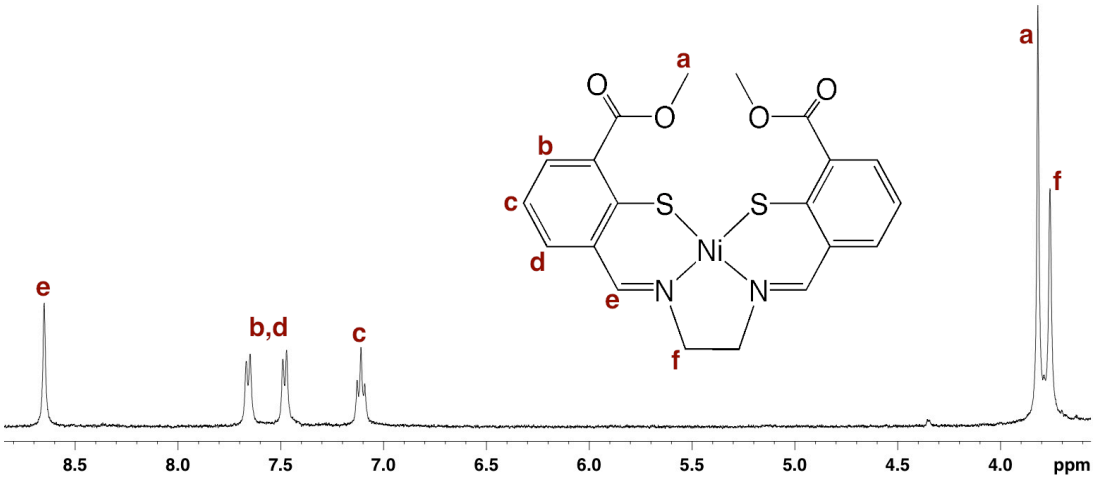

Figure 2.13. ^{1}H NMR spectrum of Ni(3-MOC-tsalen) in $(CD_3)_2SO$.

Table 2.9: Comparison of ^{1}H NMR -C*H*=N spectral resonances of Ni(3-MOC-tsalR) (R = en, pr, but, phen, dimph) and Ni(tsalR) (R = en, pr, but, phen, dimph) complexes.

Compound	**C*H*=N (*δ*)**
Ni(3-MOC-tsalen)	8.66
Ni(3-MOC-tsalpr)	8.25
Ni(3-MOC-tsalbut)	8.25
Ni(3-MOC-tsalphen)	9.50
Ni(3-MOC-tsaldimph)	9.39
Ni(tsalen)[a,84]	8.14
Ni(tsalpr)[a,89]	7.82
Ni(tsalbut)[a,86]	7.87
Ni(tsalphen)[87]	9.42
Ni(tsaldimph)[88]	8.82

Taken in dimethyl sulfoxide-d_6 unless noted otherwise; [a]Chloroform-d.

The $^{13}C\{^{1}H\}$ NMR spectrum of Ni(3-MOC-tsalen) (Figure A.1) revealed a signal for each unique carbon atom in the molecule. Signal assignments were determined by chemical shift and corroborated by Attached Proton Test (APT) and Heteronuclear Multiple Quantum Correlation (HMQC) NMR experiments (Figure A.2 and A.3). The corresponding methoxycarbonyl resonances in the spectrum were located at δ 52.52 and 168.78, while the methylene carbons of the ethylenediamine bridge were found at δ 164.75. The carbons of the phenyl ring were observed between δ 121.58 and 143.57, while the imine carbon was located at δ 164.75.

2.3.2.4 Electronic Absorption Spectroscopy of Ni(3-MOC-tsalR) (R = en, pr, but, phen, dimph)

The electronic absorption spectra of Ni(3-MOC-tsalR) (R = en, pr, but, phen, dimph) in dimethyl sulfoxide solution exhibited electronic transitions consistent with low-spin, d^8 metal centers in a square-planar ligand environment (Appendix A). The absorption features at ~270 nm were assigned as ligand $\pi \rightarrow \pi^*$ transitions, and are commonly observed in Schiff base metal complexes.[84,89,90] The spectra also contained high energy ligand-to-metal charge transfer (LMCT) bands, followed by the less intense metal-to-ligand charge transfer (MLCT) bands. The lowest intensity band, ~600 nm, was assigned as a d-d transition. A similar spectrum was observed for the low-spin square-planar Ni(tsalen) complex.[84] Electronic spectra of Ni(3-MOC-tsalen) are shown in Figure 2.14 and 2.15. A comparison of the electronic absorption data obtained for these complexes can be seen in Table 2.10.

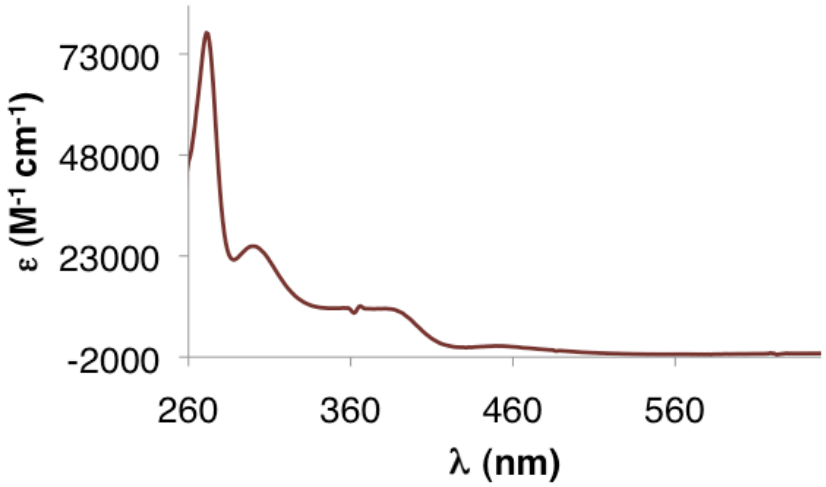

Figure 2.14. Electronic absorption spectrum of Ni(3-MOC-tsalen) in $(CH_3)_2SO$.

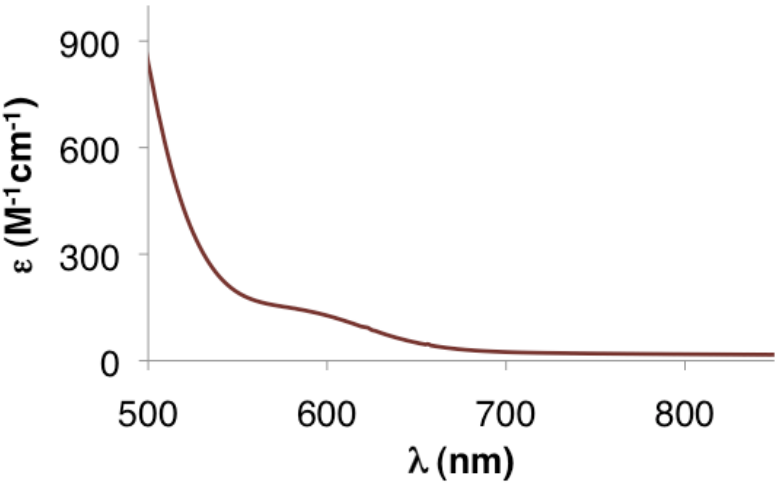

Figure 2.15. Electronic absorption spectrum of Ni(3-MOC-tsalen) in $(CH_3)_2SO$.

Table 2.10: Electronic spectral data for Ni(3-MOC-tsalR) (R = en, pr, but, phen, dimph) and Ni(tsalen).

Complex	λ_{max}, nm (ε, M^{-1} cm^{-1})
Ni(3-MOC-tsalen)	271 (76900), 299 (25700), 387 (11600), 447 (3240), 590 (161)
Ni(3-MOC-tsalpr)	270 (37400), 310 (15100), 387 (5920), 447(sh) (1840), 600 (110)
Ni(3-MOC-tsalbut)	271 (51300), 309 (24400), 394 (4810), 430(sh) (3400), 580 (234)
Ni(3-MOC-tsalphen)	292 (53100), 395 (13700), 552 (1880), 631 (1220)
Ni(3-MOC-tsaldimph)	294 (38400), 310(sh) (33600), 391 (17500), 548 (1730), 620 (1130)
Ni(tsalen)[a,84]	267 (12000), 390 (2800), 459 (616), 602 (50)

Taken in dimethyl sulfoxide unless noted otherwise; [a]Methylene Chloride.

2.3.2.5 Infrared Spectral Properties of Ni(3-MOC-tsalR) (R = en, pr, but, phen, dimph)

The solid state infrared spectra of Ni(3-MOC-tsalR) (R = en, pr, but, phen, dimph) displayed clear features for the, *ν*(C=O) and *ν*(C=N) stretches (Appendix A). Table 2.11 lists these stretching frequencies and those for the related Ni(tsalR) (R = pr, but, phen) complexes. The *ν*(C=N) stretching modes in Ni(3-MOC-tsalphen) and Ni(3-MOC-tsaldimph) are significantly lower in energy than those of Ni(3-MOC-tsalR) (R = en, pr, but). For example, the *ν*(C=N) stretching frequencies of Ni(3-MOC-tsalen) and Ni(3-MOC-tsalphen) are 1615 and 1532 cm^{-1}, respectively. This result is consistent with delocalization of π electrons of the phenylenediamine bridge over the C=N double bond. The extended conjugation reduced the double bond character in the C=N bond, resulting in absorption at lower energy. A similar effect was observed for the Ni(tsalR) (R = pr, but, phen) complexes.

Table 2.11: Infrared spectroscopic data for Ni(3-MOC-tsalR) (R = en, pr, but, phen, dimph) and Ni(tsalR) (R = pr, but, phen).

Complex	ν(C=O), cm^{-1}	ν(C=N), cm^{-1}
Ni(3-MOC-tsalen)	1722	1615
Ni(3-MOC-tsalpr)	1725	1616
Ni(3-MOC-tsalbut)	1726	1618
Ni(3-MOC-tsalphen)	1718, 1707	1532
Ni(3-MOC-tsaldimph)	1677, 1711	1528
Ni(tsalpr)[89]		1613, 1625
Ni(tsalbut)[91]		1625
Ni(tsalphen)[92]		1525

2.3.2.6 Electrochemical Characterization of Ni(3-MOC-tsalR) (R = en, pr, but, phen, dimph)

Cyclic voltammograms for the complexes Ni(3-MOC-tsalR) (R = en, pr, but, phen, dimph) are shown in Figure 2.16. Electrochemical data are listed in Table 2.12. Electrochemical experiments were performed in dimethyl sulfoxide at a scan rate of 100 mV/s. Reduction potentials were referenced to internal Fc^{+}/Fc couple at +670 mV versus NHE. Three complexes, Ni(3-MOC-tsalR) (R = en, pr, but), showed one reversible cathodic wave, assigned as the Ni(II)/Ni(I) reduction. As expected, based on their crystal structures, Ni(3-MOC-tsalen) exhibited the most negative reduction potential, $E_{1/2}$ = -1.22 V. The reduction potentials of Ni(II) are thought to be dependent on stereochemical factors. Ni(II) complexes typically prefer a square-planar geometry, while Ni(0) complexes prefer tetrahedral geometry; hence a square-planar complex with high tetrahedral distortion would favor a lower oxidation state and thus promote electrochemical reduction. For the present complexes, crystallographic data showed that with increasing methylene units in the diamine chain, the polymethylene bridges became more flexible augmenting the tetrahedral distortion of the complex

geometry. The correlation between the least negative reversible reduction potential, $E_{1/2}$ = -1.01 V, and the largest dihedral angle between the N(1)NiS(1) and N(2)NiS(2) coordination planes of the series, 13.30°, for Ni(3-MOC-tsalbut) supports this assertion. A plot of Ni(II)/Ni(I) reduction potentials versus the dihedral angles is shown in Figure 2.17. Examination of this plot confirms the correlation between the reduction potentials and the dihedral angles. Specifically, more methylene units in the bridging diamine chain leads to Ni(3-MOC-tsalR) complexes with larger dihedral angles making them easier to reduce. Further inspection of this plot shows a linear relationship (solid line) with a correlation coefficient of 0.9999 providing additional verification of this correlation. This behavior is similar to that observed for Ni(salen) (salen = *N*,*N'*-ethylenebis(salicylideneiminate) and Ni(salpr) (salpr = *N*,*N*'-1,3-propylenebis(salicylideneiminate) complexes reported previously.[93]

The cyclic voltammograms for the complexes with a phenylenediamine bridge, Ni(3-MOC-tsalR) (R= phen, dimph), were different (Figure 2.16). Both complexes displayed an irreversible cathodic peak assigned as a ligand reduction. The complex Ni(3-MOC-tsalphen) exhibited the least negative reduction potential of the series due to the electron withdrawing phenyl substituent. An analogous situation was observed for Ni(salphen) (salphen = *N,N'*-1,2-phenylenebis(salicylideneiminato) by Gosden, et al., where the reduced species was regarded as a Ni(II) complex with an anion radical.[93]

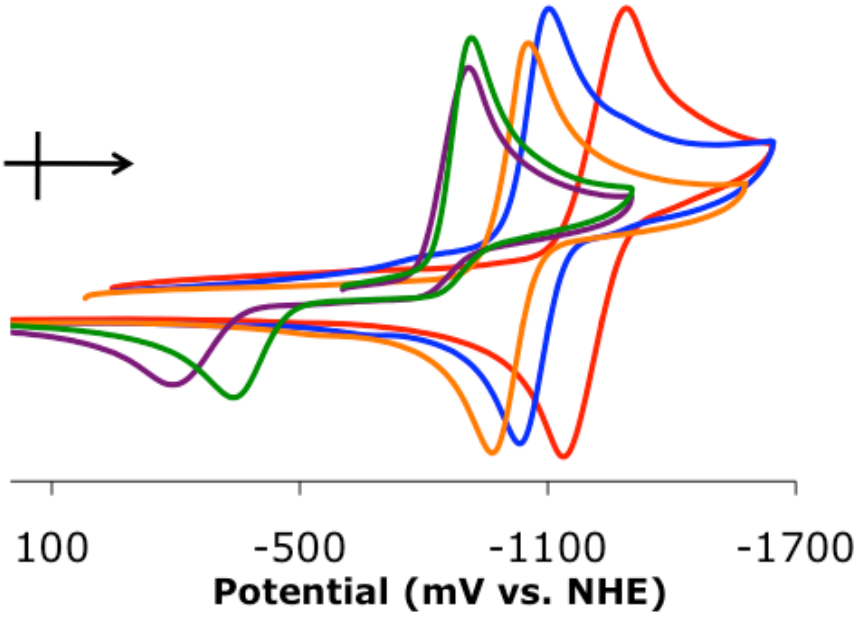

Figure 2.16. Cyclic voltammograms of Ni(3-MOC-tsalen)(–), Ni(3-MOC-tsalpr)(–), Ni(3-MOC-tsalbut)(–), Ni(3-MOC-tsalphen)(–), and Ni(3-MOC-tsaldimph)(–). Electrodes: glassy carbon (working), Ag^{+}/Ag (reference) and Pt wire (counter). Analyte solution concentrations range from 1-5 mM in 0.1 M [nBu$_4$]NPF$_6$ supporting electrolyte in dimethyl sulfoxide; scan rate of 100 mV/s. All potentials were referenced internally to Fc^{+}/Fc and reported *vs*. NHE.

Table 2.12: Electrochemical data for Ni(3-MOC-tsalR) (R = en, pr, but, phen, dimph) and Ni(salR) (R = en, pr).

	Ni(II)/Ni(I) (V)	
Ni(3-MOC-tsalen)[a]	-1.22	reversible
Ni(3-MOC-tsalpr)[a]	-1.07	reversible
Ni(3-MOC-tsalbut)[a]	-1.01	reversible
Ni(3-MOC-tsalphen)[a]	E_{pc} = -0.907, E_{pa} = -0.192	irreversible
Ni(3-MOC-tsaldimph)[a]	E_{pc} = -0.914, E_{pa} = -0.342	irreversible
Ni(salen)[b, 93]	-1.72	reversible
Ni(salpr)[b, 93]	-1.50	reversible

[a]vs. NHE (Fc^+/Fc in dimethyl sulfoxide, +0.67 V)
[b]vs. SCE (acetonitrile, 0.2 M $(C_4H_9)_4NBF_4$, complex concentration ~1 mM, Pt electrode.

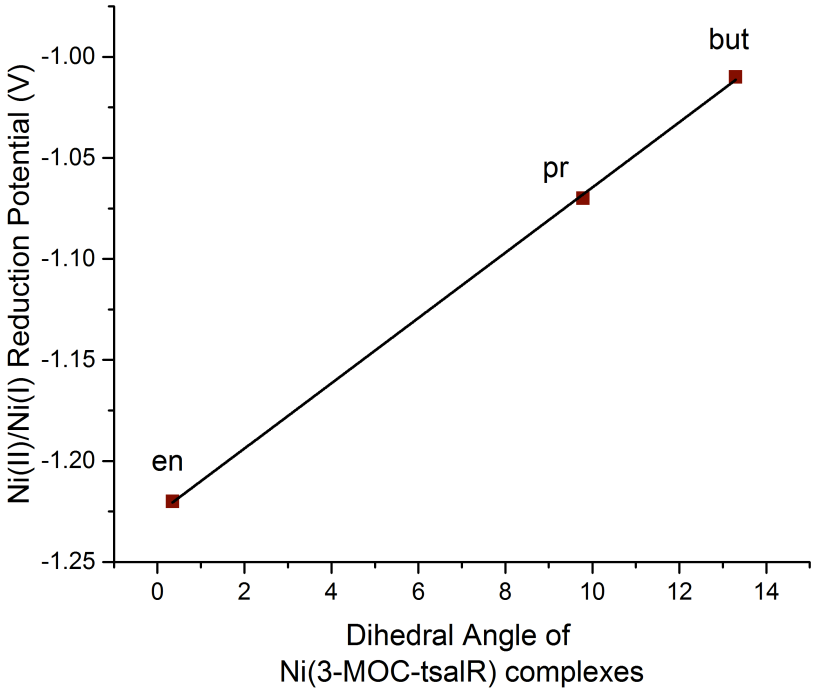

Figure 2.17. Plot of Ni(II)/Ni(I) reduction potentials versus dihedral angles of Ni(3-MOC-tsalR), the latter determined crystallographically. The dihedral angle for Ni(3-MOC-tsalbut) is the average of two crystallographically independent molecules. Linear correlation is shown with a correlation coefficient of 0.9999.

2.3.3 Synthetic Strategies Toward the Synthesis of an Asymmetric Thiophenolate-Bridged Macrocycle, H_4L^1

The mechanism of ACS catalysis is proposed to involve unprecedented bioorganometallic intermediates with distinct electronic structures. With the goal of further understanding the varying electronic structures of the proposed intermediates, the synthesis of a binucleating macrocycle with a N_4S_2 cavity consisting of imine and amide coordination sites, H_4L^1, was pursued (Figure 2.5). This macrocycle cavity should stabilize mixed valent complexes, while the different coordination sites provide a way to distinguish between the two coordinated metals. Tanaka et al.[76] previously synthesized a binucleating macrocycle with a N_4O_2 cavity and imine and amide coordination sites, H_4L^2, by the direct reaction of methyl 3-formylsalicylate and 1,2-diaminoethane (Figure 2.4). Further reaction of H_4L^2 with one or two equivalents of a nickel(II) salt in ethanol produced either the mono- or dinuclear metal complexes $Ni(H_2L^2)$ and Ni_2L^2.[76] Figure 2.18 displays the direct synthetic route undertaken to produce a more biologically relevant sulfur analogue of H_4L^2.

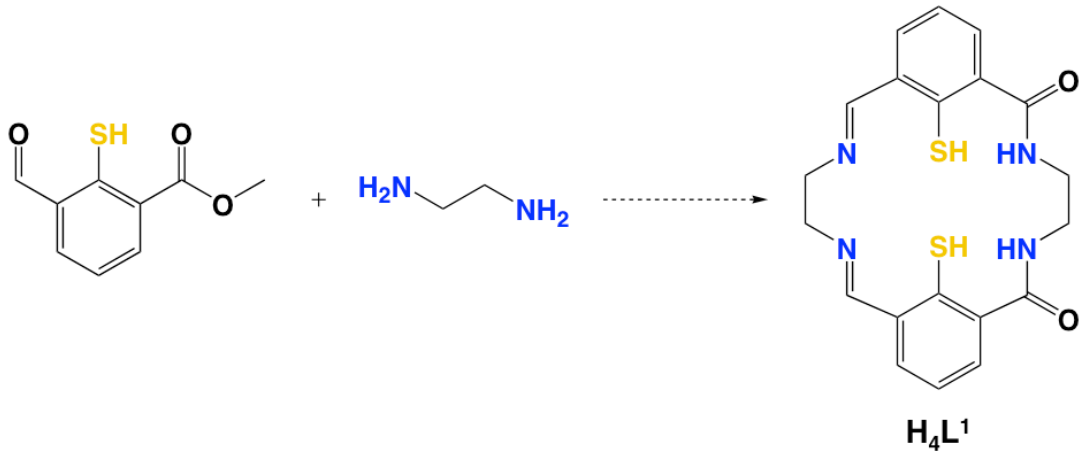

Figure 2.18. A direct macrocycle synthesis route for the formation of H_4L^1.

It was expected that methyl 3-formylthiosalicylate would react with 1,2-diaminoethane in a manner comparable to its oxygen counterpart, methyl 3-formylsalicylate, producing H_4L^1, an asymmetric binucleating macrocycle with a N_4S_2 cavity. Prior to testing this hypothesis, the preparation of methyl 3-formylthiosalicylate was attempted according to the reaction scheme depicted in Figure 2.6. The precursor complex methyl 3-formylsalicylate was synthesized according to known procedures in good yield.[80,77] A general strategy for the conversion of phenols to thiophenol via *O*- and *S*-thiocarbamates, known as a Newman-Kwart rearrangement, was then employed to yield methyl 3-formylthiosalicylate.[81] The preparation and characterization of *O*- and *S*-(methyl-3-formylsalicylate) dimethylthiocarbamate, discussed previously in this chapter, proceeded without complication. In contrast, the subsequent hydrolysis of *S*-(methyl-3-formylsalicylate) dimethylthiocarbamate to thiophenol using sodium hydroxide in methanol, followed by an acidic workup was unsuccessful. The initial change in solution, from clear to cloudy, upon addition of sodium hydroxide suggested that cleavage of the dimethylcarbamoyl fragment was successful. However, after the addition of acid to protonate the sulfur atom, no identifiable product was isolated. After numerous efforts to isolate methyl 3-formylthiosalicylate under a variety of conditions failed, the synthetic route toward H_4L^1 was altered.

Because the synthetic route failed at the acidification step-, in this new approach, Figure 2.19, *S*-(methyl-3-formylsalicylate) dimethylthiocarbamate was hydrolyzed *in situ*, prior to the introduction of the other macrocycle components, thus replacing the acidification step.

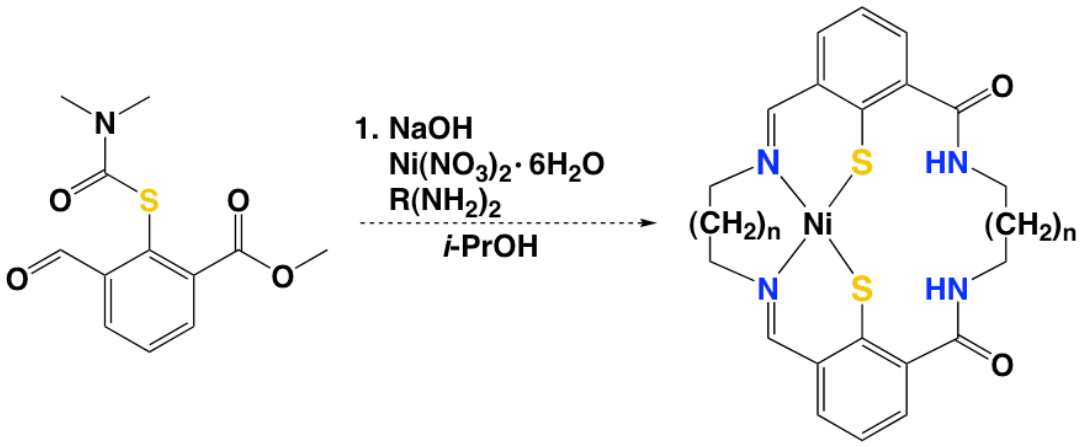

Figure 2.19. Metal-ion templated synthesis route for the formation of $Ni(H_2L^1)$.

This method was employed previously by Brooks et al.[83] for the synthesis of $[Ni_2L^3][ClO_4]_2$ and by Farsavi et al.[90] for the synthesis of $[Ni_2L^4][ClO_4]_2$ from *S*-(2,6-diformyl-4-methylphenyl) dimethylthiocarbamate (Figure 2.20). In both cases sodium hydroxide was added to a refluxing isopropyl alcohol solution of *S*-(2,6-diformyl-4-methylphenyl) dimethylthiocarbamate to initiate hydrolysis; subsequent addition of nickel(II) perchlorate hexahydrate and diamine precipitated the macrocyclic complexes.

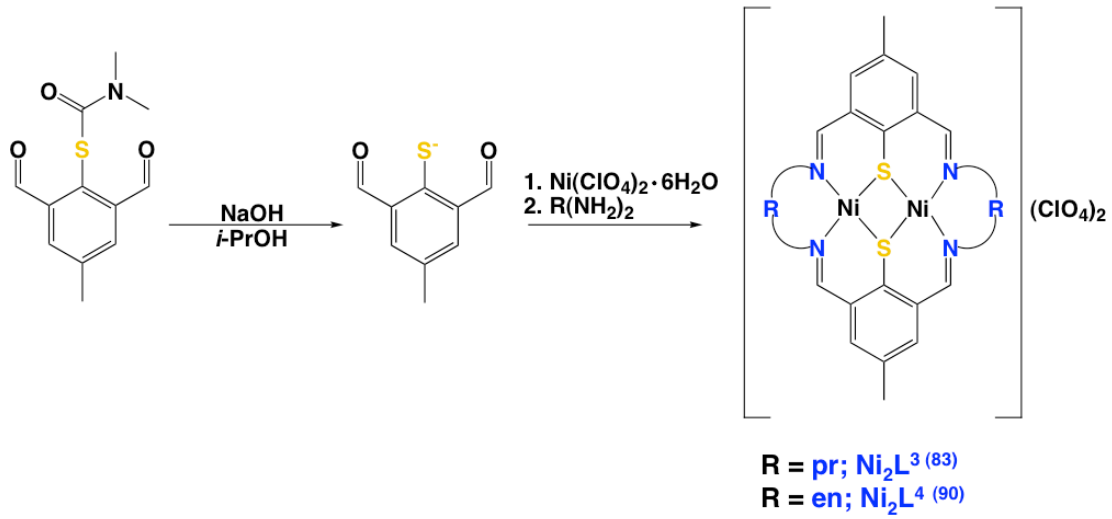

Figure 2.20. The synthesis of $[Ni_2L^3][ClO_4]_2$[83] and $[Ni_2L^4][ClO_4]_2$[90] via a metal-template route.

Attempts to prepare $Ni(H_2L^1)$ or Ni_2L^1 in a similar manner led to the isolation of the previously described Ni(3-MOC-tsalR) complex (Figure 2.10) and uncharacterizable products. The poor solubility of Ni(3-MOC-tsalR) in isopropyl alcohol prompted its immediate precipitation upon condensation with 1,2-diaminoethane in the presence of a nickel(II) salt. Efforts to combat this problem include reversing the order of substrate addition to diamine then nickel(II) salt, varying the time between additions and increasing the chain length of the diamine in an attempt to increase solubility. All attempts failed to produce a macrocyclic compound; however, a series of Ni(3-MOC-tsalR) (R = en, pr, but, phen, dimph) complexes were isolated.

A study by Cheng et al.[94], published after this work was initiated, reported a simpler one-pot synthetic procedure for the synthesis of Ni(H_2L^2) compared to that used by Tanaka et al.[76] A mixture of 3-formylsalicyclic acid, 1,2-diaminoethane, and nickel(II) acetate tetrahydrate in methanol was placed in a Parr bomb and heated at 180°C for twenty-four hours. Upon cooling the solution to room temperature red-crystals of Ni(H_2L^2) were obtained in a 100% yield.[94] Applying this method to the synthesis of H_4L^1 was less successful. When a mixture of *S*-(methyl-3-formylsalicylate) dimethylthiocarbamate, 1,4-diaminobutane, and nickel(II) acetate tetrahydrate in methanol was heated in a Parr bomb, a combination of malodorous unidentifiable products and nickel metal were obtained. In this sample reaction, no base was added to the reaction mixture to remove the dimethylcarbamoyl moiety, so if macrocyclic formation was to occur the size of the dimethylcarbamoyl would probably be too large to fit inside the cavity, which may explain why this reaction was unsuccessful in obtaining the desired product. A more promising mimic of this method, utilizing *S*-(methyl-3-formylsalicylate) dimethylthiocarbamate as a substrate, began with base-cleavage of the dimethylcarbamoyl fragment prior to the addition of diamine and nickel(II) acetate tetrahydrate to the reaction mixture. However, a combination of malodorous unidentifiable products and nickel metal were also obtained using this approach.

In a third attempt to synthesize and isolate H_4L^1, the series of Ni(3-MOC-tsalR) (R = en, pr, but, phen, dimph) complexes successfully produced and characterized previously, were utilized as the starting material in a variety of reactions (Figure 2.21). The diamagnetic mononuclear complexes possess a square-planar Ni atom in an N_2S_2 cavity formed by two imino nitrogen atoms and two thiolate sulfur

atoms with two pendant methyl ester arms ortho to the sulfur atoms (Figures 2.11 and 2.12).

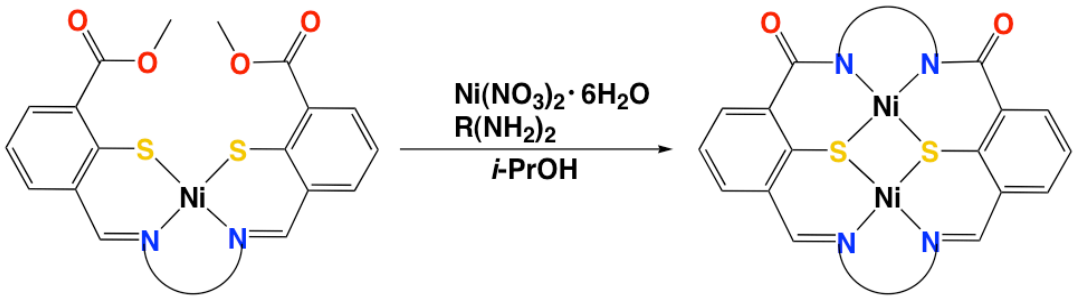

Figure 2.21. A synthetic route for the closure of a preformed half macrocycle complex.

This new approach to H_4L^1 focuses on the formation of an amide bridge between the methyl ester arms. Numerous experiments with various diamines and Ni(II) salts at different temperatures and reaction times were completed; however, all failed to generate any version of the desired complex. For example, a mixture of Ni(3-MOC-tsalpr) and 1,3-diaminopropane in methanol was heated in a Parr bomb overnight at 180°C producing unidentifiable products. The failure to form an amide bridge was probably caused by the poor solubility of the Ni(3-MOC-tsalR) complexes and the fact that alkyl esters are poor leaving groups.

All attempts at synthesizing a binucleating macrocycle with a N_4S_2 cavity consisting of imine and amide coordination sites were unsuccessful. The direct strategy approach to H_4L^1 (Figure 2.18), modeled after the synthesis of the analogous

binucleating macrocycle with a N_4O_2 cavity[76], failed during the preparation of the precursor complex methyl 3-formylthiosalicylate. The metal-template strategy (Figure 2.19), observed previously by Brooker[83] and Farsavi[90], was successful in generating the imine half of the macrocycle complex, Ni(3-MOC-tsalR) (R = en, pr, but, phen, dimph). However, poor solubility of the Ni(3-MOC-tsalR) complexes prevented the formation of the amide bridge and therefore closure of the macrocycle. This problem was addressed by attempting a one-pot synthetic procedure under solvothermal conditions, similar to those reported by Cheng et al.[94] The high temperature and pressure generated during the reaction was expected to force the synthesis of the imine and amide bridge to form NiL^1; however, malodorous unidentifiable products were obtained instead. The objective of the final strategy was to build upon the half macrocycle complex, Ni(3-MOC-tsalR) (R = en, pr, but, phen, dimph), by reacting it with a variety of diamines in effort to form amide bridges closing the macrocycle (Figure 2.21). However, poor solubility of Ni(3-MOC-tsalR) resulted in the recovery of starting material for most reactions.

The successful synthesis of a binucleating macrocycle with a N_4S_2 cavity consisting of imine and amide coordination sites is dependent on the precursor starting material. Tanaka et al.[76] used a direct synthetic reaction of heating methyl 3-formylsalicylate with 1,2-diaminoethane in the absence of solvent to form H_4L^2 (Figure 2.4). The presence of a phenol in methyl 3-formylsalicylate allows hydrogen bonding between the pairs of nitrogen donors aiding in the formation of the ring and stabilizing it once it is formed. The favorable outcome of this reaction compared to those discussed above highlights the importance of starting with a thiol head unit in the precursor complex to assist in cyclization. Templating the reaction with nickel

appeared to rectify this issue yet led to another problem, the poor solubility of Ni(3-MOC-tsalR) (R = en, pr, but, phen, dimph). After hydrolyzing *S*-(methyl-3-formylsalicylate) dimethylthiocarbamate *in situ*, a likely pathway to H_4L^1 begins with metal ion coordination and the formation of two Schiff bases followed by ring-closure via amide bond formation. The poor solubility of Ni(3-MOC-tsalR) (R =en, pr, but, phen, dimph), an intermediate on the pathway, results in its precipitation before amide bond formation. Increasing the length of the diamine bridge from en to but increases the solubility of Ni(3-MOC-tsalR) slightly; however, it was not enough to overcome the mediocre reactivity of a methyl ester toward amide formation. Further efforts toward the synthesis of the asymmetric N_4S_2 macrocycle should focus on the formation of the amide bridge. Converting the methyl ester arm of the precursor complex to a better leaving group, such as an aromatic ester, a carboxylic acid or an acyl chloride, should produce an amide at a much faster rate. The synthesis of 3-formylthiosalicylic acid as a precursor complex for the one-pot synthetic procedure under solvothermal conditions is also an attractive approach to undertake in the future.

2.4 Summary

Three mechanistic strategies were proposed for the synthesis of H_4L^1, a binucleating thiol macrocycle with imine and amide coordination sites. A direct synthesis, a metal template and a half-macrocycle closing route were all ineffective in generating H_4L^1. Despite the utilization of a variety of precursor complexes, diamines, and nickel(II) salts at different temperatures and reaction times, difficulties related to solubility and amide formation were impossible to overcome.

The synthetic route pursued in the direct synthesis strategy led to the formation and isolation of two new compounds, *O*- and *S*-(methyl-3-formylsalicylate)

dimethylthiocarbamate. The reaction of *S*-(methyl-3-formylsalicylate) dimethylthiocarbamate with Ni(II) salt and diamine via the metal template strategy, yielded a series of mononuclear Schiff base complexes, Ni(3-MOC-tsalR)(R = en, pr, but, phen, dimph) in fairly good yields (52-76%). The diamagnetic air stable complexes consist of a square-planar Ni atom in an N_2S_2 cavity formed by two thiolate sulfur atoms and two imino nitrogen atoms with two pendant methyl ester arms ortho to the sulfur atoms. The spectroscopic and crystallographic characterization of these compounds revealed the structural and electronic effect of altering the diamine backbone from a polymethylene (en, pr, but) to a phenylenediamine (phen, dimph) bridge. The X-ray structures revealed that all of the complexes displayed a small tetrahedral distortion from planarity. As the number of methylene units in the diamine backbone chain was increased, the polymethylene bridges of Ni(3-MOC-tsalR) (R = en, pr, but) became more flexible augmenting the distortion. Despite having the same number of methylene units in their respective diamine bridges, Ni(3-MOC-tsaldimph) and Ni(3-MOC-tsalphen) exhibit a tetrahedral distortion larger then that observed for Ni(3-MOC-tsalen). Due to the conjugation of electron density in the aromatic bridge, the diamine bridge of Ni(3-MOC-tsaldimph) and Ni(3-MOC-tsalphen) was forced to be planar resulting in a greater tetrahedral distortion. The extended conjugation of electron density over the Ni(3-MOC-tsaldimph) and Ni(3-MOC-tsalphen) complexes was also indicated by the low energy *ν*(C=N) stretching frequencies and the downfield chemical shifts of the imine protons observed for these complexes, compared to those observed for Ni(3-MOC-tsalR) (R = en, pr, but). Cyclic voltammetry studies of Ni(3-MOC-tsalR) (R = en, pr, but, phen, dimph) also displayed contrasting results for the different diamine backbones. The cyclic voltammograms of Ni(3-MOC-tsalR) (R =

en, pr, but) showed one reversible cathodic wave, assigned as the Ni(II)/Ni(I) reduction. As expected, as the length of the diamine backbone chain increased, Ni(3-MOC-tsalR) (R = en, pr, but) became easier to reduce in the order, but > pr > en. Ni(3-MOC-tsalR) (R = phen, dimph) exhibited an irreversible cathodic peak assigned as a ligand reduction.

Chapter 3

SYNTHESIS AND METHYL TRANSFER REACTIVITY OF (κ^2-$S^{iPr}PS^{iPr}$)$Ni(PPh_3)_2$: A MECHANISTIC MODEL OF ACETYL COENZYME A SYNTHASE

3.1 Introduction

Acetyl coenzyme A synthase (ACS) combines methyl from a methylated corrinoid iron-sulfur protein (CH_3-CoFeSP), CO from carbon monoxide dehydrogenase (COdH) and coenzyme A (CoA) to synthesize acetyl coenzyme A (acetyl-CoA). The proposed reaction involves biologically unprecedented nickel-methyl, nickel-carbonyl and acetyl-nickel intermediates. Despite extensive biochemical and spectroscopic studies, the mechanism by which acetyl-CoA is synthesized is still unknown. Unraveling the details of this mechanism will provide insight into the geometries, coordination numbers and oxidation states of nickel in biology. This chapter will focus on the lingering questions surrounding methyl group transfer. Specifically the oxidation state of the active A-cluster and the mechanism of methyl transfer from CH_3-CoFeSP to nickel will be discussed.

3.1.1 Methyl Transfer in Acetyl-Coenzyme A Synthase

The methyl group of acetyl-CoA is derived from CO_2 via the Wood-Ljungdahl pathway. Steps in this pathway involve formate dehydrogenase, a series of tetrahydrofolate (H_4folate) enzymes, methyltransferase and a corrinoid iron-sulfur protein (CoFeSP), to transform CO_2 into CH_3-CoFeSP.[13] During the final steps of acetyl-CoA synthesis, the methyl group is transferred from CH_3-Co^{3+}FeSP to the

reduced A-cluster of ACS. Kumar et al.[95] have shown that the concentration of CH_3-Co^{3+}FeSP declines at the same rate as Co^{1+}FeSP increases suggesting an S_N2-based nucleophilic displacement in which the methyl cation is transferred to nickel in a single step. The assignment of an S_N2 mechanism was supported by chiral methyl probe experiments (Figure 3.1).[96] The overall reaction proposed by the Wood-Ljungdahl pathway involves two methyl transfers. The first transfer from methyl tetrahydrofolate (CH_3-H_4folate) to CoFeSP is known to occur via an S_N2 mechanism that results in inversion of the chiral methyl group. If the second methyl transfer from CH_3-Co^{3+}FeSP to ACS also follows an S_N2 mechanism, a second inversion would result in the reaction product, acetate, having stereochemistry identical to the starting material. Lebertz et al.[96] synthesized a chiral methyl tetrahydrofolate and incubated it with cell-free extracts of *Moorella thermoacetica*, in the presence of methyl transferase, CoFeSP, CO and ACS. Following denaturation, acetate was isolated and its stereochemistry was determined to be identical to that observed for the starting material. The overall retention of stereochemistry is consistent with an S_N2 methyl transfer from CH_3-Co^{3+}FeSP to ACS.

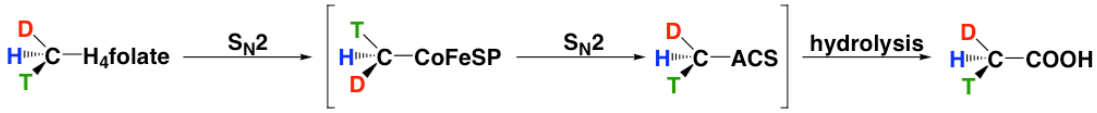

Figure 3.1. The stereochemical fate of methyl in chiral methyl transfer experiments performed by Lebertz et al.[96]

The molecular structure of the active-site cluster for ACS catalysis, the A-cluster (Figure 1.3b), contains an Fe_4S_4 cubane bridged by a cysteine (Cys) residue to a nickel atom (Ni_p, proximal to the Fe_4S_4). Ni_p is then bridged through two Cys side chain residues to a square planar nickel (Ni_d, distal to the Fe_4S_4) coordinated by the backbone nitrogen atoms of glycine (Gly) and Cys residues. Additionally a fourth, still unidentified, non-protein ligand is bound to Ni_p, completing its coordination sphere.[35,36,37] The oxidized form of the A-cluster (A_{ox}) has been formulated as $\{[Fe_4S_4]^{2+}\text{-}Ni_p^{2+}\text{-}Ni_d^{2+}\}$. As discussed earlier in Chapter 1, a variety of mechanisms have been proposed for ACS catalysis. Collectively, they can be placed into one of two distinct categories based on the oxidation state of the active A-cluster: paramagnetic or diamagnetic. In the paramagnetic mechanism Ragsdale and coworkers suggest a one-electron reduction of the A_{ox} state to a $Ni_p^{1+}Ni_d^{2+}$ species followed by methyl transfer producing a $CH_3\text{-}Ni_p^{3+}Ni_d^{2+}$ intermediate.[61,18] The diamagnetic mechanism, introduced by Lindahl and coworkers, assumes a two electron reduction of the A_{ox} state to a $Ni_p^{0}Ni_d^{2+}$ species followed by methyl transfer generating a $CH_3\text{-}Ni_p^{2+}Ni_d^{2+}$ intermediate.[62,63,17] Critics of the paramagnetic mechanism note the lack of observable EPR signals for the active A-cluster and subsequent intermediates as a major flaw. Detractors of the diamagnetic mechanism call attention to the lack of precedence for a biologically relevant zero-valent nickel species. The inability of either to directly or indirectly observe these states of the A-cluster means that there is little evidence either for or against the proposed mechanisms. The preparation of model systems for structural and spectroscopic comparison to the enzymatic systems has been undertaken.

3.1.2 Model Studies of Methyl Transfer in ACS

The desire to understand the methyl transfer reaction that occurs at the A-cluster of ACS has prompted the syntheses of active site analogues, utilizing ligands that mimic the coordination environment observed in the enzyme. Since Fe_4S_4 cubane and Ni_d are not thought to bind methyl, most model complexes have focused on emulating either the Ni_p or the bimetallic Ni_p-Ni_d environment, omitting the Fe_4S_4 cubane. Reviews give a succinct survey of model compounds that have been synthesized and analyzed.[33,70,71] Ram, et al.[97] published the first model system of ACS investigating methyl transfer (Figure 3.2a). [Ni(tmc)][OTf] (tmc = 1,4,8,11-tetramethyl-1,4,8,11-tetraazacyclotetradecane, OTf = triflate) was used as a model for the proximal nickel, and $RCo(dmgBF_2)_2py$ (R = methyl (Me), ethyl (Et), isopropyl (^{i}Pr), $dmgBF_2$ = (difluoroboryl)dimethylglyoximato, py = pyridine) as an alkyl transfer reagent. Addition of $MeCo(dmgBF_2)_2py$ to two equivalents of [Ni(tmc)][OTf] produced the Ni^{2+}-Me species, [Ni(tmc)Me][OTf], via an electron-transfer mechanism rather than an S_N2 mechanism as proposed to occur in the enzyme.[98,97] One equivalent of $[Ni(tmc)]^+$ reduced methyl-Co^{3+} to methyl-Co^{2+} followed by homolytic bond cleavage forming Co^{1+} and a methyl radical. The second equivalent of $[Ni(tmc)]^+$ then reacted with the methyl radical forming Ni^{2+}-Me. Evidence to support this mechanism included the observed rate increase of alkyl transfer, methyl < ethyl < isopropyl, which is consistent with the relative stabilities of the corresponding alkyl radicals.[98] Eckert, et al.[99] published the first investigation of methyl transfer from $MeCo(dmgBF_2)_2py$ to a Ni(0) model system utilizing $(triphos)Ni(PPh_3)$ (triphos = bis(2-diphenylphosphinoethyl)phenylphosphine, PPh_3 = triphenylphosphine) as a model for Ni_p (Figure 3.2b). $(triphos)Ni(PPh_3)$ acted as a nucleophile, attacking the Co-Me bond of $MeCo(dmgBF_2)_2py$ quantitatively forming a stable Ni^{2+}-Me species.

The Ni:Co stoichiometry of the reaction was determined to be 1:1 by Job plot analysis. A kinetic investigation of this reaction by O'Hagan[100] proposed an S_N2 mechanism for the alkyl transfer. As the steric bulk of the alkyl is increased there is a significant decrease in the transfer rate, methyl > ethyl > isopropyl, affirming the S_N2 pathway assignment.[100] Recently, the Tatsumi lab synthesized $Ni^{2+}Ni^{0}$ [101] and $Ni^{2+}Ni^{1+}$ [102] analogues of the A-cluster (Figure 3.2c and d). $Ni^{2+}(dadt^{Et})Ni^{0}(cod)$ ($dadt^{Et}$ = *N,N'*-diethyl-3,3-diazanonane-1,9-dithiolate, cod = 1,5-cyclooctadiene) was generated in situ from $Ni(dadt^{Et})$ and $Ni(cod)_2$, and then reacted with $MeCo(dmgBF_2)_2py$ and KSDmp (Dmp = 2,6-dimesitylphenyl) successively to produce $Ni(dadt^{Et})Ni(Me)(SDmp)$.[101] In a separate study, two equivalents of $Ni^{2+}(dadt^{Et})Ni^{1+}(SDmp)(PPh_3)$ were reacted with $MeCo(dmgBF_2)_2py$ and KSDmp consecutively to afford $Ni(dadt^{Et})Ni(Me)(SDmp)$.[102] According to these model studies, methyl group transfer from $MeCo(dmgBF_2)_2py$ occurred to either Ni(0) or Ni(I) complexes, indicating that either oxidation state is a possibility for the active Ni_p site during ACS catalysis.

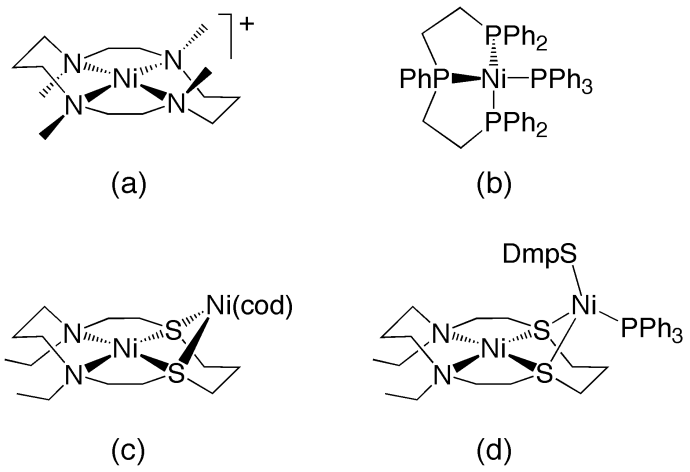

Figure 3.2. Synthetic A-cluster models used to study methyl transfer. (a) $[Ni(tmc)]^{+}$ [97] (b) (triphos)Ni(PPh_3) [99] (c) Ni($dadt^{Et}$)Ni(cod) [101] (d) $Ni^{2+}(dadt^{Et})Ni^{1+}(SDmp)(PPh_3)$.[102]

To expand upon our knowledge concerning the methyl transfer reaction, specifically the feasibility of Ni(0) to accept a methyl group from a methyl cobalt species, a new ligand, bis[2-(isopropylthio)ethyl]phenylphosphine ($S^{iPr}PS^{iPr}$, $PhP(CH_2CH_2SPr^{i})_2$), was synthesized. The utility of polydentate ligands containing sulfur and phosphorus in coordination chemistry has been extensively studied.[103,104,105,106] Most importantly, these ligands provide metal ions with a biologically relevant, sulfur-rich coordination environment for metalloenzyme modeling. $S^{iPr}PS^{iPr}$ embodied certain features that were useful in modeling the Ni_p of the A-cluster. The ligand consists of two thioether donor arms that are electronically similar to the bridging thiolates found in the enzyme active site and stabilizes the

Ni(0) and Ni(II) oxidation states. Additionally, $S^{iPr}PS^{iPr}$ provided a flexible structure to accommodate the tetrahedral geometry preferred by Ni(0) and the square planar geometry preferred by Ni(II) complexes. This chapter describes the synthesis and characterization of $S^{iPr}PS^{iPr}$ and $(\kappa^2\text{-}S^{iPr}PS^{iPr})Ni(PPh_3)_2$. In an effort to understand methyl transfer in ACS, the reaction of $(\kappa^2\text{-}S^{iPr}PS^{iPr})Ni(PPh_3)_2$ with $MeCo(dmgBF_2)_2py$ was monitored by ^1H, ^{31}P, ^2H NMR, electronic absorption and mass spectroscopies. Furthermore, the mechanism of alkyl transfer was characterized through kinetic studies including comparison to other alkyl substrates.

3.2 Experimental

3.2.1 General Procedures

Air and moisture sensitive reactions were carried out in a nitrogen or argon-filled Vacuum Atmospheres glovebox or on a manifold using standard Schlenk techniques.[78] All glassware was dried at 140 °C for at least 4 hours.

3.2.2 Physical Methods

All NMR spectra were recorded on a Bruker DRX 400 MHz spectrometer equipped with either a 5 mm QNP or a BBO probe. Data processing was performed using Bruker Topspin and MestReNova software. Chemical shifts are denoted as δ (ppm) with coupling constants reported in Hz. NMR abbreviations are as follows: s, singlet; d, doublet; sept, septet; dd, doublet of doublets; m, multiplet; br, broad. Proton and deuterium chemical shifts were referenced to residual solvent signals. ^{31}P spectra were recorded with proton decoupling and were referenced to either an internal capillary or external standard of 85% phosphoric acid in deuterium oxide or deuterated acetone. All data were collected at room temperature if not described otherwise.

Temperature calibration of the probe was conducted with neat methanol. Low and high resolution LIFDI (Liquid Injection Field Desorption Ionization)[107a,b] mass spectroscopy was performed on an AutoSpec spectrometer (Waters, Manchester, UK) with the assistance of Mr. John Dykins, University of Delaware. Samples were run in protio or deuterated solvent mixtures consisting of acetonitrile, toluene, acetone, and tetrahydrofuran. High resolution mass spectrometry using a 7-T Fourier transform ion cyclotron resonance (FT-ICR) mass spectrometer was performed with the help of Mr. Bryan Bzdek, University of Delaware. Electronic absorption data were collected using a Varian Cary 50 or Hewlett-Packard 8453 diode array spectrometer at room temperature, unless noted otherwise. The Varian Cary 50 spectrometer is equipped with a fiber optic coupler linked to Hellma quartz immersion probe, 1 cm path length. To exclude oxygen and water, samples were measured in either a custom fabricated three-neck glass vessel or a standard air-free quartz cuvette. All measurements were corrected for background by measurement of pure solvent at the desired temperature.

Crystallographic data were collected and reduced by Dr. Glenn P. A. Yap, University of Delaware. Samples were mounted onto a glass fiber using Paratone oil and cooled to the data collection temperature. Data were collected on a Bruker-AXS APEX CCD diffractometer with 0.7101 Å Mo-Kα radiation employing SMART software. The data sets were treated with SADABS absorption corrections based on redundant multi-scan data (Sheldrick, G., Bruker-AXS, 2001) and solved in the appropriate space group derived from systematic absences with SHELXTL 6.12. Crystal data collection and refinement parameters are given in Tables 3.1 and 3.2. Elemental analyses were performed by Columbia Analytical Laboratories, Inc., Tucson, Az.

3.2.3 Materials

With the exception of acetone and methanol, solvents were dried by passage through activated alumina columns[79] and oxygen was removed by sparging with nitrogen. Under an atmosphere of nitrogen, acetone was distilled from calcium sulfate. Methanol was distilled from magnesium metal/calcium hydride prior to use. Deuterated solvents were purchased from Cambridge Isotope Laboratories and dried over molecular sieves. 2-Iodopropane (Acros Organics), triphenylphosphine (Acros Organics), phenylphosphine (Alfa Aesar), *N*-butyllithium (Sigma Aldrich), ethylene sulfide (Sigma Aldrich) and bis(cyclooctadiene)nickel(0) ($Ni(cod)_2$) (Strem Chemicals) were obtained from the indicated suppliers and used without further purification. All other reagents were purchased from commercial sources and used as received, unless described otherwise. Methyl, methyl-d_3, ethyl, and isopropyl cobaloximes were prepared by previously published literature procedures.[98,108] Neopentyl cobaloxime was synthesized following the preparation reported by O'Hagan.[100]

3.2.4 Chemical Synthesis

Bis[2-(isopropylthio)ethyl]phenylphosphine; $PhP(CH_2CH_2SPr^i)_2$; $PhP(C_2H_4S^{i\text{Pr}})_2$; $S^{i\text{Pr}}PS^{i\text{Pr}}$ (**1**)

Caution: Phenylphosphine is a flammable liquid with a pungent odor. All reagents involved in the phenylphosphine reaction were added under a N_2 atmosphere that was vented through an aqueous solution of NaOCl.

$S^{i\text{Pr}}PS^{i\text{Pr}}$ was synthesized via a procedure adapted from Tereniak.[109] Phenylphosphine (5.0 g, 45 mmol) was added to a 1000-mL flask containing ~400 mL of tetrahydrofuran. The solution was cooled to -78 °C in a dry ice/acetone bath. *N*-

butyllithium (18 mL, 45 mmol, 2.5 M in hexanes) was added to the solution dropwise via syringe. After stirring for ~20 min, ethylene sulfide (2.7 mL, 45 mmol) was added to the reaction mixture using a syringe. A second addition of identical volumes of *N*-butyllithium and ethylene sulfide was performed ~30 min later as described above. The solution was stirred and permitted to warm to room temperature. Using a syringe, 2-iodopropane (9.0 mL, 90 mmol) was then added to the reaction mixture, which was further stirred at ambient temperature for 48 hr. The solution was subsequently reduced in volume under vacuum and placed in a separatory funnel. Following the addition of water and a saturated aqueous solution of sodium chloride, the organic layer was extracted with chloroform (3 x 50 mL). The combined organic extracts were washed with water (3 x 50 mL) and the resulting solution was dried over anhydrous sodium sulfate. The reaction mixture was filtered through a medium porosity frit and the solvent was removed in vacuo. The resulting oil was filtered through a small plug of silica gel with pentane to remove lithium iodide. After the solvent was removed in vacuo, the crude oil was distilled under vacuum between 145 – 150 °C, affording a colorless oil. Yield 10.12 g, 71%. ^{1}H NMR ($CDCl_3$): δ 1.19 (d, 6H, SCH(CH_3)$_2$, $^{3}J_{H\text{-}H}$ = 6.8 Hz), 1.20 (d, 6H, SCH(CH_3)$_2$), $^{3}J_{H\text{-}H}$ = 6.8 Hz), 2.00 (m, 4H, PCH_2CH$_2$S), 2.53 (m, 4H, PCH$_2$CH_2S), 2.89 (sept, 2H, SCH(CH$_3$)$_2$, $^{3}J_{H\text{-}H}$ = 6.7 Hz), 7.36 (m, 3H, P(C$_6H_5$)), 7.52 (m, 2H, P(C$_6H_5$)). ^{13}C{^{1}H} NMR ($CDCl_3$): δ 23.28 (s, 4C, SCH(*C*H$_3$)$_2$), 26.92 (d, 2C, P*C*H$_2$CH$_2$S, $^{1}J_{P\text{-}C}$ = 19.1 Hz), 28.68 (d, 2C, PCH$_2$*C*H$_2$S, $^{2}J_{P\text{-}C}$ = 14.7 Hz), 34.79 (s, 2C, S*C*H(CH$_3$)$_2$), 128.61 (d, 2C, P(*C*$_6$H$_5$), $J_{P\text{-}C}$ = 7.0 Hz), 129.30 (s, 1C, P(*C*$_6$H$_5$)), 132.44 (d, 2C, P(*C*$_6$H$_5$), $J_{P\text{-}C}$ = 19.3 Hz), 136.79 (d, 1C, P(*C*$_6$H$_5$), $J_{P\text{-}C}$ = 15.4 Hz). ^{31}P{^{1}H} NMR ($CDCl_3$): δ -24.15 (s). HR ESI MS: $C_{16}H_{27}PS_2$ calculated m/z^+: 315.1364 [MH^+], found m/z^+: 315.1363 [MH^+].

(κ^2-S$^{i\text{Pr}}$PS$^{i\text{Pr}}$)Ni(PPh$_3$)$_2$ (**2**)

A Schlenk flask was charged with Ni(cod)$_2$ (0.77 g, 2.8 mmol) dissolved in ~10 mL of toluene. Triphenylphosphine (1.47 g, 5.6 mmol) in ~10 mL of toluene was added to the flask generating a dark red solution. To this stirring mixture, **1** (0.87 g, 2.8 mmol) was added in ~5 mL of toluene. The resulting dark red/orange solution was stirred for 1 hr and then reduced in volume to ~3 mL under vacuum. Following the addition of pentane and stirring for 0.5 hr, the product precipitated from solution as an orange powder. The precipitate was collected on a medium porosity frit, washed with pentane and dried in vacuo. Yield 1.72 g, 69%. ^{1}H NMR (C_7D_8): δ 1.09 (d, 6H, SCH(CH_3)$_2$, $^3J_{H\text{-}H}$ = 6.3 Hz), 1.10 (d, 6H, SCH(CH_3)$_2$, $^3J_{H\text{-}H}$ = 6.3 Hz), 1.85 (m, 4H, PCH_2CH$_2$S), 2.45 (m, 6H, PCH$_2$CH_2S, SCH(CH$_3$)$_2$), 6.97 – 7.40 (m, 35H, P(C$_6H_5$), (-P(C$_6H_5$)$_3$)$_2$). ^{1}H NMR 240K (C_7D_8): δ = 1.07 (d, 6H, SCH(CH_3)$_2$), 1.31 (d, 6H, SCH(CH_3)$_2$), 1.78, 1.99, 2.34, 2.49, 2.73 (br, 10H, PCH_2CH_2S, SCH(CH$_3$)$_2$), 7.00 – 7.55 (m, 35H, P(C$_6H_5$), (-P(C$_6H_5$)$_3$)$_2$). ^{31}P{^{1}H} NMR 300K (C_7D_8): δ 23.04 (br, 3P). ^{31}P{^{1}H} NMR 240K: δ = 24.70 (dd, 1P, (-P(C$_6$H$_5$)$_3$)$_2$, $^2J_{P\text{-}P}$ = 55.1, 41.8 Hz), 23.27 (dd, 1P, P(C$_6$H$_5$), $^2J_{P\text{-}P}$ = 48.7, 42.4 Hz), 21.36 (dd, 1P, (-P(C$_6$H$_5$)$_3$)$_2$, $^2J_{P\text{-}P}$ = 53.9, 50.2 Hz). UV-vis (THF), λ_{max} (ε, M^{-1} cm^{-1}): 276 (15,000), 361 (11,000). High Res LIFDI: $C_{52}H_{57}NiP_3S_2$ calculated m/z^+: 896.246808, found m/z^+: 896.249400. Elemental Analysis: Anal. Calcd. for $C_{52}H_{57}NiP_3S_2$: %C 69.57; %H 6.40. Found %C 69.53; %H 6.71.

(κ^2-S$^{i\text{Pr}}$PS)$_2$Ni (**3**)

Solutions of (κ^2-S$^{i\text{Pr}}$PS$^{i\text{Pr}}$)Ni(PPh$_3$)$_2$ were unstable, turning from orange to dark red upon standing under N_2. Crystals were grown via slow evaporation of a concentrated pentane solution concurrently with crystals of (κ^2-S$^{i\text{Pr}}$PS$^{i\text{Pr}}$)Ni(PPh$_3$)$_2$. ^{1}H

NMR (C_6D_6): δ 1.14 (d, 6H, SCH(CH_3)$_2$, $^3J_{H-H}$ = 6.56 Hz), 1.23 (d, 6H, SCH(CH_3)$_2$, $^3J_{H-H}$ = 6.56 Hz), 1.90 – 3.19 (m, 18H, SC*H*(CH_3)$_2$, PC*H*$_2$C*H*$_2$S, PC*H*$_2$C*H*$_2$S$^{i\text{Pr}}$), 6.94 (br, 4H, P(C_6H_5)), 7.92 (m, 6H, P(C_6H_5)). $^{31}P\{^1H\}$ NMR (C_6D_6): δ 64.88 (s). High Res LIFDI: $C_{26}H_{40}NiP_2S_4$ calculated m/z^+: 600.084163, found m/z^+: 600.085322.

3.2.5 Reactivity Studies

Reactions of (κ^2-S$^{i\text{Pr}}$PS$^{i\text{Pr}}$)Ni(PPh_3)$_2$ with alkylcobaloximes, i.e. methyl, methyl-d_3, ethyl, isopropyl, and neopentyl, were followed and characterized by ^1H, ^2H, ^{31}P NMR, electronic absorption, and LIFDI mass spectroscopies. Equimolar amounts of (κ^2-S$^{i\text{Pr}}$PS$^{i\text{Pr}}$)Ni(PPh_3)$_2$ and alkylcobaloxime were combined in 1:1 mixtures of d^8-toluene or tetrahydrofuran and d^6-acetone or acetone, respectively, under an inert atmosphere. Aliquots were taken from the reaction mixture and analyzed for alkyl transfer by ^1H, ^2H, ^{31}P NMR, and LIFDI mass spectroscopies. Similar experimental conditions were used for electronic absorption spectroscopic measurements. Samples were extracted from a reaction mixture consisting of 0.2 mM (κ^2-S$^{i\text{Pr}}$PS$^{i\text{Pr}}$)Ni(PPh_3)$_2$ and 0.2 mM alkylcobaloxime in a 1:1 tetrahydrofuran:acetonitrile mixed solvent system. The extent of the reactions was monitored and quantitated by the concentration calculated for Co(I) formation, ε_{615} = 10,000 $M^{-1}cm^{-1}$.[99]

3.2.5.1 Reaction of (κ^2-S$^{i\text{Pr}}$PS$^{i\text{Pr}}$)Ni(PPh_3)$_2$ with $CH_3Co(dmgBF_2)_2py$

[(κ^2-S$^{i\text{Pr}}$PS$^{i\text{Pr}}$)Ni(PPh_3)(CH_3)]$^+$ (**4**): approximately 95% conversion observed by electronic absorption spectroscopy. ^1H NMR (C_7D_8:(CD_3)$_2$CO): δ 0.15 (d, 3H, C*H*$_3$, $^3J_{H-P}$ = 5.96 Hz), 1.30 (m, 12H, SCH(C*H*$_3$)$_2$), 2.63 (br, 2H, SC*H*(CH_3)$_2$), 2.92 (br, 8H, PC*H*$_2$C*H*$_2$S), 7.44 – 7.65 (m, 20H, P(C_6H_5), -P(C_6H_5)$_3$). $^1H\{^{31}P\}$ NMR (C_7D_8:(CD_3)$_2$CO): δ 0.14 (s, 3H, C*H*$_3$), 1.30 (m, 12H, SCH(C*H*$_3$)$_2$), 2.63 (br, 2H,

SC*H*$(CH_3)_2$), 2.92 (br, 8H, PCH_2CH_2S), 7.44 – 7.65 (m, 20H, P(C_6H_5, -P(C_6H_5)$_3$). ^{31}P{^{1}H} NMR (C_7D_8:$(CD_3)_2CO$): δ 49.42 (br, *P*(C_6H_5)). High Res LIFDI: $C_{35}H_{45}NiP_2S_2$ calculated m/z^+: 649.179144, found m/z^+: 649.182000.

3.2.5.2 Reaction of (κ^2-S$^{i\text{Pr}}$PS$^{i\text{Pr}}$)Ni(PPh$_3$)$_2$ with CD$_3$Co(dmgBF$_2$)$_2$py

[(κ^2-S$^{i\text{Pr}}$PS$^{i\text{Pr}}$)Ni(PPh$_3$)(CD$_3$)]$^+$ (**5**). ^{1}H NMR (C_7D_8:$(CD_3)_2CO$): δ 1.31 (m, 12H, SCH(CH_3)$_2$), 2.63 (br, 2H, SC*H*$(CH_3)_2$), 2.94 (br, 8H, PCH_2CH_2S), 7.45 – 7.65 (m, 20H, P(C_6H_5), -P(C_6H_5)$_3$). ^{2}H NMR ($(CH_3)_2CO$:$(CH_2)_4O$): δ -0.26 (s, 3D, -CD_3). ^{31}P{^{1}H} NMR (C_7D_8:$(CD_3)_2CO$): δ 49.56 (br, *P*(C_6H_5)). High Res LIFDI: $C_{35}H_{42}D_3NiP_2S_2$ calculated m/z^+: 652.197975, found m/z^+: 652.200700.

3.2.5.3 Reaction of (κ^2-S$^{i\text{Pr}}$PS$^{i\text{Pr}}$)Ni(PPh$_3$)$_2$ with neopentylCo(dmgBF$_2$)$_2$py

[(S$^{i\text{Pr}}$PS$^{i\text{Pr}}$)Ni(neopentyl)]$^+$ (**6**) : approximately 75% conversion observed by electronic spectroscopy. ^{1}H NMR (C_7D_8:$(CD_3)_2CO$): δ 0.71 (s, 9H, CH_2(CH_3)$_3$), 1.09 (s, 2H, C$H_2$$(CH_3)_3$), 1.24 (d, 6H, SCH(C$H_3$)$_2$, $^3J_{H\text{-}H}$ = 6.44 Hz), 1.32 (d, 6H, SCH(CH_3)$_2$, $^3J_{H\text{-}H}$ = 6.44 Hz), 2.60 (m, 2H, SC*H*$(CH_3)_2$), 2.85 (m, 4H, -CH_2-), 3.05 (m, 4H, -CH_2-), 7.40 – 7.65 (br, P(C_6H_5)). ^{31}P{^{1}H} NMR (C_7D_8:$(CD_3)_2CO$): δ 40.16 (s, 1P, *P*(C_6H_5)). Low Res LIFDI: $C_{21}H_{38}NiPS_2$ calculated m/z^+: 443.1, found m/z^+: 443.3.

3.2.6 Kinetic Studies of Alkyl Transfer

A Varian Cary 50 spectrophotometer equipped with a fiber optic coupler and a Hellma quartz immersion probe was used for all measurements. The probe was corrected for background by measurement of pure solvent. In a typical experiment, solutions were prepared in an argon filled glovebox immediately prior to use and were placed in a custom fabricated three-neck vessel sealed with septa/stoppers and

stopcocks as appropriate. The immersion probe was inserted under a continuous flow of nitrogen while the liquid volume in the apparatus was stirred and cooled to 12 °C using a circulatory bath. The reaction was initiated by the addition of alkylcobaloxime using a syringe needle through the rubber septum. Immediately following addition, the nitrogen flow was removed, stirring was stopped and measurement commenced. The final mixture (10 mL, 9:1 tetrahydrofuran:acetonitrile) contained: 2mM (κ^2-$S^{iPr}PS^{iPr}$)$Ni(PPh_3)_2$, 2 mM PPh_3, 5 mL tetrahydrofuran and 0.1 mM alkylcobaloxime. The extent of the reaction was monitored by following the change in absorbance at 615 nm, indicative of Co(I) formation. All measurements were run in triplicate and the average reported with standard deviation error.

3.2.7 X-ray Crystallography

3.2.7.1 (κ^2-$S^{iPr}PS^{iPr}$)$Ni(PPh_3)_2$

The crystals obtained here were consistent with those previously observed by Tereniak[109] and Eckert.[110] Crystal data collection and refinement parameters are given in Table 3.1. A single crystal was harvested and mounted using Paratone oil on a MiTeGen MicroMount. Crystallographic data were collected on two separate occasions for this molecule. Red blocks of (κ^2-$S^{iPr}PS^{iPr}$)$Ni(PPh_3)_2$ were grown by slow evaporation of a concentrated pentane solution. The assigned space group was P2(1)/c. The asymmetric unit contained two crystallographically independent molecules. Alternatively, orange blocks of (κ^2-$S^{iPr}PS^{iPr}$)$Ni(PPh_3)_2$ were grown by slow evaporation of a concentrated tetrahydrofuran solution. The assigned space group was P2(1)/c. Data were collected at 200(2) and 120(2) K, respectively.

3.2.7.2 $(\kappa^2\text{-}S^{i\text{Pr}}PS)_2Ni$

Crystal data collection and refinement parameters are given in Table 3.2. A single crystal was harvested and mounted using Paratone oil on a MiTeGen MicroMount. Data were collected at 200(2) K. Green blocks of $(\kappa^2\text{-}S^{i\text{Pr}}PS)_2Ni$ were grown by slow evaporation of a concentrated pentane solution. The asymmetric unit contained two crystallographically independent molecules. The assigned space group was P2(1)2(1)2.

Table 3.1: Crystallographic data for κ^2-($S^{i\text{Pr}}PS^{i\text{Pr}}$)$Ni(PPh_3)_2$, two crystalline phases, α[109] and β.[110]

Compound	$(\kappa^2\text{-}S^{i\text{Pr}}PS^{i\text{Pr}})Ni(PPh_3)_2$-α	$(\kappa^2\text{-}S^{i\text{Pr}}PS^{i\text{Pr}})Ni(PPh_3)_2$-β
Identification Code	Char230	Char168a
Empirical Formula	$C_{52}H_{57}NiP_3S_2$	$C_{52}H_{55}NiP_3S_2$
Formula Weight	897.72	895.70
Color, Habit	Red, Block	Orange, Block
Crystal System	Monoclinic	Monoclinic
Space Group	P2(1)/c	P2(1)/c
a, Å	11.4250(17)	13.4373(16)
b, Å	18.719(3)	16.100(2)
c, Å	43.809(7)	21.812(3)
α, deg	90	90
β, deg	96.422(2)	98.131(2)
γ, deg	90	90
V (Å^3)	9311(2)	4671.4(10)
Z	8	4
Temperature (K)	200(2)	120(2)
$Density_{calc}$, (g/cm^3)	1.281	1.274
2θ range, deg	1.18-28.27	1.99-28.28
GOF (F^2)	1.063	1.043
μ(Mo, Kα), mm^{-1}	0.644	0.642
R(F)/R_w(F)	0.0466/0.1038	0.0566/0.1361

Quantity minimized = $R(wF^2) = \Sigma[w(F_0^2\text{-}F_c^2)^2]/\Sigma[(wF_0^2)^2]^{0.5}$; $R = \Sigma\Delta/\Sigma(F_0)$, $\Delta = |(F_0\text{-}F_c)|$, $w = 1/[\sigma^2(F_0^2) + (aP)^2 + bP]$, $P = [2F_c^2 + \text{Max}(F_0, 0)]/3$

Table 3.2: Crystallographic data for $[\kappa^2\text{-}(S^{i\text{Pr}}PS)]_2Ni$.

Compound	$(\kappa^2\text{-}S^{i\text{Pr}}PS)_2Ni$
Identification Code	Char251a
Empirical Formula	$C_{26}H_{40}NiP_2S_4$
Formula Weight	601.47
Color, Habit	Green, Block
Crystal System	Orthorhombic
Space Group	P2(1)2(1)2
a, Å	24.546(19)
b, Å	9.926(8)
c, Å	12.496(10)
α, deg	90
β, deg	90
γ, deg	90
V (Å^3)	3045(4)
Z	4
Temperature (K)	200(2)
$Density_{calc}$, (g/cm^3)	1.312
2θ range, deg	1.63-28.34
GOF (F^2)	1.045
μ(Mo,Kα), mm^{-1}	1.030
$R(F)/R_w(F)$	0.0516/0.1319

Quantity minimized = $R(wF^2) = \Sigma[w(F_0^2\text{-}F_c^2)^2]/\Sigma[(wF_0^2)^2]^{0.5}$; $R = \Sigma\Delta/\Sigma(F_0)$, $\Delta = |(F_0\text{-}F_c)|$, $w = 1/[\sigma^2(F_0^2) + (aP)^2 + bP]$, $P = [2F_c^2 + \text{Max}(F_0, 0)]/3$

3.3 Results and Discussion

The Riordan laboratory has utilized organometallic nickel complexes to mimic the transfer of methyl from CH_3-CoFeSP to the proximal nickel of the A-cluster of ACS during acetyl-coenzyme A synthesis. Ram, et al.[98,97] examined methyl transfer using [Ni(tmc)][OTf] as a model for Ni_p and $MeCo(dmgBF_2)_2py$ as an alkyl transfer agent. Addition of $MeCo(dmgBF_2)_2py$ to 2 equiv of [Ni(tmc)][OTf] produced the Ni^{2+}-Me species, [Ni(tmc)Me][OTf] via an electron-transfer mechanism. Evidence to

support this mechanism included the observed rate increase of alkyl transfer, methyl < ethyl < isopropyl, which was consistent with the relative stabilities of the corresponding alkyl radicals.[98,97] Eckert, et al.[99] utilized (triphos)Ni(PPh_3) as a model for Ni_p and showed that it can act as a nucleophile attacking the Co-Me bond of $MeCo(dmgBF_2)_2py$ quantitatively forming a stable Ni^{2+}-Me species. A kinetic investigation of this reaction by O'Hagan[100] proposed an S_N2 mechanism for the alkyl transfer. As the steric bulk of the alkyl was increased there was a significant decrease in the transfer rate, methyl > ethyl > isopropyl, affirming the S_N2 assignment.[100] It is apparent from these results, that both Ni(I) and Ni(0) are viable oxidation states for intermediates formed during ACS catalysis. In addition, the ongoing debate concerning the mechanism of methyl transfer remains unsettled. To gain further insight into this reaction, present efforts focused on the preparation of a new model system. The synthesis and characterization of $S^{iPr}PS^{iPr}$, a tridentate ligand containing biologically relevant thioether arms, and (κ^2-$S^{iPr}PS^{iPr}$)Ni(PPh_3)$_2$ is reported. Additionally, the reaction of (κ^2-$S^{iPr}PS^{iPr}$)Ni(PPh_3)$_2$ and $MeCo(dmgBF_2)_2py$ was monitored by ^1H, ^{31}P, ^2H NMR and electronic absorption and mass spectroscopies. The mechanism of alkyl transfer in the model system was characterized through kinetic studies and comparison to other alkyl substrates.

3.3.1 Bis[2-(isopropylthio)ethyl]phenylphosphine; $PhP(CH_2CH_2SPr^i)_2$; $PhP(C_2H_4S^{iPr})_2$; $S^{iPr}PS^{iPr}$ (1)

Polydentate ligands containing both sulfur and phosphorus groups in their framework have been extensively used in coordination chemistry. $S^{iPr}PS^{iPr}$ incorporates important features required for models of the proximal nickel in the A-cluster. The ligand is structurally flexible to accommodate the tetrahedral geometry

preferred by Ni(0) and the square planar geometry preferred by Ni(II) complexes and the thioether donor arms are electronically similar to bridging thiolates found in the enzyme active site. The synthesis of $S^{iPr}PS^{iPr}$ was accomplished by modification of a preliminary procedure reported by this laboratory. Tereniak[109] utilized extraction with various organic solvents followed by filtration through celite and/or column chromatography for the purification of **1**. Although a moderate yield, 42%, was reported[109] the sample purity was questionable based upon varying product yields of further reactions with nickel salts. The purification method employed here, extraction with chloroform followed by filtration through silica gel and distillation, produced a higher yield, 71%, and a cleaner product based upon further reactions with $Ni(cod)_2$. A closer examination of the synthesis and spectroscopic properties of $S^{iPr}PS^{iPr}$ is presented below.

3.3.1.1 Synthesis and Properties

$S^{iPr}PS^{iPr}$ was prepared in an analogous fashion to that of bis[2-(ethylthio)ethyl]phenylphosphine ($S^{Et}PS^{Et}$)[104,111], Figure 3.3. The synthetic pathway began with formation of the dilithium 3-phenyl-3-phosphapenta-1,5-dithiolate salt generated *in situ* by nucleophilic ring cleavage of ethylene sulfide with deprotonated phenylphosphine, according to a previously published procedure.[112] Subsequently, the dilithium salt was alkylated with 2-iodopropane producing $S^{iPr}PS^{iPr}$ as a colorless oil in a 71% overall yield. It is important to note that filtration of the crude oil product through a small plug of silica gel with pentane, to remove the lithium iodide by-product, prior to vacuum distillation was critical in optimizing the yield of pure $S^{iPr}PS^{iPr}$. The presence of excess salt in the crude product pushed the vacuum

distillation temperature higher, resulting in the decomposition of a substantial fraction of the product.

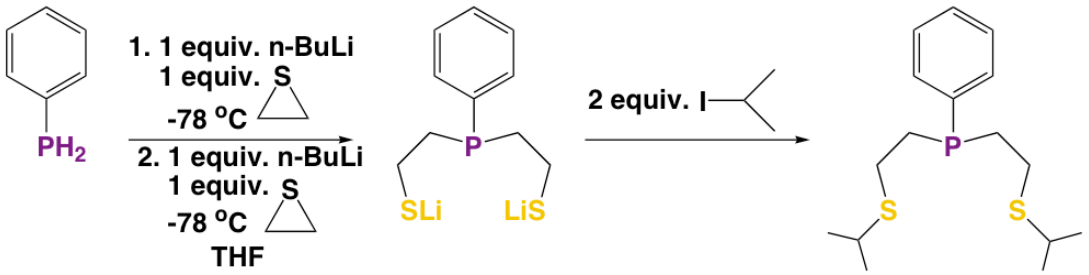

Figure 3.3. Synthesis of $S^{iPr}PS^{iPr}$.

3.3.1.2 Mass, Electronic Absorption and Nuclear Magnetic Resonance Spectroscopic Characterization

The identity and purity of the ligand was established by $^{31}P\{^{1}H\}$, ^{1}H, and $^{13}C\{^{1}H\}$ NMR and mass spectroscopies (Appendix B). The $^{31}P\{^{1}H\}$ NMR spectrum of $S^{iPr}PS^{iPr}$ showed a single peak at δ = -24.15, which is identical to that observed for $S^{Et}PS^{Et}$.[105] Figure 3.4 displays the ^{1}H NMR spectrum of **1**. It exhibits multiple resonances, with the correct integration ratio, in the aromatic and aliphatic regions. As the methyl groups in the isopropyl fragment are diastereotopic, two doublets (1.19 and 1.20 ppm, $^{3}J_{H\text{-}H}$ = 6.8 Hz) were observed for these protons. A septet at 2.89 ppm, $^{3}J_{H\text{-}H}$ = 6.7 Hz, was assigned to the isopropyl methine proton. The methylene protons of the -PCH_2CH_2S- fragment appear as complex multiplets, 2.00 and 2.53 ppm, due to ^{1}H-^{1}H and ^{1}H-^{31}P couplings. Poorly resolved multiplets in the aromatic region of the

spectrum, centered at 7.36 and 7.52 ppm, accounted for the protons of the phenyl ring. The $^{13}C\{^{1}H\}$ NMR spectrum revealed a signal for each unique carbon atom in the molecule, which in some cases were split by ^{31}P-^{13}C coupling. Signal assignments were determined by chemical shift and corroborated by Attached Proton Test (APT) and Heteronuclear Multiple Quantum Correlation (HMQC) NMR experiments. The chemical shift assignments of these spectra are consistent with the reported chemical shifts for the related $S^{Et}PS^{Et}$ ligand.[104,105] Concurrent with the data above, mass spectroscopy revealed the observed value, m/z^+ 315.1363 [MH^+], that is in excellent agreement with the theoretically calculated value, m/z^+ 315.1364 [MH^+], expected for $S^{iPr}PS^{iPr}$.

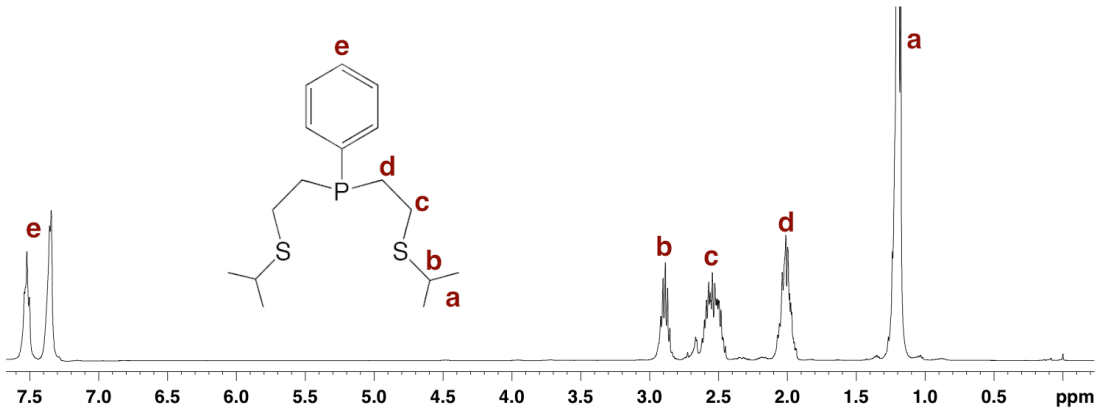

Figure 3.4. ^{1}H NMR spectrum of $S^{iPr}PS^{iPr}$ in $CDCl_3$.

3.3.2 (κ^2-$S^{iPr}PS^{iPr}$)$Ni(PPh_3)_2$ (2)

The nickel coordination chemistry of $S^{iPr}PS^{iPr}$ has been previously studied in this laboratory. The reaction of **1** with nickel halides generated square planar [($S^{iPr}PS^{iPr}$)NiX]BPh_4 (X = Cl, Br, I) complexes in low crystalline yields.[109] Preliminary reactions of **1** with $Ni(cod)_2$ and PPh_3 to form ($S^{iPr}PS^{iPr}$)$Ni(PPh_3)$ were unsuccessful. Instead, (κ^2-$S^{iPr}PS^{iPr}$)$Ni(PPh_3)_2$ was produced in a less than 1% yield. X-ray crystallography revealed that the $S^{iPr}PS^{iPr}$ ligand coordinates in a bidentate fashion to nickel with phosphorus and only one sulfur atom was coordinated. The coordination sphere was completed by two PPh_3 groups.[109,110] Tereniak[109] briefly described (κ^2-$S^{iPr}PS^{iPr}$)$Ni(PPh_3)_2$; but, never optimized the reaction conditions nor characterized the molecule spectroscopically. A closer examination of the reaction is presented below. Ultimately, **2** was obtained in high yields and its spectroscopic properties were deduced and deemed consistent with the proposed structure.

3.3.2.1 Synthesis and Properties

Figure 3.5 outlines the synthesis of (κ^2-$S^{iPr}PS^{iPr}$)$Ni(PPh_3)_2$. Introduction of two equivalents of triphenylphosphine to a solution of $Ni(cod)_2$ in toluene generated a dark red/orange solution that grew darker upon the subsequent addition of $S^{iPr}PS^{iPr}$. After stirring for approximately one hour, the solution was reduced in volume under vacuum and the product precipitated from solution by the addition of pentane. Subsequent filtration and removal of volatiles yielded (κ^2-$S^{iPr}PS^{iPr}$)$Ni(PPh_3)_2$ as a bright orange solid in 69% yield. The complex was air and moisture sensitive. It was soluble in tetrahydrofuran, toluene, benzene and slightly soluble in pentane, but decomposed slowly in solution to (κ^2-$S^{iPr}PS)_2Ni$. The purity and structure of **2** was determined by

^{1}H, $^{31}P\{^{1}H\}$, UV-vis and mass spectroscopies, elemental analysis and X-ray crystallography.

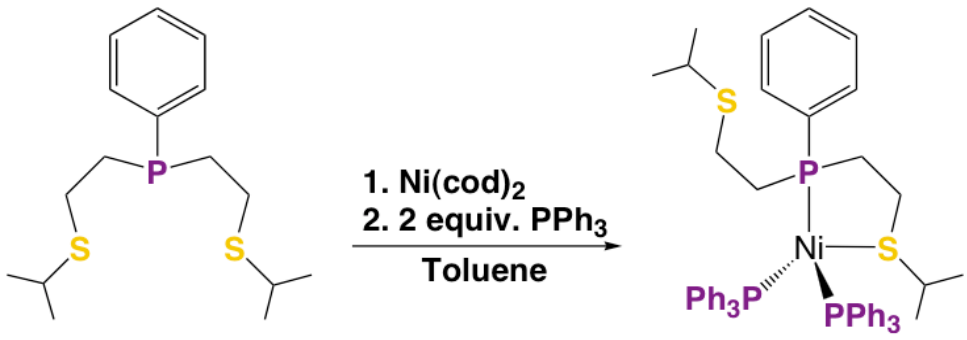

Figure 3.5. Synthesis of (κ^2-S$^{i\text{Pr}}$PS$^{i\text{Pr}}$)Ni(PPh_3)$_2$.

3.3.2.2 Molecular Structure

X-ray quality crystals grown by slow evaporation of a concentrated pentane solution exhibited unit cell dimensions consistent with those determined earlier by Tereniak and Eckert.[109,110] A thermal ellipsoid plot of the molecular structure of (κ^2-S$^{i\text{Pr}}$PS$^{i\text{Pr}}$)Ni(PPh_3)$_2$ is shown in Figure 3.6. The unit cell contained two crystallographically independent, but metrically similar, molecules. Table 3.3 contains selected metric parameters for each crystallographically independent molecule. The X-ray structure revealed that (κ^2-S$^{i\text{Pr}}$PS$^{i\text{Pr}}$)Ni(PPh_3)$_2$ contained a mononuclear four coordinate nickel(0) center in a slightly distorted tetrahedral environment. The nickel coordination sphere consisted of two triphenylphosphine ligands, and one phosphorus and sulfur atom of the S$^{i\text{Pr}}$PS$^{i\text{Pr}}$ ligand. The S$^{i\text{Pr}}$PS$^{i\text{Pr}}$ ligand adopted a κ^2-configuration

in which one thioether arm of the ligand was uncoordinated and folded back away from the metal center. The average bond lengths and angles for both crystallographically independent complexes are discussed below.

The average Ni-$S_{thioether}$ and Ni-P_{Ph} bond lengths of (κ^2-$S^{iPr}PS^{iPr}$)Ni(PPh_3)$_2$ were 2.2541(7) Å and 2.1611(7) Å, respectively. A comparable Ni(0) complex, (arom-PSMe)$_2$Ni^0 (arom-PSMe = *o*-(diphenylphosphino)thioanisole) prepared and characterized by Darensbourg and coworkers, exhibited an average Ni-$S_{thioether}$ bond distance of 2.205(2) Å and an average Ni-P_{Ph2} bond distance of 2.143(2) Å.[113] The Ni-$S_{thioether}$ and Ni-P_{Ph} distances of **2** are slightly longer compared to the Ni-$S_{thioether}$ and Ni-P_{Ph2} distances of (arom-PSMe)$_2$Ni^0 due to the stronger electron donating properties of the -CH_2CH_2- phosphino thioether bridge compared to the -Ph- phosphino thioether bridge. The average Ni-P_{PPh3} bond length for (κ^2-$S^{iPr}PS^{iPr}$)Ni(PPh_3)$_2$ at 2.1751(7) Å is similar to the Ni-P_{PPh3} bond distance in (triphos)Ni(PPh_3) at 2.1526(10) Å.[99] The Ni-P_{PPh3} bond distances were 2.1657(7) Å and 2.1844(6) Å for Ni-$P3_{PPh3}$ and Ni-$P2_{PPh3}$, respectively. The Ni-$P2_{PPh3}$ bond is marginally longer due to steric interactions with the isopropyl group. The average P1-Ni-S1 bite angle of 90.84(3)° for (κ^2-$S^{iPr}PS^{iPr}$)Ni(PPh_3)$_2$ reflects the steric constraint imposed by five-membered chelate ring formation. Likewise the average P1-Ni-P2 angle of 110.26(2)°, S1-Ni-P2 angle of 108.53(3)°, and P1-Ni-P3 angle of 113.23(3)° in complex **2** were slightly irregular; however, the angle between the normals of the planes defined by P1-Ni-S2 and P3-Ni-P2 was 87.73°.

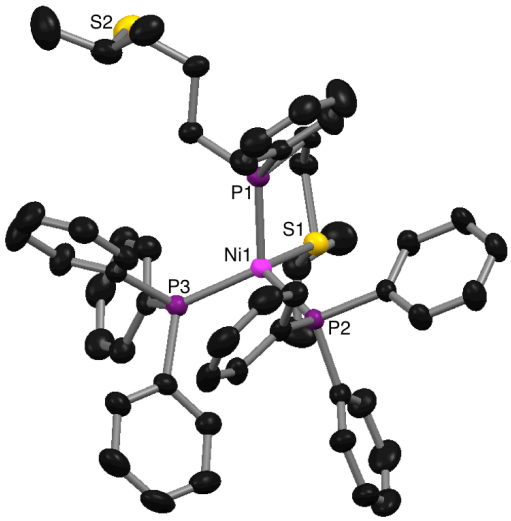

Figure 3.6. Molecular Structure of (κ^2-S$^{i\text{Pr}}$PS$^{i\text{Pr}}$)Ni(PPh$_3$)$_2$. Hydrogen atoms have been omitted for clarity.[109]

Table 3.3: Selected bond lengths (Å) and bond angles (°) for each crystallographically independent molecule of (κ^2-S$^{i\text{Pr}}$PS$^{i\text{Pr}}$)Ni(PPh$_3$)$_2$.[109]

	Length (Å)		**Angle (°)**
Ni1-P1	2.1619(7)	P1-Ni1-S1	90.84(2)
Ni1-S1	2.2550(7)	P1-Ni1-P2	110.61(2)
Ni1-P2	2.1855(6)	P1-Ni1-P3	113.66(2)
Ni1-P3	2.1665(7)	S1-Ni1-P2	108.43(3)
		S1-Ni1-P3	117.61(2)
		P2-Ni1-P3	113.53(3)

	Length (Å)		**Angle (°)**
Ni2-P4	2.1602(7)	P4-Ni2-S3	90.83(3)
Ni2-S3	2.2532(7)	P4-Ni2-P5	109.91(2)
Ni2-P5	2.1832(6)	P4-Ni2-P6	112.80(3)
Ni2-P6	2.1649(7)	S3-Ni2-P5	108.63(3)
		S3-Ni2-P6	118.09(3)
		P5-Ni2-P6	114.19(3)

3.3.2.3 Mass, Electronic Absorption and Nuclear Magnetic Resonance Spectroscopic Characterization

The formulation of (κ^2-S$^{i\text{Pr}}$PS$^{i\text{Pr}}$)Ni(PPh$_3$)$_2$ was also established by LIFDI mass spectrometry data. High resolution experimental and theoretical mass spectra of **2** are shown in Figure 3.7. The observed m/z^+, 896.2494, for the parent ion was in excellent agreement with the theoretically calculated value, m/z^+, 896.2468. Likewise, the observed isotope pattern was consistent with the proposed formula. Elemental analysis data, calculated %C 69.57, %H 6.40 and measured %C 69.53, %H 6.71, confirmed analytical purity of the bulk samples with elemental composition consistent with (κ^2-S$^{i\text{Pr}}$PS$^{i\text{Pr}}$)Ni(PPh$_3$)$_2$.

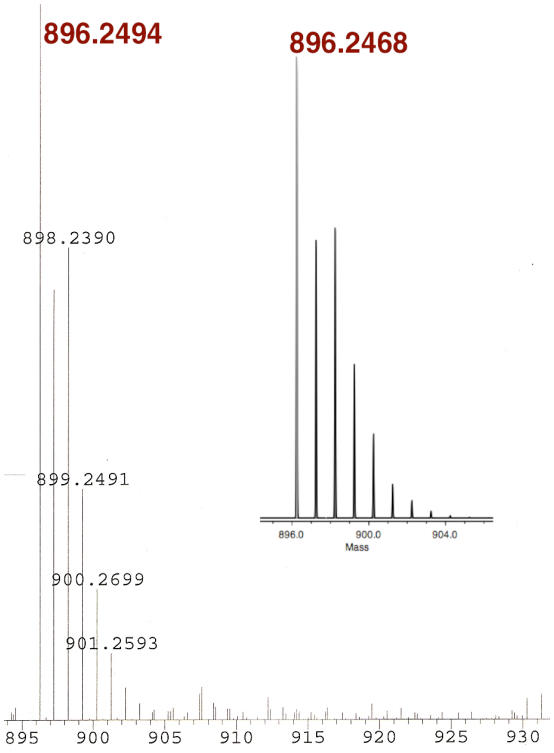

Figure 3.7. High Resolution LIFDI spectrum of (κ^2-S$^{i\text{Pr}}$PS$^{i\text{Pr}}$)Ni(PPh$_3$)$_2$. Inset shows theoretically calculated spectrum.

The electronic absorption spectrum of (κ^2-S$^{i\text{Pr}}$PS$^{i\text{Pr}}$)Ni(PPh_3)$_2$ (Appendix B) in tetrahydrofuran solution exhibited electronic transitions consistent with a d^{10} metal center in a tetrahedral ligand environment, i.e. no ligand field transitions. The spectrum contains absorption bands at λ_{max} (ε, M^{-1} cm^{-1}): 276 (15,000) and 361 (11,000) nm. The absorption feature at 361 nm was assigned as a Ni→PPh_3 metal-to-ligand charge transfer band (MLCT), given the presence of the π-accepting PPh_3 ligand. Similar absorption features have been reported for other tetrahedral nickel(0) complexes such as (triphos)Ni(PPh_3), which displayed λ_{max} (ε, M^{-1} cm^{-1}): 210 (150,000), 260 (22,000) and 365 (21,000).[99]

Variable temperature $^{31}P\{^1H\}$ and ^1H NMR spectra revealed (κ^2-S$^{i\text{Pr}}$PS$^{i\text{Pr}}$)Ni(PPh_3)$_2$ to be fluxional in solution. At room temperature, 300K, the $^{31}P\{^1H\}$ NMR spectrum of **2** in toluene exhibited overlapping resonances at δ 23.04. As the sample temperature was lowered, the initially broad peak resolved into three doublets of doublets at 240K. The temperature dependent spectra, 300 – 200K, are shown in Figure 3.8a. The three signals were assigned to the three non-equivalent phosphorus found in (κ^2-S$^{i\text{Pr}}$PS$^{i\text{Pr}}$)Ni(PPh_3)$_2$. The center signal, δ 23.27 was due to the phenylphosphine group of S$^{i\text{Pr}}$PS$^{i\text{Pr}}$ while the other two signals, δ 24.70 and 21.36, were assigned to the two triphenylphosphine ligands. A global fitting option of MestReNova software was used to simulate the NMR spectrum and determine the coupling constants. Figure 3.8b shows that the simulated and experimental spectra compare well to one another. The three P atoms were coupled to each other with the average coupling constants of $^2J_{P\text{-}P}$ = 42.06 Hz, $^2J_{P\text{-}P}$ = 49.45 Hz and $^2J_{P\text{-}P}$ = 54.45 Hz.

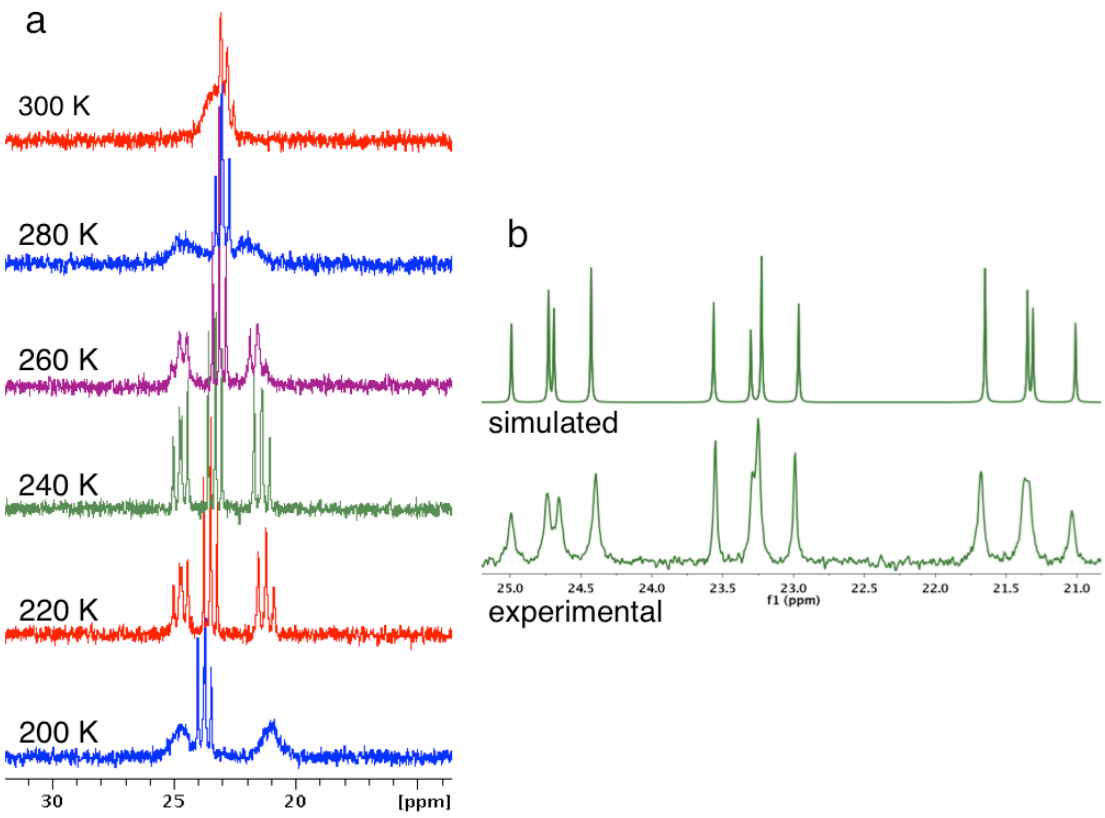

Figure 3.8. (a) Temperature dependence of the $^{31}P\{^{1}H\}$ NMR spectrum of (κ^2-$S^{iPr}PS^{iPr}$)$Ni(PPh_3)_2$. (b) Simulated and experimental $^{31}P\{^{1}H\}$ NMR spectra of (κ^2-$S^{iPr}PS^{iPr}$)$Ni(PPh_3)_2$.

The variable temperature ^{1}H NMR spectra of (κ^2-$S^{iPr}PS^{iPr}$)$Ni(PPh_3)_2$ are shown in Figure 3.9. The spectrum observed at 300K exhibited four resonances for the aliphatic protons of $S^{iPr}PS^{iPr}$. Two doublets at δ 1.09 and 1.10 ($^{3}J_{H\text{-}H}$ = 6.3 Hz) integrated to twelve protons and were assigned to the isopropyl methyl groups. The

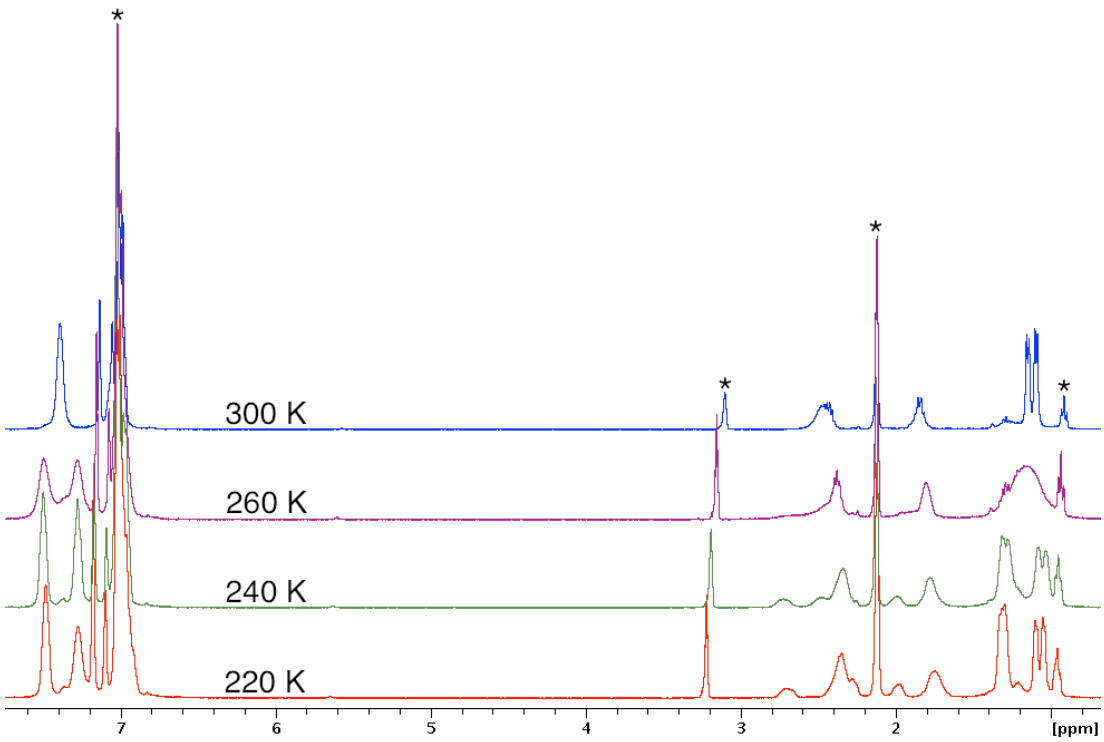

Figure 3.9. Temperature dependence of the ^{1}H NMR spectrum of (κ^2-$S^{iPr}PS^{iPr}$)Ni(PPh_3)$_2$. * denotes residual solvent signals.

resonance at 1.85 ppm integrated to four protons corresponding to the methylene protons of the thioether arm. The resonance at 2.45 ppm integrated to six protons and was assigned to methylene protons of the thioether arm plus the isopropyl methine protons. Multiple overlapping features between δ = 7 and 8 corresponded to the phenyl protons of $S^{iPr}PS^{iPr}$ and triphenylphosphine. Upon cooling the sample to 240K, new resonances with the correct integration ratio, emerged for the aliphatic protons of

$S^{iPr}PS^{iPr}$. The doublets assigned to the isopropyl methyl groups broaden and decoalesced into two new broad doublets at δ = 1.07 and 1.31. The resonances due to the methylene and isopropyl methine protons of the coordinated and uncoordinated thioether arm, 1.85 and 2.45 ppm, separated into 5 very broad signals between 1.7 and 3.0 ppm. The aromatic protons of triphenylphosphine were also split into two new features; the multiplet overlapping resonances between δ 7.00 and 7.50 were ascribed to the phenyl protons of $S^{iPr}PS^{iPr}$ and triphenylphosphine.

These results suggested that although $S^{iPr}PS^{iPr}$ is coordinated in a bidentate fashion, the thioether arms of $(\kappa^2\text{-}S^{iPr}PS^{iPr})Ni(PPh_3)_2$ undergo exchange between coordinated and uncoordinated positions. At room temperature, exchange was fast on the NMR timescale resulting in a situation where the methylene, isopropyl methine, and isopropyl methyl protons of the thioether arms were chemically equivalent. Similar to the ^1H NMR spectrum of $S^{iPr}PS^{iPr}$ (Figure 3.4), the NMR spectrum showed one set of peaks for the protons of the two thioether arms. Separate resonances for the methylene, isopropyl methine, and isopropyl methyl protons of the coordinated and uncoordinated thioether arms of **2** were distinguished at lower temperatures where exchange was slower. In accord with the results obtained from the variable temperature ^1H NMR study, the $^{31}P\{^1H\}$ NMR of $(\kappa^2\text{-}S^{iPr}PS^{iPr})Ni(PPh_3)_2$ showed one broad resonance for the two triphenylphosphine ligands at 300K, which split into two doublets of doublets at 240K. The division of the triphenylphosphine signal is consequence of the different environments felt by the ligands when exchange of the thioether arms is slow.

3.3.2.4 (κ^2-$S^{iPr}PS^{iPr}$)$Ni(PPh_3)_2$ Molecular Structure

According to its structural features, the phosphino-thioether ligand, $S^{iPr}PS^{iPr}$, can behave as a potential tridentate ligand to nickel metal ions via its phosphorus donor atom and two thioether arms. Reactions of **1** with nickel halides generated tridentate [($S^{iPr}PS^{iPr}$)NiX]BPh_4 (X = Cl, Br, I) complexes.[109] However, as observed earlier[109] and confirmed here, the reaction of $S^{iPr}PS^{iPr}$, $Ni(cod)_2$ and PPh_3 produced the bidentate complex, (κ^2-$S^{iPr}PS^{iPr}$)$Ni(PPh_3)_2$, whether one or two equivalents of PPh_3 were used in the reaction. The disparity in the $S^{iPr}PS^{iPr}$ binding modes, tridentate vs. bidentate, arises from electronic differences between the nickel atoms. The greater Lewis acidity of Ni(II) as compared to Ni(0) (d^8 vs. d^{10}) leads to a greater stabilization of the Ni(II) metal with both thioether arms of the ligand bound. The Ni(0) metal is electron rich, therefore, no further electronic stabilization is gained from the binding of the second thioether arm. A comparison of the average Ni-S bond lengths, 2.2541(7) Å and 2.1816(10) Å for (κ^2-$S^{iPr}PS^{iPr}$)$Ni(PPh_3)_2$ and [($S^{iPr}PS^{iPr}$)NiCl]BPh_4 [109], respectively, is indicative of the weaker thioether interactions observed for Ni(0) as compared to Ni(II).

The electronic properties of triphenylphosphine and the thioether donor arms affect the ligand binding mode observed in **2** as well. Specifically, the strong π-acceptor quality of triphenylphosphine promoted its preferential binding to nickel over the more basic thioether arms, resulting in a binding ratio of 2:1. The lability of the thioether arms was evident in the variable temperature NMR spectral studies of (κ^2-$S^{iPr}PS^{iPr}$)$Ni(PPh_3)_2$, vide supra. At room temperature, thioether exchange was fast on the NMR timescale. Rigo et al.[114] previously observed this favored binding with the ligand, P-SEt (P-SEt = 1-(thioethyl)-2-(diphenylphosphino)ethane). Upon reaction of $Ni(P\text{-}SEt)_2$ with CO to form $Ni(CO)_2(P\text{-}SEt)_2$, the P-SEt ligand acted as monodentate

with no thioethyl groups bound to nickel.[114] These structures confirmed the importance of the electronic influence of the ancillary ligand in phosphino-thioether complexes. Thus, the coordination mode of $S^{iPr}PS^{iPr}$ nickel complexes should be persuaded by the nature of the accompanying phosphine ligands.

In an attempt to produce a tridentate complex, the more basic trimethylphosphine (PMe_3) ligand was substituted for PPh_3 in Figure 3.5. However, experiments conducted with various stoichiometries of PMe_3, $S^{iPr}PS^{iPr}$, and $Ni(cod)_2$ at different reaction times all resulted in the retention of free $S^{iPr}PS^{iPr}$ and numerous uncharacterizable products; no formation of $(S^{iPr}PS^{iPr})NiPMe_3$ was detected. In addition to altering the electronics of the reaction, substituting the smaller phosphine, PMe_3, for PPh_3 influences the steric factors involved in the binding mode as well. Motivated by these results the reaction in Figure 3.5 was repeated with tricyclohexylphosphine (PCy_3), a comparatively more basic and bulkier phosphine than either PMe_3 or PPh_3. Nonetheless, numerous experiments with various stoichiometries of PCy_3, $S^{iPr}PS^{iPr}$, and $Ni(cod)_2$ at different temperatures and reaction times all failed to produce a characterizable product. In the case of (κ^2-$S^{iPr}PS^{iPr}$)$Ni(PPh_3)_2$ it appeared that complex formation was due to a unique combination of electronic and steric factors.

3.3.3 (κ^2-$S^{iPr}PS)_2Ni$ (3)

The conversion of thioether complexes into thiolate compounds by S-dealkylation has been observed in numerous nickel and palladium metal complexes of PS donor ligands.[113,115,116,117,106] Such alkyl extrusions may result from photoreactions[113,115] or reactions with nucleophiles under a variety of conditions.[116,117,106] It is noteworthy, that Darensbourg and coworkers have previously

observed this behavior in a series of nickel(0) complexes. Photolysis of (arom-PSMe)$_2$Ni^0 (arom-PSMe = Ph$_2$P(*o*-C$_6$H$_4$)SMe)[113] and (PSSP)Ni^0 (PSSP = Ph$_2$P(CH$_2$)$_2$S(CH$_2$)$_3$S(CH$_2$)$_2$PPh$_2$)[115] yielded neutral dithiolate nickel(II) complexes and organic products derived from alkyl radicals. With this precedence of S-dealkylation in low-valent nickel complexes, the instability of complex **2** was not surprising.

3.3.3.1 Synthesis and Properties

The synthesis of (κ^2-S$^{i\text{Pr}}$PS)$_2$Ni was achieved by the decomposition of (κ^2-S$^{i\text{Pr}}$PS$^{i\text{Pr}}$)Ni(PPh$_3$)$_2$. Complex **2**, which was stable in the solid state under inert atmosphere, slowly decomposed in solution as indicated by its color change from orange to dark green. The reaction was monitored by ^{31}P{^{1}H} NMR spectroscopy. A room temperature spectrum of (κ^2-S$^{i\text{Pr}}$PS$^{i\text{Pr}}$)Ni(PPh$_3$)$_2$ obtained immediately after dissolution in d-toluene is shown in Figure 3.10. A spectrum of the same sample recorded approximately 6 hours later (Figure 3.10) showed the growth of three resonances at δ = -5.32, 63.57 and 64.21 along with a decrease of features attributed to complex **2**. The two singlets at δ 63.57 and 64.21 were assigned to the *cis* and *trans* isomers of (κ^2-S$^{i\text{Pr}}$PS)$_2$Ni, respectively, while the signal at δ -5.32 was attributed to uncoordinated triphenylphosphine. Upon extended observation (~22 hours), the resonances for (κ^2-S$^{i\text{Pr}}$PS$^{i\text{Pr}}$)Ni(PPh$_3$)$_2$ continued to decrease while the signals due to (κ^2-S$^{i\text{Pr}}$PS)$_2$Ni and triphenylphosphine increased in intensity. The nature of **3** was established unambiguously by an X-ray crystal structure determination. Crystals of *trans*-(κ^2-S$^{i\text{Pr}}$PS)$_2$Ni were grown concurrently with crystals of (κ^2-S$^{i\text{Pr}}$PS$^{i\text{Pr}}$)Ni(PPh$_3$)$_2$ via slow evaporation of a concentrated pentane solution.

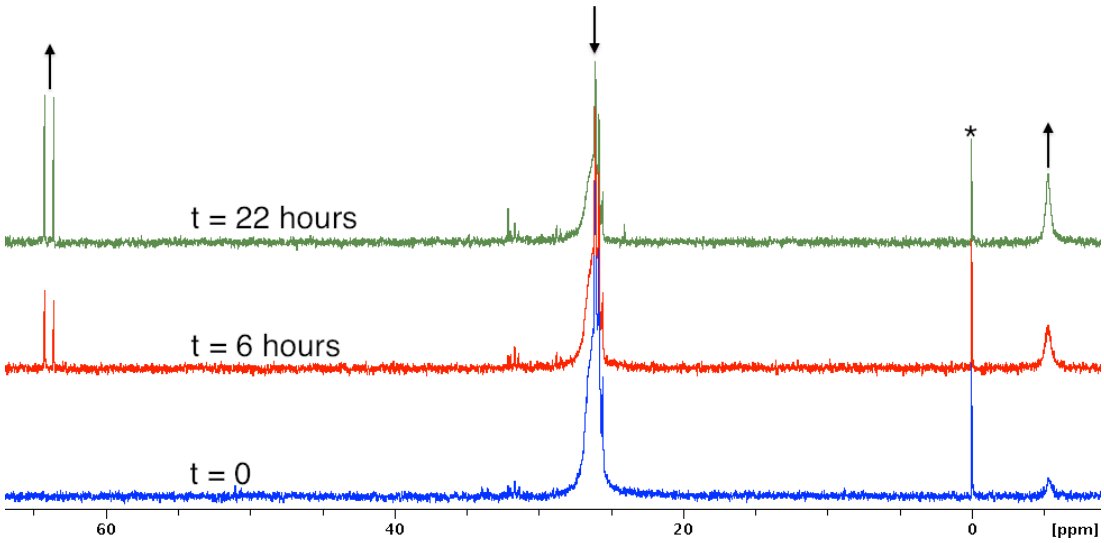

Figure 3.10. $^{31}P\{^{1}H\}$ NMR spectrum of (κ^2-S$^{i\text{Pr}}$PS$^{i\text{Pr}}$)Ni(PPh$_3$)$_2$ decomposing to (κ^2-S$^{i\text{Pr}}$PS)$_2$Ni over time. * denotes internal standard phosphoric acid in deuterium oxide.

3.3.3.2 Molecular Structure

A thermal ellipsoid plot of the molecular structure of *trans*-(κ^2-S$^{i\text{Pr}}$PS)$_2$Ni is shown in Figure 3.11. The unit cell contained two crystallographically independent, but metrically similar, molecules. Table 3.4 contains selected metric parameters for each crystallographically independent molecule. The X-ray structure revealed that (κ^2-S$^{i\text{Pr}}$PS)$_2$Ni contained a mononuclear four coordinate nickel(II) center in a square-planar environment, with thiolate and phosphine donors from two opposing S$^{i\text{Pr}}$PS ligands located in a *trans* arrangement. The S$^{i\text{Pr}}$PS ligand adopted a κ^2-configuration in

which the uncoordinated thioether arm and the phenyl ring attached to phosphorus were on opposite sides of the NiP_2S_2 plane. The average bond lengths and angles for both crystallographically independent complexes are discussed below.

The sum of the angles about the nickel atom in complex **3**, 361.24°, supported the assignment of square-planar geometry. The S-Ni-S(1a) and P-Ni-P(1a) angles of 173.52(7)° and 169.14(6)° were also indicative of the observed geometry. The P(1)-Ni-S(1) angle within the chelate was 88.54(7)°, slightly smaller than the S(1)-Ni-P(1a) angle between the ligands of 92.08(7)°. The average Ni-S and Ni-P bond distances for *trans*-(κ^2-S$^{i\text{Pr}}$PS)$_2$Ni were 2.1648(16) and 2.1591(16) Å, respectively. These distances are consistent with other square planar nickel(II) structurally characterized phosphinothiolate complexes in the literature, namely $(PS)_2Ni$ (PS = $Ph_2PCH_2CH_2S$)[118] and $(arom\text{-}PS)_2Ni$ (arom-PS = $Ph_2P(o\text{-}C_6H_4)S$)[113]. The solid-state structures of these complexes, revealed Ni-S and Ni-P bond distances of 2.174(1) and 2.186(1) Å[118], and 2.166(3) and 2.173(3) Å[113], respectively.

The mechanism proposed for the decomposition of (κ^2-S$^{i\text{Pr}}$PS$^{i\text{Pr}}$)Ni$(PPh_3)_2$ to (κ^2-S$^{i\text{Pr}}$PS)$_2$Ni involves S-dealkylation. Examples of C-S bond cleavage induced by photochemistry have been previously observed in nickel(0) complexes with phosphino-thioether donor ligands.[113,115] Although the role of photochemistry was not defined and no attempts were made to establish the mechanism or characterize any intermediates experimentally, a plausible pathway for the S-dealkylation of (κ^2-S$^{i\text{Pr}}$PS$^{i\text{Pr}}$)Ni$(PPh_3)_2$ is suggested. Homolytic cleavage of the S_{bound}-C likely follows a photochemical event and affords a Ni(I) complex and an isopropyl radical. The highly reactive Ni(I) species then ultimately forms (κ^2-S$^{i\text{Pr}}$PS)$_2$Ni and organic products, such as 2,3-dimethylbutane, are composed from isopropyl radicals. This mechanistic

hypothesis serves as a working guide for further synthetic work towards isolating pathway products and intermediates.

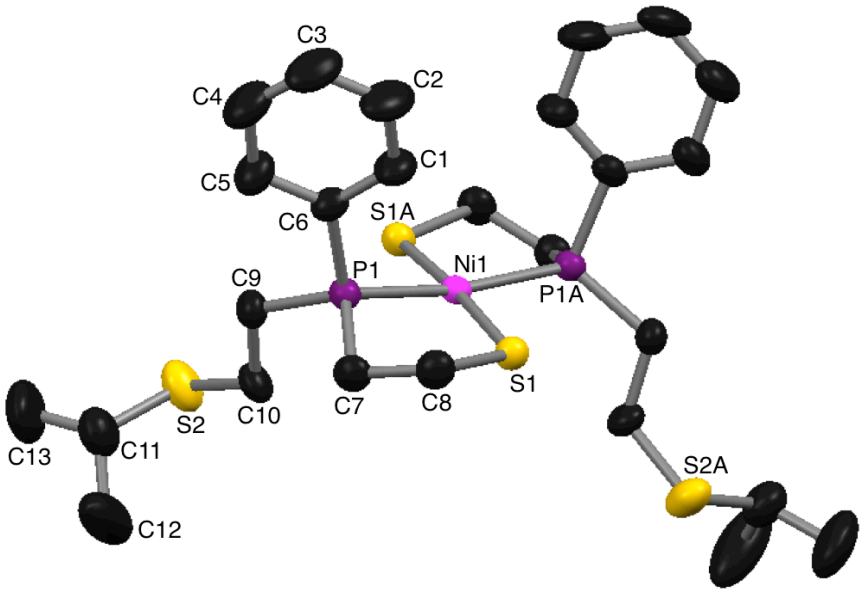

Figure 3.11. Molecular structure of $(\kappa^2\text{-}S^{i\text{Pr}}PS)_2Ni$. Hydrogen atoms have been omitted for clarity.

Table 3.4: Selected bond lengths (Å) and bond angles (°) for each crystallographically independent molecule of *trans*-(κ^2-S$^{i\text{Pr}}$PS)$_2$Ni.

	Length (Å)		**Angle (°)**
Ni1-P1	2.1589(15)	P1-Ni1-S1	88.87(7)
Ni1-P1A	2.1588(15)	P1-Ni1-P1A	169.86(6)
Ni1-S1	2.1662(16)	P1-Ni1-S1A	91.72(7)
Ni1-S1A	2.1662(16)	S1-Ni1-P1A	91.72(7)
		S1-Ni1-S1A	173.38(6)
		P1A-Ni-S1A	88.87(7)

	Length (Å)		**Angle (°)**
Ni2-P2	2.1593(16)	P2-Ni2-S3	88.21(7)
Ni2-P2A	2.1593(16)	P2-Ni2-P2A	168.14(6)
Ni2-S3	2.1634(16)	P2-Ni2-S3A	92.44(7)
Ni2-S3A	2.1634(16)	S3-Ni2-P2A	92.44(7)
		S3-Ni2-S3A	173.66(7)
		P2A-Ni2-S3A	88.21(7)

3.3.3.3 Mass and Nuclear Magnetic Resonance Spectroscopic Characterization

The formulation of (κ^2-S$^{i\text{Pr}}$PS)$_2$Ni was also established by high resolution LIFDI mass spectrometry data (Appendix B). The observed m/z^+, 600.0853 for the parent ion was in excellent agreement with the theoretically calculated value, m/z^+, 600.0842. Likewise, the observed isotope pattern was consistent with the proposed formula.

The ^{31}P{^{1}H} NMR spectrum of *trans*-(κ^2-S$^{i\text{Pr}}$PS)$_2$Ni showed a single peak at δ = 64.88 ppm (Appendix B). Figure 3.12 displays the ^{1}H NMR spectrum of **3**. It exhibited multiplet resonances, with the correct integration ratio, in the aromatic and aliphatic regions. The two doublets (δ = 1.14 and 1.23, $^3J_{H\text{-}H}$ = 6.56 Hz) corresponded to the methyl groups of the isopropyl fragment. The isopropyl methine proton and the

methylene protons of the -PCH_2CH_2S- fragment appeared as broad complex multiplets between 1.90 and 3.19 ppm, due to ^1H-^1H and ^1H-^{31}P couplings. Broad peaks in the aromatic region of the spectrum, centered at 6.94 and 7.92 ppm, accounted for the protons of the phenyl ring.

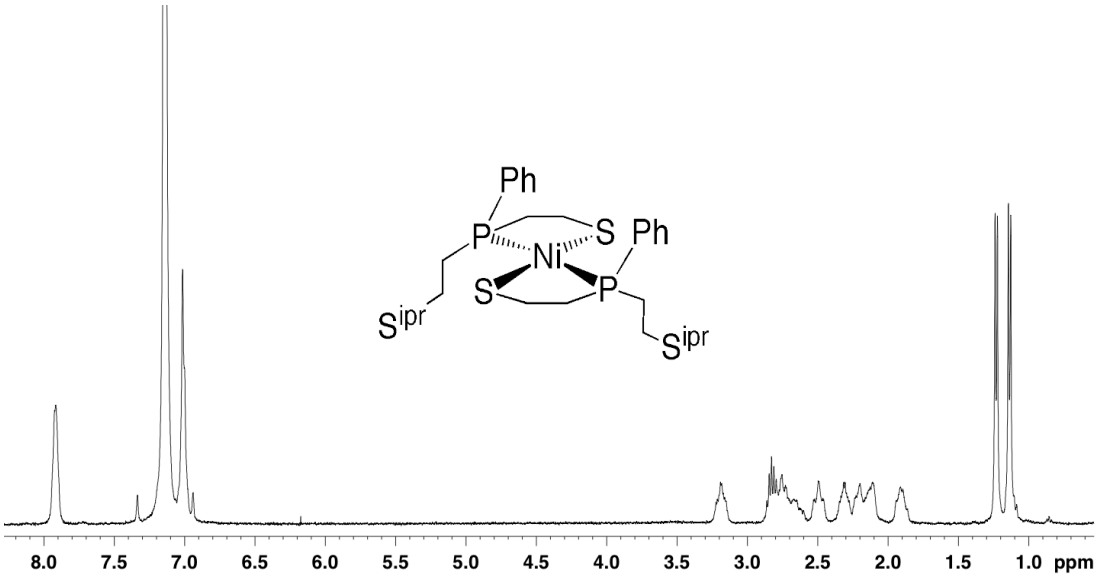

Figure 3.12. ^1H NMR spectrum of *trans*-(κ^2-$S^{iPr}PS)_2Ni$ in C_6D_6.

3.3.3.4 Discussion

Solutions of (κ^2-$S^{iPr}PS^{iPr}$)$Ni(PPh_3)_2$ were unstable, turning from orange to dark red upon standing under inert atmospheres. The decomposition to (κ^2-$S^{iPr}PS)_2Ni$ was monitored by $^{31}P\{^1H\}$ NMR spectroscopy (Figure 3.10). The growth of two singlets at δ 63.57 and 64.21 was attributed to isomers of **3**. The two isomers presumably differed

with thiolate and phosphine donors from two opposing $S^{iPr}PS$ ligands located in a *cis* (δ 63.57), or *trans* (δ 64.21) arrangement. A singlet was displayed for both isomers because the phosphorus atoms from the two opposing $S^{iPr}PS$ ligands are equivalent by symmetry; the phosphorus atoms in both complexes lie on either side of a C_2 axis. Crystallization from pentane yielded only the *trans* isomer, wherein the phenyl rings attached to phosphorus and the uncoordinated thioether arms of the $S^{iPr}PS$ ligand were on opposite sides of the NiP_2S_2 plane. The preferential crystallization of the *trans* isomer was likely due to steric factors and structural molecular packing forces that constrained the ligands to opposite sides of the plane.

The formation of $(\kappa^2\text{-}S^{iPr}PS)_2Ni$ as a result of S-dealkylation is not without precedent. As mentioned earlier, the occurrence of C-S bond cleavage in Ni^0 complexes with phosphino thioether donor ligands is well documented by Darensbourg and coworkers.[113,115] In the presence of light, a series of Ni^0 complexes demonstrated instability with respect to alkyl group loss, generating dithiolate Ni^{2+} complexes and organic products derived from carbon radicals. For example, a solution of $(arom\text{-}PSMe)_2Ni^0$ changed color within a day under ambient lighting or within 15 min under photolytic conditions.[113] The resulting ^1H NMR spectrum of the solution displayed resonances consistent with the formation of $(arom\text{-}PS)_2Ni^{II}$ and ethane, indicative of the generation of methyl radicals during decomposition. Evidence to support the production of methyl radicals was provided by photolysis of $(arom\text{-}PSMe)_2Ni^0$ in the presence of the alkyl radical trapping agent TEMPO (2,2,6,6-tetramethylpiperidinyloxy). As expected, $(arom\text{-}PS)_2Ni^{II}$ and TEMPO-Me (2,2,6,6-tetramethyl-1-piperidinylmethoxide) were formed.[113] Although the details of this reaction mechanism were not completely understood, EPR spectroscopy confirmed the

generation of a Ni^{1+} species during the homolytic cleavage of the C-$S_{thioether}$ bond.[113] Darensbourg and coworkers suggested that despite the role of photochemistry not being mechanistically defined, an attractive explanation was that "metal to ligand charge transfer from $Ni_{d\pi} \rightarrow S\text{-}C_{\sigma*}$ effects bond weakening, and in some cases, as those examined here, this electronic excitation is accessed photochemically."[115]

In the case of $(\kappa^2\text{-}S^{i\text{Pr}}PS^{i\text{Pr}})Ni(PPh_3)_2$ decomposition, the $^{31}P\{^1H\}$ NMR spectrum recorded after 22 hours displayed resonances consistent with starting material, the formation of $(\kappa^2\text{-}S^{i\text{Pr}}PS)_2Ni$, and free triphenylphosphine. No attempts were made to either identify intermediates or establish a plausible pathway for this reaction. However, given the similarities to $(arom\text{-}PSMe)_2Ni^0$, one argument is that S-dealkylation of $(\kappa^2\text{-}S^{i\text{Pr}}PS^{i\text{Pr}})Ni(PPh_3)_2$ was induced by exposure to light. The average Ni-$S_{thioether}$ and S_{bound}-C bond lengths of $(\kappa^2\text{-}S^{i\text{Pr}}PS^{i\text{Pr}})Ni(PPh_3)_2$, 2.2541(7) Å and 1.840(3) Å respectively, are comparable to those found in $(arom\text{-}PSMe)_2Ni^0$ (Ni-$S_{thioether}$ = 2.205(2) Å and S-C = 1.814(7) Å).[113] The slight differences are attributed to the stronger electron donating properties of the $-CH_2CH_2-$ phosphino thioether bridge compared to the -Ph- phosphino thioether bridge. A resemblance was also seen in the electronic absorption spectrums of **2** (λ_{max} (ε, M^{-1} cm^{-1}): 276 (15,000) and 361 (11,000) nm) and $(arom\text{-}PSMe)_2Ni^0$ (λ_{max} (ε, M^{-1} cm^{-1}): 284 (2320) and 394 (1120) nm).[113] Furthermore, reduced metal complexes are sensitive toward C-S bond cleavage due to partial back-donation of metal electrons into an S-C π^* orbital. The S-dealkylation of only the Ni-bound thioether in $(\kappa^2\text{-}S^{i\text{Pr}}PS^{i\text{Pr}})Ni(PPh_3)_2$ reinforced this idea. The S_{bound}-C bond length, 1.840(3) Å, is longer than the $S_{unbound}$-C bond length, 1.818(3) Å, consistent with the presence of nickel to sulfur π back-donation. In order to identify intermediates and establish the mechanism associated with the formation of

(κ^2-S$^{i\text{Pr}}$PS)$_2$Ni further studies need to be completed. The photolysis of (arom-PSMe)$_2$Ni^0 provides a working model for future experiments.[113]

3.3.4 Alkyl Transfer Studies

With the successful synthesis of (κ^2-S$^{i\text{Pr}}$PS$^{i\text{Pr}}$)Ni(PPh$_3$)$_2$, the reactivity of this complex with alkylcobaloximes, i.e. methyl, methyl-d$_3$, ethyl, isopropyl and neopentyl, was explored. These studies provide a model for methyl transfer from CH$_3$-CoFeSP to the proximal nickel of the A-cluster of ACS during acetyl coenzyme A synthesis. The choice of RCo(dmgBF$_2$)$_2$py as a model for cobalamin was based upon previous alkyl transfer studies[98,100,99,97] and the ability to systematically alter the alkyl substituent with ease. As noted above, this laboratory has previously examined alkyl transfer using [Ni^{1+}(tmc)][OTf][98,97] and (triphos)Ni^0(PPh$_3$)[99,100] as models for Ni$_p$. Despite exhibiting different nickel oxidation states, the methyl transfer was successful for both systems. Motivated by these results, and in conjunction with the desire to understand methyl transfer in ACS better, the reactivity of **2** was explored. The reaction of methyl and methyl-d$_3$ derivatives of RCo(dmgBF$_2$)$_2$py with **2** led to the formation of the respective alkyl species, [(κ^2-S$^{i\text{Pr}}$PS$^{i\text{Pr}}$)Ni(PPh$_3$)R]$^+$. However for the ethyl and isopropyl derivatives, β-hydrogen elimination prevented the formation of the corresponding alkyl nickel species. To confirm β-hydrogen elimination as a decomposition pathway, the reaction of (neopentyl)Co(dmgBF$_2$)$_2$(py) with (κ^2-S$^{i\text{Pr}}$PS$^{i\text{Pr}}$)Ni(PPh$_3$)$_2$ was explored. A closer examination of these reactions is presented below.

3.3.4.1 Reaction of (κ^2-S$^{i\mathrm{Pr}}$PS$^{i\mathrm{Pr}}$)Ni(PPh$_3$)$_2$ with RCo(dmgBF$_2$)$_2$py, R = CH$_3$ or CD$_3$

Combining equimolar amounts of (κ^2-S$^{i\mathrm{Pr}}$PS$^{i\mathrm{Pr}}$)Ni(PPh$_3$)$_2$ in tetrahydrofuran and CH$_3$Co(dmgBF$_2$)$_2$py in acetonitrile, under an inert atmosphere (Figure 3.13) resulted in an immediate color change from orange to dark blue, corresponding to the formation of [(κ^2-S$^{i\mathrm{Pr}}$PS$^{i\mathrm{Pr}}$)Ni(PPh$_3$)(CH$_3$)][Co(dmgBF$_2$)$_2$PPh$_3$]. The electronic spectrum of the products was dominated by Co^{1+} formation, as a result, the extent of the reaction was monitored and quantified by its concentration, ε_{615} = 10,000 M^{-1}cm^{-1}.[99] The rate of methyl transfer was fast with 95% conversion observed after ~30 mins. (Appendix B) Attempts to establish the stoichiometry of the reaction via a Job plot analysis were unsuccessful due to the competing formation of (κ^2-S$^{i\mathrm{Pr}}$PS)$_2$Ni. An analogous transfer reaction was conducted with CD$_3$Co(dmgBF$_2$)$_2$py to confirm the presence of a Ni^{II}-methyl product. The product of both reactions, [(κ^2-S$^{i\mathrm{Pr}}$PS$^{i\mathrm{Pr}}$)Ni(PPh$_3$)R][Co(dmgBF$_2$)$_2$PPh$_3$], where R = CH$_3$ (**4**) or CD$_3$ (**5**), was characterized by ^{31}P{^{1}H}, ^{1}H, ^{1}H{^{31}P}, ^{2}H NMR and LIFDI mass spectroscopies.

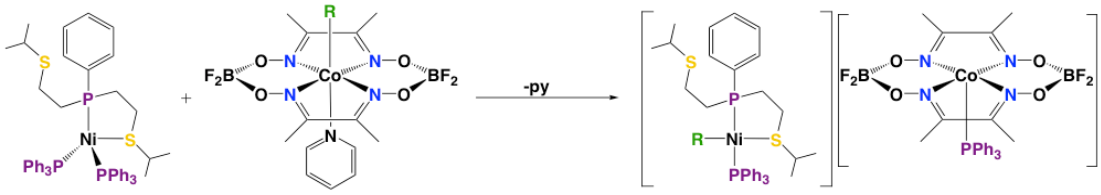

Figure 3.13. Reaction of (κ^2-S$^{i\mathrm{Pr}}$PS$^{i\mathrm{Pr}}$)Ni(PPh$_3$)$_2$ with RCo(dmgBF$_2$)$_2$py, where R = CH$_3$, CD$_3$, CH$_2$CH$_3$, CH(CH$_3$)$_2$ or CH$_2$C(CH$_3$)$_3$.

3.3.4.1.1 Mass and Nuclear Magnetic Resonance Spectroscopic Characterization

The elemental composition of $[(\kappa^2\text{-}S^{i\text{Pr}}PS^{i\text{Pr}})Ni(PPh_3)R]^+$, where R = CH_3 (**4**) or CD_3 (**5**), was determined by high resolution LIFDI mass spectrometry. The experimental and theoretical mass spectra of **4** and **5** are shown in Figure 3.14a and b. The observed m/z^+ 649.182000 for the parent ion was in excellent agreement with the theoretically calculated value, m/z^+ 649.179144 for **4**. Likewise the observed m/z^+ 652.200700, was in excellent agreement with the theoretically calculated value, m/z^+ 652.197975 for **5**. The observed isotope patterns were consistent with the proposed formulas for both compounds.

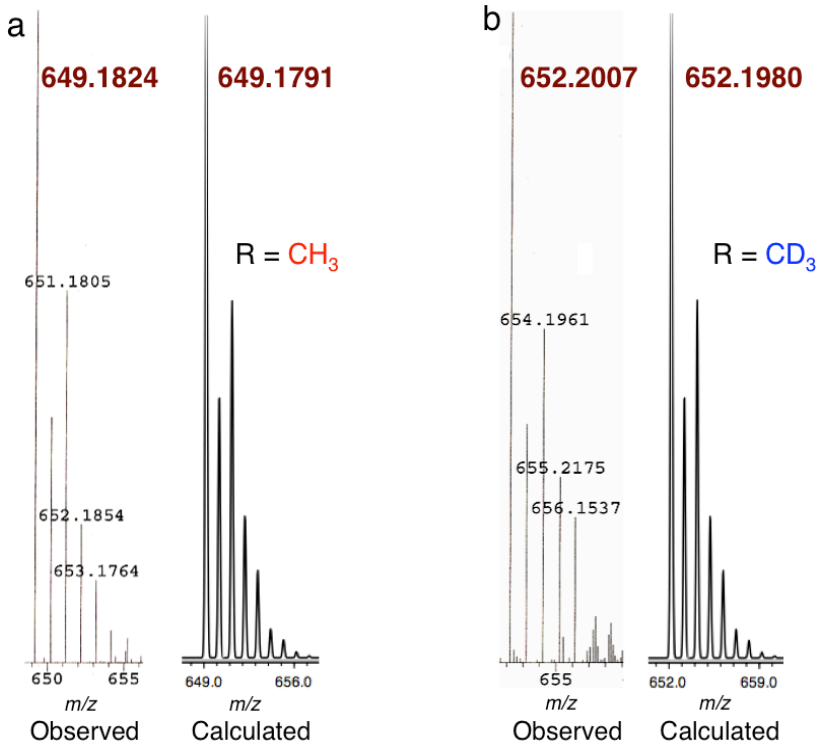

Figure 3.14. High Resolution LIFDI spectra of (a) $[(\kappa^2\text{-}S^{i\text{Pr}}PS^{i\text{Pr}})Ni(PPh_3)CH_3]^+$ and (b) $[(\kappa^2\text{-}S^{i\text{Pr}}PS^{i\text{Pr}})Ni(PPh_3)CD_3]^+$.

Samples extracted from equimolar mixtures of (κ^2-$S^{iPr}PS^{iPr}$)$Ni(PPh_3)_2$ in d^8-toluene and $RCo(dmgBF_2)_2py$ in d^6-acetone were analyzed for alkyl transfer by $^{31}P\{^1H\}$, ^1H, $^1H\{^{31}P\}$, and ^2H NMR spectroscopy. The $^{31}P\{^1H\}$ NMR spectrum of [(κ^2-$S^{iPr}PS^{iPr}$)$Ni(PPh_3)R]^+$, where R = CH_3 or CD_3, exhibited noticeable changes in the chemical shifts compared to those observed for (κ^2-$S^{iPr}PS^{iPr}$)$Ni(PPh_3)_2$ (Appendix B). Complexes **4** and **5** displayed broad downfield shifts of the signals ascribed to the phenylphosphine group of $S^{iPr}PS^{iPr}$ to δ 49.42 and 49.56, respectively, from δ 23.04 for (κ^2-$S^{iPr}PS^{iPr}$)$Ni(PPh_3)_2$. Additionally broad chemical shifts corresponding to triphenylphosphine and $[Co(dmgBF_2)_2PPh_3]^-$ were observed at -7.97 and 37.58 ppm. The axial ligand exchange at cobalt from pyridine to triphenylphosphine has been previously observed and was therefore, not surprising.[99]

Figure 3.15a displays the ^1H NMR spectrum of methyl transfer from $CH_3Co(dmgBF_2)_2py$ to (κ^2-$S^{iPr}PS^{iPr}$)$Ni(PPh_3)_2$. The spectrum shows growth of new resonances for $[Co(dmgBF_2)_2PPh_3]^-$ and loss of resonances attributed to the methyl groups of $CH_3Co(dmgBF_2)_2py$. New signals were also present for [(κ^2-$S^{iPr}PS^{iPr}$)$Ni(PPh_3)(CH_3)]^+$. A multiplet at 1.30 ppm corresponded to the methyl groups of the isopropyl fragment. The isopropyl methine protons and the methylene protons of the -PCH_2CH_2S- fragment appeared as broad complex multiplets at 2.63 and 2.92 ppm, due to ^1H-^1H and ^1H-^{31}P couplings. Poorly resolved broad resonances between 7.44 and 7.65 ppm, in the aromatic region of the spectrum, accounted for the protons of the phenyl rings. The most important chemical shift of the spectrum was a new resonance, δ = 0.15, assigned to the Ni-methyl moiety. This resonance integrated to three protons and couples to the phosphorus nuclei of $S^{iPr}PS^{iPr}$ ($^3J_{H\text{-}P}$ = 5.96 Hz). In the $^1H\{^{31}P\}$ NMR spectrum (Figure 3.15c) of the transfer reaction, this coupling

disappeared as expected and the remaining chemical shifts were identical to those noted above. This observation was consistent with the assignment of $\delta = 0.15$ as the methyl group of $[(\kappa^2\text{-}S^{i\text{Pr}}PS^{i\text{Pr}})Ni(PPh_3)(CH_3)]^+$. Further evidence corroborating methyl transfer was provided by the ^1H NMR spectrum of alkyl transfer from $CD_3Co(dmgBF_2)_2py$ to $(\kappa^2\text{-}S^{i\text{Pr}}PS^{i\text{Pr}})Ni(PPh_3)_2$ (Figure 3.15b). The spectrum showed identical features to those observed in Figure 3.15a for protio-methyl transfer with one exception, the resonance for Ni-CH_3, $\delta = 0.15$, was absent. The ^2H NMR spectrum of this reaction (Figure 3.16) confirmed the transfer of a methyl group with a single resonance at $\delta = -0.26$ assigned to Ni-CD_3. Taken together, these observations provide evidence for the successful transfer of methyl and the formation of a new Ni^{II}-methyl species, $[(\kappa^2\text{-}S^{i\text{Pr}}PS^{i\text{Pr}})Ni(PPh_3)(CH_3)]^+$.

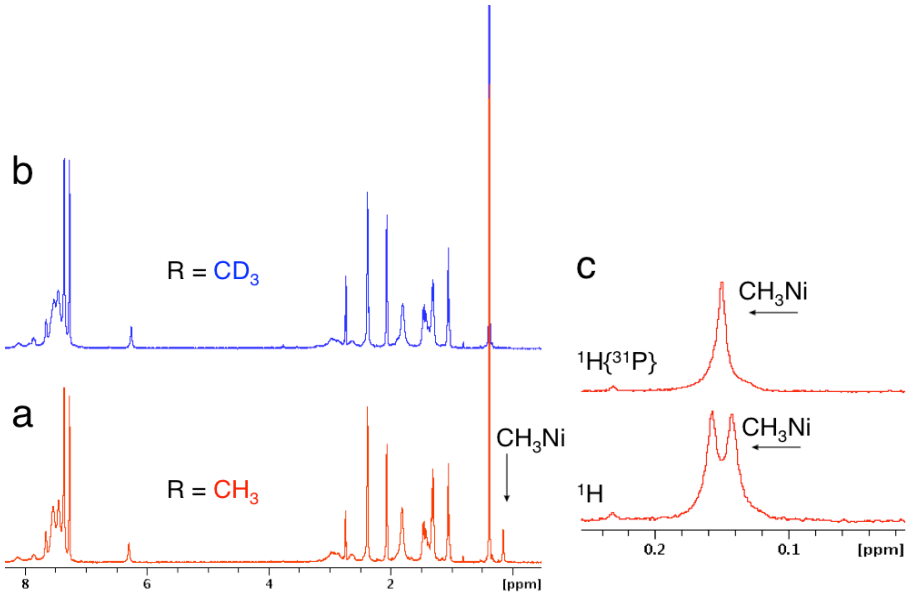

Figure 3.15. ^1H NMR spectra of (a) $[(\kappa^2\text{-}S^{i\text{Pr}}PS^{i\text{Pr}})Ni(PPh_3)(CH_3)]^+$, and (b) $[(\kappa^2\text{-}S^{i\text{Pr}}PS^{i\text{Pr}})Ni(PPh_3)(CD_3)]^+$ in $C_7D_8/(CD_3)_2CO$). (c) Comparison of Ni-CH_3 resonances exhibited by ^1H and $^1H\{^{31}P\}$ NMR spectra.

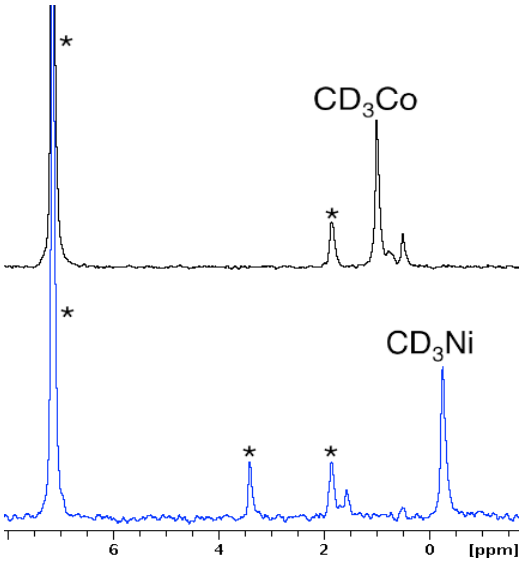

Figure 3.16. ^{2}H NMR spectra of $CD_3Co(dmgBF_2)_2py$ (black) and [(κ^2-$S^{iPr}PS^{iPr}$)Ni(PPh_3)(CD_3)]$^+$ (blue). * denotes residual solvent signals.

3.3.4.1.2 Discussion

Collectively, these data suggest that $CH_3Co(dmgBF_2)_2py$ quantitatively methylates the Ni(0) complex (κ^2-$S^{iPr}PS^{iPr}$)Ni(PPh_3)$_2$. Although attempts to grow crystals of [(κ^2-$S^{iPr}PS^{iPr}$)Ni(PPh_3)(CH_3)]$^+$ were unsuccessful, the proposed formulation was consistent with the spectral data. High resolution LIFDI mass spectrometry confirmed the elemental composition of **4**. The $^{31}P\{^{1}H\}$ NMR spectrum of [(κ^2-$S^{iPr}PS^{iPr}$)Ni(PPh_3)(CH_3)]$^+$ exhibited resonances (δ_{PPh} = 49.42 and δ_{PPh3} = -7.97) that are comparable to those observed for the similar, structurally characterized complex NiMe(P^nS)(PMe_3) (P^nS = (3-diphenylphosphanyl)-2-thionaphtholato)[119] (δ_{PPh2} =

50.02 and δ_{PCH3} = -22.7). Additional evidence was provided by the ^{1}H and ^{2}H, and $^{1}H\{^{31}P\}$ NMR spectra of **4** and **5**. The most notable feature in the ^{1}H NMR spectrum of $[(\kappa^2\text{-}S^{i\text{Pr}}PS^{i\text{Pr}})Ni(PPh_3)(CH_3)]^+$ was the resonance at 0.15 ppm, a doublet with $^{3}J_{H\text{-}P}$ = 5.96 Hz, assigned to Ni-CH_3. This shift is akin to that seen in [(triphos)NiMe][Co(dmgBF$_2$)$_2$py] (0.34 ppm)[99], [(triphos)NiMe]OTf (0.04 ppm)[99] and NiMe(P^nS)(PMe$_3$) (-0.29 ppm).[119] Furthermore, the absence of the methyl resonance in the ^{1}H NMR spectrum of $[(\kappa^2\text{-}S^{i\text{Pr}}PS^{i\text{Pr}})Ni(PPh_3)(CD_3)]^+$ in conjunction with the presence of the methyl resonance in the ^{2}H NMR spectrum of the same complex confirmed the assignment. In the ^{31}P-decoupled ^{1}H NMR spectrum of **4** the Ni-CH_3 doublet simplified to a singlet. The existence of coupling between methyl protons and phosphorus clearly indicated that both moieties were bound to nickel. $[(\kappa^2\text{-}S^{i\text{Pr}}PS^{i\text{Pr}})Ni(PPh_3)(CH_3)]^+$ is expected to adopt a square planar geometry with the methyl group *trans* to the thioether donor. This assumption is based on similar Ni^{2+}-methyl complexes, [(triphos)NiMe]OTf[99] and NiMe(P^nS)(PMe$_3$)[119], whose structures have been established as square planar by X-ray diffraction studies. Moreover, square-planar geometry is typical for d^8 Ni(II) complexes with strong field ligands, e.g. methyl.

To corroborate the formation of $[(\kappa^2\text{-}S^{i\text{Pr}}PS^{i\text{Pr}})Ni(PPh_3)(CH_3)]^+$ via methyl transfer from $CH_3Co(dmgBF_2)_2py$, its independent synthesis was pursued. Several experiments conducted with various stoichiometries of PPh_3, $S^{i\text{Pr}}PS^{i\text{Pr}}$, $Ni(cod)_2$ and MeOTf at different temperature and reaction times each resulted in numerous uncharacterizable products. Substituting MeI for MeOTf produced similar negative results. Likewise, the reaction of $(\kappa^2\text{-}S^{i\text{Pr}}PS^{i\text{Pr}})Ni(PPh_3)_2$ with either MeOTf or MeI at different temperatures and reaction times produced unfavorable results. Despite these

failed attempts at independent synthesis, the formation of [(κ^2-$S^{iPr}PS^{iPr}$)Ni(PPh_3)(CH_3)]$^+$ was substantiated by the spectral data discussed above. Future endeavors into this reaction, should focus on the metathetical reaction of [($S^{iPr}PS^{iPr}$)NiX]BPh_4 (X = Cl, Br, I) with a Grignard reagent (i.e. MeMgBr).

3.3.4.2 Reaction of (κ^2-$S^{iPr}PS^{iPr}$)Ni(PPh_3)$_2$ with RCo($dmgBF_2$)$_2$py, R = CH_2CH_3, $CH(CH_3)_2$, or $CH_2C(CH_3)_3$

To gain insight into the aforementioned mechanism of methyl transfer, the reactions of ethyl, isopropyl and neopentyl derivatives of RCo($dmgBF_2$)$_2$py with (κ^2-$S^{iPr}PS^{iPr}$)Ni(PPh_3)$_2$ were investigated. Combining equimolar amounts of (κ^2-$S^{iPr}PS^{iPr}$)Ni(PPh_3)$_2$ in tetrahydrofuran and RCo($dmgBF_2$)$_2$py, R = CH_2CH_3 or $CH(CH_3)_2$, in acetonitrile, under an inert atmosphere, resulted in a color change from orange to blue-green over time. The electronic spectrum of the products was dominated by the formation of Co^{1+}. Samples abstracted from equimolar mixtures of (κ^2-$S^{iPr}PS^{iPr}$)Ni(PPh_3)$_2$ in d^8-toluene and RCo($dmgBF_2$)$_2$py in d^3-acetonitrile were analyzed for alkyl transfer by ^{1}H NMR spectroscopy. Figure 3.17 displays ^{1}H NMR spectra recorded for ethyl transfer from CH_3CH_2Co($dmgBF_2$)$_2$py to (κ^2-$S^{iPr}PS^{iPr}$)Ni(PPh_3)$_2$. Over time the resonances due to starting material disappear; however, there was no visible growth of resonances corresponding to the formation of [(κ^2-$S^{iPr}PS^{iPr}$)Ni(PPh_3)(CH_2CH_3)]$^+$. Instead a new resonance, δ = 5.79, corresponding to ethylene increased over time. An analogous situation was seen for isopropyl transfer from $(CH_3)_2$CHCo($dmgBF_2$)$_2$py to (κ^2-$S^{iPr}PS^{iPr}$)Ni(PPh_3)$_2$. New resonances assigned to propylene increased as the resonances due to starting material disappeared, without the observation of any features corresponding to the formation of [(κ^2-$S^{iPr}PS^{iPr}$)Ni(PPh_3)($CH(CH_3)_2$)]$^+$. The lack of notable features indicative of nickel-alkyl

complex formation and the presence of ethylene and propylene suggested the existence of a β-hydrogen elimination decomposition pathway for these complexes. The proposed mechanistic pathway for these reactions begins with alkyl transfer to nickel followed by β-hydrogen elimination forming a nickel-hydride complex and subsequent homolytic Ni-H bond cleavage to yield a nickel(I) complex. All attempts to identify nickel-hydride, nickel(I), or any other nickel-containing complexes as intermediates or products of these reactions were unsuccessful.

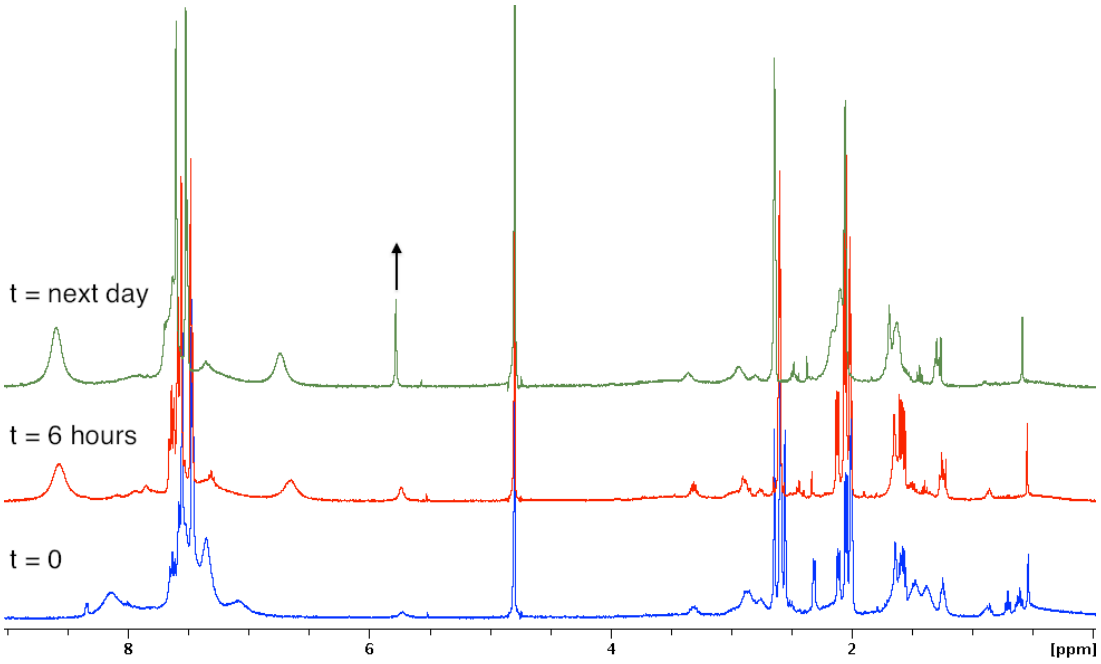

Figure 3.17. The time course of the reaction of $CH_3CH_2Co(dmgBF_2)_2py$ and (κ^2-$S^{iPr}PS^{iPr}$)$Ni(PPh_3)_2$ monitored by ^1H NMR spectroscopy.

To confirm β-hydrogen elimination as the decomposition pathway, the reaction of $((CH_3)_3CCH_2)Co(dmgBF_2)_2py$ with $(\kappa^2\text{-}S^{iPr}PS^{iPr})Ni(PPh_3)_2$ was examined, as the neopentyl group is not subject to this pathway as it does not have β-hydrogens. Combining equimolar amounts of $(\kappa^2\text{-}S^{iPr}PS^{iPr})Ni(PPh_3)_2$ in tetrahydrofuran and $((CH_3)_3CCH_2)Co(dmgBF_2)_2py$ in acetonitrile, under an inert atmosphere resulted in a color change from orange to blue. The electronic spectrum of the products was dominated by Co^{1+} absorption bands as a result, the extent of the reaction was monitored and quantified by its concentration, ε_{615} = 10,000 $M^{-1}cm^{-1}$.[99] The rate of neopentyl transfer is slow with 75% conversion observed after ~20 h (Figure 3.18).

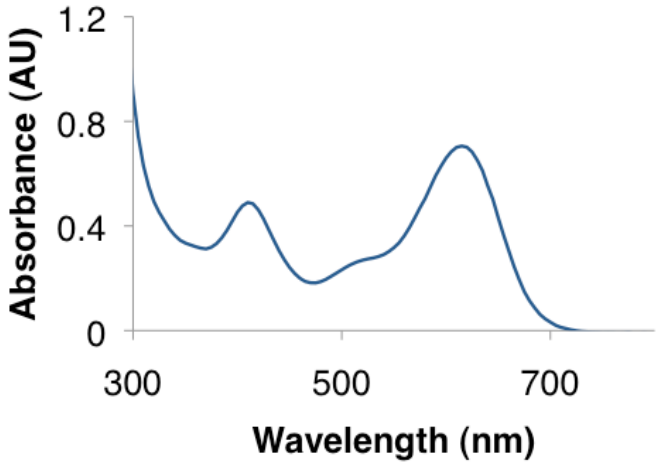

Figure 3.18. The electronic spectrum of a mixture of $(\kappa^2\text{-}S^{iPr}PS^{iPr})Ni(PPh_3)_2$ and neopentyl$Co(dmgBF_2)_2py$ in tetrahydrofuran/acetonitrile after ~20 h. The amount of Co^{1+} formed was approximately 75% based on the concentration calculated for ε_{615} = 10 000 M^{-1} cm^{-1}.[99]

Samples extracted from equimolar mixtures of (κ^2-S$^{i\text{Pr}}$PS$^{i\text{Pr}}$)Ni(PPh_3)$_2$ in d^8-toluene and ((CH_3)$_3$$CCH_2$)Co(dmg$BF_2$)$_2$py in d^6-acetone were analyzed for alkyl transfer by ^{1}H and ^{31}P{^{1}H} NMR spectroscopy. The ^{1}H NMR spectrum (Figure 3.19) exhibits resonances consistent with a stable neopentyl-nickel complex, [(S$^{i\text{Pr}}$PS$^{i\text{Pr}}$)Ni($CH_2C(CH_3)_3$]$^+$. Singlet resonances at 0.71 and 1.09 ppm correspond to the methyl groups and the α-protons of the neopentyl fragment, respectively. Two doublets at 1.24 and 1.32 ppm were assigned to the isopropyl methyl groups of S$^{i\text{Pr}}$PS$^{i\text{Pr}}$, while the isopropyl methine protons and the methylene protons of the -PCH_2CH_2S- fragment appeared as broad complex multiplets between 2.60 and 3.05 ppm, due to ^{1}H-^{1}H and ^{1}H-^{31}P couplings. Poorly resolved features in the aromatic region of the spectrum accounted for the protons of the phenyl ring. The ^{31}P{^{1}H} NMR spectrum displayed one signal at 40.16 ppm assigned to the phenylphosphine group of S$^{i\text{Pr}}$PS$^{i\text{Pr}}$ (Appendix B). The elemental composition of [(S$^{i\text{Pr}}$PS$^{i\text{Pr}}$)Ni($CH_2C(CH_3)_3$]$^+$ was determined by low resolution LIFDI mass spectrometry. The observed m/z^+, 443.3 for the parent ion is in excellent agreement with the theoretically calculated value, m/z^+, 443.3. Likewise, the observed isotope pattern was consistent with the proposed formula (Appendix B).

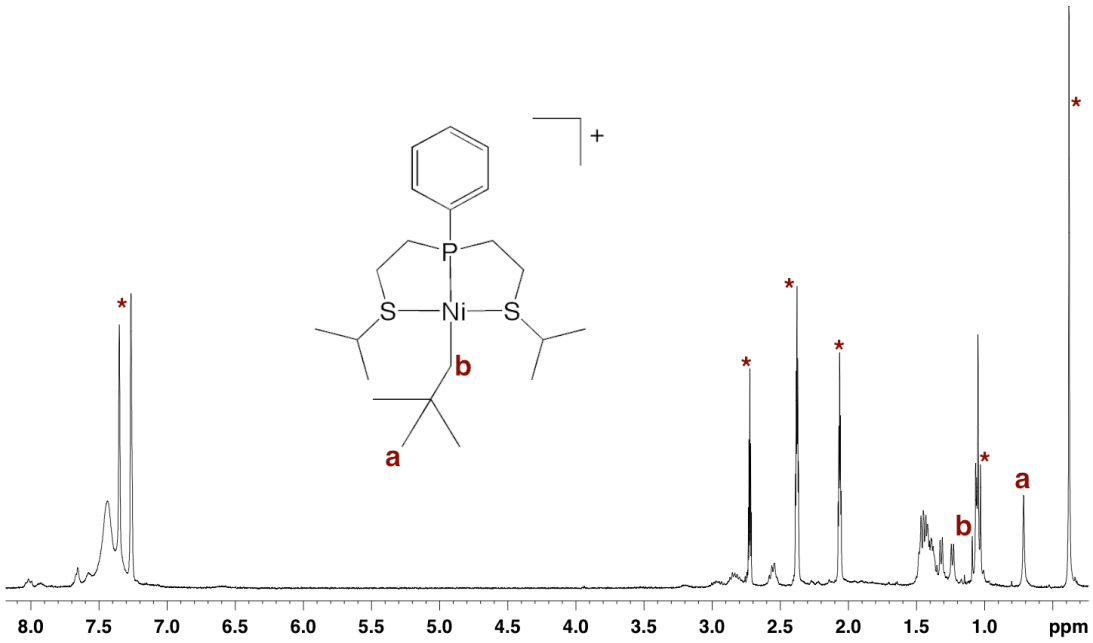

Figure 3.19. ^{1}H NMR spectrum of $[(S^{iPr}PS^{iPr})Ni(CH_2C(CH_3)_3]^+$ in $C_7D_8/(CD_3)_2CO$). * denotes residual solvent signals.

The observed spectroscopic data shown for transfer from $((CH_3)_3CCH_2)Co(dmgBF_2)_2py$ to $(\kappa^2\text{-}S^{iPr}PS^{iPr})Ni(PPh_3)_2$ confirmed the formation of a stable alkyl-nickel(II) species. This finding is positive evidence for a β-hydrogen elimination decomposition pathway for the ethyl and isopropyl $S^{iPr}PS^{iPr}$ nickel(II) complexes. An analogous situation was described by O'Hagan for the reaction of $(triphos)Ni(PPh_3)$ with $RCo(dmgBF_2)_2py$, where R = CH_2CH_3 or $CH(CH_3)_2$.[100] According to electronic absorption spectroscopy, both reactions formed Co^{1+} species. However, neither reaction displayed ^{1}H NMR spectral resonances corresponding to the

formation of an alkyl-nickel product. Similar to the transfer reactions discussed above, resonances due to ethylene and propylene were observed instead. Additionally, a transient proton resonance consistent with a nickel-hydride was seen and verified by independent synthesis. The disappearance of this species and the formation of a new paramagnetic complex over time supported the proposed mechanistic pathway of, alkyl transfer to nickel followed by β-hydrogen elimination and subsequent homolytic Ni-H bond cleavage yielding a nickel(I) complex, $[(triphos)Ni(PPh_3)]^+$.[100] A similar pathway is proposed for alkyl transfer in the complexes discussed here, $RCo(dmgBF_2)_2py$, R = CH_2CH_3 or $CH(CH_3)_2$ to $(\kappa^2\text{-}S^{i\text{Pr}}PS^{i\text{Pr}})Ni(PPh_3)_2$. Future work should include the independent preparation of the pathway intermediates, alkyl, hydride and reduced $S^{i\text{Pr}}PS^{i\text{Pr}}$ nickel complexes, to provide a comparison for the spectroscopic properties reported here.

3.3.5 Kinetics

It has been shown that $(\kappa^2\text{-}S^{i\text{Pr}}PS^{i\text{Pr}})Ni(PPh_3)_2$ can act as a nucleophile attacking the Co-R bond of $RCo(dmgBF_2)_2py$ forming a stable Ni-alkyl species. Methyl transfer was fast with 95% conversion observed after ~30 min. Neopentyl transfer was quantitatively slower, with 75% conversion observed after ~20 hr. The products of these reactions were consistent with an S_N2 mechanism of transfer. The kinetics of alkyl transfer were examined to provide support for this mechanistic assignment. Figure 3.20 displays the proposed mechanism. Loss of triphenylphosphine results in a three-coordinate $(\kappa^2\text{-}S^{i\text{Pr}}PS^{i\text{Pr}})Ni(PPh_3)$ species which subsequently attacks the Co-Me bond of $CH_3Co(dmgBF_2)_2py$, via an S_N2 mechanism, forming $[(\kappa^2\text{-}S^{i\text{Pr}}PS^{i\text{Pr}})Ni(PPh_3)(CH_3)]^+$ and $[Co(dmgBF_2)_2PPh_3]^-$. Assuming steady state conditions for the three-coordinate nickel species results in the rate law shown in Figure 3.21.

The kinetic model of alkyl transfer assumed the equilibrium loss of triphenylphosphine in the first step of the reaction and rate limiting alkyl transfer in the second step. These assumptions were based on the kinetic characterization[100] of methyl transfer from $MeCo(dmgBF_2)_2py$ to a similar Ni(0) complex, $(triphos)Ni(PPh_3)$, which proceeds by a mechanism analogous to the one proposed in Figure 3.20.

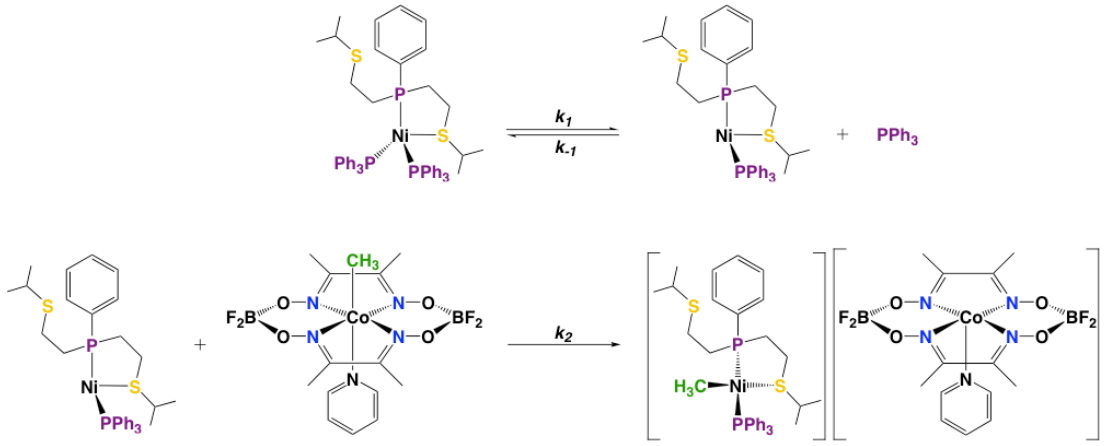

Figure 3.20. Proposed mechanistic scheme for methyl transfer.

$$\frac{d[Co^{I}][NiMe]}{dt} = \frac{k_1 k_2[(\kappa^2\text{-}S^{i\text{Pr}}PS^{i\text{Pr}})Ni(PPh_3)_2][MeCo]}{k_{-1}[PPh_3] + k_2[MeCo]}$$

Figure 3.21. Proposed rate law of methyl transfer.

Kinetic data were obtained for the reactions of $(\kappa^2\text{-}S^{i\text{Pr}}PS^{i\text{Pr}})Ni(PPh_3)_2$ with $RCo(dmgBF_2)_2py$, where R = CH_3 or CH_2CH_3. The reactions were monitored by

following the growth of $[Co(dmgBF_2)_2PPh_3]^-$ at λ_{max} = 615 nm. The assay mixtures contained Co-R as the limiting reagent and at least 20-fold excess of triphenylphosphine and $(\kappa^2\text{-}S^{iPr}PS^{iPr})Ni(PPh_3)_2$. Each k_{obs} value was determined by taking the mean of three values from individual runs. A control experiment, i.e., a mixture of $(\kappa^2\text{-}S^{iPr}PS^{iPr})Ni(PPh_3)_2$ and triphenylphosphine, showed no decomposition to $(\kappa^2\text{-}S^{iPr}PS)_2Ni$, which would interfere with the measurements of absorption. Examples of the spectral changes observed during the course of a typical reaction are shown for methyl and ethyl transfer in Figures 3.22 to 3.25 and in Appendix B.

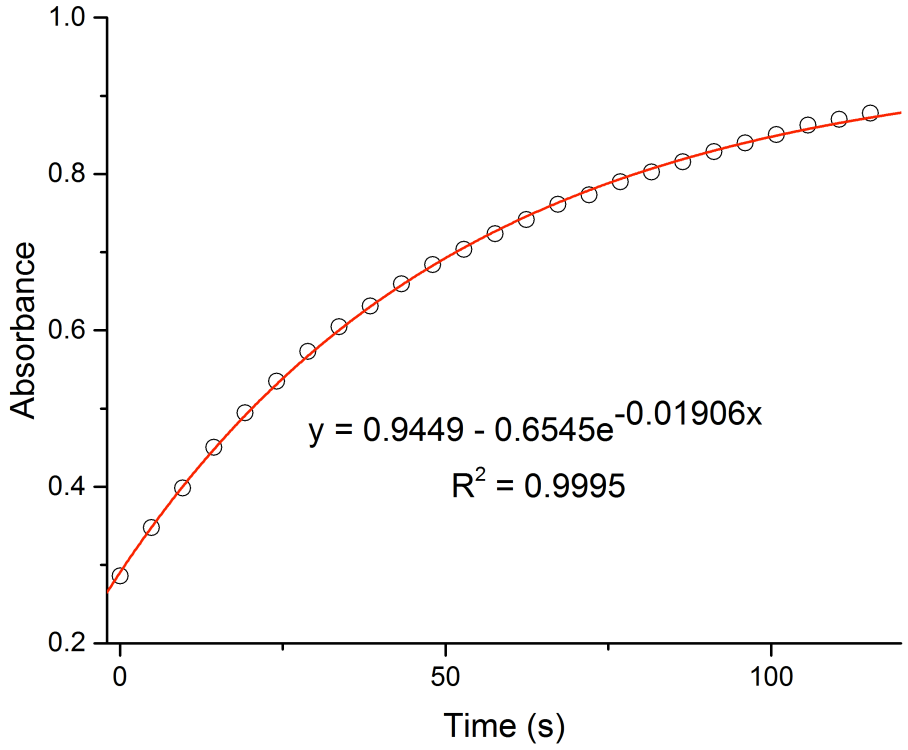

Figure 3.22. Representative kinetic trace for the reaction of $(\kappa^2\text{-}S^{iPr}PS^{iPr})Ni(PPh_3)_2$ with $CH_3Co(dmgBF_2)_2py$ over three half lives. The reaction was monitored by following the growth of $[Co(dmgBF_2)_2PPh_3]^-$ at λ_{max} = 615 nm over time.

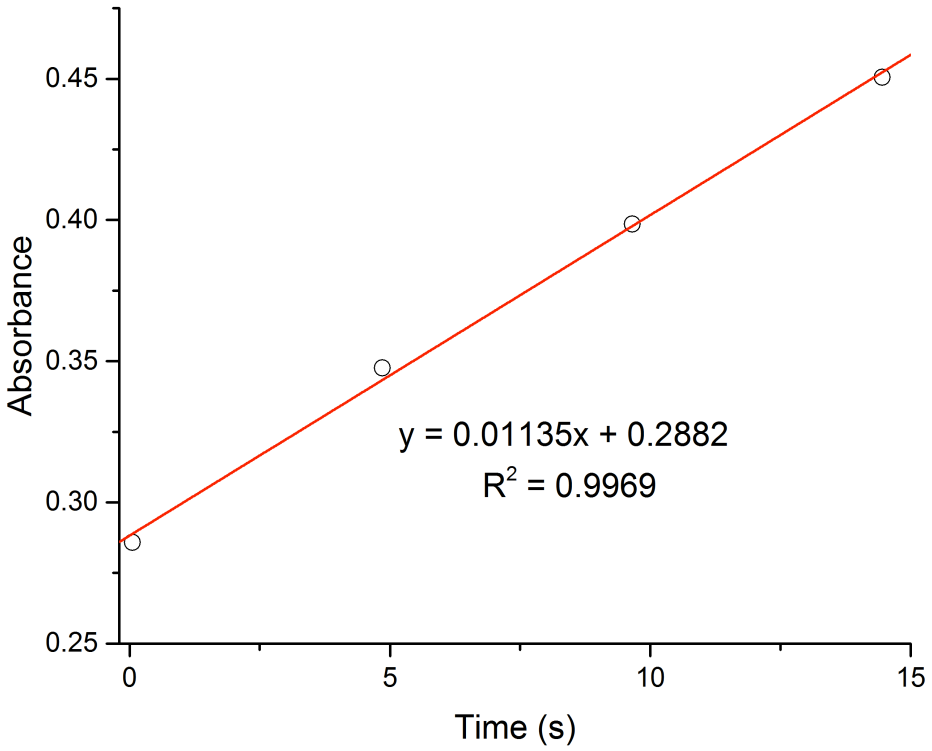

Figure 3.23. Plot of the initial rate of the reaction of (κ^2-S$^{i\text{Pr}}$PS$^{i\text{Pr}}$)Ni(PPh_3)$_2$ with $CH_3Co(dmgBF_2)_2py$. The reaction was monitored by following the growth of $[Co(dmgBF_2)_2PPh_3]^-$ at λ_{max} = 615 nm over time.

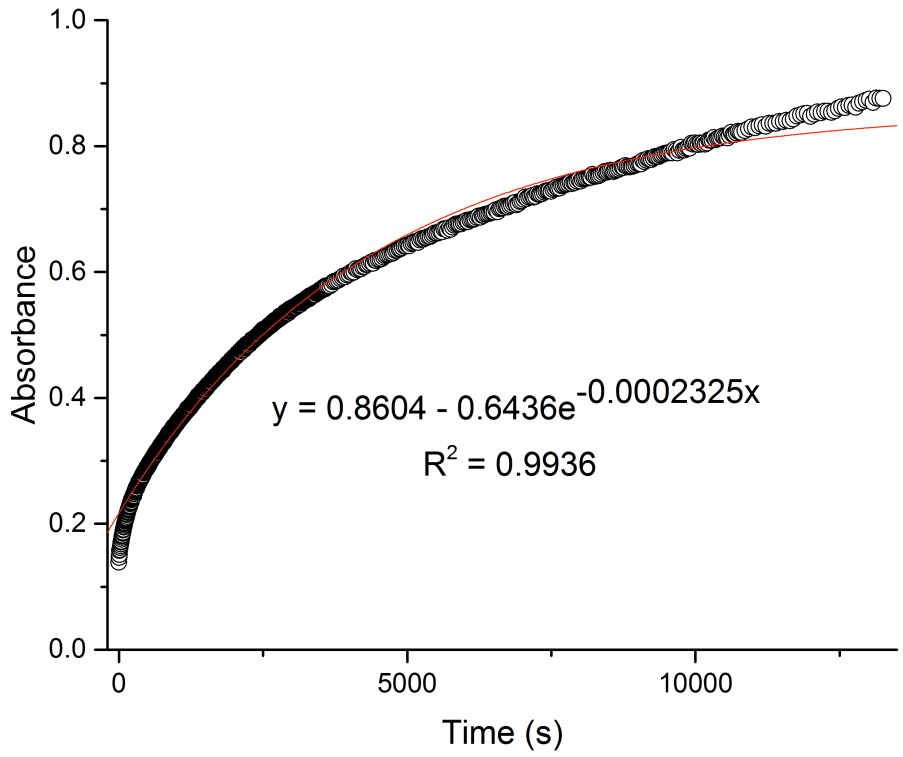

Figure 3.24. Representative kinetic trace for the reaction of (κ^2-S$^{i\text{Pr}}$PS$^{i\text{Pr}}$)Ni(PPh_3)$_2$ with $CH_3CH_2Co(dmgBF_2)_2py$ over three half lives. The reaction was monitored by following the growth of $[Co(dmgBF_2)_2PPh_3]^-$ at λ_{max} = 615 nm over time.

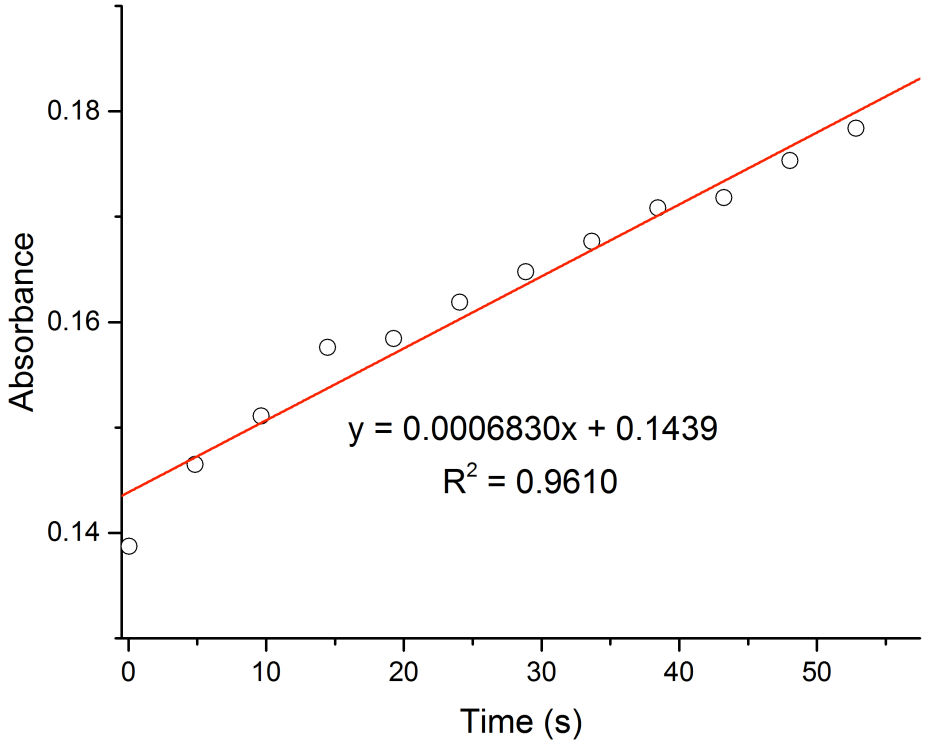

Figure 3.25. Plot of the initial rate of the reaction of (κ^2-S$^{i\text{Pr}}$PS$^{i\text{Pr}}$)Ni(PPh_3)$_2$ with $CH_3CH_2Co(dmgBF_2)_2py$. The reaction was monitored by following the growth of $[Co(dmgBF_2)_2PPh_3]^-$ at λ_{max} = 615 nm over time.

The rate of alkyl transfer decreased by two orders of magnitude when the alkyl was changed from methyl (k_{obs} = 1.9(6) x 10^{-2} s^{-1}) to ethyl (k_{obs} = 2.1(9) x 10^{-4} s^{-1}). As the steric bulk of the alkyl was increased, the rate of the reaction decreased. Although the rate of transfer for neopentyl was not investigated for this system, the rate would be expected to follow the established trend and decrease by approximately another two orders of magnitude. The predicted rate decrease is consistent with the observed experimental data for neopentyl transfer, 75% conversion after ~20 hours, compared

to methyl transfer, 95% conversion after ~30 min. The trend of rate constants, R = CH_3 > CH_2CH_3, is in agreement with the proposed S_N2 transfer mechanism. For an electron transfer mechanism the opposite trend would be seen, R = CH_3 < CH_2CH_3, the increased steric bulk of the alkyl is consistent with the relative stability of the corresponding alkyl radical. This trend was observed previously for alkyl transfer to [Ni(tmc)][OTf] by Ram et al.[98]

Previous work by O'Hagan demonstrated that alkyl transfer from $RCo(dmgBF_2)_2py$ to (triphos)Ni(PPh_3) is analogous to that observed above.[100] Increasing the steric bulk of the alkyl from methyl to ethyl to isopropyl decreased the rate of the reaction, consistent with an S_N2 mechanism. The rate of alkyl transfer decreased by two orders of magnitude when the alkyl was changed from methyl (k_{obs} = 1.7(3) x 10^{-3} s^{-1}) to ethyl (k_{obs} = 8.9(2) x 10^{-5} s^{-1}).[100] However, these rates are slightly slower then those reported earlier for the analogous reactions of (κ^2-$S^{iPr}PS^{iPr}$)Ni(PPh_3)$_2$ with $RCo(dmgBF_2)_2py$ (R = CH_3: k_{obs} = 1.9(6) x 10^{-2} s^{-1}; R = CH_3CH_2: k_{obs} = 2.1(9) x 10^{-4} s^{-1}). The effectiveness of a nucleophile displacing the leaving group in an S_N2 characterized reaction is directly related to the rate of the reaction. Reasons for the differences in these rates can be attributed to the steric and electronic influences of triphos and $S^{iPr}PS^{iPr}$ on the nucleophilicity of nickel. For (triphos)Ni, the bis-chelate and –PPh_2 substituents restricted the size of the pocket at the metal center slowing nucleophilic attack of the cobalt methyl group. For (κ^2-$S^{iPr}PS^{iPr}$)Ni(PPh_3), the mono-chelate along with the bound –S^{iPr} and –PPh_3 substituents created a comparably larger more flexible pocket at the metal center resulting in a quicker nucleophilic attack on the cobalt methyl group. The flexibility of the ligand pocket is important since the alkyl transfer reactions discussed here are accompanied by a change in the nickel

coordination geometry from tetrahedral to square planar. The fluxional behavior ascribed to the thioether arms of (κ^2-S$^{i\text{Pr}}$PS$^{i\text{Pr}}$)Ni(PPh$_3$)$_2$ supports a facile geometric change and therefore, a faster rate of reaction. The lower nucleophilicity of (triphos)Ni compared to (κ^2-S$^{i\text{Pr}}$PS$^{i\text{Pr}}$)Ni(PPh$_3$) was also due to the donor strength of the triphos and S$^{i\text{Pr}}$PS$^{i\text{Pr}}$ ligands. The possibility of back-bonding was much greater in (triphos)Ni than in (κ^2-S$^{i\text{Pr}}$PS$^{i\text{Pr}}$)Ni(PPh$_3$), based on the fact that phosphine ligands are better π-acceptors than thioether ligands. Removing electron density from nickel for back-bonding reduced its nucleophilicity, subsequently slowing the rate of reaction. Both systems showed that the zero-valent nickel oxidation state is capable of nucleophilic attack on a Co-Me of a cobalamin analogue forming a Ni-Me intermediate, suggesting that the S_N2 methyl transfer in ACS can proceed through a Ni^0 intermediate.

3.4 Summary

Efforts to model the methyl transfer step from CH_3-CoFeSP to the proximal nickel of the A-cluster of ACS/COdH during acetyl coenzyme A synthesis were performed by utilizing, S$^{i\text{Pr}}$PS$^{i\text{Pr}}$, a tridentate ligand composed of thioether donor arms that are electronically similar to bridging thiolates found in the enzyme active site. This chapter presented the synthesis and isolation of S$^{i\text{Pr}}$PS$^{i\text{Pr}}$. The data discussed have shown that S$^{i\text{Pr}}$PS$^{i\text{Pr}}$ is a capable ligand for zerovalent and divalent nickel. (κ^2-S$^{i\text{Pr}}$PS$^{i\text{Pr}}$)Ni(PPh$_3$)$_2$ was synthesized and characterized, both structurally and spectroscopically, as a four-coordinate pseudo-tetrahedral Ni^0 complex. The structure of (κ^2-S$^{i\text{Pr}}$PS$^{i\text{Pr}}$)Ni(PPh$_3$)$_2$ was interrogated by variable-temperature NMR spectroscopy. These experiments determined that the thioether arms of (κ^2-S$^{i\text{Pr}}$PS$^{i\text{Pr}}$)Ni(PPh$_3$)$_2$ are labile, undergoing exchange between coordinated and uncoordinated positions. The synthesis of (κ^2-S$^{i\text{Pr}}$PS)$_2$Ni was achieved by the

decomposition of (κ^2-$S^{iPr}PS^{iPr}$)$Ni(PPh_3)_2$ via S-dealkylation. (κ^2-$S^{iPr}PS)_2Ni$ crystallized as a four-coordinate square planar Ni^{2+} complex. $S^{iPr}PS^{iPr}$ has been demonstrated to be a competent ligand for nickel complexes of multiple oxidation states and geometries.

The reactions presented herein described the reactivity of (κ^2-$S^{iPr}PS^{iPr}$)$Ni(PPh_3)_2$ with alkylcobaloximes, i.e. methyl, methyl-d_3, ethyl, isopropyl and neopentyl. The reaction of (κ^2-$S^{iPr}PS^{iPr}$)$Ni(PPh_3)_2$ with $RCo(dmgBF_2)_2py$, where R = CH_3 or CD_3, led to the formation of the respective alkyl species, [(κ^2-$S^{iPr}PS^{iPr}$)$Ni(PPh_3)R$][$Co(dmgBF_2)_2PPh_3$]. Electronic absorption data suggested that $CH_3Co(dmgBF_2)_2py$ can quantitatively methylate the Ni^0 complex, (κ^2-$S^{iPr}PS^{iPr}$)$Ni(PPh_3)_2$. The structure of [(κ^2-$S^{iPr}PS^{iPr}$)$Ni(PPh_3)CH_3]^+$ was investigated by NMR and LIFDI mass spectroscopies. These experiments determined that the ^1H NMR spectrum of [(κ^2-$S^{iPr}PS^{iPr}$)$Ni(PPh_3)CH_3]^+$ has a new resonance, $\delta = 0.15$, assigned to the Ni-methyl moiety and an elemental composition consistent with the proposed formula. The ^1H NMR spectrum of [(κ^2-$S^{iPr}PS^{iPr}$)$Ni(PPh_3)CD_3]^+$ was nearly identical to the spectrum of [(κ^2-$S^{iPr}PS^{iPr}$)$Ni(PPh_3)CH_3]^+$ with one exception, as anticipated the resonance for Ni-CH_3 was absent. The ^2H NMR spectrum of [(κ^2-$S^{iPr}PS^{iPr}$)$Ni(PPh_3)CD_3]^+$ confirmed the transfer of a methyl group with a single resonance at $\delta = -0.26$ assigned to Ni-CD_3. Taken together, these observations provide evidence for the successful transfer of methyl, forming a new Ni-methyl species, [(κ^2-$S^{iPr}PS^{iPr}$)$Ni(PPh_3)CH_3]^+$, and the existence of (κ^2-$S^{iPr}PS^{iPr}$)$Ni(PPh_3)_2$ as a valuable model of the A-cluster of ACS.

Reactions of (κ^2-$S^{iPr}PS^{iPr}$)$Ni(PPh_3)_2$ with $RCo(dmgBF_2)_2py$, where R = CH_3CH_2 or $CH(CH_3)_2$, yielded ethylene and propylene, respectively, rather than the corresponding Ni-alkyl complex. This difference in reactivity is readily explained by

the existence of a β-hydrogen elimination decomposition pathway for these complexes. This pathway was verified by spectroscopic data showing successful alkyl transfer from $((CH_3)_3CCH_2)Co(dmgBF_2)_2py$, which lack a β-hydrogen, to (κ^2-$S^{iPr}PS^{iPr}$)$Ni(PPh_3)_2$. The proposed mechanistic pathway for ethyl and isopropyl transfer begins with alkyl transfer to nickel followed by β-hydrogen elimination and subsequent homolytic Ni-H bond cleavage yielding a Ni(I) complex. Although no Ni-hydride or Ni(I) complexes are detected during this reaction, they were spectroscopically observed by O'Hagan in the analogous reactions of $(triphos)Ni(PPh_3)$ with $RCo(dmgBF_2)_2py$, where R = CH_3CH_2 or $CH(CH_3)_2$.[100]

It has been shown that (κ^2-$S^{iPr}PS^{iPr}$)$Ni(PPh_3)_2$ can act as a nucleophile attacking the Co-Me bond of $MeCo(dmgBF_2)_2py$ forming a stable Ni-Me species. The proposed mechanism begins with loss of triphenylphosphine forming a three-coordinate species, which subsequently attacks the Co-Me bond via an S_N2 mechanism. The significant decrease in the observed transfer rate as the steric bulk of the alkyl increases, reinforces the S_N2 mechanistic assignment. The methyl transfer step from CH_3-CoFeSP to the proximal nickel of the A-cluster of ACS/COdH during acetyl coenzyme A synthesis is also proposed to proceed via an S_N2 mechanism. This model system suggests that the methyl-transfer in ACS can proceed through a Ni^0 intermediate.

REFERENCES

1. Sigel, A., Sigel, H., Sigel, R. *Nickel and Its Surprising Impact in Nature*; John Wiley and Sons Ltd: England, 2007.

2. Weeks, M. E. *J. Chem. Educ.* **1932**, *9*, 22-30.

3. Howard-White, F. B. *Nickel An Historical Review*; D. Van Nostrand Company Inc.: Princeton, 1963.

4. Baldwin, W. H. *J. Chem. Educ.* **1931**, *8*, 1749-1761.

5. Mond, L., Langer, C., Quincke, F. *J. Chem. Soc., Trans.* **1890**, *57*, 749-753.

6. Kauffman, G. B. *Alfred Werner Founder of Coordination Chemistry*; Springer-Verlag: Berlin, 1966.

7. Hausinger, R. P. *Biochemistry of Nickel*; Plenum Press: New York, 1993.

8. Bartha, R., Ordal, E. *J. Bacteriol.* **1965**, *89*, 1015-1019.

9. (a) Bertrand, D., De Wolf, A. *C. R. Acad. Sci. Hebd. Paris* **1967**, *265*, 1053-1055. (b) Lancaster, J. R. *The Bioinorganic Chemistry of Nickel*; VCH Publishers, Inc.: United States of America, 1988.

10. (a) Nielsen, F. H., Sauberlich, H. E. *Proc. Soc. Exp. Biol. Med.* **1970**, *134*, 845-849. (b) Nielsen, F. H., Ollerich, D. A. *Fed. Proc.* **1974**, *33*, 1767-1772.

11. Dixon, N. E., Gazzola, C., Blakely, R. L., Zerner, B. *J. Am. Chem. Soc.* **1975**, *97*, 4131-4133.

12. Boer, J. L., Mulrooney, S. B., Hausinger, R. P. *Arch. Biochem. Biophys.* **2014**, *544*, 142-152.

13. Ragsdale, S. W. *Crit. Rev. Biochem. Mol. Biol.* **2004**, *39*, 165-195.

14. Ragsdale, S. W. *BioFactors* **1997**, *6*, 3-11.

15. Mulrooney, S. B., Hausinger, R. P. *FEMS Microbiol. Rev.* **2003**, *27*, 239-261.

16. Shively, J. M., Barton, L. L. *Variations in Autotrophic Life*; Academic Press Limited: San Diego, 1991.

17. Lindahl, P. A. *J. Biol. Inorg. Chem.* **2004**, *9*, 516-524.

18. Bender, G., Ragsdale, S. W., *Biochemistry* **2011**, *50*, 276-286.

19. Ragsdale, S. W., *J. Inorg. Biochem.* **2007**, *101*, 1657-1666.

20. Huber, C., Wächtershäuser, G. *Science* **1997**, *276*, 245-247.

21. Lindahl, P. A., Chang, B. *Origins of Life and Evolution of the Biosphere* **2001**, *31*, 403-434.

22. Russell, M. *American Scientist* **2006**, *94*, 32-39.

23. Russell, M. J., Martin, W. *Trends Biochem. Sci.* **2004**, *29*, 358-363.

24. Kung, Y., Drennan, C. L. *Curr. Opin. Chem. Biol.* **2011**, *15*, 276-283.

25. Falkowski, P., Scholes, R. J., Boyle, E., Canadell, J., Canfield, D., Elser, J., Gruber, N., Hibbard, K., Högberg, P., Linder, S., Mackenzie, F. T., Moore III, B., Pedersen, T., Rosenthal, Y., Seitzinger, S., Smetacek, V., Steffen, W. *Science* **2000**, *290*, 291-296.

26. Ragsdale, S. W., Pierce, E. *Biochim. Biophys. Acta, Proteins Proteomics* **2008**, *1784*, 1873-1898.

27. Drake, H. L. *Acetogenesis*; Chapman & Hall: New York, 1994.

28. Grahame, D. A. *J. Biol. Chem.* **1991**, *266*, 22227-22233.

29. Spormann, A. M., Thauer, R. K. *Arch. Microbiol* **1988**, *150*, 374-380.

30. Can, M., Armstrong, F. A., Ragsdale, S. W. *Chem. Rev.* **2014**, *114*, 4149-4174.

31. Wieringa, K. T. *Antonie van Leeuwenhoek* **1939**, *6*, 251-262.

32. Barker, H. A., Kamen, M. D. *Proc. Natl. Acad. Sci. U.S.A.* **1945**, *31*, 219-225.

33. Hegg, E. L. *Acc. Chem. Res.* **2004**, *37*, 775-783.

34. Ragsdale, S. W., Wood, H. G. *J. Biol. Chem.* **1985**, *260*, 3970-3977.

35. Doukov, T. I., Iverson, T. M., Seravalli, J., Ragsdale, S. W., Drennan, C. L. *Science* **2002**, *298*, 567-572.

36. Darnault, C., Volbeda, A., Kim, E. J., Legrand, P., Vernède, X., Lindahl, P. A., Fontecilla-Camps, J. C. *Nat. Struct. Biol.* **2003**, *10*, 271-279.

37. Svetlitchnyi, V., Dobbek, H. Meyer-Klaucke, W., Meins, T., Thiele, B., Römer, P., Huber, R., Meyer, O. *Proc. Natl. Acad. Sci. U.S.A.* **2004**, *101*, 446-451.

38. Bramlett, M. R., Tan, X., Lindahl, P. A., *J. Am. Chem. Soc.* **2003**, *125*, 9316-9317.

39. Seravalli, J., Xiao, Y., Gu, W., Cramer, S. P., Antholine, W. E., Krymov, V., Gerfen, G. J., Ragsdale, S. W. *Biochemistry* **2004**, *43*, 3944-3955.

40. Gencic, S., Grahame, D. A. *J. Biol. Chem.* **2003**, *278*, 6101-6110.

41. Tan, X., Bramlett, M. R., Lindahl, P. A. *J. Am. Chem. Soc.* **2004**, *126*, 5954-5955.

42. Drennan, C. L., Heo, J., Sintchak, M. D., Schreiter, E., Ludden, P. W. *Proc. Natl. Acad. Sci. U.S.A.* **2001**, *98*, 11973-11978.

43. Dobbek, H., Svetlitchnyi, V., Gremer, L., Huber, R., Meyer, O. *Science* **2001**, *293*, 1281-1285.

44. Dobbek, H., Svetlitchnyi, V., Liss, J., Meyer, O. *J. Am. Chem. Soc.* **2004**, *126*, 5382-5387.

45. Kung, Y., Doukov, T. I., Seravalli, J., Ragsdale, S. W., Drennan, C. L. *Biochemistry* **2009**, *48*, 7432-7440.

46. Jeoung, J., Dobbek, H. *Science* **2007**, *318*, 1461-1464.

47. Gong, W., Hao, B., Wei, Z., Ferguson, Jr., D. J., Tallant, T., Krzycki, J. A., Chan, M. K. *Proc. Natl. Acad. Sci. U.S.A.* **2008**, *105*, 9558-9563.

48. Jeoung, J., Dobbek, H. *J. Am. Chem. Soc.* **2009**, *131*, 9922-9923.

49. Jeoung, J., Dobbek, H. *J. Biol. Inorg. Chem.* **2012**, *17*, 167-173.

50. Maynard, E. L., Lindahl, P. A. *J. Am. Chem. Soc.* **1999**, *121*, 9221-9222.

51. Seravalli, J., Ragsdale, S. W. *Biochemistry* **2000**, *39*, 1274-1277.

52. Doukov, T., Blasiak, L., Seravalli, J., Ragsdale, S. W., Drennan, C. L., *Biochemistry* **2008**, *47*, 3474-3483.

53. Majumdar, A., *Dalton Trans.* **2014**, *43*, 12135-12145.

54. Riordan, C. G. *J. Biol. Inorg. Chem.* **2004**, *9*, 542-549.

55. Lindahl, P. A., Ragsdale, S. W., Münck, E. *J. Biol. Chem.***1990**, *265*, 3880-3888.

56. Xia, J., Hu, Z., Popescu, C. V., Lindahl, P. A., Münck, E. *J. Am. Chem. Soc.* **1997**, *119*, 8301-8312.

57. Fan, C., Gorst, C. M., Ragsdale, S. W., Hoffman, B. M. *Biochemistry* **1991**, *30*, 431-435.

58. Ragsdale, S. W., Wood, H. G., Antholine, W. E., *Proc. Natl. Acad. Sci. U.S.A.* **1985**, *82*, 6811-6814.

59. Kumar, M., Ragsdale, S. W. *J. Am. Chem. Soc.* **1992**, *114*, 8713-8715.

60. Chen, J., Huang, S., Seravalli, J., Gutzman Jr., H., Swartz, D. J., Ragsdale, S. W., Bagley, K. A. *Biochemistry* **2003**, *42*, 14822-14830.

61. Seravalli, J., Ragsdale, S. W. *J. Biol. Chem.* **2008**, *283*, 8384-8394.

62. Bramlett, M. R., Stubna, A., Tan, X., Surovtsev, I. V., Münck, E., Lindahl, P. A. *Biochemistry* **2006**, *45*, 8674-8685.

63. Tan, X., Surovtsev, I. V., Lindahl, P. A. *J. Am. Chem. Soc.* **2006**, *128*, 12331-12338.

64. Seravalli, J., Kumar, M., Ragsdale, S. W. *Biochemistry* **2002**, *41*, 1807-1819.

65. Tan, X., Sewell, C., Yang, Q., Lindahl, P. A. *J. Am. Chem. Soc.* **2003**, *125*, 318-319.

66. Shanmugasundaram, T., Wood, H. G. *J. Biol. Chem.* **1992**, *267*, 897-900.

67. Barondeau, D. P., Lindahl, P. A. *J. Am. Chem. Soc.* **1997**, *119*, 3959-3970.

68. Maynard, E. L., Sewell, C., Lindahl, P. A. *J. Am. Chem. Soc.* **2001**, *123*, 4697-4703.

69. Tan, X. S., Sewell, C., Lindahl, P. A., *J. Am. Chem. Soc.* **2002**, *124*, 6277-6284.

70. Evans, D. J. *Coord. Chem. Rev.* **2005**, *249*, 1582-1595.

71. Harrop, T. C., Mascharak, P. K. *Coord. Chem. Rev.* **2005**, *249*, 3007-3024.

72. Harrop, T. C., Olmstead, M. M., Mascharak, P. K. *J. Am. Chem. Soc.* **2004**, *126*, 14714-14715.

73. Harrop, T. C., Olmstead, M. M., Mascharak, P. K. *Inorg. Chem.* **2006**, *45*, 3424-3436.

74. Krishnan, R., Riordan, C. G. *J. Am. Chem. Soc.* **2004**, *126*, 4484-4485.

75. William Dougherty Doctoral Dissertation

76. Tanaka, M., Fujii, Y., Ōkawa, H., Shinmyozu, T., Inazu, T. *Chem. Lett.* **1987**, 1673-1674.

77. Gypser, A *et al.* U.S. Patent 6,593,315 B2, 2003.

78. Shriver, D. F., Drezdzon, M. A. *The Manipulation of Air Sensitive Compounds, 2nd Ed.*; John Wiley & Sons, Inc.: New York, 1986.

79. Pangborn, A. B., Giardello, M. A., Grubbs, R. H., Rosen, R. K., Timmers, F. J. *Organometallics* **1996**, *15*, 1518-1520.

80. Filler, R., Lin, S., Zhang, Z. *J. Fluorine Chem.* **1995**, *74*, 69-75.

81. Newman, M., Karnes, H. *J. Org. Chem.* **1996**, *31*, 3980-3984.

82. Flores-Figueroa, A. Arista-M., V, Talancón-Sánchez, D., Castillo, I. *J. Braz. Chem. Soc.* **2005**, *16*, 397-403.

83. Brooker, S., Croucher, P. D., Roxburgh, F. M. *J. Chem. Soc., Dalton Trans.* **1996**, 3031-3037.

84. Goswami, N., Eichhorn, D. M. *Inorg. Chim. Acta* **2002**, *303*, 271-276.

85. Gomes, L., Pereira, E., Castro, B. *Acta Cryst.* **1999**, *C55*, 1061-1063.

86. Taylor, M., Reglinski, J., Wallace, D. *Polyhedron* **2004**, *23*, 3201-3209.

87. Smeets, W. J. J., Spek, A. L., Henderson, R. K., Bouwman, E., Reedijk, J. *Acta Cryst.* **1997**, *C53*, 1564-1566.

88. Henderson, R. K.; Bouwman, E., Reedijk, J., Powell *Acta Cryst.* **1996**, *C52*, 2696-2698.

89. Gomes, L., Pereira, E., Castro, B. *J. Chem. Soc., Dalton Trans.* **2000**, 1373-1379.

90. Farsavi, F., Golchoubian, H. *Phosphorus, Sulfur, and Silicon* **2006**, *181*, 1277-1283.

91. Butin, K. P., Moiseeva, A. A., Beloglazkina, E. K., Chudinov, Y. B., Chizhevskii, A. A., Mironov, A. V., Tarasevich, B. N., Lalov, A. V., Zyk, N. V. *Russ. Chem. Bull., Int. Ed.* **2005**, *54*, 173-188.

92. Stenson, P. A., Board, A., Marin-Becerra, A., Blake, A. J., Davies, E. S., Wilson, C., McMaster, J., Schröder, M. *Chem. Eur. J.* **2008**, *14*, 2564-2576.

93. Gosden, C., Kerr, J. B., Pletcher, D., Rosas, R. *J. Electroanal. Chem.* **1981**, *117*, 101-107.

94. Cheng, K., You, Z., Zhu, H. *Aust. J. Chem.* **2007**, *60*, 375-379.

95. Kumar, M., Qui, D., Spiro, T. G., Ragsdale, S. W. *Science*, **1995**, *270*, 628-630.

96. Lebertz, H., Simon, H., Courtney, L. F., Benkovic, S. J., Zydowsky, L. D., Lee, K., Floss, H. G., *J. Am. Chem. Soc.* **1987**, *109*, 3173-3174.

97. Ram, M. S., Riordan, C. G. *J. Am. Chem. Soc.* **1995**, *117*, 2365-2366.

98. Ram, M. S., Riordan, C. G., Yap, G. P. A., Liable-Sands, L., Rheingold, A. L., Marchaj, A., Norton, J. R. *J. Am. Chem. Soc.* **1997**, *119*, 1648-1655.

99. Eckert, N. A., Dougherty, W. G., Yap, G. P. A., Riordan, C. G., *J. Am. Chem. Soc.* **2007**, *129*, 9286-9287.

100. Molly O'Hagan Doctoral Dissertation

101. Ito, M., Kotera, M., Matsumoto, T., Tatsumi, K. *Proc. Natl. Acad. Sci. U.S.A.* **2009**, *106*, 11862-11866.

102. Matsumoto, T., Ito, M., Kotera, M., Tatsumi, K. *Dalton Trans.* **2010**, *39*, 2995-2997.

103. Dilworth, J. R., Wheatley, N. *Coord. Chem. Rev.* **2000**, *199*, 89-158.

104. Siclovan, O. P., Angelici, R. J. *Inorg. Chem.* **1998**, *37*, 432-444.

105. McGuinness, D. S., Wasserscheid, P., Morgan, D. H., Dixon, J. T. *Organometallics* **2005**, *24*, 552-556.

106. Lockyer, T. N. *Aust. J. Chem.* **1974**, *27*, 259-267.

107. (a) Linden, H. B. *Eur. J. Mass Spectrom.* **2004**, *10*, 459-468. (b) Gross, J. H., Nieth, N., Linden, H. B., Blumbach, U., Richter, F. J., Tauchert, M. E., Tompers, R., Hofmann, P. *Anal. Bioanal. Chem.* **2006**, *386*, 52-58.

108. Schrauzer, G. N. *Acc. Chem. Res.* **1968**, *1*, 97-103.

109. Steve Tereniak Undergraduate Thesis

110. Eckert, Unpublished Results

111. Blower, P. J., Dilworth, J. R., Leigh, J., Neaves, B. D., Normanton, F. B., Hutchinson, J., Zubieta, J. A. *J. Chem. Soc. Dalton Trans.* **1985**, 2647-2653.

112. Muñoz, J. A., Escriche, L., Casabó, J., Pérez-Jiménez, C. Kivekäs, R., Sillanpää, R. *Inorg. Chim. Acta* **1997**, *257*, 99-104.

113. Kim, J. S., Reibenspies, J. H., Darensbourg, M. Y. *J. Am. Chem. Soc.* **1996**, *118*, 4115-4123.

114. Rigo, P., Bressan, M., Basato, M. *Inorg. Chem.* **1979**, *18*, 860-863.

115. Kim, J. S., Reibenspies, J. H., Darensbourg, M. Y. *Inorg. Chim. Acta* **1996**, *250*, 283-294.

116. Roundhill, D. M., Roundhill, S. G. N., Beaulieu, W. B., Bagchi, U. *Inorg. Chem.* **1980**, *19*, 3365-3373.

117. Livingstone, S. E., Lockyer, T. N. *Inorg. Nucl. Chem. Lett.* **1967**, *3*, 35-38.

118. Hsiao, Y., Chojnacki, S. S., Hinton, P., Reibenspies, J. H., Darensbourg, M. Y. *Organometallics* **1993**, *12*, 870-875.

119. Kraikivskii, P. B., Frey, M., Bennour, H. A., Gembus, A., Hauptmann, R., Svoboda, I., Fuess, H., Saraev, V. V., Klein, H. *J. Organomet. Chem.* **2009**, *694*, 1869-1876.

Appendix A

ADDITIONAL SPECTROSCOPIC CHARACTERIZATION OF *N,N'*-BIS(3-METHOXYCARBONYLTHIOSALICYLIDENE)-R-DIAMINONICKEL(II) COMPLEXES

A.1 *N,N'*-bis(3-methoxycarbonylthiosalicylidene)ethylenediaminonickel Ni(3-MOC-tsalen) (3)

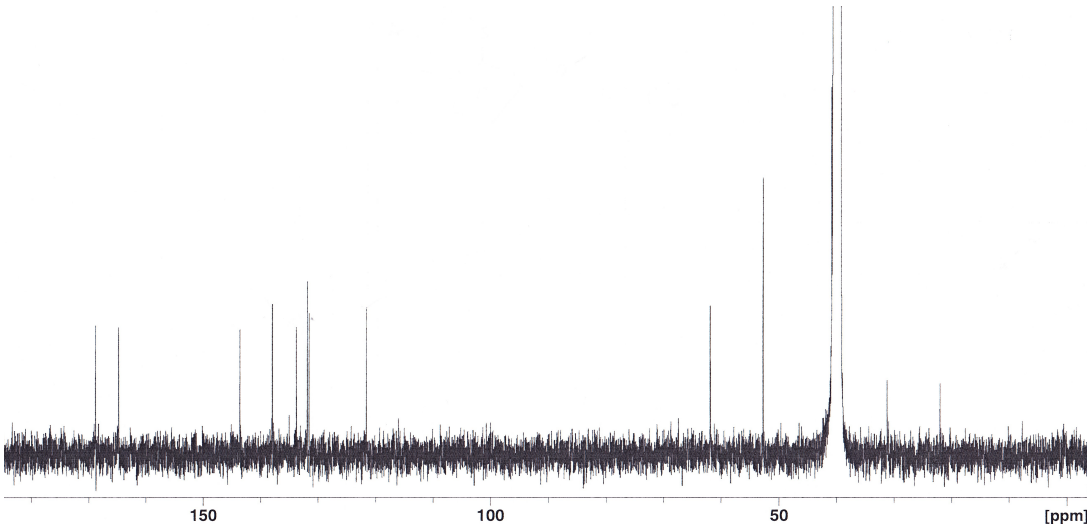

Figure A.1. $^{13}C\{^{1}H\}$ NMR spectrum of Ni(3-MOC-tsalen) in $(CD_3)_2SO$.

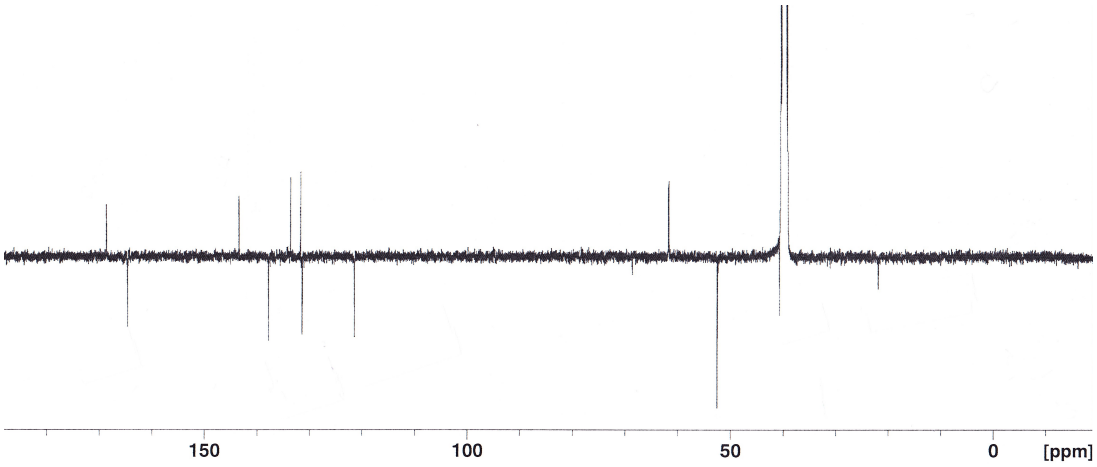

Figure A.2. ^{13}C APT NMR spectrum of Ni(3-MOC-tsalen) in $(CD_3)_2SO$.

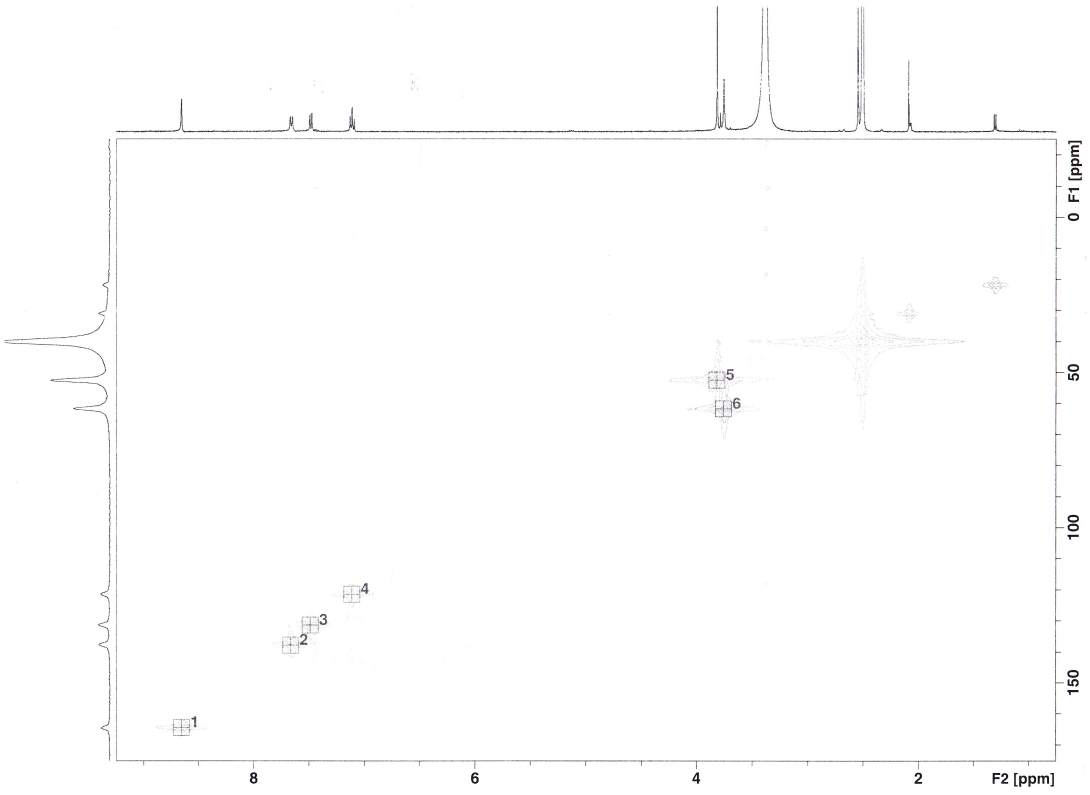

Figure A.3. Ni(3-MOC-tsalen) ^{13}C-HMQC spectrum in $(CD_3)_2SO$.

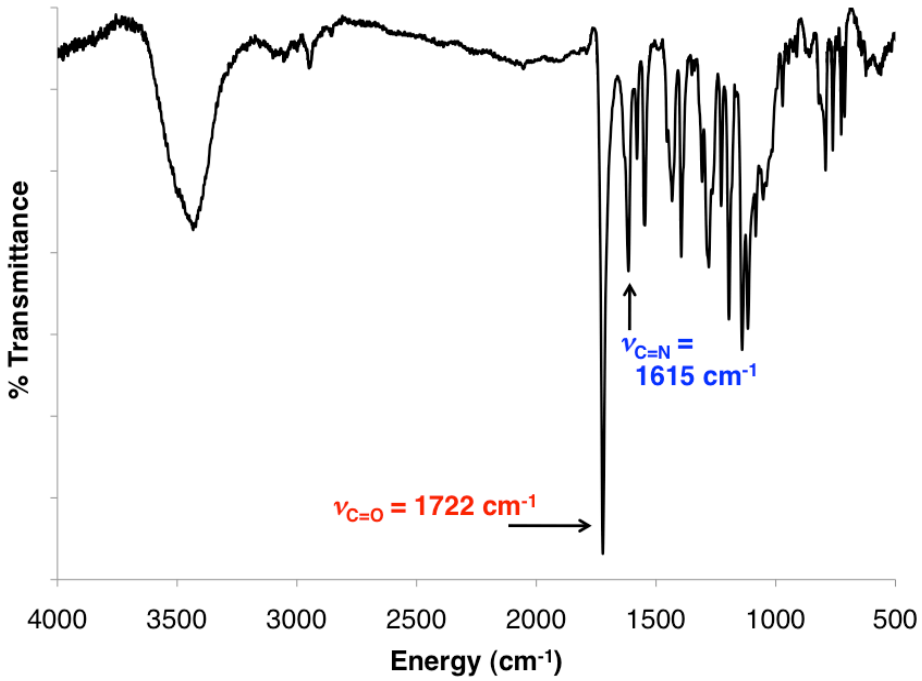

Figure A.4. Infrared spectrum of Ni(3-MOC-tsalen) (KBr pellet).

A.2 *N,N'*-bis(3-methoxycarbonylthiosalicylidene)propylenediaminonickel Ni(3-MOC-tsalpr) (4)

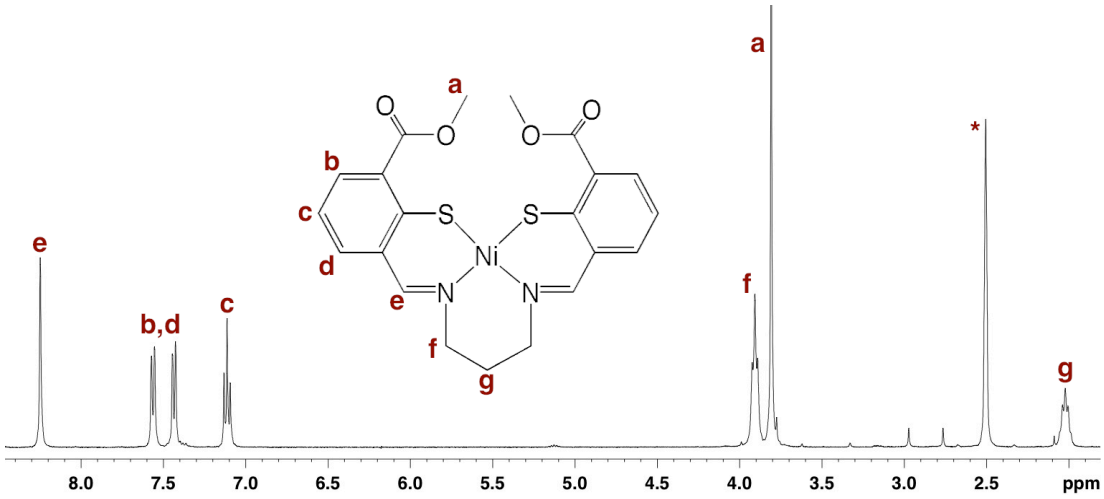

Figure A.5. ^{1}H NMR spectrum of Ni(3-MOC-tsalpr) in $(CD_3)_2SO$. * denotes residual solvent signals.

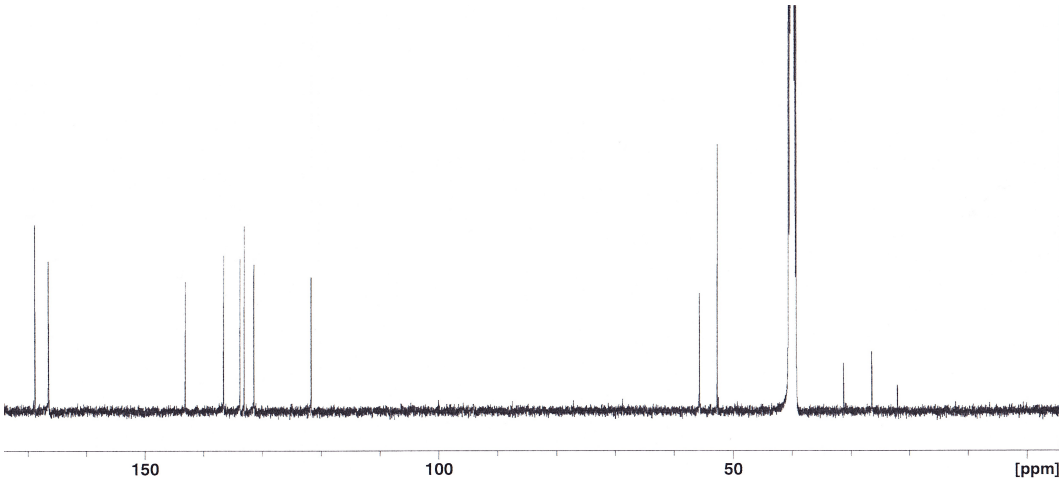

Figure A.6. $^{13}C\{^{1}H\}$ NMR spectrum of Ni(3-MOC-tsalpr) in $(CD_3)_2SO$.

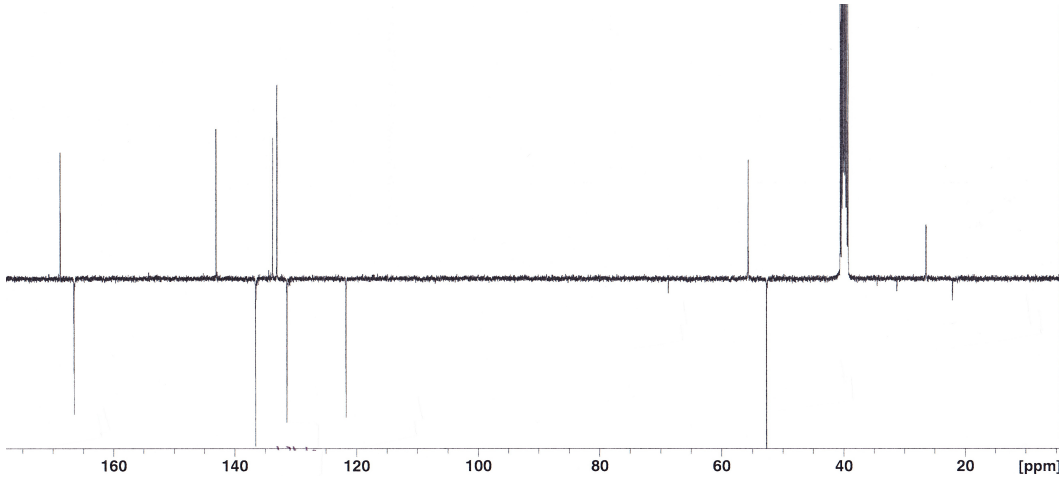

Figure A.7. ^{13}C APT NMR spectrum of Ni(3-MOC-tsalpr) in $(CD_3)_2SO$.

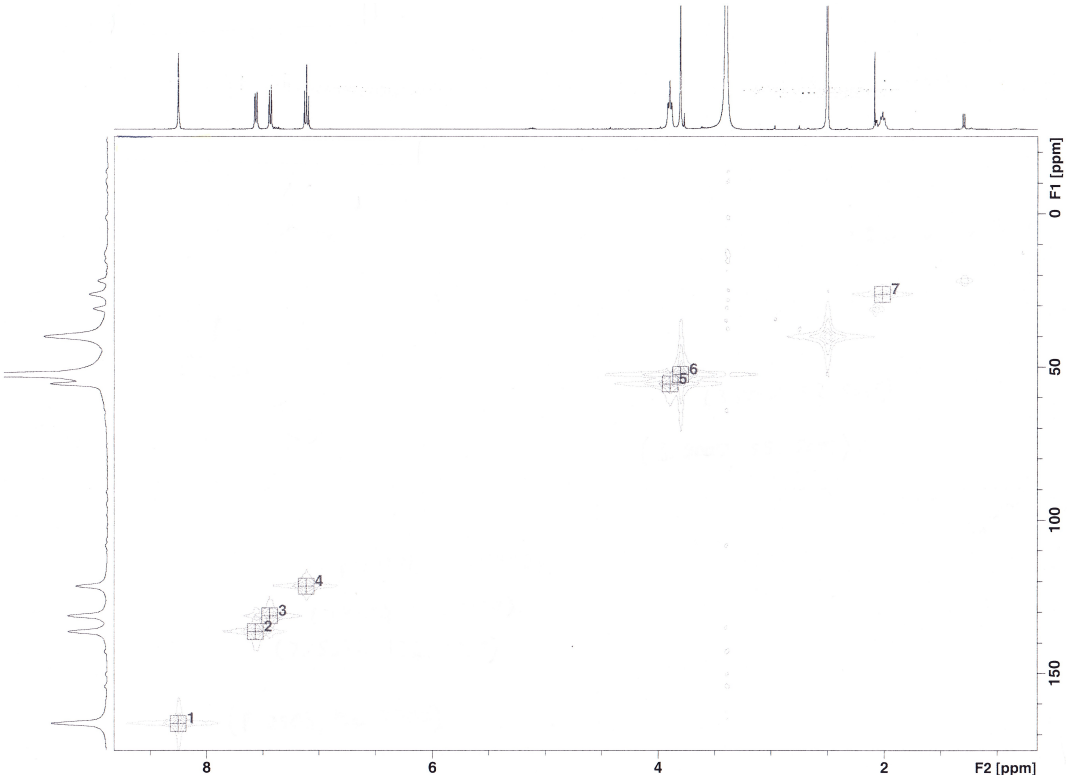

Figure A.8. Ni(3-MOC-tsalpr) ^{13}C-HMQC spectrum in $(CD_3)_2SO$.

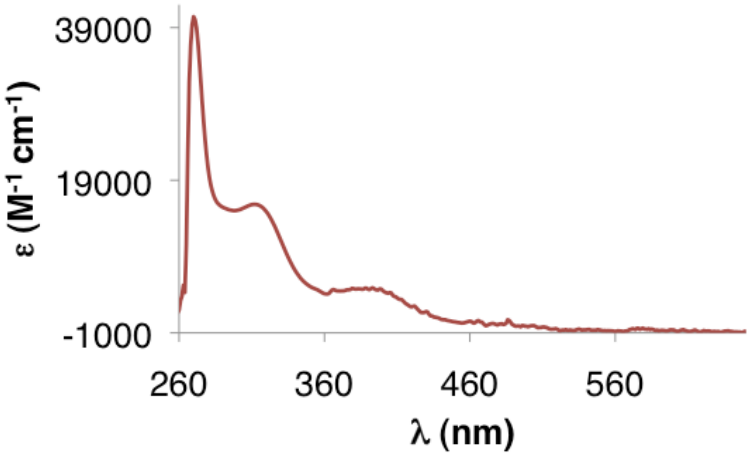

Figure A.9. Electronic absorption spectrum of Ni(3-MOC-tsalpr) in $(CH_3)_2SO$.

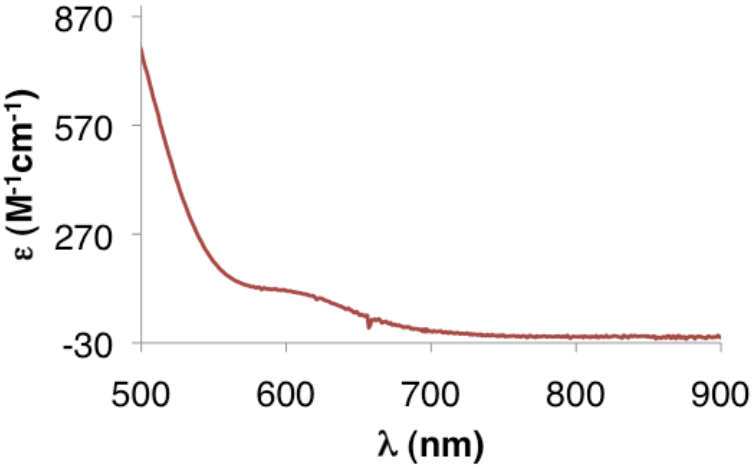

Figure A.10. Electronic absorption spectrum of Ni(3-MOC-tsalpr) in $(CH_3)_2SO$.

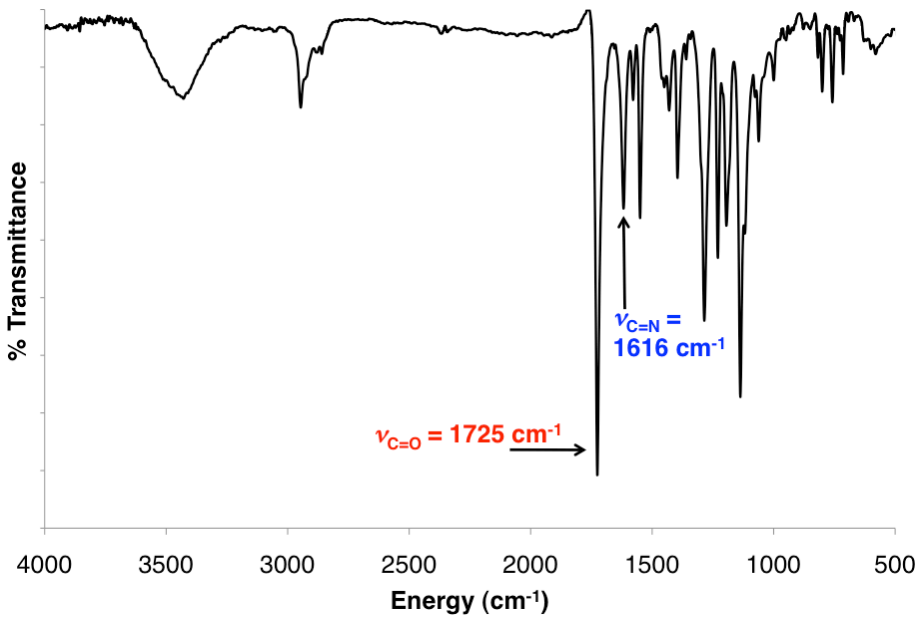

Figure A.11. Infrared spectrum of Ni(3-MOC-tsalpr) (KBr pellet).

A.3 *N,N'*-bis(3-methoxycarbonylthiosalicylidene)tetramethylenediaminonickel Ni(3-MOC-tsalbut) (5)

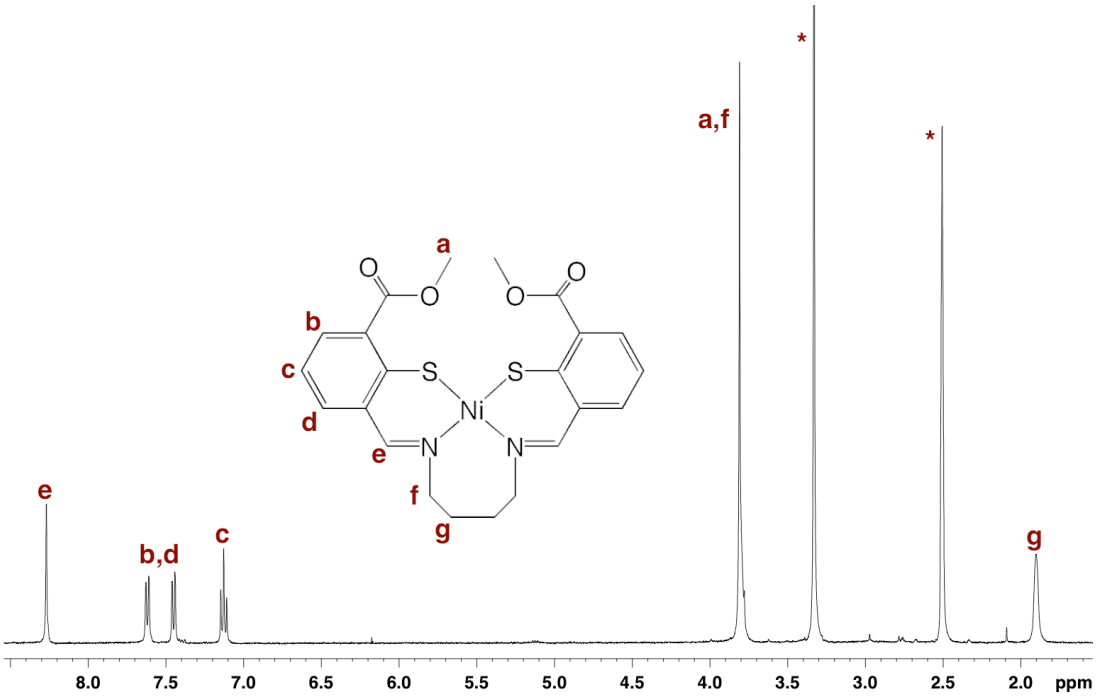

Figure A.12. ^{1}H NMR spectrum of Ni(3-MOC-tsalbut) in $(CD_3)_2SO$. * denotes residual solvent signals.

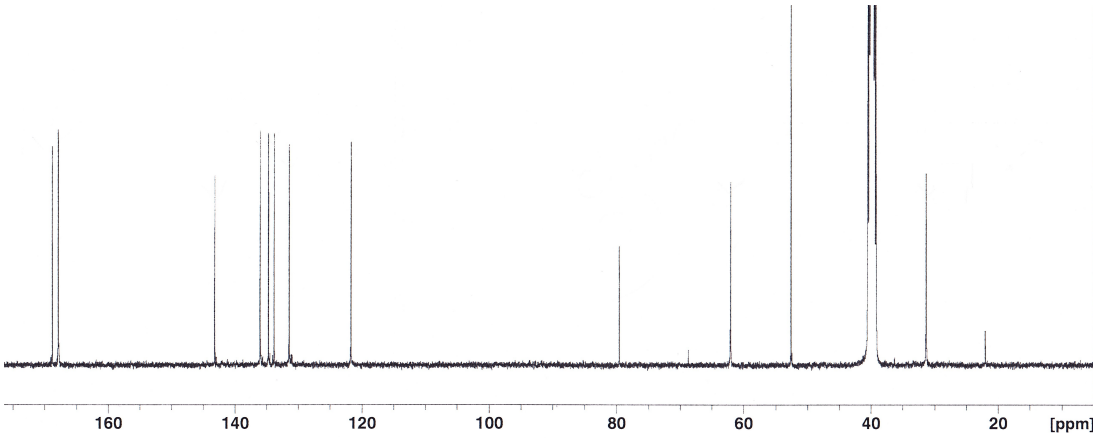

Figure A.13. $^{13}C\{^{1}H\}$ NMR spectrum of Ni(3-MOC-tsalbut) in $(CD_3)_2SO$.

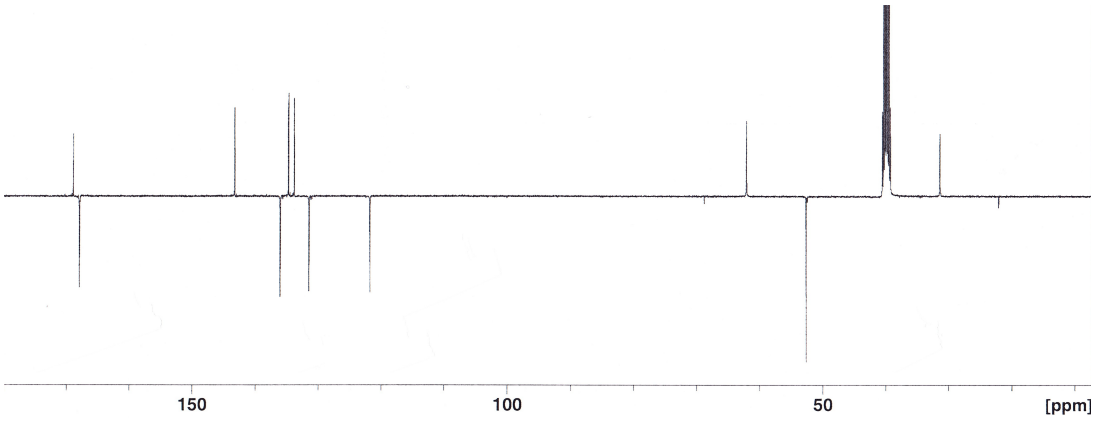

Figure A.14. ^{13}C APT NMR spectrum of Ni(3-MOC-tsalbut) in $(CD_3)_2SO$.

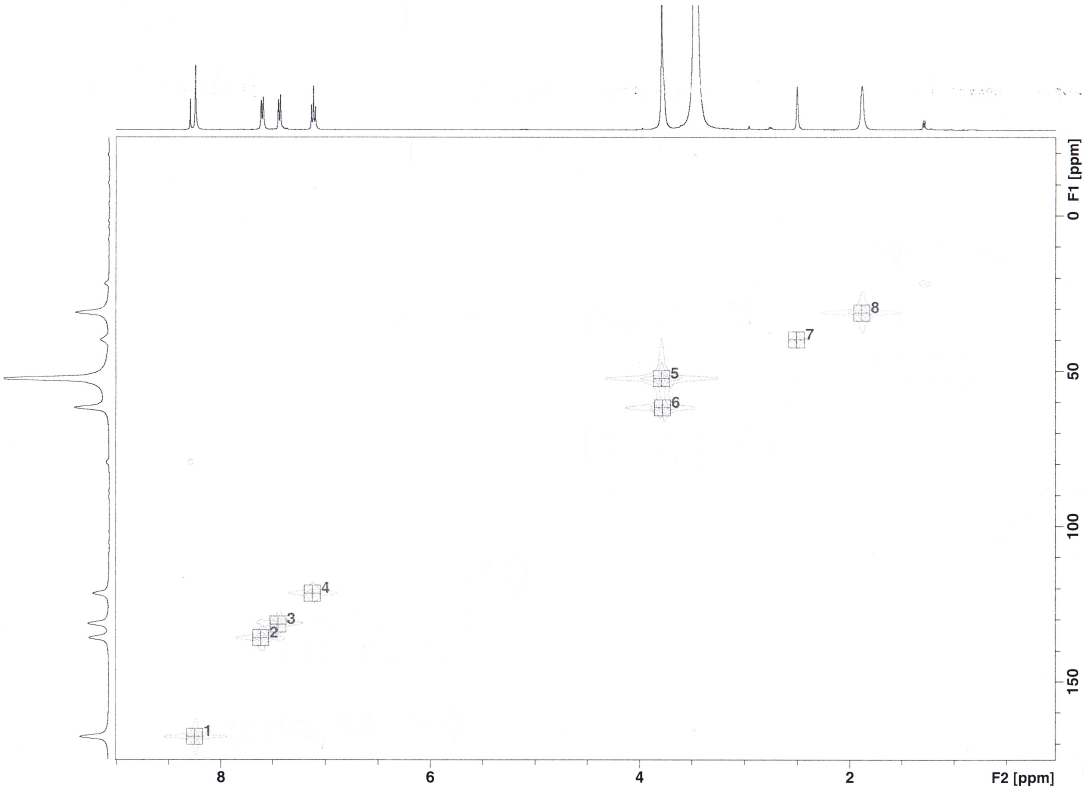

Figure A.15. Ni(3-MOC-tsalbut) ^{13}C-HMQC spectrum in $(CD_3)_2SO$.

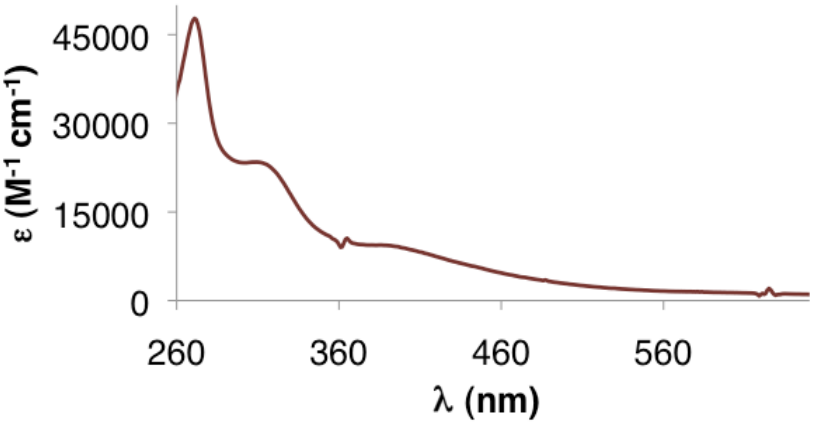

Figure A.16. Electronic absorption spectrum of Ni(3-MOC-tsalbut) in $(CH_3)_2SO$.

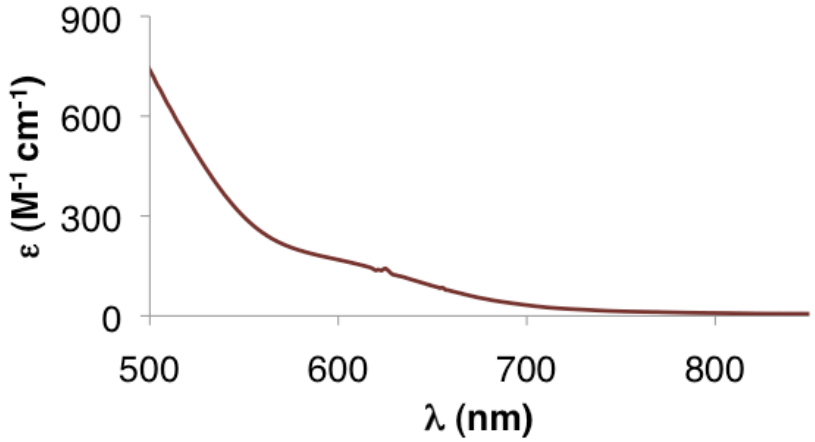

Figure A.17. Electronic absorption spectrum of Ni(3-MOC-tsalbut) in $(CH_3)_2SO$.

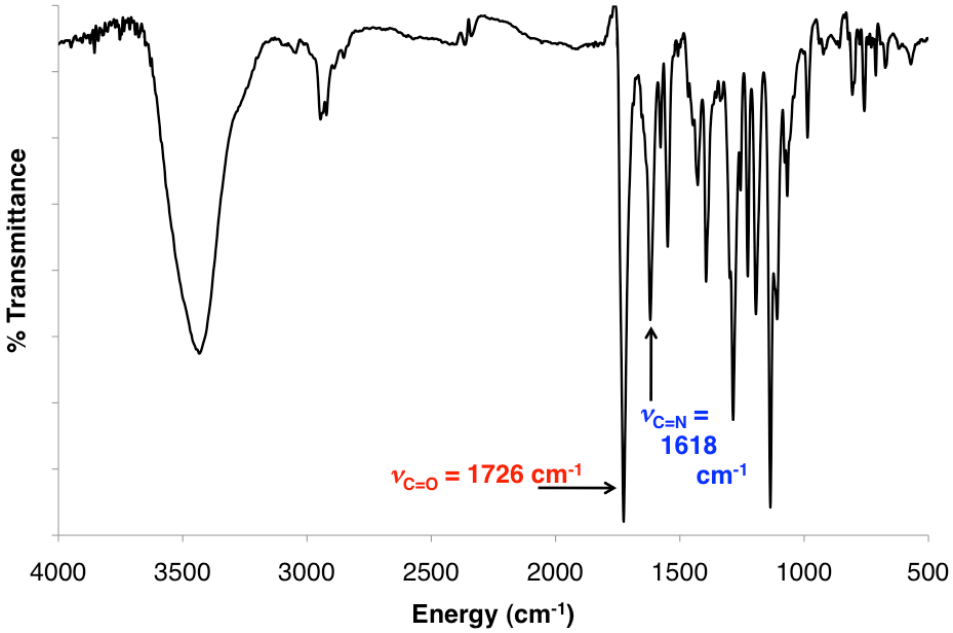

Figure A.18. Infrared spectrum of Ni(3-MOC-tsalbut) (KBr pellet).

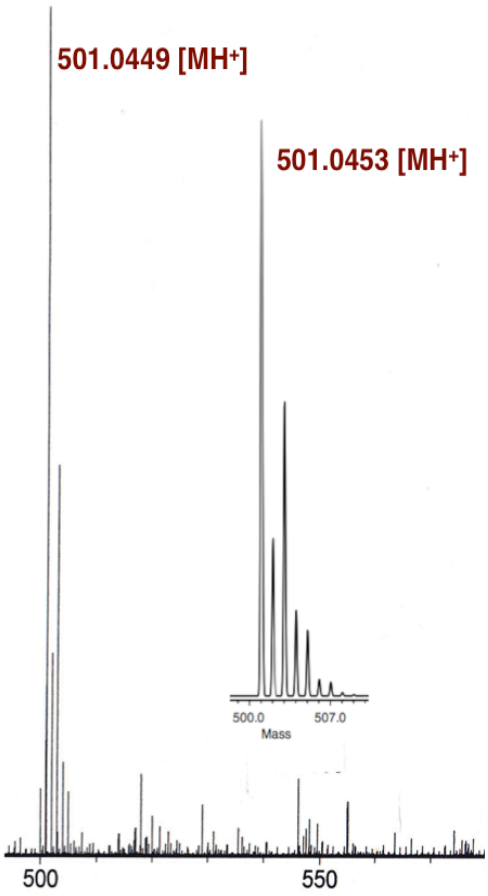

Figure A.19. High Resolution ESI mass spectrum of Ni(3-MOC-tsalbut). Inset shows theoretically calculated spectrum.

A.4 *N,N'*-bis(3-methoxycarbonylthiosalicylidene)-*o*-phenylenediaminonickel Ni(3-MOC-tsalphen) (6)

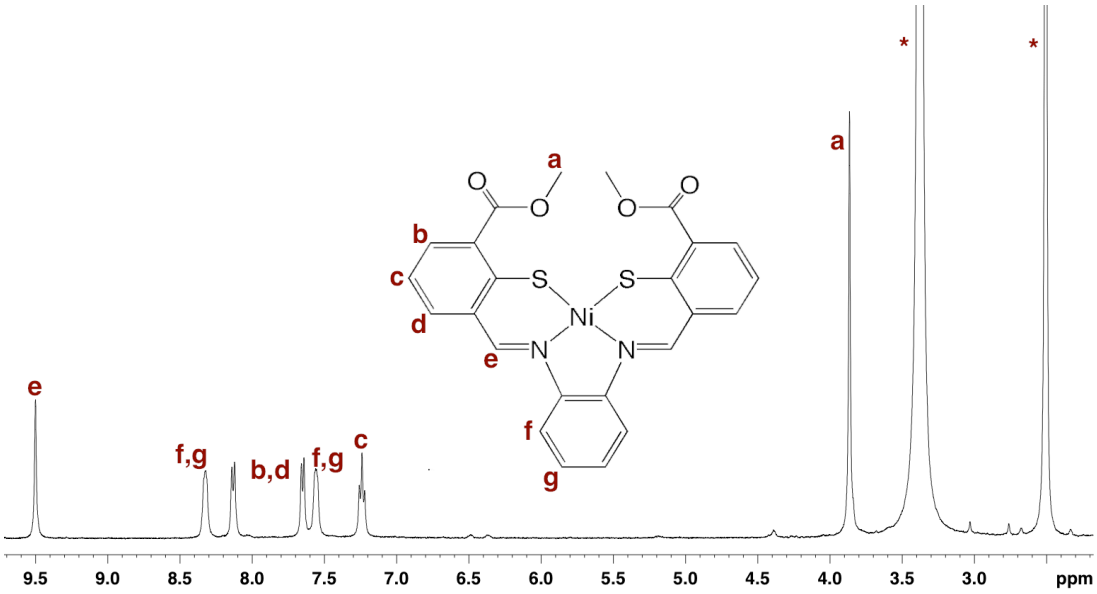

Figure A.20. ^{1}H NMR spectrum of Ni(3-MOC-tsalphen) in $(CD_3)_2SO$. * denotes residual solvent signals.

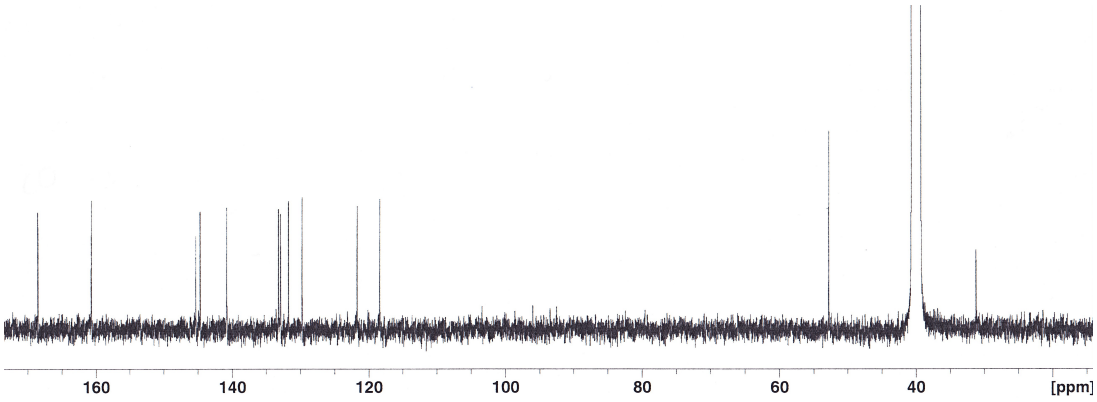

Figure A.21. $^{13}C\{^{1}H\}$ NMR spectrum of Ni(3-MOC-tsalphen) in $(CD_3)_2SO$.

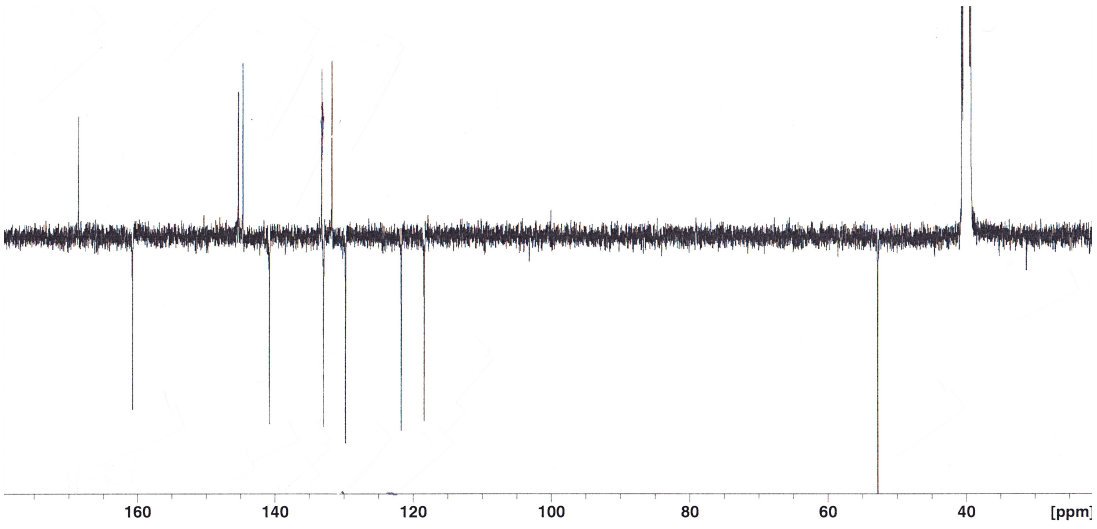

Figure A.22. ^{13}C APT NMR spectrum of Ni(3-MOC-tsalphen) in $(CD_3)_2SO$.

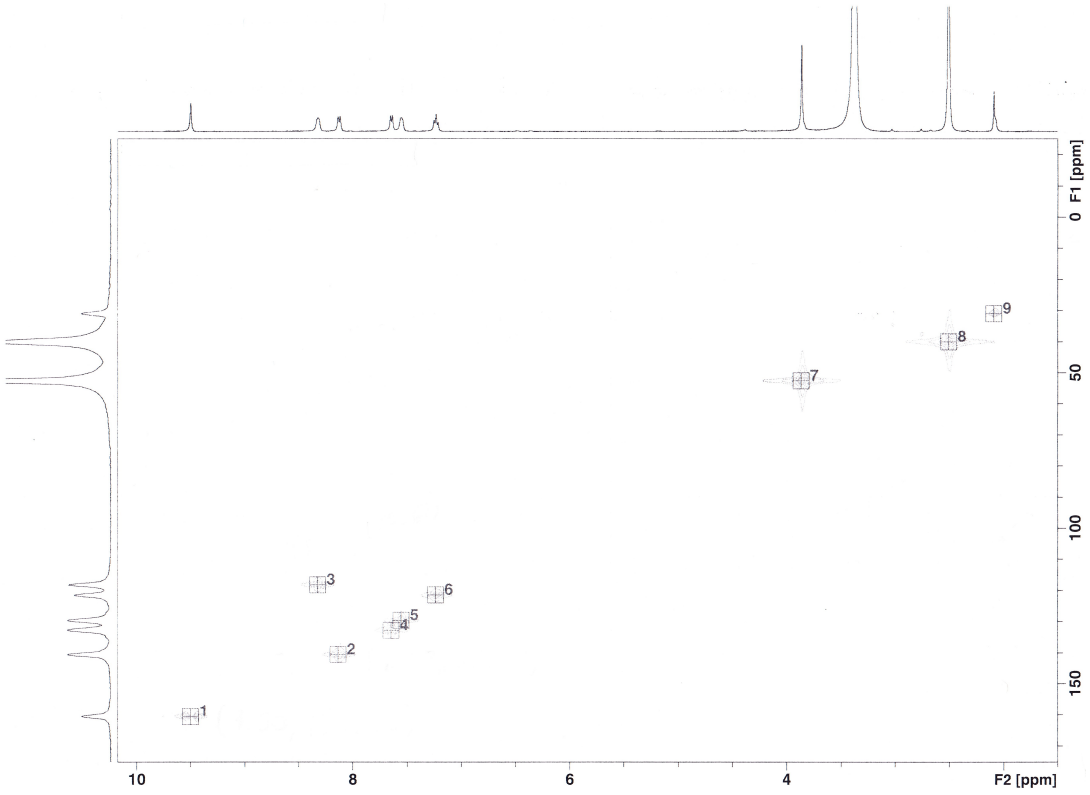

Figure A.23. Ni(3-MOC-tsalphen) ^{13}C-HMQC spectrum in $(CD_3)_2SO$.

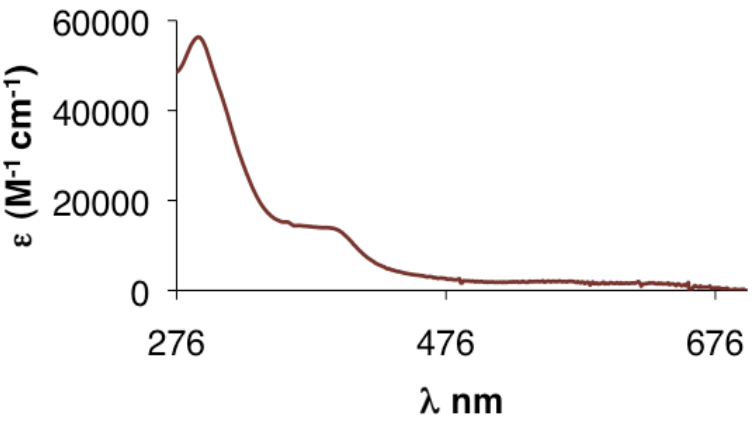

Figure A.24. Electronic absorption spectrum of Ni(3-MOC-tsalphen) in $(CH_3)_2SO$.

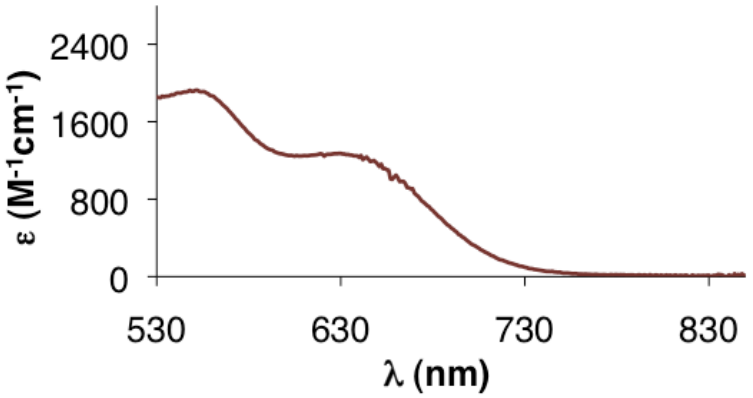

Figure A.25. Electronic absorption spectrum of Ni(3-MOC-tsalphen) in $(CH_3)_2SO$.

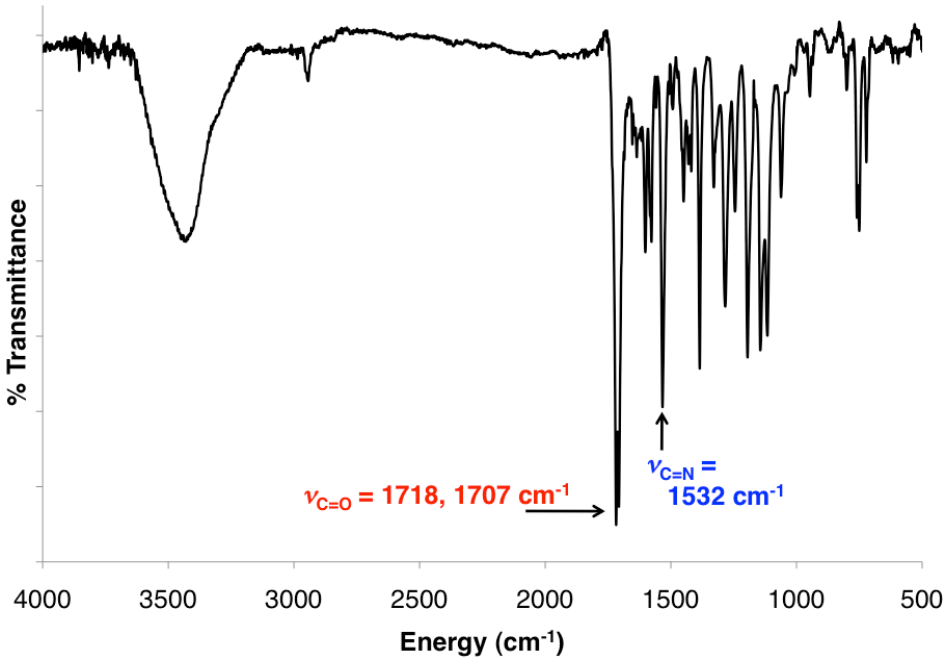

Figure A.26. Infrared spectrum of Ni(3-MOC-tsalphen) (KBr pellet).

A.5 *N,N'*-bis(3-methoxycarbonylthiosalicylidene)dimethyl-*o*-phenylenediaminonickel, Ni(3-MOC-tsaldimph) (7)

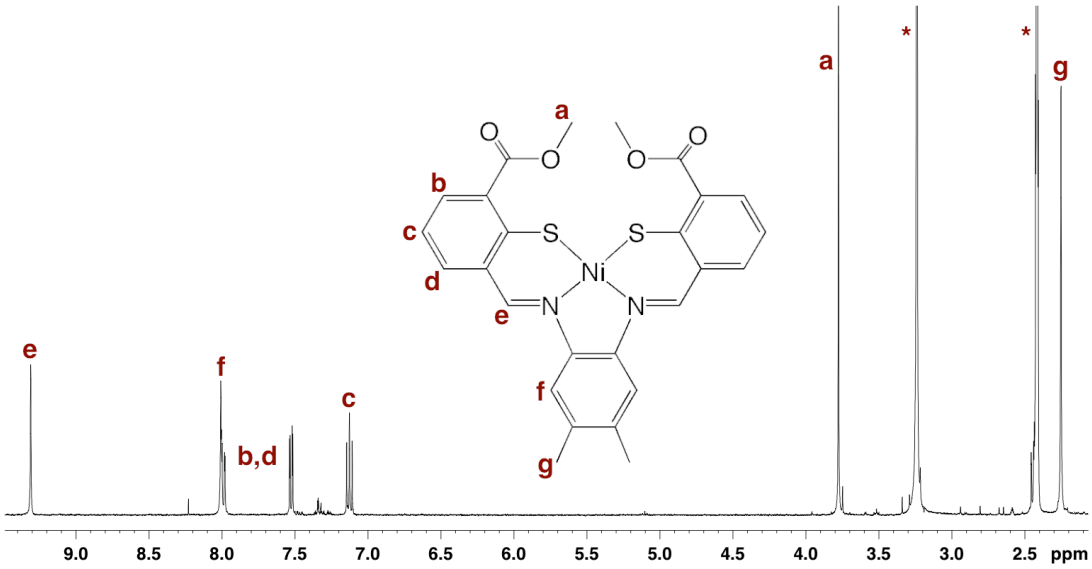

Figure A.27. ^{1}H NMR spectrum of Ni(3-MOC-tsaldimph) in $(CD_3)_2SO$. * denotes residual solvent signals.

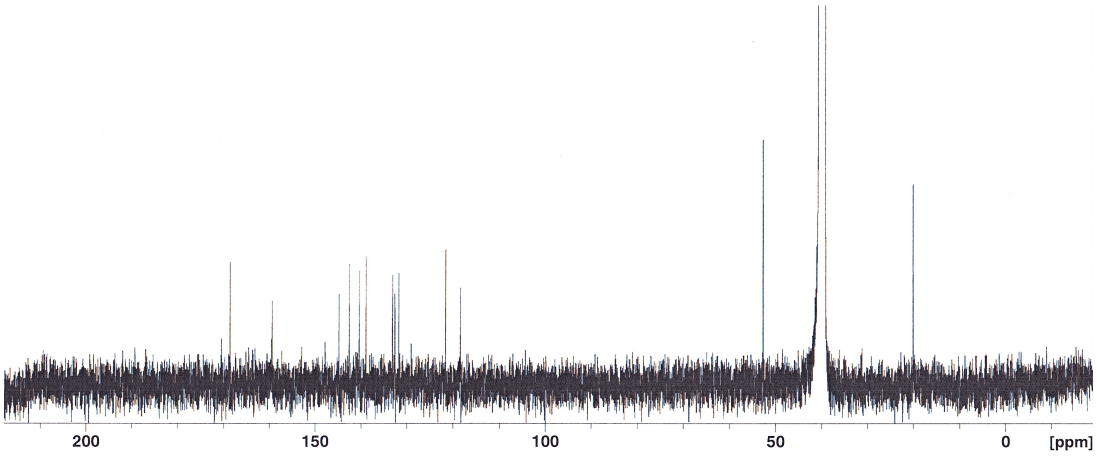

Figure A.28. $^{13}C\{^{1}H\}$ NMR spectrum of Ni(3-MOC-tsaldimph) in $(CD_3)_2SO$.

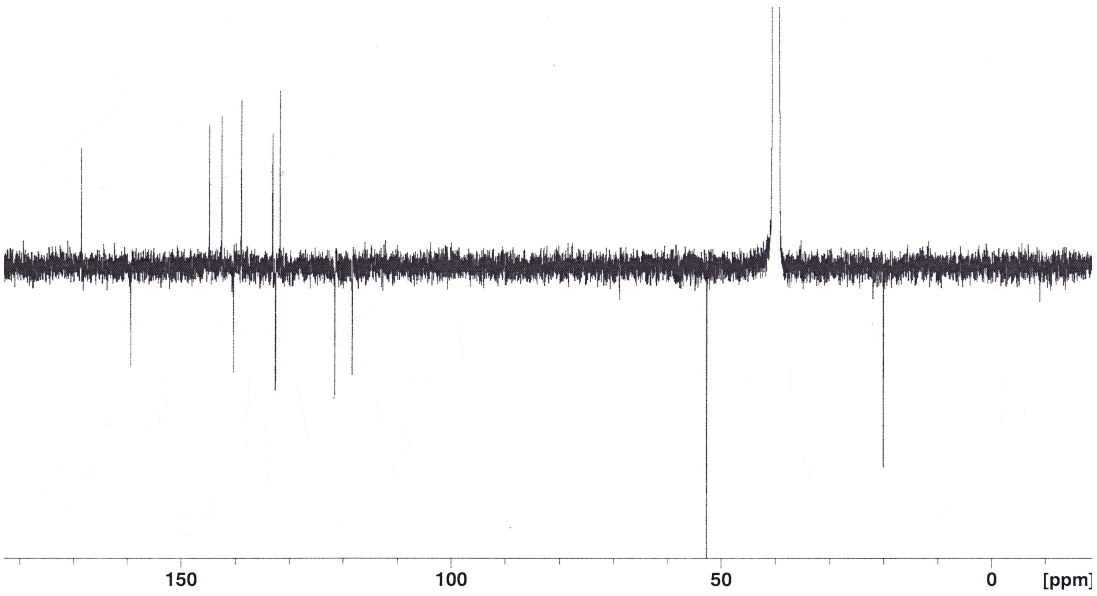

Figure A.29. ^{13}C APT NMR spectrum of Ni(3-MOC-tsaldimph) in $(CD_3)_2SO$.

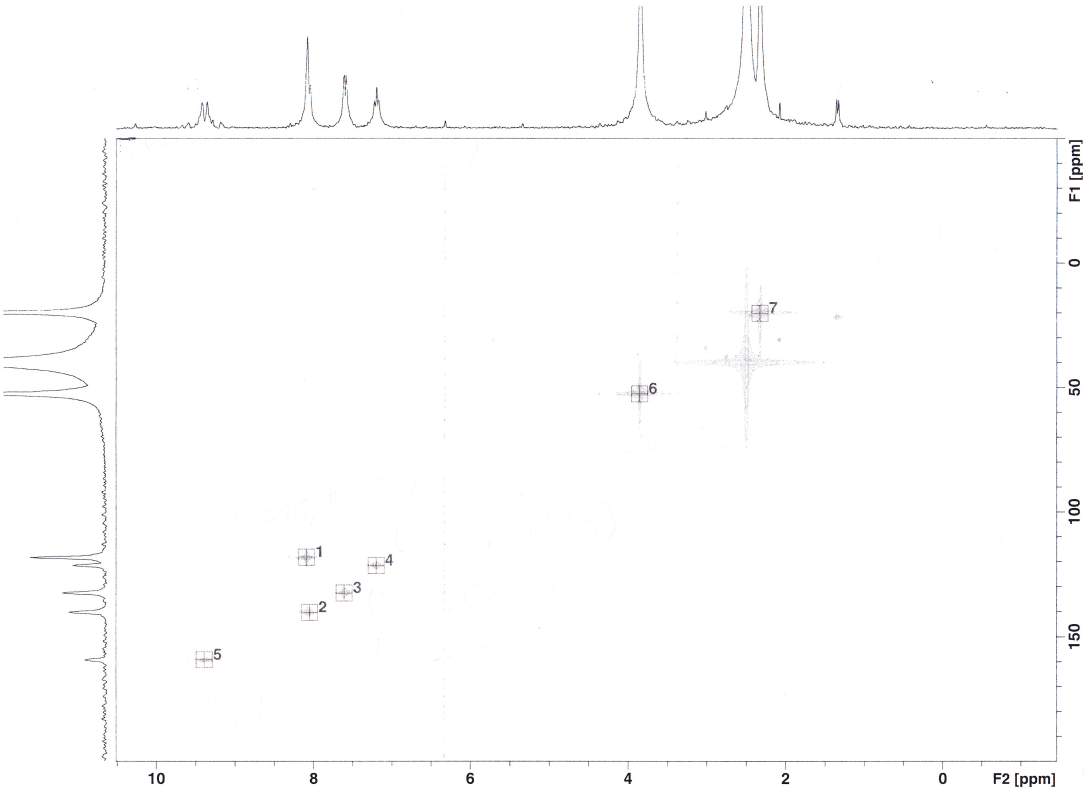

Figure A.30. Ni(3-MOC-tsaldimph) ^{13}C-HMQC spectrum in $(CD_3)_2SO$.

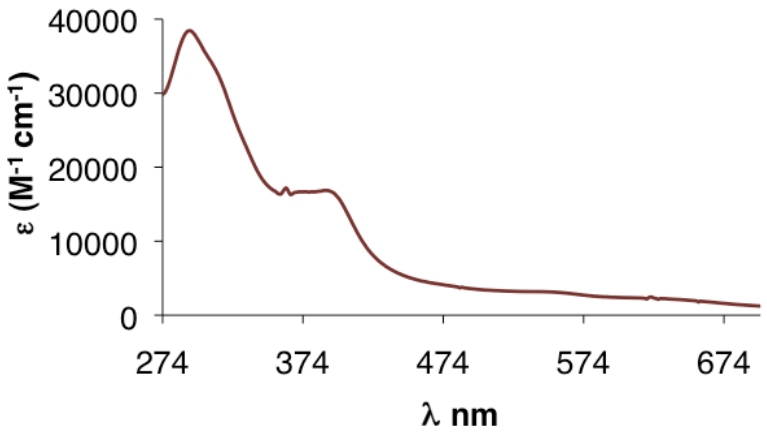

Figure A.31. Electronic absorption spectrum of Ni(3-MOC-tsaldimph) in $(CH_3)_2SO$.

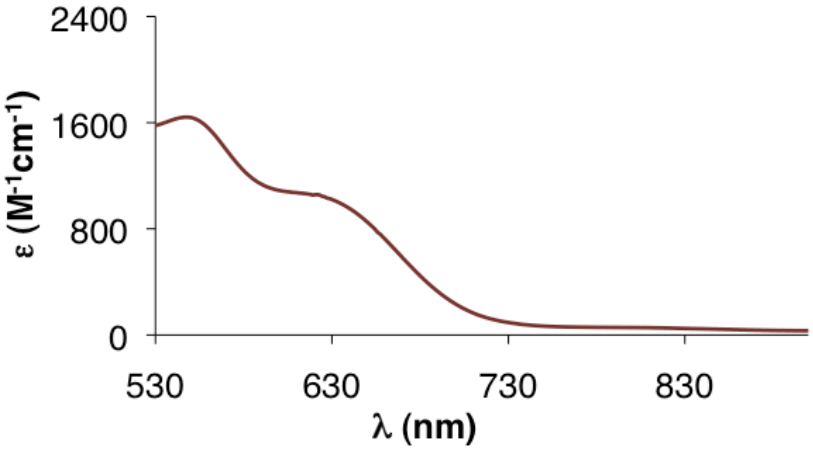

Figure A.32. Electronic absorption spectrum of Ni(3-MOC-tsaldimph) in $(CH_3)_2SO$.

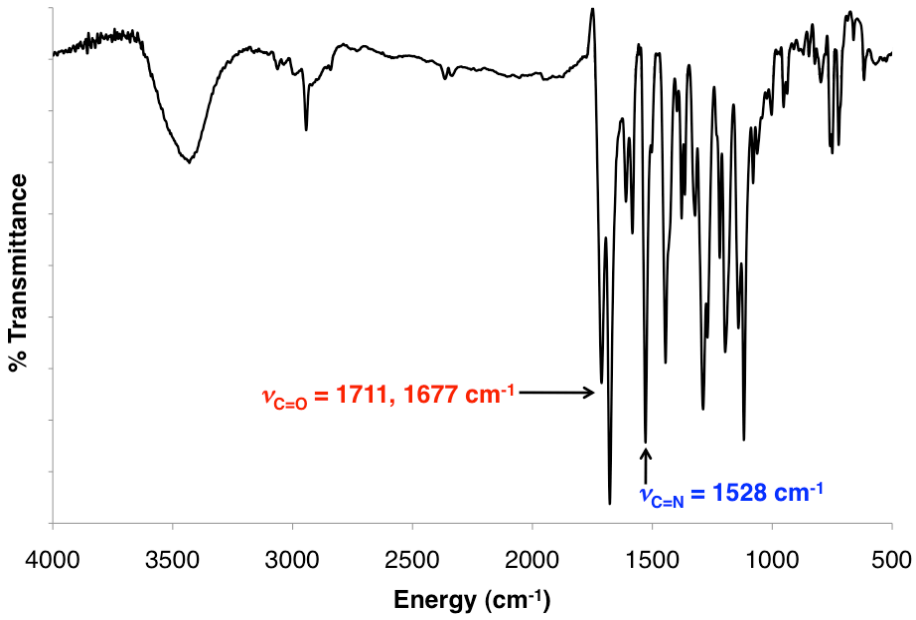

Figure A.33. Infrared spectrum of Ni(3-MOC-tsaldimph) (KBr pellet).

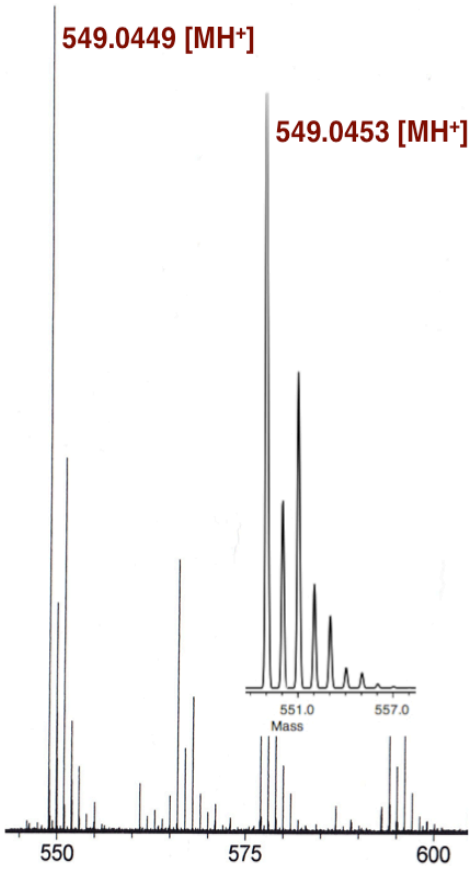

Figure A.34. High Resolution ESI mass spectrum of Ni(3-MOC-tsaldimph). Inset shows theoretically calculated spectrum.

Appendix B

ADDITIONAL SPECTROSCOPIC CHARACTERIZATION OF THE PHOSPHINOTHIOETHER COMPLEXES DISCUSSED IN CHAPTER 3

B.1 Bis[2-(isopropylthio)ethyl]phenylphosphine, $S^{iPr}PS^{iPr}$, $PhP(CH_2CH_2SPr^i)_2$ (1)

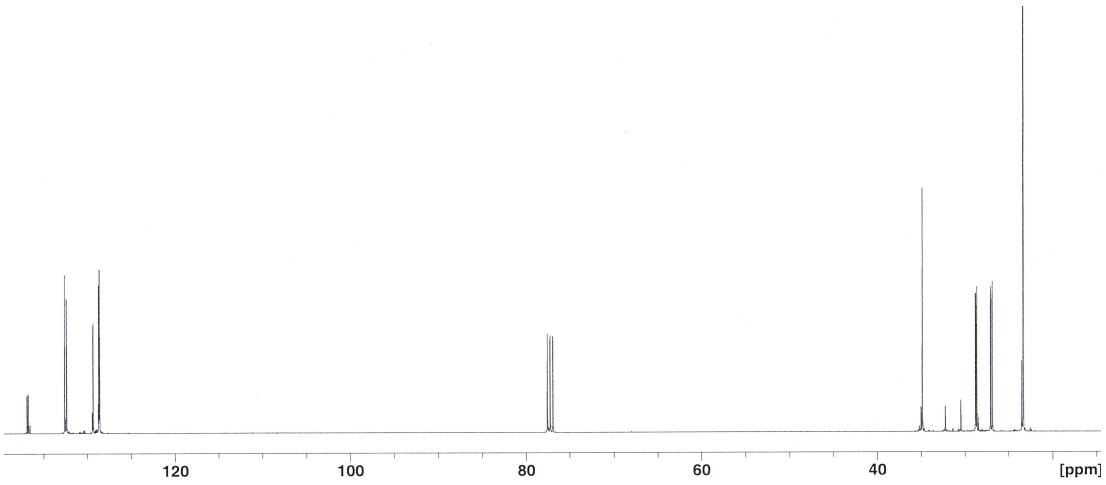

Figure B.1. $^{13}C\{^1H\}$ NMR spectrum of $S^{iPr}PS^{iPr}$ in $CDCl_3$.

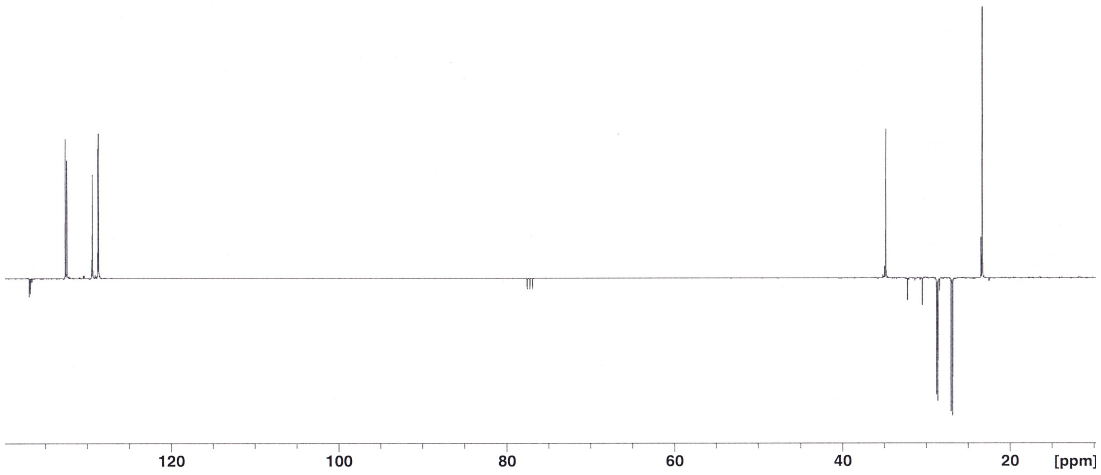

Figure B.2. ^{13}C APT NMR spectrum of $S^{i\text{Pr}}PS^{i\text{Pr}}$ in $CDCl_3$.

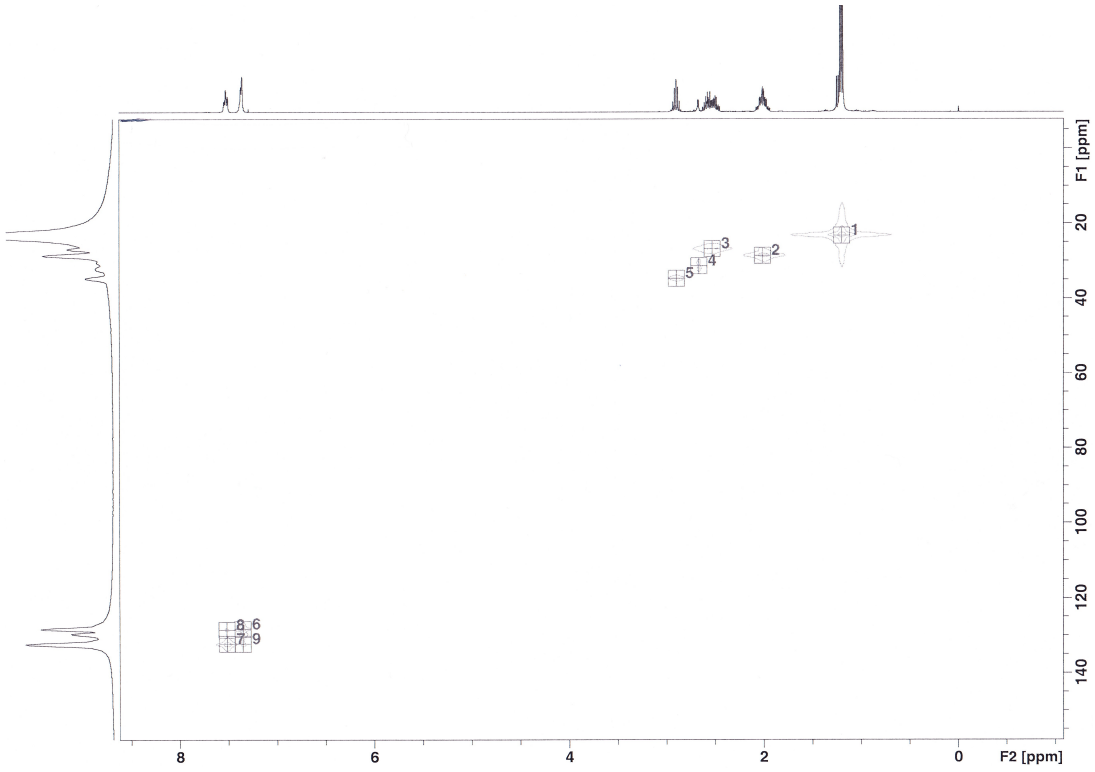

Figure B.3. S$^{i\text{Pr}}$PS$^{i\text{Pr}}$ ^{13}C-HMQC in $CDCl_3$.

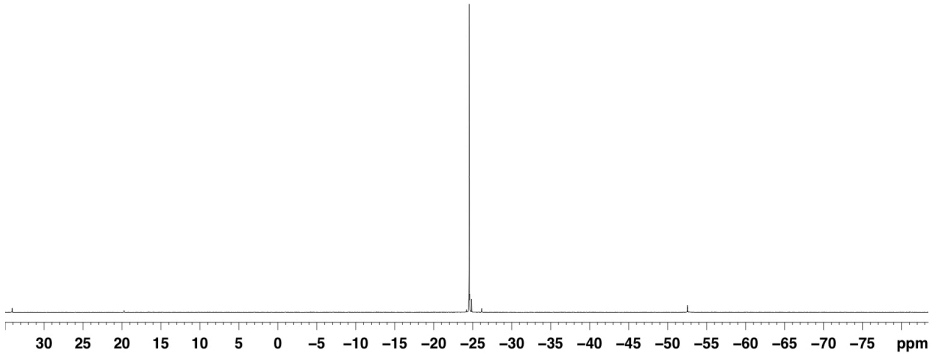

Figure B.4. $^{31}P\{^{1}H\}$ NMR spectrum of $S^{iPr}PS^{iPr}$ in $CDCl_3$.

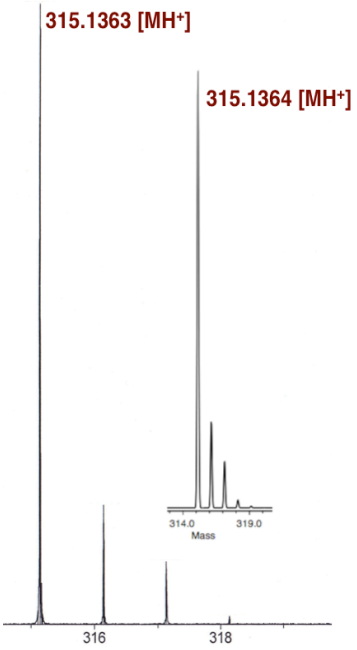

Figure B.5. High Resolution ESI mass spectrum of $S^{iPr}PS^{iPr}$. Inset shows theoretically calculated spectrum.

B.2 (κ^2-S$^{i\mathrm{Pr}}$PS$^{i\mathrm{Pr}}$)Ni(PPh$_3$)$_2$ (2)

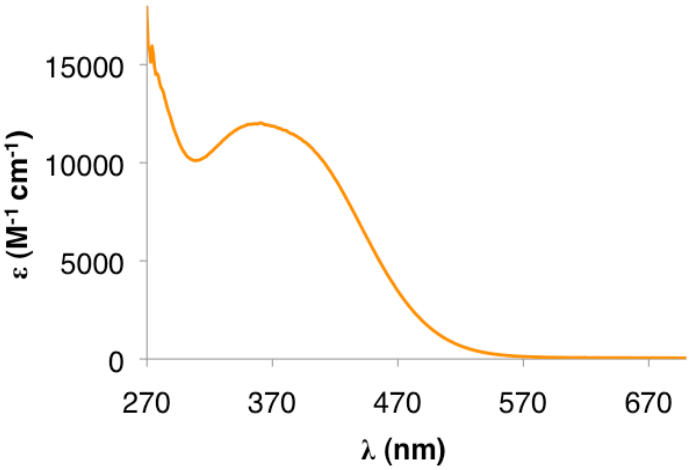

Figure B.6. Electronic absorption spectrum of (κ^2-S$^{i\mathrm{Pr}}$PS$^{i\mathrm{Pr}}$)Ni(PPh$_3$)$_2$ in tetrahydrofuran.

B.3 (κ^2-S$^{i\mathrm{Pr}}$PS)$_2$Ni (3)

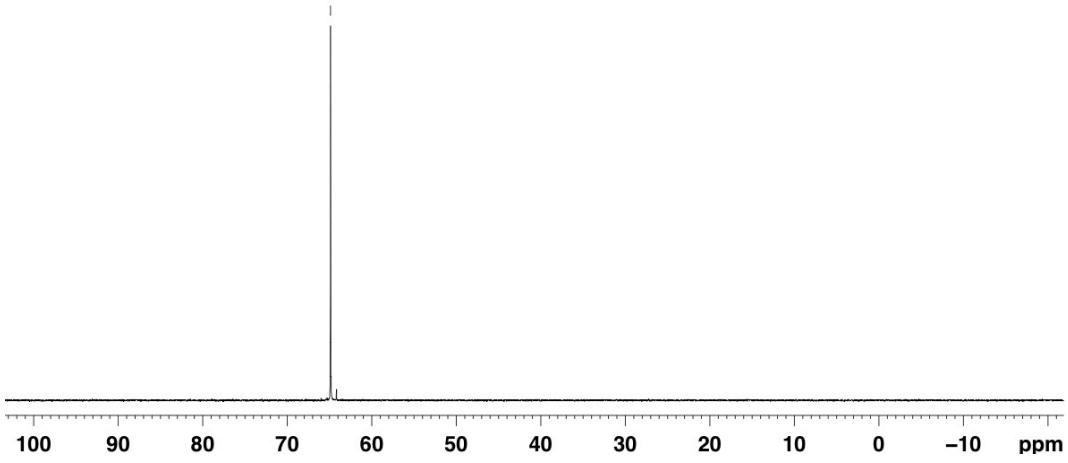

Figure B.7. ^{31}P{^{1}H} NMR spectrum of *trans*-(κ^2-S$^{i\mathrm{Pr}}$PS)$_2$Ni in C_6D_6.

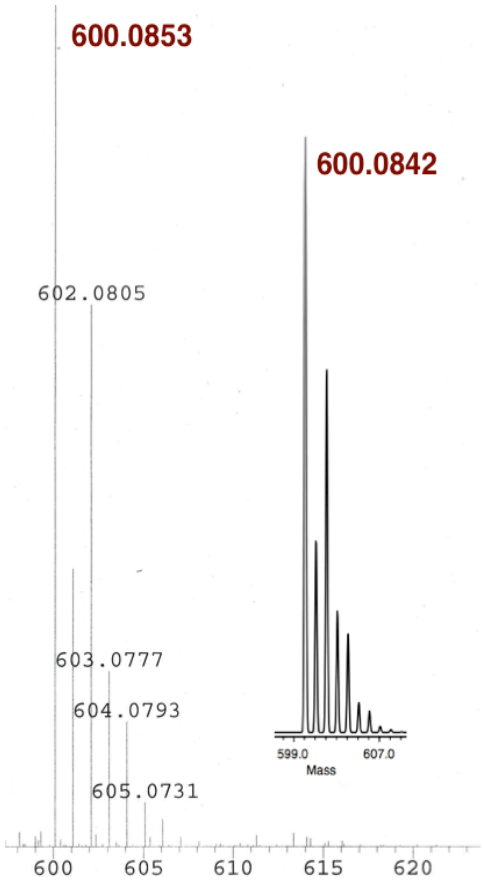

Figure B.8. High Resolution LIFDI mass spectrum of $(\kappa^2\text{-}S^{i\text{Pr}}PS)_2Ni$. Inset shows theoretically calculated spectrum.

B.4 Reaction of (κ^2-$S^{iPr}PS^{iPr}$)$Ni(PPh_3)_2$ with $RCo(dmgBF_2)_2py$, R = CH_3 or CD_3

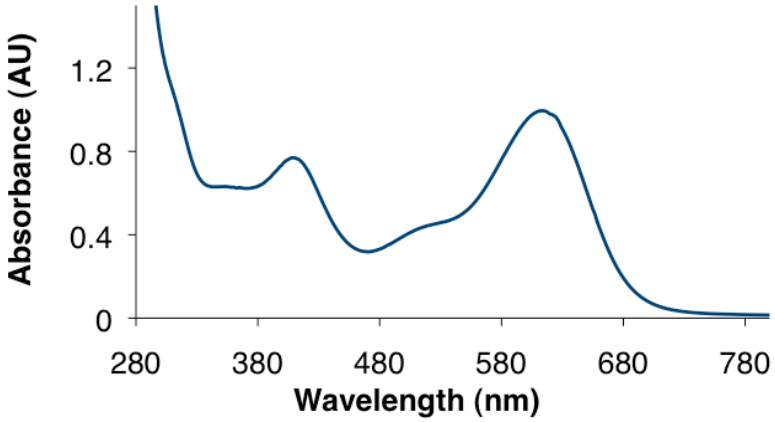

Figure B.9. The electronic spectrum of a mixture of (κ^2-$S^{iPr}PS^{iPr}$)$Ni(PPh_3)_2$ and $CH_3Co(dmgBF_2)_2py$ in tetrahydrofuran after ~30 mins. The amount of Co^{1+} formed was approximately 95% based on the concentration calculated for ε_{615} = 10 000 M^{-1} cm^{-1}.[99]

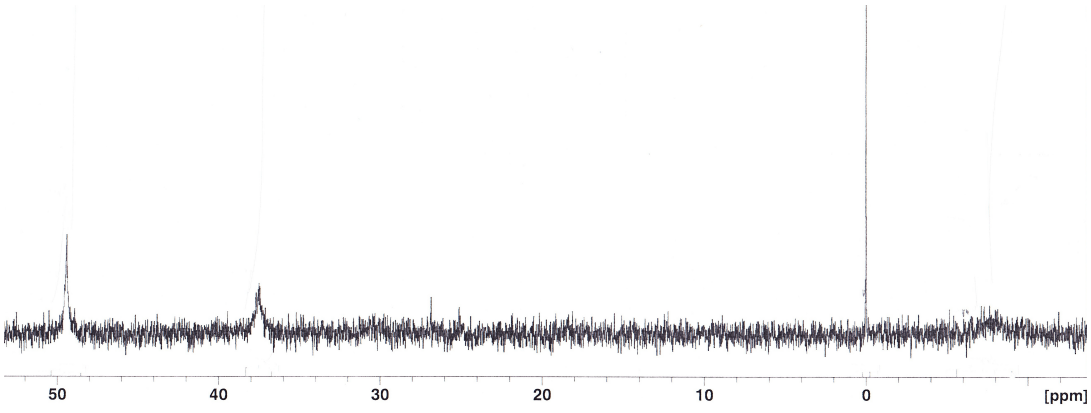

Figure B.10. $^{31}P\{^1H\}$ NMR spectrum of [(κ^2-$S^{iPr}PS^{iPr}$)$Ni(PPh_3)(CH_3)$][$Co(dmgBF_2)_2PPh_3$] in $C_7D_8/(CD_3)_2CO$. Referenced to internal standard H_3PO_4 in $(CD_3)_2CO$.

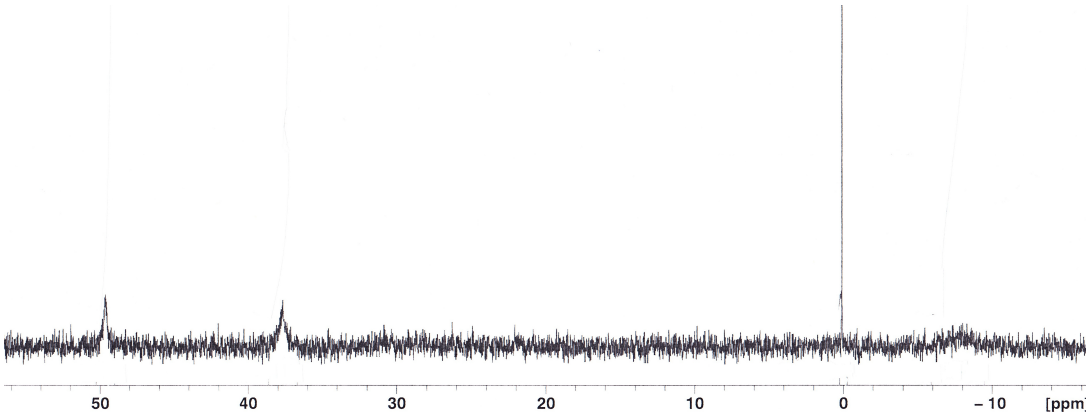

Figure B.11. $^{31}P\{^{1}H\}$ NMR spectrum of [(κ^2-$S^{iPr}PS^{iPr}$)Ni(PPh_3)(CD_3)][Co($dmgBF_2$)$_2PPh_3$] in C_7D_8/$(CD_3)_2CO$. Referenced to internal standard H_3PO_4 in $(CD_3)_2CO$.

B.5 Reaction of (κ^2-$S^{iPr}PS^{iPr}$)Ni(PPh_3)$_2$ with neopentylCo($dmgBF_2$)$_2$py

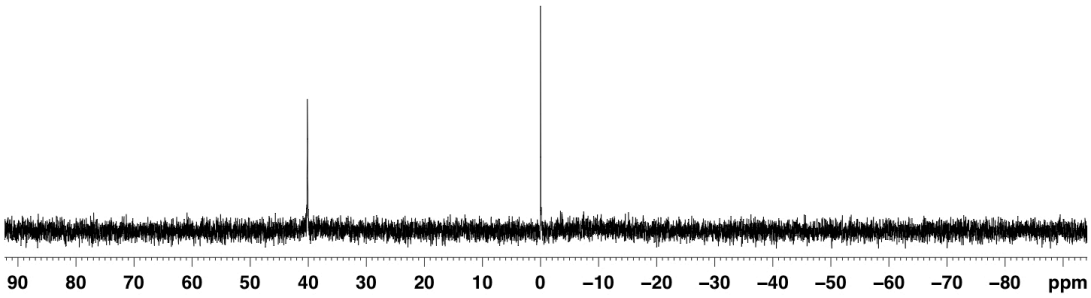

Figure B.12. $^{31}P\{^{1}H\}$ NMR spectrum of [($S^{iPr}PS^{iPr}$)Ni(neopentyl)][Co($dmgBF_2$)$_2$py] in C_7D_8/$(CD_3)_2CO$. Referenced to internal standard H_3PO_4 in $(CD_3)_2CO$.

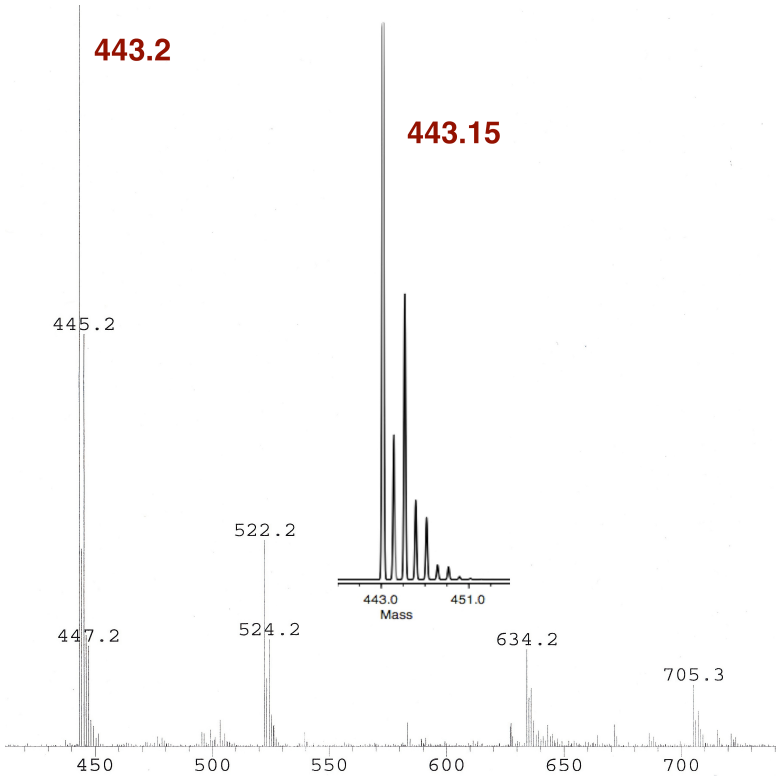

Figure B.13. Low Resolution LIFDI mass spectrum of [($S^{iPr}PS^{iPr}$)Ni(neopentyl)]. Inset shows theoretically calculated spectrum.

B.6 Kinetics

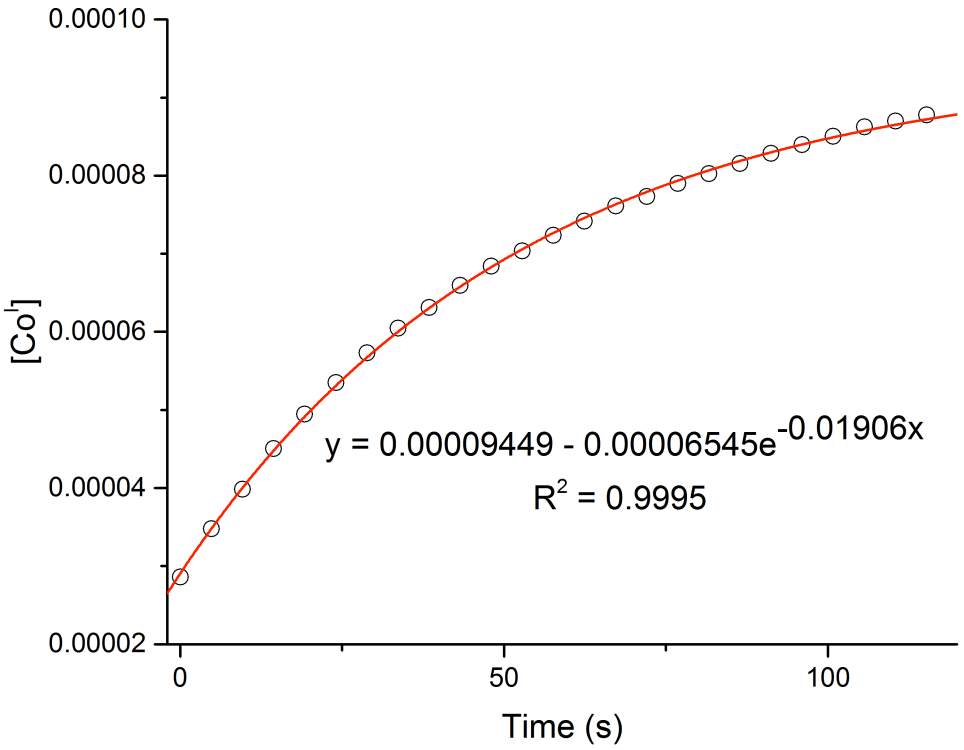

Figure B.14. Representative kinetic trace for the reaction of (κ^2-S$^{i\text{Pr}}$PS$^{i\text{Pr}}$)Ni(PPh$_3$)$_2$ with CH$_3$Co(dmgBF$_2$)$_2$py over three half lives. The reaction was monitored by following the growth of [Co(dmgBF$_2$)$_2$PPh$_3$]$^-$ at λ_{max} = 615 nm over time.

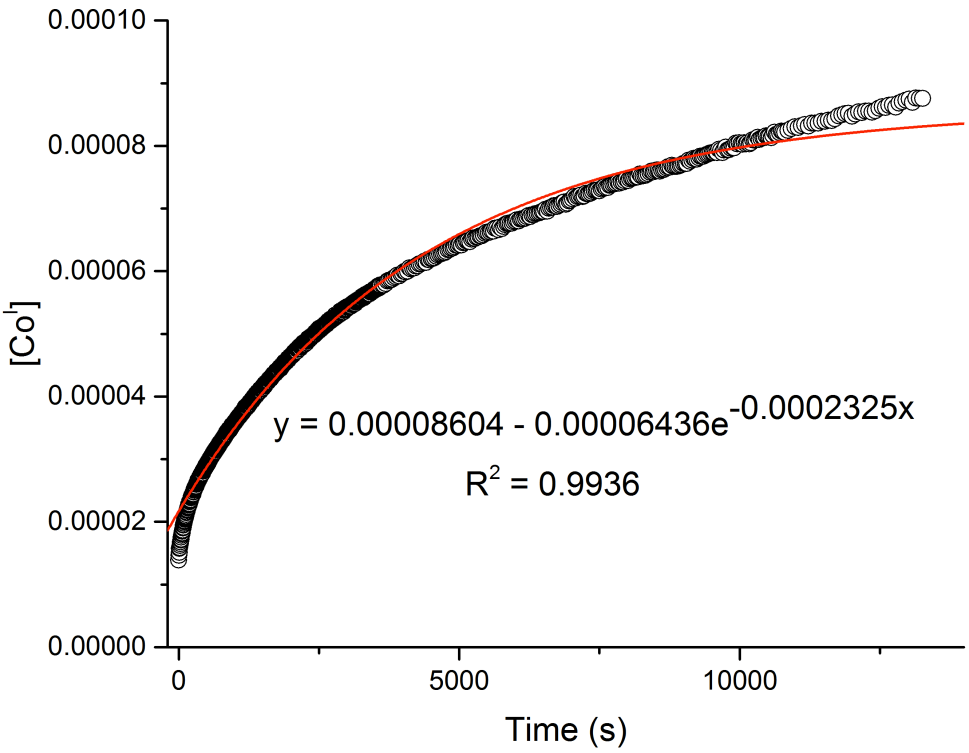

Figure B.15. Representative kinetic trace for the reaction of (κ^2-S$^{i\text{Pr}}$PS$^{i\text{Pr}}$)Ni(PPh_3)$_2$ with $CH_3CH_2Co(dmgBF_2)_2py$ over three half lives. The reaction was monitored by following the growth of $[Co(dmgBF_2)_2PPh_3]^-$ at λ_{max} = 615 nm over time.

Appendix C

PERMISSION LICENSES

ELSEVIER LICENSE
TERMS AND CONDITIONS

Nov 05, 2014

This is a License Agreement between Megan P Shalaida ("You") and Elsevier ("Elsevier") provided by Copyright Clearance Center ("CCC"). The license consists of your order details, the terms and conditions provided by Elsevier, and the payment terms and conditions.

All payments must be made in full to CCC. For payment instructions, please see information listed at the bottom of this form.

Supplier	Elsevier Limited The Boulevard,Langford Lane Kidlington,Oxford,OX5 1GB,UK
Registered Company Number	1982084
Customer name	Megan P Shalaida
Customer address	1443 White Spruce Drive TOMS RIVER, NJ 08753
License number	3502720728518
License date	Nov 05, 2014
Licensed content publisher	Elsevier
Licensed content publication	Current Opinion in Chemical Biology
Licensed content title	A role for nickel–iron cofactors in biological carbon monoxide and carbon dioxide utilization
Licensed content author	Yan Kung,Catherine L Drennan
Licensed content date	April 2011
Licensed content volume number	15
Licensed content issue number	2
Number of pages	8
Start Page	276
End Page	283
Type of Use	reuse in a thesis/dissertation
Portion	figures/tables/illustrations
Number of figures/tables/illustrations	1
Format	both print and electronic
Are you the author of this Elsevier article?	No
Will you be translating?	No
Title of your thesis/dissertation	Synthesis and Reactivity of Acetyl Coenzyme A Synthase Active Site Analogues
Expected completion date	Dec 2014
Estimated size (number of pages)	218

Elsevier VAT number	GB 494 6272 12
Price	0.00 USD
VAT/Local Sales Tax	0.00 USD / 0.00 GBP
Total	**0.00 USD**
Terms and Conditions	

INTRODUCTION

1. The publisher for this copyrighted material is Elsevier. By clicking "accept" in connection with completing this licensing transaction, you agree that the following terms and conditions apply to this transaction (along with the Billing and Payment terms and conditions established by Copyright Clearance Center, Inc. ("CCC"), at the time that you opened your Rightslink account and that are available at any time at http://myaccount.copyright.com).

GENERAL TERMS

2. Elsevier hereby grants you permission to reproduce the aforementioned material subject to the terms and conditions indicated.
3. Acknowledgement: If any part of the material to be used (for example, figures) has appeared in our publication with credit or acknowledgement to another source, permission must also be sought from that source. If such permission is not obtained then that material may not be included in your publication/copies. Suitable acknowledgement to the source must be made, either as a footnote or in a reference list at the end of your publication, as follows:
"Reprinted from Publication title, Vol /edition number, Author(s), Title of article / title of chapter, Pages No., Copyright (Year), with permission from Elsevier [OR APPLICABLE SOCIETY COPYRIGHT OWNER]." Also Lancet special credit - "Reprinted from The Lancet, Vol. number, Author(s), Title of article, Pages No., Copyright (Year), with permission from Elsevier."
4. Reproduction of this material is confined to the purpose and/or media for which permission is hereby given.
5. Altering/Modifying Material: Not Permitted. However figures and illustrations may be altered/adapted minimally to serve your work. Any other abbreviations, additions, deletions and/or any other alterations shall be made only with prior written authorization of Elsevier Ltd. (Please contact Elsevier at permissions@elsevier.com)
6. If the permission fee for the requested use of our material is waived in this instance, please be advised that your future requests for Elsevier materials may attract a fee.
7. Reservation of Rights: Publisher reserves all rights not specifically granted in the combination of (i) the license details provided by you and accepted in the course of this licensing transaction, (ii) these terms and conditions and (iii) CCC's Billing and Payment terms and conditions.
8. License Contingent Upon Payment: While you may exercise the rights licensed immediately upon issuance of the license at the end of the licensing process for the transaction, provided that you have disclosed complete and accurate details of your proposed use, no license is finally effective unless and until full payment is received from you (either by publisher or by CCC) as provided in CCC's Billing and Payment terms and conditions. If full payment is not received on a timely basis, then any license preliminarily granted shall be deemed automatically revoked and shall be void as if never granted. Further, in the event that you breach any of these terms and conditions or any of CCC's Billing and Payment terms and conditions, the license is automatically revoked and shall be void as if never granted. Use of materials as described in a revoked license, as well as any use of the materials beyond the scope of an unrevoked license, may constitute copyright infringement and publisher reserves the right to take any and all action to protect its copyright in the materials.
9. Warranties: Publisher makes no representations or warranties with respect to the licensed material.
10. Indemnity: You hereby indemnify and agree to hold harmless publisher and CCC, and their respective officers, directors, employees and agents, from and against any and all claims arising out of your use of the licensed material other than as specifically authorized pursuant to this license.
11. No Transfer of License: This license is personal to you and may not be sublicensed, assigned, or transferred by you to any other person without publisher's written permission.
12. No Amendment Except in Writing: This license may not be amended except in a writing signed by both parties (or, in the case of publisher, by CCC on publisher's behalf).
13. Objection to Contrary Terms: Publisher hereby objects to any terms contained in any purchase order, acknowledgment, check endorsement or other writing prepared by you, which terms are inconsistent with these terms and conditions or CCC's Billing and Payment terms and conditions. These terms and conditions, together with CCC's Billing and Payment terms and conditions (which are incorporated herein), comprise the entire agreement between you and publisher (and CCC) concerning this licensing transaction. In the event of any conflict between your obligations established by these terms and conditions and those established by CCC's Billing and Payment terms and conditions, these terms and conditions shall control.
14. Revocation: Elsevier or Copyright Clearance Center may deny the permissions described in this License at their sole discretion, for any reason or no reason, with a full refund payable to you. Notice of such denial will be made using the contact information provided by you. Failure to receive such notice will not alter or invalidate the denial. In no event will Elsevier or Copyright Clearance Center be responsible or liable for any costs, expenses or damage incurred by you as a result of a denial of your permission request, other than a refund of the amount(s) paid by you to Elsevier and/or Copyright Clearance Center for

denied permissions.

LIMITED LICENSE

The following terms and conditions apply only to specific license types:

15. **Translation**: This permission is granted for non-exclusive world **English** rights only unless your license was granted for translation rights. If you licensed translation rights you may only translate this content into the languages you requested. A professional translator must perform all translations and reproduce the content word for word preserving the integrity of the article. If this license is to re-use 1 or 2 figures then permission is granted for non-exclusive world rights in all languages.

16. **Posting licensed content on any Website**: The following terms and conditions apply as follows: Licensing material from an Elsevier journal: All content posted to the web site must maintain the copyright information line on the bottom of each image; A hyper-text must be included to the Homepage of the journal from which you are licensing at http://www.sciencedirect.com/science/journal/xxxxx or the Elsevier homepage for books at http://www.elsevier.com; Central Storage: This license does not include permission for a scanned version of the material to be stored in a central repository such as that provided by Heron/XanEdu.

Licensing material from an Elsevier book: A hyper-text link must be included to the Elsevier homepage at http://www.elsevier.com . All content posted to the web site must maintain the copyright information line on the bottom of each image.

Posting licensed content on Electronic reserve: In addition to the above the following clauses are applicable: The web site must be password-protected and made available only to bona fide students registered on a relevant course. This permission is granted for 1 year only. You may obtain a new license for future website posting.

For journal authors: the following clauses are applicable in addition to the above: Permission granted is limited to the author accepted manuscript version* of your paper.

***Accepted Author Manuscript (AAM) Definition:** An accepted author manuscript (AAM) is the author's version of the manuscript of an article that has been accepted for publication and which may include any author-incorporated changes suggested through the processes of submission processing, peer review, and editor-author communications. AAMs do not include other publisher value-added contributions such as copy-editing, formatting, technical enhancements and (if relevant) pagination.

You are not allowed to download and post the published journal article (whether PDF or HTML, proof or final version), nor may you scan the printed edition to create an electronic version. A hyper-text must be included to the Homepage of the journal from which you are licensing at http://www.sciencedirect.com/science/journal/xxxxx. As part of our normal production process, you will receive an e-mail notice when your article appears on Elsevier's online service ScienceDirect (www.sciencedirect.com). That e-mail will include the article's Digital Object Identifier (DOI). This number provides the electronic link to the published article and should be included in the posting of your personal version. We ask that you wait until you receive this e-mail and have the DOI to do any posting.

Posting to a repository: Authors may post their AAM immediately to their employer's institutional repository for internal use only and may make their manuscript publically available after the journal-specific embargo period has ended.

Please also refer to Elsevier's Article Posting Policy for further information.

18. **For book authors** the following clauses are applicable in addition to the above: Authors are permitted to place a brief summary of their work online only.. You are not allowed to download and post the published electronic version of your chapter, nor may you scan the printed edition to create an electronic version. **Posting to a repository:** Authors are permitted to post a summary of their chapter only in their institution's repository.

20. **Thesis/Dissertation**: If your license is for use in a thesis/dissertation your thesis may be submitted to your institution in either print or electronic form. Should your thesis be published commercially, please reapply for permission. These requirements include permission for the Library and Archives of Canada to supply single copies, on demand, of the complete thesis and include permission for Proquest/UMI to supply single copies, on demand, of the complete thesis. Should your thesis be published commercially, please reapply for permission.

Elsevier Open Access Terms and Conditions

Elsevier publishes Open Access articles in both its Open Access journals and via its Open Access articles option in subscription journals.

Authors publishing in an Open Access journal or who choose to make their article Open Access in an Elsevier subscription journal select one of the following Creative Commons user licenses, which define how a reader may reuse their work: Creative Commons Attribution License (CC BY), Creative Commons Attribution – Non Commercial - ShareAlike (CC BY NC SA) and Creative Commons Attribution – Non Commercial – No Derivatives (CC BY NC ND)

Terms & Conditions applicable to all Elsevier Open Access articles:

Any reuse of the article must not represent the author as endorsing the adaptation of the article nor should the article be modified in such a way as to damage the author's honour or reputation.

The author(s) must be appropriately credited.

THE AMERICAN ASSOCIATION FOR THE ADVANCEMENT OF SCIENCE LICENSE TERMS AND CONDITIONS

Nov 05, 2014

This is a License Agreement between Megan P Shalaida ("You") and The American Association for the Advancement of Science ("The American Association for the Advancement of Science") provided by Copyright Clearance Center ("CCC"). The license consists of your order details, the terms and conditions provided by The American Association for the Advancement of Science, and the payment terms and conditions.

All payments must be made in full to CCC. For payment instructions, please see information listed at the bottom of this form.

License Number	3502730807969
License date	Nov 05, 2014
Order Content Publisher	The American Association for the Advancement of Science
Order Content Publication	Science
Order Content Title	A Ni-Fe-Cu Center in a Bifunctional Carbon Monoxide Dehydrogenase/ Acetyl-CoA Synthase
Order Content Author	Tzanko I. Doukov, Tina M. Iverson, Javier Seravalli, Stephen W. Ragsdale, Catherine L. Drennan
Order Content Date	Oct 18, 2002
Volume number	298
Issue number	5593
Type of Use	Thesis / Dissertation
Requestor type	Scientist/individual at a research institution
Format	Print and electronic
Portion	Figure
Number of figures/tables	1
Order reference number	None
Title of your thesis / dissertation	Synthesis and Reactivity of Acetyl Coenzyme A Synthase Active Site Analogues
Expected completion date	Dec 2014
Estimated size(pages)	218
Total	**0.00 USD**

Terms and Conditions

American Association for the Advancement of Science TERMS AND CONDITIONS

Regarding your request, we are pleased to grant you non-exclusive, non-transferable permission, to republish the AAAS material identified above in your work identified above, subject to the terms and conditions herein. We must be contacted for permission for any uses other than those specifically identified in your request above.

The following credit line must be printed along with the AAAS material: "From [Full Reference Citation]. Reprinted with permission from AAAS."

All required credit lines and notices must be visible any time a user accesses any part of the AAAS material and must appear on any printed copies and authorized user might make.

This permission does not apply to figures / photos / artwork or any other content or materials included in your work that are credited to non-AAAS sources. If the requested material is sourced to or references non-AAAS sources, you must obtain authorization from that source as well before using that material. You agree to hold harmless and indemnify AAAS against any claims arising from your use of any content in your work that is credited to non-AAAS sources.

If the AAAS material covered by this permission was published in Science during the years 1974 - 1994, you must also obtain

are distributed only in conjunction with your textbook at no additional cost to the user:

- Password-protected website
- Instructor's image CD/DVD and/or PowerPoint resource
- Student CD/DVD

All companions must contain instructions to users that the AAAS material may be used for non-commercial, classroom purposes only. Any other uses require the prior written permission from AAAS.

If your license is for the use of AAAS Figures/Tables, then the electronic rights granted herein permit use of the Licensed Material in any Custom Databases that you distribute the electronic versions of your textbook through, so long as the Licensed Material remains within the context of a chapter of the title identified in your request and cannot be downloaded by a user as an independent image file.

Rights also extend to copies/files of your Work (as described above) that you are required to provide for use by the visually and/or print disabled in compliance with state and federal laws.

This permission only covers a single edition of your work as identified in your request.

FOR NEWSLETTERS:

Permission covers print and/or electronic versions, provided the AAAS material reproduced as permitted herein remains in situ and is not exploited separately (for example, if permission covers the use of a full text article, the article may not be offered for access or for purchase as a stand-alone unit)

FOR ANNUAL REPORTS:

Permission covers print and electronic versions provided the AAAS material reproduced as permitted herein remains in situ and is not exploited separately (for example, if permission covers the use of a full text article, the article may not be offered for access or for purchase as a stand-alone unit)

FOR PROMOTIONAL/MARKETING USES:

Permission covers the use of AAAS material in promotional or marketing pieces such as information packets, media kits, product slide kits, brochures, or flyers limited to a single print run. The AAAS Material may not be used in any manner which implies endorsement or promotion by the American Association for the Advancement of Science (AAAS) or Science of any product or service. AAAS does not permit the reproduction of its name, logo or text on promotional literature.

If permission to use a full text article is permitted, The Science article covered by this permission must not be altered in any way. No additional printing may be set onto an article copy other than the copyright credit line required above. Any alterations must be approved in advance and in writing by AAAS. This includes, but is not limited to, the placement of sponsorship identifiers, trademarks, logos, rubber stamping or self-adhesive stickers onto the article copies.

Additionally, article copies must be a freestanding part of any information package (i.e. media kit) into which they are inserted. They may not be physically attached to anything, such as an advertising insert, or have anything attached to them, such as a sample product. Article copies must be easily removable from any kits or informational packages in which they are used. The only exception is that article copies may be inserted into three-ring binders.

FOR CORPORATE INTERNAL USE:

The AAAS material covered by this permission may not be altered in any way. No additional printing may be set onto an article copy other than the required credit line. Any alterations must be approved in advance and in writing by AAAS. This includes, but is not limited to the placement of sponsorship identifiers, trademarks, logos, rubber stamping or self-adhesive stickers onto article copies.

If you are making article copies, copies are restricted to the number indicated in your request and must be distributed only to internal employees for internal use.

If you are using AAAS Material in Presentation Slides, the required credit line must be visible on the slide where the AAAS material will be reprinted

If you are using AAAS Material on a CD, DVD, Flash Drive, or the World Wide Web, you must include the following notice in any electronic versions, either adjacent to the reprinted AAAS material or in the terms and conditions for use of your electronic products: "Readers may view, browse, and/or download material for temporary copying purposes only, provided these uses are for noncommercial personal purposes. Except as provided by law, this material may not be further reproduced, distributed, transmitted, modified, adapted, performed, displayed, published, or sold in whole or in part, without prior written permission from the publisher." Access to any such CD, DVD, Flash Drive or Web page must be restricted to your organization's employees only.

FOR CME COURSE and SCIENTIFIC SOCIETY MEETINGS:

Permission is restricted to the particular Course, Seminar, Conference, or Meeting indicated in your request. If this license covers a text excerpt or a Full Text Article, access to the reprinted AAAS material must be restricted to attendees of your event only (if you have been granted electronic rights for use of a full text article on your website, your website must be password protected, or access restricted so that only attendees can access the content on your site).

If you are using AAAS Material on a CD, DVD, Flash Drive, or the World Wide Web, you must include the following notice in any electronic versions, either adjacent to the reprinted AAAS material or in the terms and conditions for use of your electronic

Gratis licenses (referencing $0 in the Total field) are free. Please retain this printable license for your reference. No payment is required.